1996

Polar intermetallic compounds of the silicon and arsenic family elements and their ternary hydrides and fluorides

Efigenio Alejandro León-Escamilla
Iowa State University

INFORMATION TO USERS

This manuscript has been reproduced from the microfilm master. UMI films the text directly from the original or copy submitted. Thus, some thesis and dissertation copies are in typewriter face, while others may be from any type of computer printer.

The quality of this reproduction is dependent upon the quality of the copy submitted. Broken or indistinct print, colored or poor quality illustrations and photographs, print bleedthrough, substandard margins, and improper alignment can adversely affect reproduction.

In the unlikely event that the author did not send UMI a complete manuscript and there are missing pages, these will be noted. Also, if unauthorized copyright material had to be removed, a note will indicate the deletion.

Oversize materials (e.g., maps, drawings, charts) are reproduced by sectioning the original, beginning at the upper left-hand corner and continuing from left to right in equal sections with small overlaps. Each original is also photographed in one exposure and is included in reduced form at the back of the book.

Photographs included in the original manuscript have been reproduced xerographically in this copy. Higher quality 6" x 9" black and white photographic prints are available for any photographs or illustrations appearing in this copy for an additional charge. Contact UMI directly to order.

UMI

A Bell & Howell Information Company
300 North Zeeb Road, Ann Arbor MI 48106-1346 USA
313/761-4700 800/521-0600

Polar intermetallic compounds of the silicon and arsenic family elements and their ternary hydrides and fluorides

by

Efigenio Alejandro León-Escamilla

A dissertation submitted to the graduate faculty

in partial fulfillment of the requirements for the degree of

DOCTOR OF PHILOSOPHY

Major: Inorganic Chemistry

Major Professor: John D. Corbett

Iowa State University

Ames, Iowa

1996

Graduate College

Iowa State University

This is to certify that the doctoral dissertation of

Efigenio Alejandro León-Escamilla

has met the dissertation requirements of Iowa State University

Signature was redacted for privacy.

Major Professor

Signature was redacted for privacy.

For the Major Program

Signature was redacted for privacy.

For the Graduate College

TABLE OF CONTENTS

CHAPTER I. GENERAL INTRODUCTION

Our ability to understand, and possibly to predict, the properties of intermetallic compounds on the basis of their structural information is many times limited by uncertainties about their correct compositions. The unsuspected presence of adventitious impurities in a compound may lead one to draw inaccurate, or equivocal, conclusions about their unexplained behaviors. The occurrence of such situations in the published literature has been quite frequent. For instance, the inadvertent presence of hydrogen impurities in what was thought to be pure calcium prompted Smith and Bernstein[1] to assign a hexagonal allotropic form to calcium. Subsequent investigation by Peterson and Fattore[2] showed the hexagonal phase was an intermediate in the binary calcium–hydrogen system. In similar circumstances, an hexagonal allotrope of ytterbium metal was later established as an ytterbium hydride compound.[3]

Adventitious impurities in an intermetallic compound may stabilize a phase in a particular structure that would otherwise not form in the binary system. Such stabilization processes are probably electronically driven. Examples in literature of impurity-stabilized compounds are vast. Thus, many of the so-called Nowotny phases are, or were thought to be, compounds stabilized by non-metallic impurities.[4,5] The presence and stabilizing effects of impurities were not recognized until higher quality reagents and more accurate and thoughtful experimental techniques were available, and there was need to reconsider conflictive information already reported. As an illustration, arguments of dimorphism between a hexagonal and a tetragonal structure for La_5Sn_3 were clarified by Kwon and Corbett.[6] They demonstrated that the hexagonal phase was an oxygen-stabilized compound, La_5Sn_3O.

The structures of intermetallic compounds formed by the combinations of pre- and post-transition elements can frequently be rationalized by the Zintl principles from the chemist's point of view. Schäfer and coworkers[7,8,9] have particularly demonstrated that a great many favorable combinations of structures and compositions can be classified as Zintl phases. The Zintl concept,[10] in a very simple way, is based on the assumption that the electropositive element, of say a binary phase A_xB_y, transfers all its electrons to the electronegative element (B) which uses these extra electrons to form

covalent bonds (B-B), i.e., two-center two-electron bonds and localized nonbonding pairs. It is believed that the elements tend to do this in order to achieve closed shell configurations. The apparent closed shell configurations of Zintl phases suggest their properties should be those of semiconductive and diamagnetic compounds. It is remarkable how a set of simple principles enables us to repeatedly predict the electronic and magnetic properties of numerous intermetallic compounds. Recently, however, it has been found that several compounds that structurally qualify as Zintl phases are metallic conductors.[11,12] Arguments of weak cation–anion and cation–cation electronic interactions had been invoked to explain such unexpected behavior.[13,14,15]

Studies on the stabilizing effect of interstitial hydrogen in intermetallics are sparse. Most of these studies has been directed to understanding the dynamics of hydrogen absorption and have been encouraged by the potential of the materials for hydrogen storage and hydrogen pumps.[16,17,18] Additionally, most of the experiments in this area have been limited to the lanthanide elements. Hydrogen, a common and sizable impurity in alkaline-earth metals,[19] has been repeatedly ignored as far as its participation in reactions with the latter metals. Presumption of its "inactive spectator" role is, many times, equivocal. Suspicions about the involvement of hydrogen in the solid state chemistry of the alkaline-earth and divalent rare-earth metal pnictides originated after ambiguities between experimental evidence obtained in this laboratory and previous literature reports were found.

In an attempt to clarify several ambiguities from previous reports, we have through careful and purposeful work investigated the interstitial-stabilizing influence of hydrogen in the alkaline-earth and divalent rare-earth metal compounds with pnictides, tetrelides and trielides. Because there was no precedent for this subject, the present study was limited to phases with A_5B_3 stoichiometry for which several repetitive contradictions seem to exist. Work with several of the trivalent rare-earth metals was pursued as well to support arguments and conclusions about the divalent systems. Several compounds with stoichiometries different than A_5B_3 were also investigated; however, their study was only pursued when they were considered of special interest. Because of the similitude in size and, often, chemistry, between the fluoride and hydride

ions in the solid state, several experiments with metal fluorides were carried out for further evidence on the findings in the intermetallic–hydrogen systems. In an effort to define boundaries to the use of the Zintl concepts to predict properties, the magnetic susceptibility and electrical resistivity measurements as functions of temperature were made on several compounds. Extended Hückel MO band calculations were performed as well to better discern the observed structure–properties relationships.

CHAPTER II. EXPERIMENTAL

Materials

Source

High purity elements and salts were used as reagents in all the reactions performed. Alkaline-earth metals (Ae) and several rare-earth metals (RE) were dehydrogenated prior to use. Table II-1 consolidates information about the source and purity of the materials employed as reagents.

Most of the synthetic work was consistently carried out following the well established techniques developed in Corbett group.[20] A few variations to these techniques were devised and will be mentioned in some more detail.

Handling

Because several reagents and products are highly sensitive to air, their handling require of inert atmospheres and high vacuum techniques. All the reactions were loaded in a helium-filled high quality dry-box from Vacuum Atmospheres Co., model DLX-001-Sp. This dry-box is equipped with a water sensor of Panametrics Systems model 3A. The work was routinely carried out under a humidity regime of 0.2-0.4 ppm of water. The reaction containers were opened in a nitrogen-filled box equipped with a Panametrics Systems model 700 water sensor and a microscope. The microscope facilitated the visual inspection of the products as well as selection and mounting of crystals inside glass capillaries.

Containers

Because of its inertness to most of the reagents, tantalum metal was used as reaction container. Additionally, Ta metal at temperatures higher than 550°C acts as semipermeable membrane that allows hydrogen to pass through[21] but it reacts with carbon and oxygen. However, prolonged exposure to hydrogen at high temperatures, T > 1100°C, may lead to tantalum embrittlement.[22]

Seamless tantalum tubing of ~6.3 mm o.d. (1/4 inch) was cut in 38 mm lengths and cleaned with an acid solution until evolution of NO_x gases ceased. The Ta cleaning

Table II-1. Materials.

Reagent	Source	Purity
$H_2(g)$	Matheson	99.999%
$D_2(g)$	Matheson	99.5%
Ca	APL Eng.Labs.	99.99%
Sr	APL Eng.Labs.	99.95%
Ba	APL Eng.Labs.	99.9%
Y	Ames Lab.[a]	
La	Ames Lab.	
Sm	Ames Lab.	
Eu	Ames Lab.	
Gd	Ames Lab.	
Tb	Ames Lab.	
Dy	Ames Lab.	
Ho	Ames Lab.	
Er	Ames Lab.	
Tm	Ames Lab.	
Yb	Ames Lab.	
Zn	Fisher Scientific	99.99%
Ga	Johnson-Matthey	99.999%
In	Cerac	99.999%
Tl	Johnson-Matthey	99.998%
Si		Electronic Grade
Ge	Aesar	99.999%
Sn	Baker's Analyzed	99.999%
Pb	Aesar	99.9999%
As	Aldrich	99.9999%
Sb	Aesar	99.999%
Bi	Oak Ridge Nat.Lab.	Reactor Grade
CaH_2	In lab. preparation	
SrH_2	In lab. preparation	
BaH_2	In lab. preparation	
$SmH_{2.5}$	In lab. preparation	
EuH_2	In lab. preparation	
GdH_3	In lab. preparation	
YbH_2	In lab. preparation	
CaF_2	In lab. preparation	
SrF_2	In lab. preparation	
BaF_2	In lab. preparation	
YF_3	Ames Lab.	
GdF_3	Ames Lab.	
Al_2O_3	ICN Pharmaceuticals	Col.Chromatography

[a] All Ames Lab. metals have a purity > 99.99%.

acid solution was prepared as 55% H_2SO_4, 25% HNO_3 and 20% HF of concentrated acids. This acid solution was rinsed off with abundant deionized water. The cleaned tubes were then dried in the air, avoiding their contact with dust or grease.

Once cleaned, the tubes were crimped on one end and welded in either a helium or an argon-filled arc-welder. The reagents, metals and salts were loaded in the glove-box through the open end, which was crimped and later welded-off. Exposure of the reagents to air was minimized by transferring the ready-to-weld containers from the He-box to the welder in closed tubes. A total of ~250 mg of reactants was loaded in each reaction. This amount of material was regularly sufficient to characterize the products, i.e. Guinier powder patterns, magnetic and electrical resistivity measurements.

Dehydrogenation of Metals

The hydrogen content of the alkaline-earth and rare-earth metals was decreased by heating the metals under dynamic high vacuum. Commercial alkaline-earth metals are known to contain between 6-20% at.wt. of hydrogen,[19] information that seldom is reported. Rare-earth metals, on the other hand, are much less hydrogen contaminated. The content of hydrogen in these metals may increase as the materials are exposed to humidity.

Small pieces of a metal were placed in a Ta container which was arc-welded-shut. The closed Ta container was then encapsulated in a fused silica jacket that in turn was connected to a high vacuum system. Before connection, the inside of the jacket was first washed with a once-used Ta cleaning solution and rinsed off with abundant deionized water. The high vacuum system was equipped with a mercury diffusion pump, and routine work with this system was at a vacuum below discharge of the Tesla coil, i.e. ~10^{-5}–10^{-6} torr. A cold trap cooled with liquid N_2 was placed between the line and the silica jacket.

The metals were heated for several hours at approximately 100–200°C below their respective melting points. This heat treatment lasted between 8 and 24 hours depending on the amount of material to be dehydrogenated. Specifics about the heat treatment and completion of a dehydrogenation reaction in a metal were estimated from

the reported metal hydride decomposition isotherms.[23] Cleaned metals were taken out of their containers just prior to use. The resulting cleaned metals appeared shinier and brighter than those without thermal treatment.

Preparation of Metal Fluorides (MF_2)

Alkaline-earth-metal carbonates ($AeCO_3$) and hydrofluoric acid were reacted to prepare the metal fluorides. Approximately two equivalents of concentrated HF, 45% vol, were slowly added to a stirred suspension of one equivalent of $AeCO_3$ in 200 ml of water. Two more equivalents of HF solution were added when evolution of CO_2 gas ceased. This acidic solution was stirred overnight. The majority of the acidic solution was decanted, and the solid filtrated and washed on a Buchner funnel until the wash water was neutral in pH. The solid was then dried under vacuum at 400°C for about 24 hours. A fine white powder resulted from these reactions, yield ~80%. Guinier x-ray powder patterns were used to confirm the products as single phase.

Preparation of Binary Metal Hydrides (MH_x)

Binary metal hydrides were prepared by the direct reactions between hydrogen gas and the metals. Small pieces of a metal were placed in a previously cleaned molybdenum boat inside a finger-like fused silica vessel. The boat was made of a small piece of Mo foil and was cleaned in boiling conc. HCl for ~20 min. before use.

The reaction vessel was thrice evacuated and filled with H_2 gas before initiating the reaction. Each metal was slowly heated up to a temperature between 400°C and 600°C at constant hydrogen pressure, ~600 to 700 torr. The specific conditions to hydrogenate a metal were based upon their reported AH_x decomposition isotherms.[23] The onset of reaction was recognized by a drop in the gas pressure and was considered terminated, when an increment in temperature was accompanied by a parallel increment in pressure. Products were then annealed under H_2 at about 10 to 20°C below the maximum reaction temperature for 4 to 12 hours. Table II-2 summarizes some information about the preparation and characteristics of the binary metal hydrides synthesized. Identification of the products was made by Guinier x-ray powder patterns.

Table II-2. Some experimental condition and characteristics of the binary metal-hydrides prepared.

Compound[a]	Synthesis Temp.(°C)	H_2 Pressure (torr)	Product Color (after grinding)	Structure type[b]
CaH_2	600	650	white	ACS
SrH_2	400	650	white	ACS
BaH_2	480	700	white	ACS
$SmH_{2.5}$	420	600	black	HOH
EuH_2	700	670	dark-brown	ACS
YbH_2	550	665	brown	ACS
GdH_3	500	650	dark-grey	HOH

[a] The cell dimensions of the products corresponded to the reported compositions.
[b] Structure type: ACS= Anti-Co_2Si-type (Pnma, #62).
HOH= HoH_3-type (P3c1, #165).

The cell dimensions of these hydrides agreed with constants for the reported compositions.[23,24] All products were single phases.

Preparation of Binary and Ternary Intermetallic Compounds

Binary intermetallic compounds and then ternary hydrides and fluorides compounds were prepared by the direct reaction between the elements and the binary metal hydrides or fluorides. Two techniques were essentially followed: (a) reactions in sealed fused silica containers, and (b) reactions in absence of hydrogen or under dynamic vacuum.

Reactions in presence of hydrogen or in sealed SiO_2 containers (sc)

Reactions that involved binary hydrides and dehydrogenated metals were loaded in Ta containers which were then encapsulated in fused silica (SiO_2) jackets. To

minimize the presence of impurities in the systems, the insides of the jackets were washed with once-used Ta-cleaning solution and sufficient deionized water. The jackets were then evacuated to 10^{-6} torr, flamed and sealed off. Flaming of the jacket was necessary to decrease the amount of water released from the dehydration of the fused-silica. Reduction of the water generated by the silica tubes provides a significant amount of hydrogen to the reactions, as it will be evidenced in our results.

For the purpose of controlling the availability of hydrogen in each reaction, only one Ta container was encapsulated per SiO_2 jacket. The transparency of Ta to hydrogen at high temperatures was the restricting factor. In general the reactions were loaded according to the equation:

$$5\text{-}y/2\ A_{cleaned} + y/2\ AH_2 + 3\ (Pn,Tt,Tr) \longrightarrow A_5(Pn,Tt,Tr)_3H_y$$

(loaded compositions: y= 0.0, 0.5, 1.0 and 2.0)

Reactions loaded following this sc technique were heated to maximum temperatures of 1200°C. Problems related to softening of the silica jacket[25] or Ta leakage from internal pressure buildup were never experienced; nonetheless, caution was exercised at all times. Reactions carried out by this sc technique are labeled as $A_5(Pn,Tt,Tr)_3H_y$, y= 0.0, 0.5, 1.0 and 2.0, throughout this work. Reactions carried out under these conditions but without added hydrogen and using noncleaned metals (A') are referred as $A'_5(Pn,Tt,Tt)_3$ and specified as sc.

Reactions in absence of hydrogen or under dynamic vacuum (dv)

Reaction in absence of hydrogen were carried out under continuous high vacuum conditions. The fused silica jacket, as a modification to the previous technique, was connected to the high vacuum line throughout the entire heating cycle, although several limitations arose from this technique. The system was set up as the one described for the dehydrogenation of metals.

Because the success of an experiment greatly depended on the quality of the

high vacuum, the heating sequences were planned keeping in mind the reliability of the high vacuum line. As a consequence, long heating cycles were avoided. Additionally, because of the experimental set up, a rapid quenching from high temperatures was troublesome and limited to very few reactions. Quenching a reaction from high temperatures required the fast removal of the furnace from the line followed by rapid cooling of the samples with a stream of liquid N_2. Safety reason impeded us from making this experience a common procedure, as breakage of the vacuum line may occur. A maximum temperature of 1200°C was used in these reactions. Problems of softening and collapsing of the fused silica jacket were never experienced.

Preparation of Ternary Deuterides

Samples for powder neutron diffraction, $Ca_5Bi_3D_x$ and $Ca_5Sn_3D_x$, were prepared in a two-step experiment. The first step, dehydrogenation of metals, was carried out with the reagents heated at 1100°C or 1200°C for two hours under continuous vacuum. The second step, reaction with D_2 gas, was carried under a constant D_2 pressure of ~400 torr for one hour at 1100°C. Thereafter, the temperature was slowly decreased to 850°C and kept there for 72 hours followed by a slow cooling to room temperature. After the reactions, the tantalum containers were very brittle. Consequently, the target products were separated from the tantalum fragments by visual inspection.

Furnaces

Marshall tube furnaces were used to heat reactions below 1200°C; for higher temperatures an Astro High Temperature vacuum furnace model 1000-2560-FP20 from Thermal Technology was used. This high temperature furnace consists of two chambers separated by a gas-tight alumina muffle tube, with each chamber equipped with a high vacuum system. The internal chamber, where the samples are placed, is mainly evacuated by a turbomolecular pump to maintain an environment low of hydrocarbons. The external chamber, where the graphite heating elements are located, is evacuated with an oil-diffusion pump. Vacuums regimes of 10^{-7} and 10^{-6} torr were typical of each chamber. Quenching reactions from high temperatures was not possible with this

furnace.

Several reactions that involved rare-earth metals were carried out in an induction furnace powered by a Lepel Power Supply model T-20-3-KC-A-S. The sample chamber in this furnace works under a continuous high vacuum conditions, p~ 10^{-7} torr.

Characterization Techniques

Identification of Products and Lattice Parameters Calculation

Guinier X-ray powder patterns were used to evaluate the purity of products and to obtain their lattice parameters. Patterns were taken with Simon-Guinier cameras from Enraf-Nonius, model FR552, using monochromated Cu α_1 radiation (λ= 1.54056 Å). These cameras are designed to work under continuous rough vacuum conditions. A representative sample of the product was mixed with NIST (NBS) silicon as an internal standard and placed between two pieces of Scotch™ tape that served as an impromptu sample holder and sealant from the atmosphere. Exposure of the mounted samples to air was minimized as much as possible by transferring the samples from the glovebox to the cameras in closed containers.

Identification and yield estimation were made by matching experimental and calculated model patterns. The program POWDERV7[26] and its plotting subroutines were used to calculate and plot the ideal Guinier powder patterns. Intensity of lines, 2θ regions, cell size and symmetry are weighting factors that were considered to guesstimate the yield of a phase from line intensities. Consequently, high quality powder patterns were critical to effectuate reliable evaluations.

Calculation of the lattice parameters from indexed powder patterns was done with the least squares program LATT.[27] Previous to indexing, the patterns were read and digitized with the Line Scanner LS20 of KEJ Instruments, Sweden. Standardization of the digitized patterns, as function of the Si lines locations, was done with the program SCANPI8[28] for a wavelength of λ= 1.54056 Å (Cu_{α_1}). All the lattice dimensions reported in this work were calculated from patterns that were read with the Line Scanner. Four standard silicon lines were the minimum necessary to consider a pattern satisfactorily read and ready to index.

Single Crystal X-Ray Work

The crystallographic work was initiated by evaluating the diffracting quality of a crystal through its Laue photos. Subsequent single crystal x-ray work varied, depending upon the availability of information about the specific compound. When its structure, based on Guinier information, was isotypic with a known structure type, and important to the research, the crystal was passed directly to the single-crystal diffractometer. On the other hand, when ambiguity regarding the symmetry and space group of a new phase existed, Weissenberg and precession layer photographs were taken. In cases where suspicions about presence of a superstructure existed, overexposed Weissenberg or precession photos were taken as well.

Two single-crystal x-ray diffractometers were regularly used to collect data, the four-circle rotating anode Rigaku AFC6R and the Enraf-Nonius CAD4. Both diffractometers are automated and set to use graphite monochromated Mo K_α radiation, λ= 0.7169 Å. The cell type was normally determined after indexing 20 to 25 reflections found through the SEARCH subroutines of each instrument's software. Selection of the cell on which to collect data was based on the indexed reflections and known information about the phase, i.e. powder film work, single crystal and axial photographs. All data sets were collected redundant and at room temperature. Three intense reflections were used as standard to monitor the crystal alignment or decay, although sample decomposition was never observed.

Data processing included Lorentz polarization correction and empirical absorption correction using an average ψ-scan measurement obtained from three or four reflections with χ>80°. Two-theta dependent empirical absorption corrections, DIFABS,[29] were applied as well. This last correction was found useful when poor ψ-dependent corrections were observed. The data were then averaged in the corresponding point group to generate a reduced set that would be used in the structure determination and refinement.

If a compound adopted a known structure type, the positional parameters of the parent phase were used as initial model for the refinement. Otherwise the model was obtained by direct methods with the SHELX86[30] program. Structural refinements with a

set of observed reflections ($I > 3.00\sigma_I$) were then done using a full matrix least-squares calculation with the TEXSAN[31] software package from Molecular Structures Corp. Results of refinements and structural information are summarized in tables throughout this work. Notice that for cases where DIFABS absorption correction was applied, the reported transmission factors are relative and exceed the 1.00 upper limit. Guinier lattice constants were used to calculated bond distances and angles, as these constants are commonly more accurate than those calculated by the single crystal diffractometer programs.

Statistical tests and terms reported in the tables are following defined:

Residual factors for refinement based on F:

$$R = \Sigma \; | |F_o| - |F_c| | \; / \; \Sigma \, |F_o|$$

$$R_w = \left[\left(\Sigma \, w \, (|F_o| - |F_c|)^2 \; / \; \Sigma \, w \, F_o^{\,2} \right) \right]^{1/2}$$

$$w = 1/\sigma_F^{\,2}$$

The equivalent isotropic temperature factor:[32]

$$B_{eq} = (8\pi^2/3) \; \Sigma_i \; \Sigma_j \; U_{ij} a_i^* a_j^* \vec{a}_i \cdot \vec{a}_j$$

Coefficients U_{ij} of the anisotropic temperature factors:

$$T = \exp(-2\pi^2(a^{*2}U_{11}h^2 + b^{*2}U_{22}k^2 + c^{*2}U_{33}l^2 + 2a^*b^*U_{12}hk + 2a^*c^*U_{13}hl + 2b^*c^*U_{23}kl))$$

Powder Neutron Diffraction

The neutron diffraction data for $Ca_5Bi_3D_x$ and $Ca_5Sn_3D_x$ were taken in the High-Resolution Powder Diffractometer HB-4[33] at the Oak Ridge National Lab. neutron facility by Prof. C. Stassis and Dr. P Dervenagas from the Solid State Physics, Ames Lab. The

neutron beam at this facility is generated by the decay of highly enriched ^{235}U, and is monochromated by the (115) reflection of a Ge crystal, oriented to give a wavelength λ=1.4177 Å. The instrument is equipped with a bank of 32 equally spaced ^{3}He detectors for scattering angles between 11 and 135°, that give a resolution minimum of $\Delta d/d = 2 \times 10^{-3}$.

Approximately 2.5 and 3.0 g of powdered $Ca_5Bi_3D_x$ and $Ca_5Sn_3D_x$, respectively, were transferred in a He dry-box to vanadium cans, and placed in the diffractometer. The vanadium cans were sealed with indium metal through screw on caps. The data were collected at room temperature and for full scans, 11 to 135°, over ~20 hours per sample. The process and refinement of the data was done with GSAS[34] software for Rietveld structure analysis by Dr. Dervenagas with the general-least-squares program GENLES.

The statistical terms reported in tables are defined:

Residual factors or quality of the refinement;

$$R_p = (\Sigma |I_o - I_c|) / \Sigma I_o$$

$$R_{wp} = (M / \Sigma w I_o^2)^{1/2}$$

where;[35] $M = \Sigma w(I_o - I_c)^2$

The reduced χ^2 or "goodness of fit":

$$\chi^2 = M / (N_{obs} - N_{var})$$

The isotropic temperature factor U_{iso}:

$$T = \exp (-8\pi^2 U_{iso} \sin^2\theta / \lambda^2)$$

Electrical Resistivity Measurements

The electrical resistivity measurements were made by the electrodeless Q method on samples of high purity, estimated > 90%. The resistivity of the sample is evaluated as function of the quality factor (Q) of a closed circuit at a given temperature. The Q readings were made with a Hewlett-Packard model 4342A Q meter over the temperature range of approximately 100 to 298K. These resistivity values are based on the skin response of the sample to a field of constant frequency, usually 35 MHz, passing through a coil that surrounds the sample container. The variation in quality factor of the circuit is read with (Q) and without the sample (Q_o) at a given temperature, normally $Q > Q_o$.[36]

Sieved particles of averaged size (a) are diluted in an insulating Al_2O_3-matrix and sealed under He in a 10 mm o.d. Pyrex tube that serves as sample container. The electrical resistivity is calculated from the following equations:

$$\rho = B\,(Va)/\Delta(1/Q)$$

where:

$$\Delta(1/Q) = (1/Q) - (1/Q_o)$$

where ρ is the electrical resistivity (Ω·m), B is a constant for the instrument and coil used ($B = 4.84 \times 10^5$),[37] V is the volume of pure phase (m^3) calculated from the weight-density ratio, and *a* is the average radius of the particles (m). These equations assume that the samples are diamagnetic or weakly paramagnetic; various corrections need to be included otherwise. The resistivity values obtained from this method are approximately within a factor of three of those measured by four-probe methods.[38]

The resistivity values in this work are reported in units of micro-ohm centimeter (μ-Ω·cm) and the temperature resistivity coefficient (as %) are calculated from the slope of the ρ versus T curves ($[\partial\rho/(\rho_o\partial T)]\cdot 100$) in K^{-1},[39] where ρ_o is the resistivity of the sample at the highest temperature measured.

Magnetic Susceptibility Measurements

A superconducting-quantum-interference-device magnetometer SQUID from Quantum Design was used to measure the magnetic properties of the samples. The magnetometer is operated by Mr. J. Ostenson from Solid State Physics, Ames Lab. Magnetic susceptibility as a function of temperature was measured from 6 to 300K at a field of 3 Tesla unless otherwise indicated. The sample was held between two fused silica rods that fit inside a 5 mm o.d. SiO_2 tube that functioned as the sample holder.[40] The samples are sealed under He gas.

All the magnetic susceptibility values (χ) reported in this work were corrected for both sample holder[40] and diamagnetic core[41] corrections. For samples that followed a paramagnetic Curie-Weiss temperature behavior, their effective magnetic moment (μ_{eff}) and Weiss temperature (θ) was calculated from the linear regression of the $1/\chi$ versus T plots, commonly for T > 100K. Nonlinear corrections to χ–T data gave, in several cases, doubtful effective moment values. Consequently, and in order to be consistent throughout this work, they were not applied.

Theoretical Calculations

Electronic structure calculations utilized the extended Hückel approach[42] within the tight-binding approximation.[43] Energy density of states (DOS) and crystal orbital overlap population curves (COOP) were evaluated using special k point sets,[44] with the tight-binding overlaps included within two neighboring unit cells along every translation vector. The atomic orbital parameters used in the calculations are listed in Table II-3.

Table II-3. Parameters used for EHMO band calculations.

Atom	Orbital	H_{ii} (eV)	ξ_{i1}	Ref.
H	1s	-13.60	1.30	45
Ca	4s	-7.00	1.10	45
	4p	-4.00	1.10	
Sr	5s	-6.62	1.21	45
	5p	-3.92	1.21	
Ba	6s	-6.32	1.23	46
	6p	-3.85	1.23	
Ge	4s	-16.00	2.16	45
	4p	-9.00	1.85	
Sn	5s	-16.16	2.12	45
	5p	-8.32	1.82	
Sb	5s	-18.80	2.32	45
	5p	-11.70	2.00	
Bi	6s	-7.79	2.56	45
	6p	-15.19	2.07	
Tl	6s	-11.60	2.52	45
	6p	-5.80	1.77	

CHAPTER III. PNICTIDE SYSTEMS

$A_5Pn_3H_x$ Systems

Introduction

Problems with the alkaline-earth-metal and divalent rare-earth-metal pnictides, A_5Pn_3, were evident after we noticed several inconsistencies in their behaviors and reported cell dimensions.[24] Subsequently, no clear structural trends could be found for these compounds. Predictions by Bruzzone et al.[47] about the structures of unknown Ae_5Pn_3 compounds would ordinarily fail. Phases like Ca_5As_3, $Sr_5(As,Sb)_3$ $Ba_5(As,Sb,Bi)_3$, $Sm_5(Sb,Bi)_3$, Eu_5As_3 and Yb_5As_3 were known to crystallize solely in the hexagonal Mn_5Si_3-type structure (M). Others phases like Ca_5Bi_3, $Eu_5(Sb,Bi)_3$ and Yb_5Bi_3 were reported only with the orthorhombic β-Yb_5Sb_3 structure type (Y), and compounds like Ca_5Sb_3, Sr_5Bi_3 and Yb_5Sb_3 were considered dimorphic with the hexagonal structure as the higher temperature phase. A recent report included Sr_5Sb_3 as one additional example of a dimorphic system.[48]

Preparations of single phase products of the assumed dimorphic compounds were in fact not always possible. Such incapacities to prepare high-yield phases led to uncertainties about the formulation of the orthorhombic Yb_5Sb_3 versus Yb_5Sb_2[49] because reactions with excess rare-earth metal were necessary to modestly increase the yield of the Y phase. Arguments about slow transformation between the M and Y forms of Yb_5Sb_3 were drawn after finding that long annealing periods were needed to transform the M form into the Y. The opposite conversion, Y to M, was never successful, and a mixture of products was always observed.

Suspicions about the involvement of a stabilizing impurity in either of these structures, M or Y, as well as difficulties in reproducing the reported lattice parameters motivated W.-M. Humg[50] to search for evidence about the temperature, or the composition, variable that controlled the distribution between the orthorhombic and the hexagonal structures. Although he was not able to find any variable that caused the phase transformation in Ca_5Sb_3 or Sr_5Bi_3 phases, he was able to prepare single-phase products through the inclusion of halides as ternary stabilizing elements. Hence, the hexagonal phase (M-type) was stabilized with chloride or bromide ions, i.e., Ca_5Sb_3Cl,

$Ca_5Bi_3(Cl,Br)$, Sr_5Sb_3Cl, $Ba_5Sb_3(Cl,Br)$ and $Ba_5Bi_3(Cl,Br)$. Such ease with which the M-type phases bind certain interstitial atoms was already known in the so-called Nowotny phases, e.g., $Ti_5Sb_3C_x$.[4]

The hexagonal M structure (Mn_5Si_3-type, $P6_3/mcm$, sp.gr.#193, Z=2) can be described in part as infinite chains of confacial $^1_\infty[Mn(2)_{6/2}Si_{6/2}]$ trigonal antiprims along 0,0,z. Figure III-1 illustrates the [001] projection of this cell where the lines between atoms are drawn to help visualize structural characteristics. The confacial antiprismatic feature is also known in the structure of condensed cluster compounds KMo_3S_3 or so-called Chevrel phases.[51] The Mn_5Si_3 structure also contains linear chains of Mn atoms, $^1_\infty[Mn(1)_2Si_{6/2}]$, along 1/3, 2/3, z and 2/3, 1/3, z with a relatively short Mn–Mn repeat of c/2. The Mn atoms in the linear chain are in fact bound to six of the same Si atoms in a quasi-trigonal-antiprismatic fashion. Figure III-2 gives a side view of the two chains that extent along the c-axis and their immediate environments.

It should be recognized that one of the most interesting features of this structure are the interstitial sites within the confacial chains, shown as Z in Figure III.2. Understanding of the structure and its electronic requirements led Y.-U. Kwon[52] to develop a ample interstitial chemistry for the Zr_5Sn_3 host, Zr_5Sn_3Z with Z= B, C, N, O, Al, Si, P, S, Cu, Zn, Ga, Ge, Sn, As and Se. Similarly, Guloy[53] developed the interstitially stabilized chemistry of Ca_5Pb_3Z, e.g. Z= V, Cr, Ni, Co, Cu, Zn, Ru, Ag, Cd. The binary Ca_5Pb_3 crystallizes in a distorted version of the Mn_5Si_3 structure.

The orthorhombic Y structure (β-Yb_5Sb_3-type, Pnma, sp.gr.#62, Z= 4)[54] can be described in terms of very similar (but not superimposed) layers of Yb atoms at y= 1/4 and y= 3/4 that are related by glide planes normal to the a- and c-axis, or by inversion through 1/2,1/2,1/2, see Figure III-3. Two layers define nominal trigonal prisms that are interconnected by sharing all edges parallel to b, and each is centered by a Sb atom near y= 1/2 (or 0). This array is infinite along b as well with the trigonal prisms sharing opposite triangular faces. Large hexagonal channels around 0,y,1/2 that are generated by the array of condensed prisms contain two additional Yb atoms near y=0, 1/2 and two Sb atoms at y= 1/4, 3/4.

Hurng[50] was able to prepare ternary derivatives with the Y structure by inserting

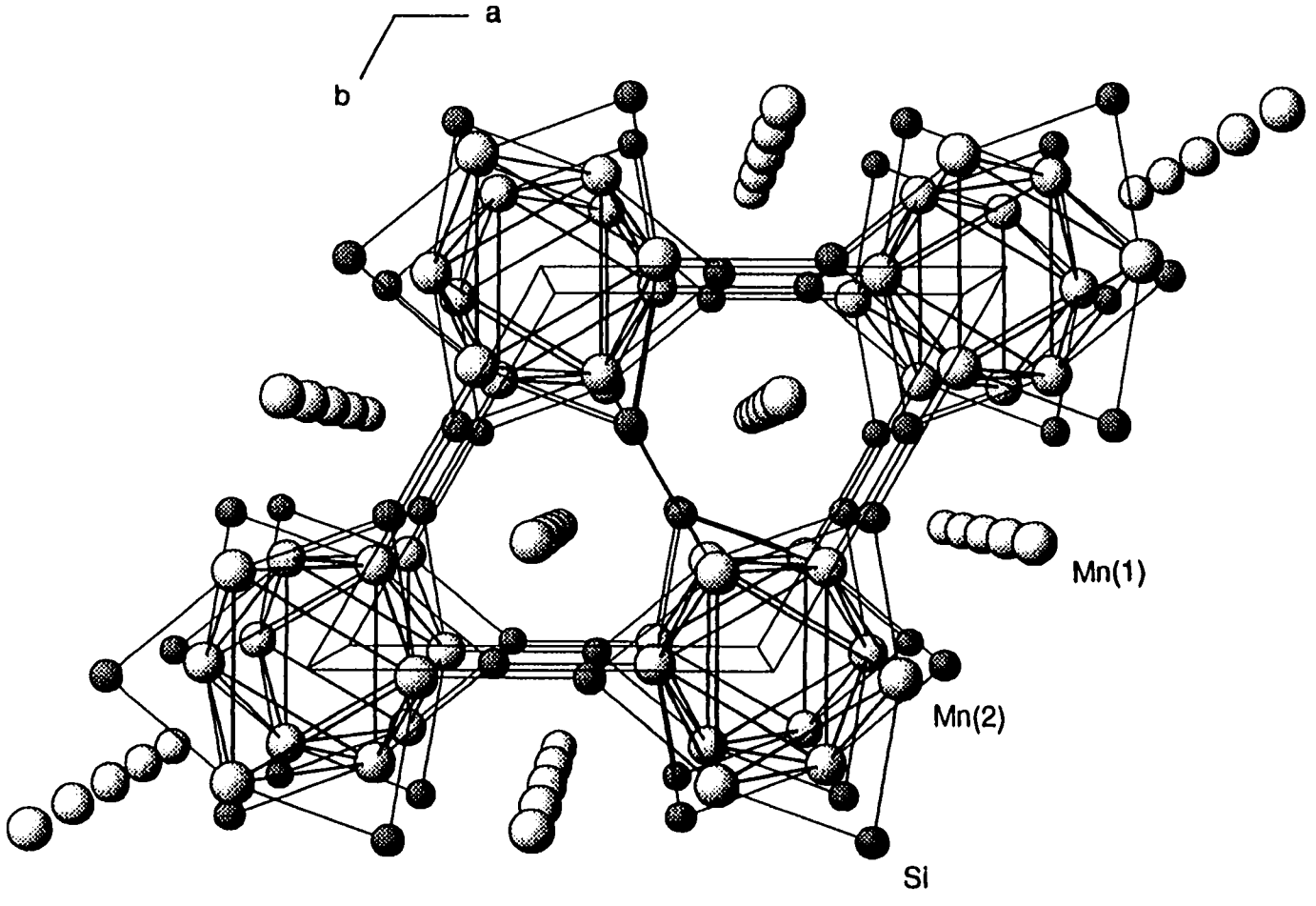

Figure III-1. The extended view of the Mn_5Si_3 structure projected along [001]. Large and small (dark) spheres represent Mn and Si atoms respectively.

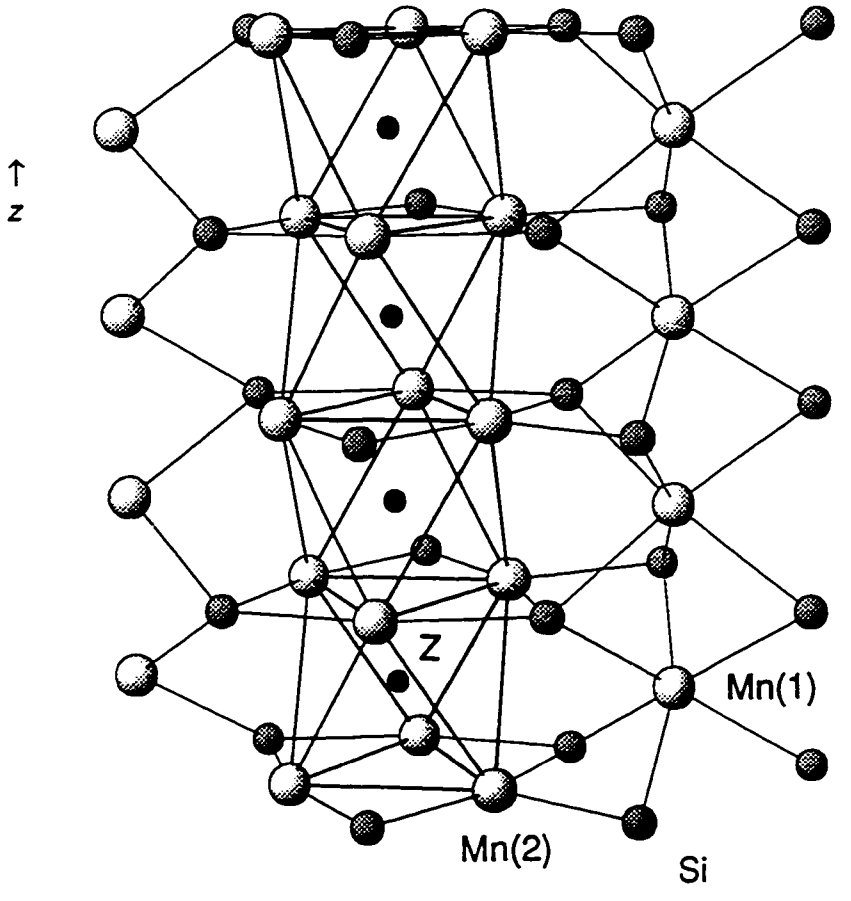

Figure III-2. Structural features of the stuffed-Mn_5Si_3 type structure. Side view of the confacial $^1_\infty[Mn(2)_{6/2}Si_{6/2}]$ chain and the linear chain $^1_\infty[Mn(1)_2Si_{6/2}]$. Large and medium spheres represent Mn and Si, respectively. Small dark spheres (Z) show the interstitial site.

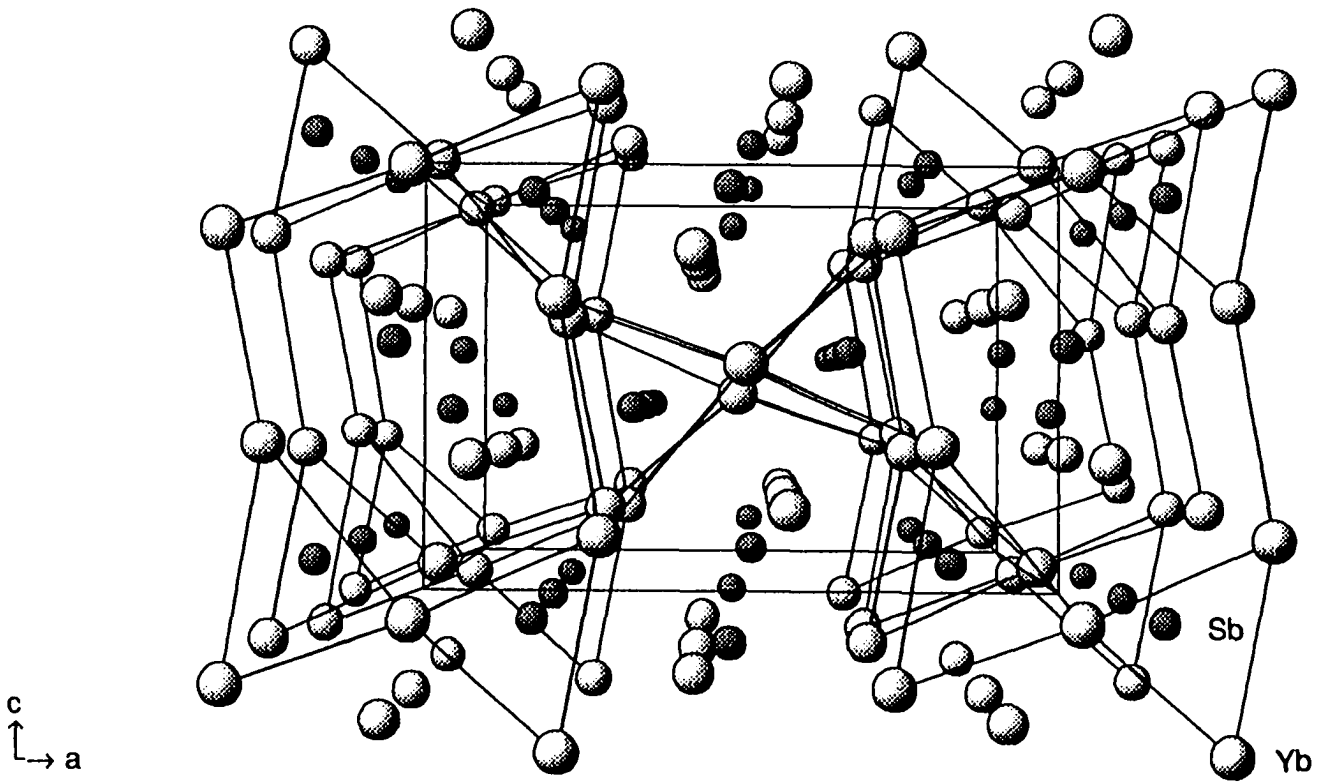

Figure III-3. The [010] perspective of the β-Yb_5Sb_3 structure type. Large and small spheres represent Yb and Sb atoms, respectively. Lines between atoms highlight the edge-sharing trigonal prismatic arrangements that define the larger hexagonal channels of Yb atoms.

fluoride ions in distorted tetrahedral sites, i.e., Ca_5Sb_3F and Ca_5Bi_3F. Figure III-4 shows as shaded tetrahedra the positions of these interstitial sites in the structure of Ca_5Sb_3F in which, for clarity, line convergence points mark the Ca atom positions. Orthorhombic derivatives of Ba_5Sb_3 or Ba_5Bi_3 were never found, or oxygen stabilized compounds, $Ae_5Pn_3O_x$, in reference to Ae_4Pn_2O phases.[55]

Both M and Y structures characteristically present long Pn–Pn interatomic distances that allow one to rule out any bonding interaction between these atoms. In connection with the Zintl ideas, one could assign a trinegative oxidation state to each pnictide ion and predict a one electron excess per formula in Ae_5Pn_3 compounds ($5Ae^{2+}$, $3P^{3-}$, e^-). Consequently, all of the binaries Ae_5Pn_3 are expected to display a metallic-like behavior, and ternary halides, subject to a similar electron count, are presumed to be semiconductive species. Electrical resistivity measurements done by L. Wolfe[56] on Ca_5Bi_5F and Ba_5Sb_3Cl confirmed these phases to be semiconductors with gap energies of ~0.07 and 0.09 eV, respectively. However, similar measurements on Ba_5Sb_3 also indicated a semiconductive compound with Eg ~0.30 eV.

Because of the prevailing discrepancies in structure–properties relationships and reported inabilities to prepare single phase products of some Ae_5Pn_3, we persisted in a search for a third stabilizing impurity element in these systems. Hydrogen, a common impurity of alkaline-earth and rare-earth metals, was thought capable of influencing the unexpected behavior in these compounds, including the debatable M ↔ Y phase transformation as well. Such an hypothesis was proven correct by the careful reactions of alkaline-earth or divalent rare-earth metal and the pnictogens (As, Sb and Bi) in presence and absence of hydrogen, or fluoride. Consequently, single phase products were successfully prepared.

Results and Discussion

$Ba_5Sb_3H_x$

In a chronological manner, the first system on which the influence of hydrogen was studied was Ba_5Sb_3. The measured semiconducting properties of this barium antimonide could not satisfactorily be explained based on the available structural

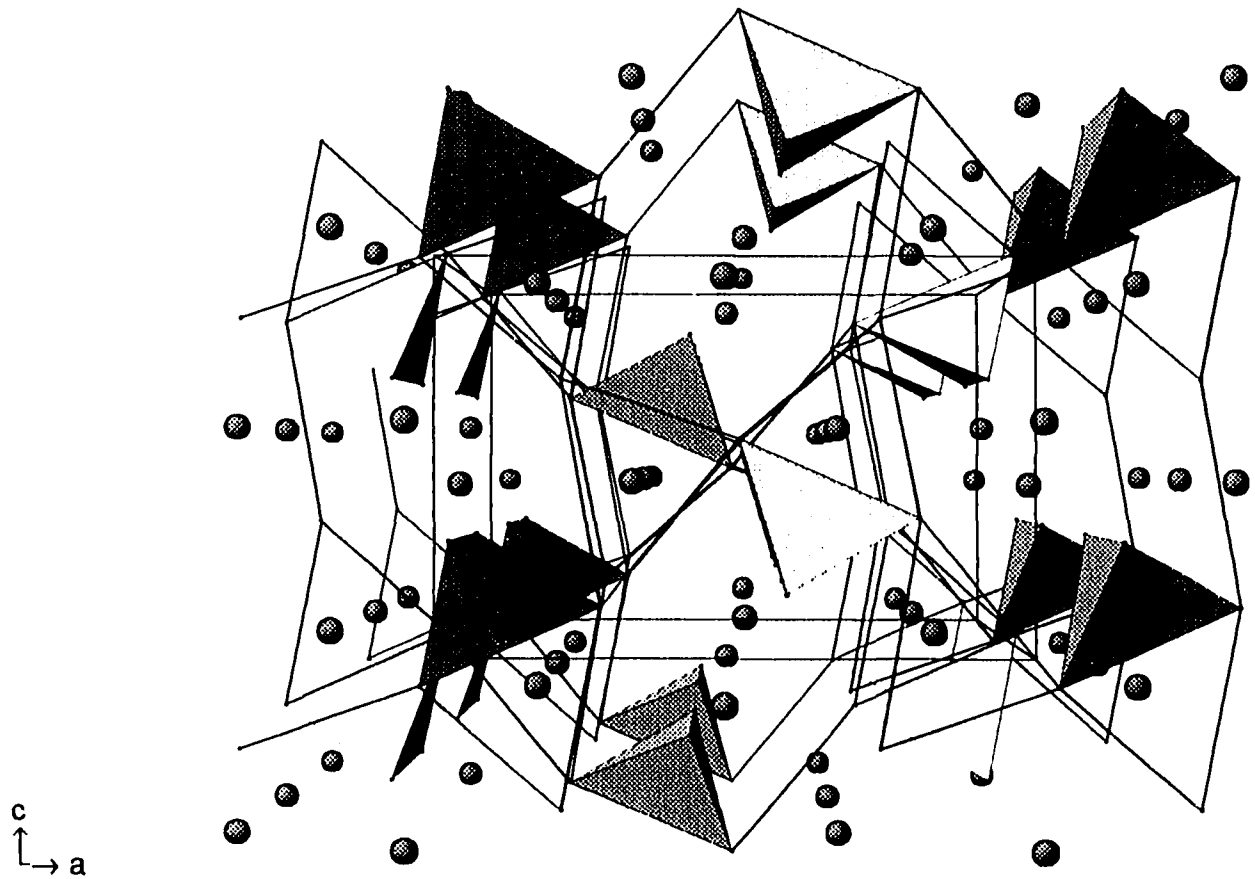

Figure III-4. The [010] perspective of the Ca_5Sb_3F structure. Shaded tetrahedra represent the interstitial sites where the fluoride ions are located. Line convergence points represent Ca atoms and dark spheres Sb atoms.

information. An ordered deficiency of one of the crystallographic cation sites manifested as a superstructure could have cleared the problem; however, long exposure Weissenberg and precession photographs did not show evidence of such a superlattice. Consequently the presence of a third element, hydrogen, was seriously considered.

Reactions between antimony and barium, at the proper stoichiometry, carried out under both dynamic vacuum (dv) and sealed container (sc) conditions gave Ba_5Sb_3 in the M structure type, rxns A15 and A11, respectively, Table III-1. Their cell volumes showed a significant decrement of ~1.60% (see Table III-2) that positively indicated their inequality, where the latter compound was believed to be a ternary hydride (A11). Absence of hydrogen in the phases prepared under dv conditions was inferred from the reproducibility of their lattice parameters, rxns A7, A12 and A15. A decrement in cell dimensions from the binary to the hydrided phase is reasonable if we consider that hydrogen is strongly bonding inside the compound. When the hydride ion is present in the interstitial site surrounded by barium atoms, a strong cation–anion coulombic interaction is envisioned. This interaction will be manifested as a reduction in the cell size. In other words, when the interstitial ion is absent, the cation–cation repulsive interactions will prompt an expansion of the cell. Some hydrogen storage materials show a weak metal–hydrogen binding interactions[57] that are reflected as increments in the cell volumes upon increment of their hydrogen contents.

Hydrogenation of Ba_5Sb_3 was done by directly reacting the previously prepared binary (A12) with H_2 gas at 400°C in a Mo boat, rxn A13. The product of this reaction (A13) remained in the M structure. However, its cell volume decreased by ~2.50%, from 677.2(2) to 660.9(6) $Å^3$. Careful measurement of the H_2 gas consumption during the reaction indicated a formula of $Ba_5Sb_3H_{-1}$ for the product of A13, i.e. the valence composition. Partial oxidation of the product to form Ba_4Sb_2O, a consequence of the experimental conditions, was observed as well.

Inclusion of hydrogen in a systematic and more controlled manner was achieved by reacting dehydrogenated Ba-metal, Sb and BaH_2 in sealed silica containers, rxns A26 to A29. Cell dimensions of the M products decreased as the hydrogen availability was increased, ceasing to change at about the valence, or Zintl, composition ($Ba_5Sb_3H_{1.0}$) in

Table III-1. Distribution of products for reactions $Ba_5Sb_3(H,F)_x$.

Rxn. No.	Loaded Composition[a]	Conditions[b]		Product Distribution[c]
A11	Ba_5Sb_3	i	sc	M ~100%
A15	Ba_5Sb_3	i	dv	M ~100%
A7	Ba_5Sb_3	ii	sc/dv	M ~100%
A12	Ba_5Sb_3	ii	dv	M ~100%
A13	Rxn A12	iii	sc-hg	M ~95%, Ox
A26	$Ba_5Sb_3H_{0.0}$	i	sc	M ~93%, T ~5%, Ox
A27	$Ba_5Sb_3H_{0.5}$	i	sc	M ~94%, T ~4%, Ox
A28	$Ba_5Sb_3H_{1.0}$	i	sc	M ~96%, Ox
A29	$Ba_5Sb_3H_{2.0}$	i	sc	M ~94%, T ~4%, Ox
AF1	Ba_5Sb_3F	i	dv	ATP ~80%, T ~15%, BaF_2 ~5%

[a] Reactions denoted $Ba_5Sb_3H_{x.0}$ were loaded with dehydrogenated Ba metal.
[b] Conditions: i) Reaction at 1100°C for 2h then 10°C/h to 650°C, followed by cooling to room temperature.
ii) Same as (i) then reheated at 850°C for 3 days under vacuum.
iii) Dehydrogenated phase heated in presence of hydrogen gas at 400°C.
sc = Reaction in a sealed fused silica container.
dv = Reaction under dynamic vacuum.
hg = Reaction under constant pressure of hydrogen gas.
[c] Estimated from Guinier powder patterns. M= Mn_5Si_3-type, T= $Ca_{16}Sb_{11}$-type, Ox= Ba_4Sb_2O (anti-K_2NiF_4-type), ATP= anti-Th_3P_4-type.

concordance with the results of reaction A13. A cell volume variation of ~2.53% is calculated between the binary (dv reaction) and the, probable, fully hydrided phase. Since no hydrogen quantification experiments were performed, one cannot assert that such a stoichiometric composition indeed was achieved. Lack of the Y-type structure in this system makes the M form a broad hydrogen getter. The graphical representations of the variations in lattice dimensions and volume of products A26 to A29 are given in Figure III-5, where the results of A12, labeled as dv, were included for comparison purposes. From the first two plots of this figure one can see that the a-axis reaches its

Table III-2. Lattice dimensions of the $Ba_5Sb_3(H,F)_x$ compounds.

Rxn No.	Loaded Comp.[a]	Str.Type/ Conds.[b]	a (Å)	c (Å)	Vol.(Å^3)	c/a	Ref.
	Ba_5Sb_3	M/sc	9.97(1)	7.73(2)	665(2)	0.775	58
	Ba_5Sb_3	M/sc	9.964(3)	7.694(4)	661.5(5)	0.772	50
	Ba_5Sb_3	M/sc	9.969(3)	7.733(6)	665.5(7)	0.776	56
A11	Ba_5Sb_3	M/dv	9.977(1)	7.727(2)	666.1(3)	0.774	
A7	Ba_5Sb_3	M/sc/dv	10.023(2)	7.786(3)	677.4(4)	0.777	
A12	Ba_5Sb_3	M/dv	10.020(1)	7.788(2)	677.2(2)	0.777	
A15	Ba_5Sb_3	M/sc	10.018(2)	7.788(4)	676.9(5)	0.777	
A13	Rxn A12	M/sc-hg	9.968(3)	7.680(6)	660.9(6)	0.770	
A26	$Ba_5Sb_3H_{0.0}$	M/sc	9.974(2)	7.745(4)	667.3(5)	0.776	
A27	$Ba_5Sb_3H_{0.5}$	M/sc	9.972(1)	7.673(2)	660.8(3)	0.769	
A28	$Ba_5Sb_3H_{1.0}$	M/sc	9.973(1)	7.671(2)	660.7(2)	0.769	
A29	$Ba_5Sb_3H_{2.0}$	M/sc	9.972(2)	7.672(3)	660.8(4)	0.770	
AF1	Ba_5Sb_3F	ATP/dv	10.5686(4)		1180.4(1)	1.000	

[a] Reactions denoted $Ba_5Sb_3H_{X.0}$ were loaded with dehydrogenated Ba metal.
[b] Cells indexed for M= Mn_5Si_3-type and ATP= anti-Th_3P_4-type structure.
Conditions: dv= dynamic vacuum, sc= sealed container and hg= reaction in presence of H_2 gas.

minimum value more rapidly than the c-axis, respective changes of 0.43 and 0.79%. The large influence of the atomic interactions along the linear chain in the M structure justifies the observed trend, see Figure III-2.

Importantly, the product of reaction A26, $Ba_5Sb_3H_{0.0}$, although loaded without hydrogen gave a set of cell dimensions that corresponded to those of a ternary hydride phase. One possible explanation to this result is that some contamination of the Ba metal may have occurred during its handling, as Ba metal is an excellent hydrogen getter.[19] However, as Gregory and Rustad[59] demonstrated in their experiments involving metals and halogens at elevated temperatures that silica dehydration can become a significant source of water in a reaction. Therefore, the hydrogen in A26 certainly originated from the silica container. Hydrogen generated from the decomposition of water by Ta metal can easily be picked up by the binary phase already formed, as proved with reactions A12 and A13. On the other hand, the oxygen generated in this reaction corrodes the Ta metal or forms Ba_4Sb_2O. This is in general theme for all reactions in sc conditions.

A minor second phase identified in products A26 to A29 is $Ba_{16}Sb_{11}$. This phase is isostructural with the tetragonal $Ca_{16}Sb_{11}$-type structure (T) originally discovered by Hurng.[60] Because the binaries with the T-type structure are new compounds, their discussion is reserved for latter section of this work. Traces of the oxide Ba_4Sb_2O (anti-K_2NiF_4-type) were identified in products A26 to A29 as well, its presence is an indication that exposure of Ba metal to air, or H_2O, occurred.

Specific reactions to test the reversibility of the hydrogenation reaction, M $\rightleftharpoons$ MH (MH being the hydrogen-stuffed M form), were not performed, although, its feasibility is already inferred from the information given in Tables III-1 and III-2. Hence, dehydrogenation of the ternary hydride ($MH \rightarrow M + H_2$) is assumed from the results of reaction A7, where a hydrided phase originally prepared under sc conditions was heated at 850°C under vacuum, i.e., dehydrogenation conditions. Cell dimensions of the final product are equivalent to those of other reactions under dynamic vacuum, A7 and A15. The opposite reaction, hydrogenation ($MH \leftarrow M + H_2$), is elucidated by reactions A12 and A13.

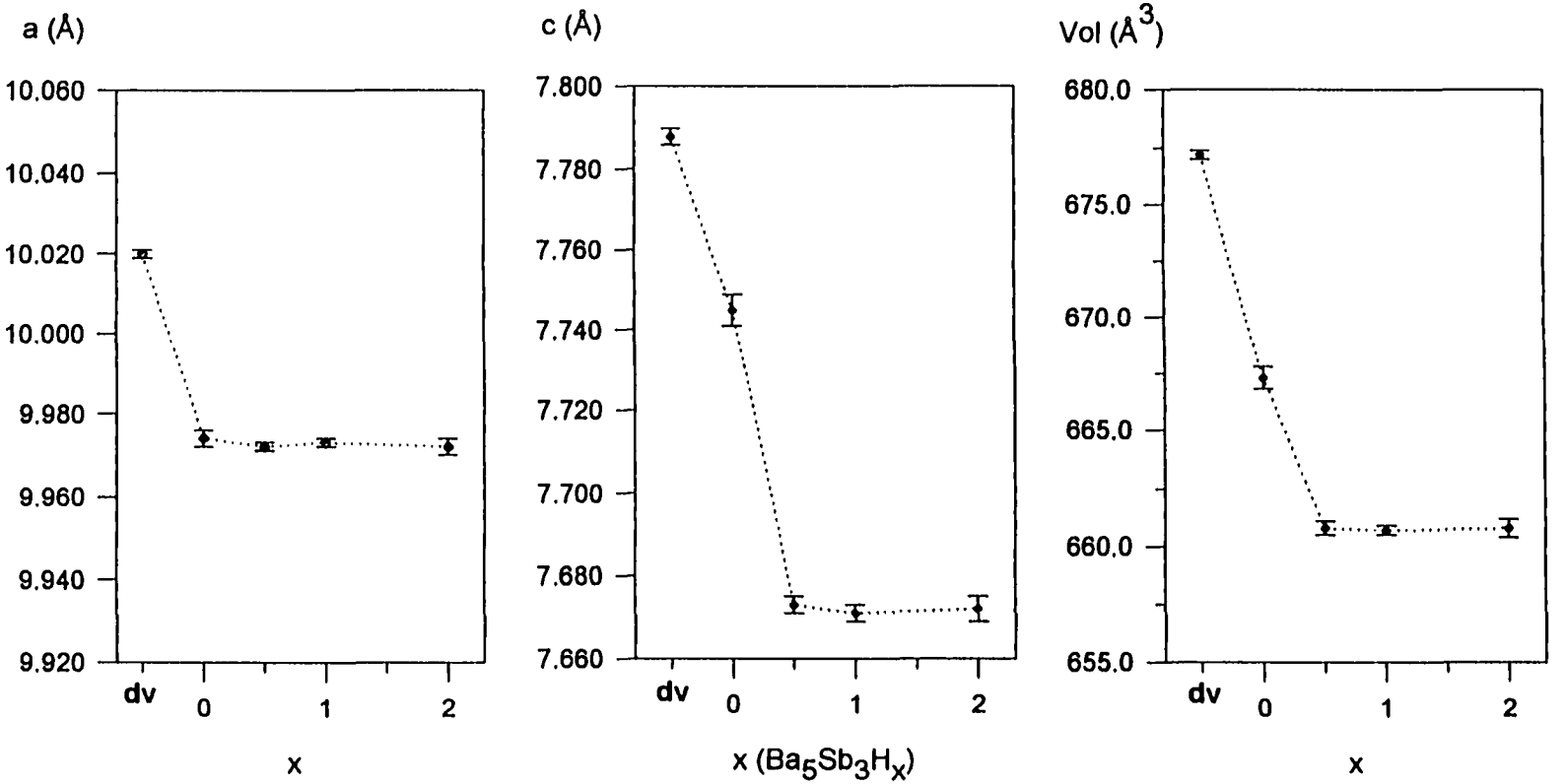

Figure III-5. Graphical representation of the changes in lattice parameters of $Ba_5Sb_3H_x$ as function of loaded hydrogen (x=0.0, 0.5, 1.0, 2.0). Cell parameters of a phase prepared under dynamic vacuum are included for comparison purposes (labeled as dv on the abscissas). Bars represent the single standard deviations.

X-Ray solution to the structure of A11, $Ba_5Sb_3(H_{\sim 0.7})$, gives a more precise information about geometry and interatomic distances in the structure when related to the original crystallographic report by Eisenmann[58] in 1975. The hydrogen content in sample A11 was estimated from its cell volume, and through interpolation between the ideal volume limits; $Ba_5Sb_3H_0$ (dv, rxn A12) and $Ba_5Sb_3H_1$ (sc, rxn A28). Of course, it is assumed that there is a linear dependence on the cell volume versus hydrogen content. Tables III-3 and III-4 contain some of the crystallographical and refined x-ray structural information of this ternary hydride. The hydrogen position is assumed at ~ 0,0,0, inside the trigonal antiprismatic cavity. The Ba(2) atoms that form this cavity are quite anisotropic in their thermal parameters. The needle-like shape of the crystal and a poor absorption correction to the data are blamed for this feature. Statistical distribution of hydrogen in the cavities may also account for the Ba(2) anisotropicity.

The arrangement of Ba(2) in atoms in the structure, as depicted in Figure III-6, is indeed trigonal antiprismatic. Interatomic Ba-Ba distances on the triangular face normal to z, d= 4.328(1) Å, are about 0.27 Å smaller than those parallel to z, d= 4.6010(9) Å. Such elongation of the antiprismatic arrangement may be determined by the Ba(1)–Ba(1) interactions along the linear chain. The Ba(1)–Ba(1) interatomic distance, 3.632(1) Å, is about 8.3% shorter than twice the metallic radii of the element, 3.926 Å.[61] Distances Sb–Ba are 3.4279(6) Å to the confacial chain, Ba(2), and 3.6324(4) Å to the linear chain, Ba(1). A calculated Ba–H interatomic distance of ~3.158 A is greater than that predicted by the summation of the crystal radii of Ba^{2+} and H^- of ~2.60 Å[62] (H^- after Marek and Corbett[57]). It is quite possible that hydrogen may be located off the center of the cavity, closer to the top or base of the antiprism of Ba(2) atoms.

It is conceivable that the large cavity size in Ba_5Sb_3 is the reason why both Hurng and I were unable to prepare Ba_5Sb_3F with the hexagonal structure. Reactions between Ba, Sb and BaF_2 (rxn AF1) gave the cubic anti-Th_3P_4-type structure (ATP) in high yields. This cubic phase is plausibly a fluoride-stabilized compound because it is unreported for the binary Ba–Sb system. The Th_3P_4-type structure ($I\bar{4}3d$, sp.gr. #220, Z=4)[63] cannot be described in a straightforward manner and, as illustrated in Figure III-7, it represents a complex set of sharing polyhedra such that the Th atoms (Sb in Ba_4Sb_3)

Table III-3. Crystallographic Data of $Ba_5Sb_3H_{\sim 0.7}$.

	$Ba_5Sb_3H_{\sim 0.7}$
Crystal from rxn.	A11
Space group	$P6_3/mcm$
Lattice parameters[a]	
a (Å)	9.977(1)
c (Å)	7.727(2)
Volume ($Å^3$)	666.1(3)
Z	2
Density calc. (g/cm^3)	5.244
Crystal dimensions (mm)	0.10x0.10x0.33
Diffractometer	Rigaku AFC6R
Collected octants	±h,k,l
Scan type	ω-2θ
Transmission range	0.554–1.000
Absorption coefficient (cm^{-1})	205.1
Number of reflections	
Measured	1348
Independent (observed[b])	277(214)
R_{ave} (%)[c]	4.18
No. of refined variables	12
R/R_w (%)	1.4/1.7
Goodness of fit	1.766
Secondary extinction coefficient	$7.3(4) \times 10^{-7}$
Max./min. peak in ΔF map. ($e^- Å^{-3}$)	0.85/-0.61

[a] Lattice parameters calculated from Guinier powder patterns.
[b] Observed reflections; $I \geq 3.00\sigma_I$.
[c] Average for all data; $I > 0$.

Table III-4. Refined crystallographic data for $Ba_5Sb_3H_{\sim 0.7}$, positional and thermal parameters and important interatomic distances (Å).

Positional parameters.

Atom	x	y	z	$B_{eq}(Å^2)$
Ba(1)	1/3	2/3	0	1.16(2)
Ba(2)	0.25042(7)	0	1/4	1.85(4)
Sb	0.60830(6)	0	1/4	0.96(4)
(H	0	0	0)	

Thermal parameters.

Atom	U_{11}	U_{22}	U_{33}	U_{12}	U_{13}	U_{23}
Ba(1)	0.0173(3)	U_{11}	0.0096(4)	½U_{11}	0	0
Ba(2)	0.0166(3)	0.0096(3)	0.0422(6)	½U_{22}	0	0
Sb	0.0097(3)	0.0082(4)	0.0183(4)	½U_{22}	0	0

Important interatomic distances.

Atom(1) – Atom(2)	d(Å)	Atom(1) – Atom(2)	d(Å)
Sb – Ba(1) (6x)	3.6324(4)	Ba(1) – Ba(1) (2x)	3.864(1)
Sb – Ba(2) (2x)	3.4279(6)	Ba(1) – Ba(2) (6x)	4.2693(6)
Sb – Ba(2) (1x)	3.571(1)	Ba(2) – Ba(2) (2x)	4.328(1)
Sb – Ba(2) (2x)	4.113(1)	Ba(2) – Ba(2) (4x)	4.6010(9)
Sb – Sb (2x)	4.427(1)		

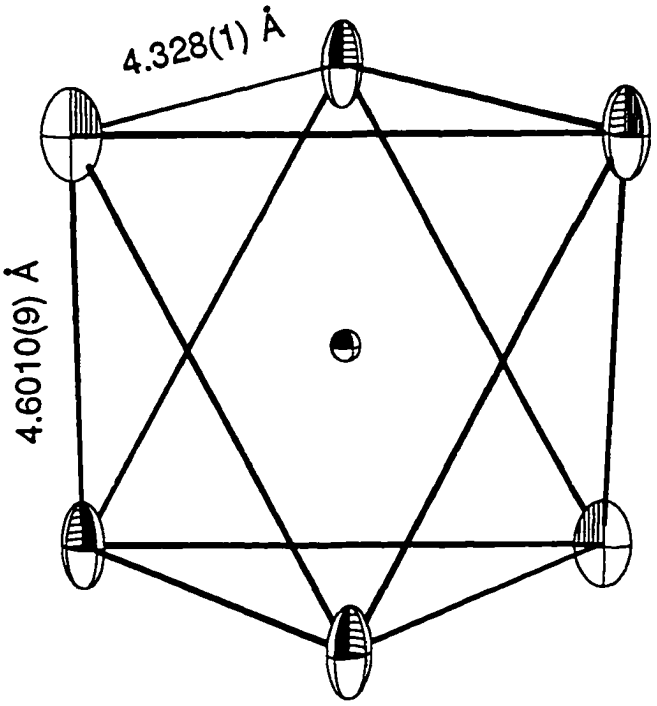

Figure III-6. Trigonal antiprismatic arrange of Ba(2) atoms in $Ba_5Sb_3(H_{\sim 0.7})$. Interatomic Ba-Ba distances on the planes normal to z are shorter than those parallel to it. Ellipsoid in the center represents hydrogen.

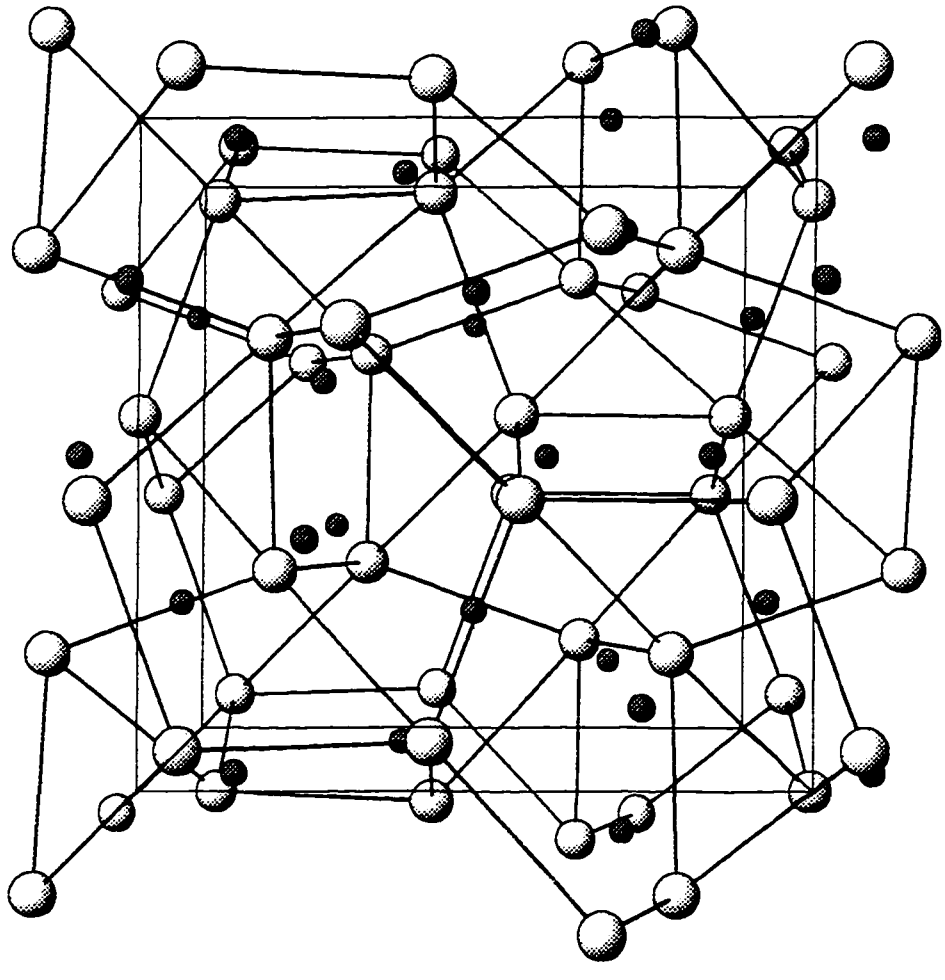

Figure III-7. A [100] projection of the cubic Th_3P_4-type structure. Large and small spheres represent P and Th atoms, respectively. Lines between P atoms do not signify bonds.

are surrounded by eight P (Ba) atoms in a octaverticon (a strongly distorted cube), making the Th(Sb) atoms isolated from each other. An octaverticon of P atoms is depicted in Figure III-8. The distances from the center of this polyhedra to its eight vertices fall into two groups of four. The P(Ba) atoms are surrounded by six Th(Sb) atoms in a distorted octahedral arrangement. Interestingly, distorted tetrahedral cavities are formed by the connectivity between octaverticons; Figure III-9 highlights these cavities. Atomic substitution in the tetrahedral interstitial sites (@ 7/8,0,1/4) makes the $Au_3Y_3Sb_4$-type structure.

Because the antimony atoms in the ATP structure are isolated, their occupancy is determined by the electron availability in the compound, i.e., from $4Ba^{2+}$. Alkaline-earth-metal and divalent rare-earth-metal pnictides with this cubic structure are expected to present fractional occupancy on the pnictogen atom site as found for Sr_3P_2, Ba_3P_2,[64] Eu_3P_2 and Eu_3As_2.[65] Electronic requirements and possibly interstitial fluoride substitution suggest a composition of $Ba_4Sb_{2.5}F_{0.5}$ for the major phase in reaction AF1. Such a composition agrees with the ternary $Ba_4Sb_{2.5}I_{0.5}$ prepared by Hurng, although mixing of Sb and I atoms found on the anionic site make this latter phase structurally inequivalent to the ternary fluoride, $Ba_4Sb_{2.5}F_{0.5}$.

$Ca_5Sb_3H_x$

Once we established the role of hydrogen in the Ba_5Sb_3 system, the succeeding problem to solve was the questionable dimorphism of Ca_5Sb_3. Inability to prepare single phase products and discrepancies in the reported lattice parameters of the Y phase were problems that could not adequately be explained. Hurng's work on this system did not give a solution about a variable, either composition or temperature, that would govern the phase transformation between the orthorhombic Y and hexagonal M structures. Nonetheless, he was able to show that single M-type phases formed when the metals are heated above 1100°C and that either of these structures could be interstitial stabilized by halide ions. The preference for any structure appeared controlled by the size of the halide ion. Hence, the fluoride ion would stabilize phases in the Y structure and larger ions, i.e., chloride and bromide, would stabilize the M structure.

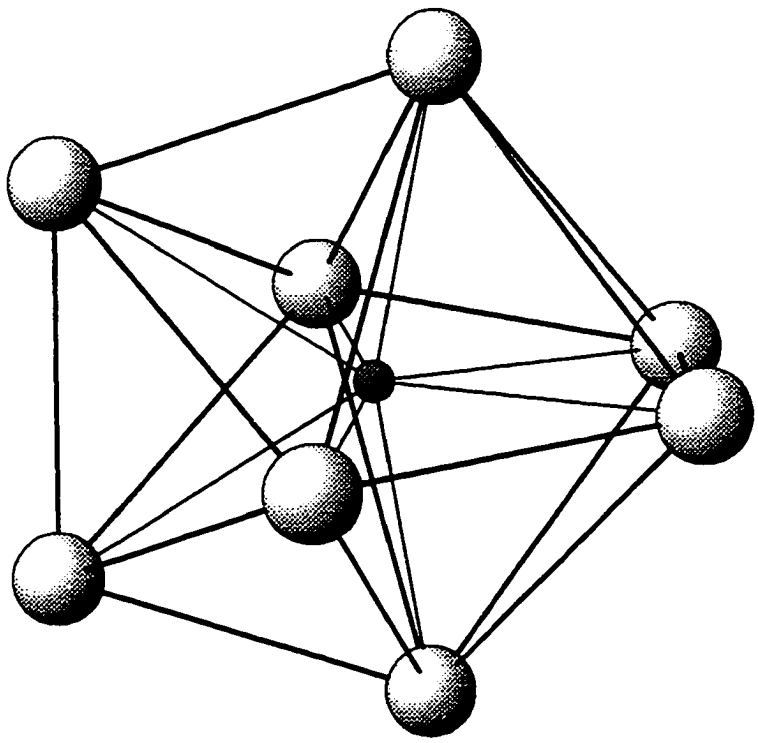

Figure III-8. Detail of the cubic Th_3P_4-type structure. Octaverticon polyhedron of P atoms that coordinate Th.

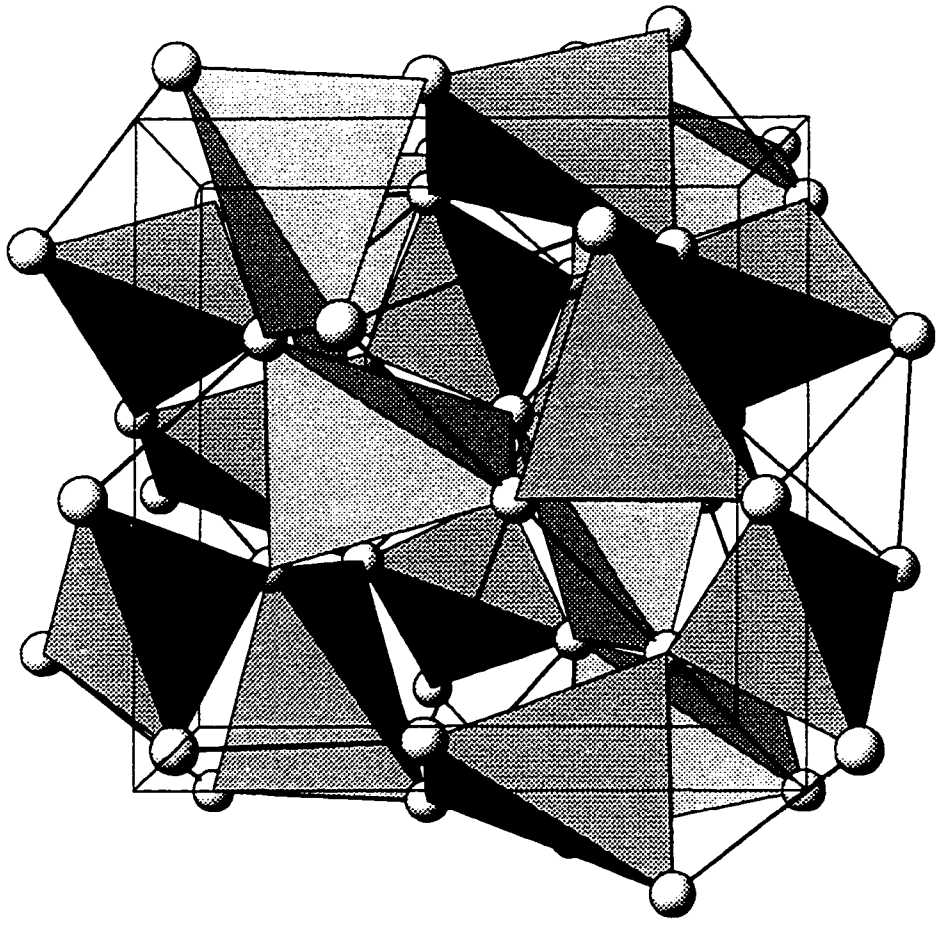

Figure III-9. Detail of the Th_3P_4-type structure. Interstitial cavities in the structure are highlighted as shaded tetrahedra of P atoms. For clearness the Th atoms are not included in the picture.

Because the fluoride and hydride ions have similar effective ionic radii in solid state compounds, it appeared reasonable to speculate that Y-Ca_5Sb_3 could be a hydrogen-stabilized compound. Experiments in the absence and presence of hydrogen were, therefore, pursued.

When the reaction between the elements or a previously synthesized Y-Ca_5Sb_3 are heated above 1000°C under vacuum, single phase M-type products are consistently obtained; rxns D8 and D5 in Table III-5. When untreated Ca metal is used as reagent and the reactions are carried in sc conditions, rxns D2 and D3, the product is a mixture of M and Y phases, and when hydrogen is purposely included, the Y-type phase is the major or only product, rxns D12 to D14. Consequently, Y-$Ca_5Sb_3H_x$ is a hydrogen-stabilized compound, and the biphasic products are the result of hydrogen contaminated Ca metal plus water from the silica container.

Cell dimensions of the phases prepared in the assured absence of hydrogen are consistently reproducible, rxns D5, D8 and D11 in Table III-6, and are comparable to previous reported values. Therefore M-Ca_5Sb_3 can be considered a binary phase. Structural solution of a crystal from D8 indicates that the binary compound is stoichiometric, $Ca_{5.0(1)}Sb_3$. Tables III-7 and III-8 summarize the crystallographic and refined information data about this compound. Characteristic of M-Ae_5Pn_3 compounds is the shortest cation–cation contact in the linear chain of Ca atoms, $d_{Ca(1)-Ca(1)}$= 3.5127(2) Å. This interatomic distance is about that calculated from the Ca metallic radii (2 x 1.734= 3.468 Å).[61] As in the case of $Ba_5Sb_3H_{\sim 0.7}$ (A11), the interatomic Ca(2)–Ca(2) distances in the confacial antiprism are less between the atoms on the plane normal to z than those parallel to it, 3.949(4) Å versus 4.188(1) Å.

As earlier mentioned, the orthorhombic Y phase forms when the reactions are carried in presence of hydrogen, with a noticeable increase in yield as the amount of hydrogen is augmented as well, rxns D11 to D14. Water from the silica container is blamed for the results of reaction D11, $Ca_5Sb_3H_{0.0}$, where a fraction of the product had the orthorhombic structure. Single Y-phase products are achieved from the loaded compositions $Ca_5Sb_3H_{1.0}$ to $Ca_5Sb_3H_{2.0}$. Figure III-10 shows a graphical representation of the variation in yield of Y and M phases with hydrogen loaded, where it is notable that

Table III-5. Distribution of products for reactions $Ca_5Sb_3(H,F)_x$.

Rxn. No.	Loaded Composition[a]	Conditions[b]		Product Distribution[c]
D2[d]	Ca_5Sb_3	i	sc	Y ~80%, M ~15%, Ox
D3[e]	Ca_5Sb_3	ii	sc	Y ~98%, M ~2%
D5	Ca_5Sb_3	iii	sc/dv	M ~98%, T ~2%
D8	Ca_5Sb_3	ii	dv	M ~98%, T ~2%
D7	Rxn. D5	iv	sc	Y ~70%, M ~25%, T ~5%
D11	$Ca_5Sb_3H_{0.0}$	ii	sc	M ~95%, Y ~5%
D12	$Ca_5Sb_3H_{0.5}$	ii	sc	Y ~95%, M ~5%
D13	$Ca_5Sb_3H_{1.0}$	ii	sc	Y ~100%
D14	$Ca_5Sb_3H_{2.0}$	ii	sc	Y ~100%
DF1	Ca_5Sb_3F	ii	dv	Y ~90%, T ~7%, CaF_2 ~3%

[a] Reactions denoted $Ca_5Pn_3H_{x.0}$ were loaded with dehydrogenated Ca metal.
[b] Conditions: i) Reaction at 1100°C for 2h. Quenched from 850°C after 14 days.
ii) Reaction 1100°C,4–8h then 10–12°C/h to 650°C.
iii) Reaction at 1000°C for 2h then 10°C/h to 650°C.
iv) Heated at 850°C for 10 days then quenched to room temperature.
sc = Reaction in a sealed fused silica container.
dv = Reaction under dynamic vacuum.
[c] Estimated from Guinier powder patterns. M= Mn_5Si_3-type, Y= β-Yb_5Sb_3-type, T= $Ca_{16}Sb_{11}$-type, Ox= Ca_4Sb_2O (anti-K_2NiF_4-type structure).
[d] Calcium metal from Ames Laboratory.
[e] Calcium metal from APL Engineering Labs.

high yield of the of Y phase are already obtained for low hydrogen loads, rxn D12. These augmented yields are indication that the orthorhombic phase can be stabilized with fractional quantities of hydrogen, $Ca_5Sb_3H_x$ ($x<1.0$), since dehydrogenated Ca under sc conditions gives low yields of Y-form (D11).

Although no experiments were performed to determine directly the homogeneity range of hydrogen in the compound, the calculated overall cell volume decrement may certainly be related to it. Figures III-11 and III-12 shows the graphic representation of

Table III-6. Lattice dimensions of $Ca_5Sb_3(H,F)_x$ compounds.

Rxn No.	Loaded Comp.[a]	Str.Type/ Conds.[b]	a (Å)	b (Å)	c (Å)	Vol.(Å^3)	c/a	c/b	Ref.
	Ca_5Sb_3	M/sc	9.024		7.057	497.7	0.782		47
	Ca_5Sb_3	M/sc	9.0321(3)		7.0280(8)	496.5(7)	0.778		50
D5	Ca_5Sb_3	M/dv	9.0314(3)		7.0254(4)	496.26(4)	0.778		
D8	Ca_5Sb_3	M/dv	9.0312(3)		7.0254(4)	496.24(4)	0.778		
D11	$Ca_5Sb_3H_{0.0}$	M/sc	9.0315(2)		7.0251(3)	496.25(3)	0.778		
	Ca_5Sb_3	Y/sc	12.502(8)	9.512(7)	8.287(7)	985(2)	0.663	0.871	66
	Ca_5Sb_3	Y/sc	12.537(4)	9.555(2)	8.296(2)	993.8(8)	0.662	0.868	50
D2	Ca_5Sb_3	Y/sc/dv	12.552(2)	9.563(1)	8.298(1)	996.1(2)	0.661	0.868	
D12	$Ca_5Sb_3H_{0.5}$	Y/sc	12.522(1)	9.561(1)	8.298(1)	993.4(2)	0.663	0.868	
D13	$Ca_5Sb_3H_{1.0}$	Y/sc	12.4506(8)	9.5811(6)	8.3098(6)	991.3(2)	0.668	0.867	
D14	$Ca_5Sb_3H_{2.0}$	Y/sc	12.445(2)	9.583(2)	8.312(1)	991.3(3)	0.668	0.867	
	Ca_5Sb_3F	Y/sc	12.442(2)	9.653(2)	8.381(2)	1006.6(6)	0.674	0.868	45
DF1	Ca_5Sb_3F	Y/dv	12.453(2)	9.648(2)	8.363(1)	1004.7(3)	0.671	0.867	

[a] Reactions denoted $Ca_5Pn_3H_{X.0}$ were loaded with dehydrogenated Ca metal.
[b] Powder patterns indexed for M= hexagonal Mn_5Si_3 and Y= orthorhombic β-Yb_5Sb_3 structures types.
Conditions: dv = reaction under dynamic vacuum, sc = reaction in a sealed container.

Table III-7. Crystallographic Data of $(Ca,Yb)_5Sb_3$.

	Ca_5Sb_3	Yb_5Sb_3
Crystal from rxn.	D8	E17
Space Group	$P6_3/mcm$(#193)	$P6_3/mcm$
Lattice parameters[a]		
a (Å)	9.0312(3)	9.0366(6)
c (Å)	7.0254(4)	6.9044(9)
Volume ($Å^3$)	496.24(4)	488.27(9)
Z	2	2
Density calc. (g/cm^3)	3.785	9.323
Crystal dimensions (mm)	0.10x0.16x0.16	0.09x0.014x0.18
Diffractometer	Enraf-Nonius CAD4	Rigaku AFC6R
Collected octants	h,k,±l	h,±k,l
Scan type	ω-2θ	ω-2θ
Transmission range	0.875–1.262	0.760–1.198
Absorption coefficient (cm^{-1})	106.2	630.5
Number of reflections		
Measured	1057	1006
Independent (observed[b])	208(186)	212(130)
R_{ave} (%)	3.43	9.45(obs[b])
No. of refined variables	12	13
R/R_w (%)	2.5/3.5	4.1/4.0
Goodness of fit	1.717	1.251
Secondary extinction coeff. (x 10^{-7})	22(3)	7.3(8)
Max./min. peak in ΔF map ($e^- Å^{-3}$)	1.27/-1.25	3.18/-3.90

[a] Lattice parameters calculated from Guinier powder patterns.
[b] Observed reflections; $I \geq 3\sigma_I$.

Table III-8. Refined positional and thermal parameters and selected interatomic distances for $(Ca,Yb)_5Sb_3$ phases in Mn_5Si_3-type structure.

Atom	x	y	z	$B_{eq}(Å^2)$	U_{11}	U_{22}	U_{33}	U_{12}	U_{13}	U_{23}
	Ca_5Sb_3 (D8)									
Ca(1)	1/3	2/3	0	0.97(6)	0.0163(8)	U_{11}	0.006(1)	$½U_{11}$	0	0
Ca(2)	0.2525(3)	0	1/4	1.6(1)	0.0161(9)	0.013(1)	0.033(1)	$½U_{22}$	0	0
Sb	0.61089(7)	0	1/4	0.82(5)	0.0109(5)	0.0102(5)	0.0099(5)	$½U_{22}$	0	0
	Yb_5Sb_3 (E17)									
Yb(1)	1/3	2/3	0	1.32(6)	0.020(1)	U_{11}	0.009(1)	$½U_{11}$	0	0
Yb(2)	0.2521(2)	0	1/4	1.8(1)	0.021(1)	0.018(1)	0.028(1)	$½U_{22}$	0	0
Sb	0.6106(3)	0	1/4	1.2(2)	0.017(2)	0.016(2)	0.013(2)	$½U_{22}$	0	0

Selected interatomic distances (Å).

Atom(1) – Atom(2)	Ca_5Sb_3	Yb_5Sb_3	Atom(1) – Atom(2)	Ca_5Sb_3	Yb_5Sb_3
Sb – A(1) (6x)	3.2992(2)	3.2821(9)	A(1) – A(1) (2x)	3.5127(2)	3.4512(3)
Sb – A(2) (2x)	3.0879(6)	3.090(2)	A(1) – A(2) (6x)	3.857(1)	3.846(1)
Sb – A(2) (1x)	3.237(2)	3.238(4)	A(2) – A(2) (2x)	3.949(4)	3.943(4)
Sb – A(2) (2x)	3.7232(9)	3.667(1)	A(2) – A(2) (4x)	4.188(1)	4.134(1)
Sb – Sb (2x)	4.0436(6)	3.987(3)			

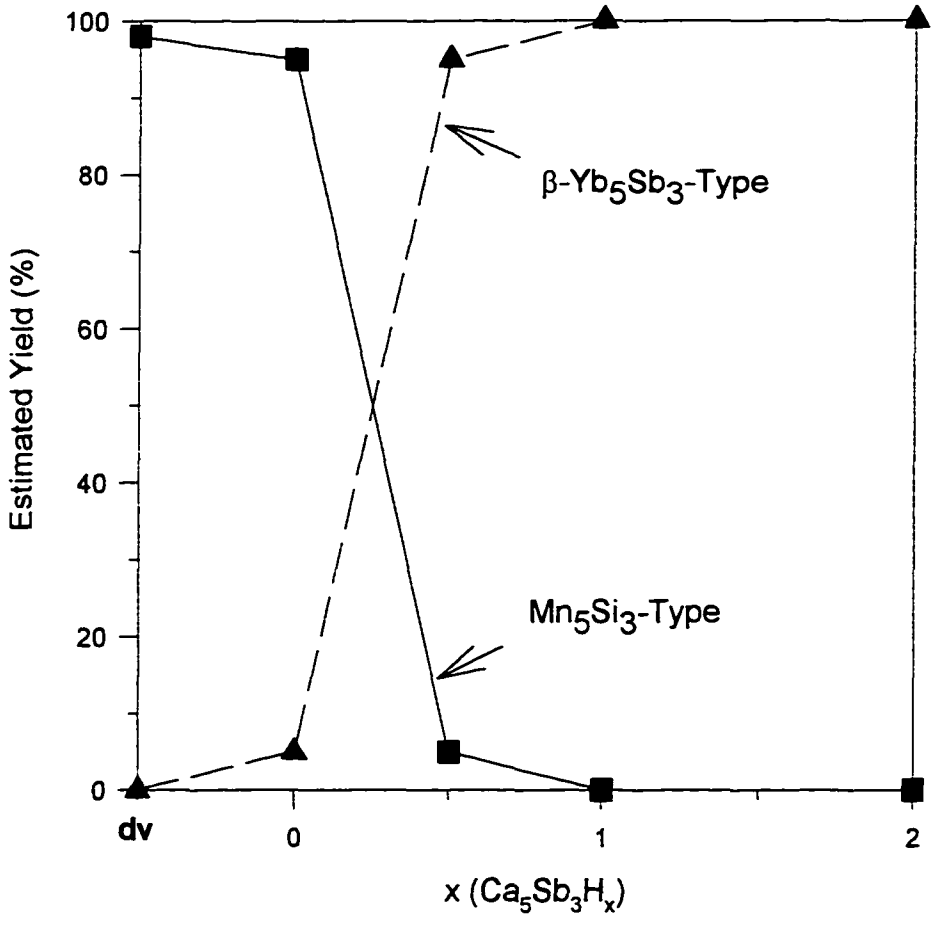

Figure III-10. Graphical representation of the estimated product distribution of reactions $Ca_5Sb_3H_x$, x= 0.0, 0.5, 1.0 and 2.0 (D11 to D14). Data labeled as dv on the abscissa are from sample D8.

calculated cell parameters as function of loaded hydrogen for reactions D12 to D14. Cell axis dimensions and volumes cease to change at about the valence compound, or Zintl composition, $Ca_5Sb_3H_{1.0}$ (Ca^{2+}, $3Sb^{3-}$, H^-). A large decrement of ~0.57% in the a-axis is accompanied by increments of ~0.21 and 0.14% for the b and c axes respectively, that result in an overall 0.48% cell volume decrement as hydrogen content increases. The inequivalent changes in cell axes are conceivably caused by a tetrahedral interstice resizing that is required to accommodate the hydride ion, as demonstrated by Hurng for the fluoride ion. The fluoride ion in Y-Ca_5Sb_3F is located inside an irregular tetrahedral cavity formed by three crystallographically distinct calcium atoms, see Figure III-4. Cell dimensions reported by Hurng for this ternary fluoride are ~0.19 % larger than those calculated for the equivalent phase prepared in this work, rxn DF1. Although the H^- and F^- ions have a similar size in solid state compounds, the ion volume contribution of the latter is slightly larger.[67] This difference is consistent with the observed volumes for $Ca_5Sb_3H_{\sim 1}$ and Ca_5Sb_3F. Consequently, the smaller volume of $Ca_5Sb_3F_{1-y}$ prepared in this approach is probably F^- deficient. The experimental conditions used in this synthesis impeded the formation of $Ca_5Sb_3H_x$ and did not allow a complete equilibration of the product; thus, formation of a solid solution of ternary hydride and fluoride can be ruled out. On the other hand the experimental conditions followed by Hurng to prepare the fluoride included the reaction in an induction furnace and a long annealing of the sample afterwards, which may have allowed the complete equilibration of the product to form $Ca_5Sb_3F_{1.0(1)}$.[50]

Conversion of the M-Ca_5Sb_3 into Y-$Ca_5Sb_3H_x$ is achieved by hydrogenation of the M form, by the fused silica dehydration during extended annealing periods in the closed containers, rxn D7. Heating the orthorhombic phase at 1000°C under vacuum gives the hexagonal form back, rxn D5. Interestingly, samples in either M or Y form that were reheated at 1000°C did not melt as it would have been predicted by the Ca–Sb phase diagram reported by Niyazova et al.[68] Such a diagram is consequently unreliable; it indicates that Ca_5Sb_3 melts incongruently at 825°C and that no solid phase exists above 985°C in the whole range of $CaSb_x$ compositions. Notin and coworkers[69] in a recent reevaluation of the diagram suggests the peritectic temperature at 996°C instead, and

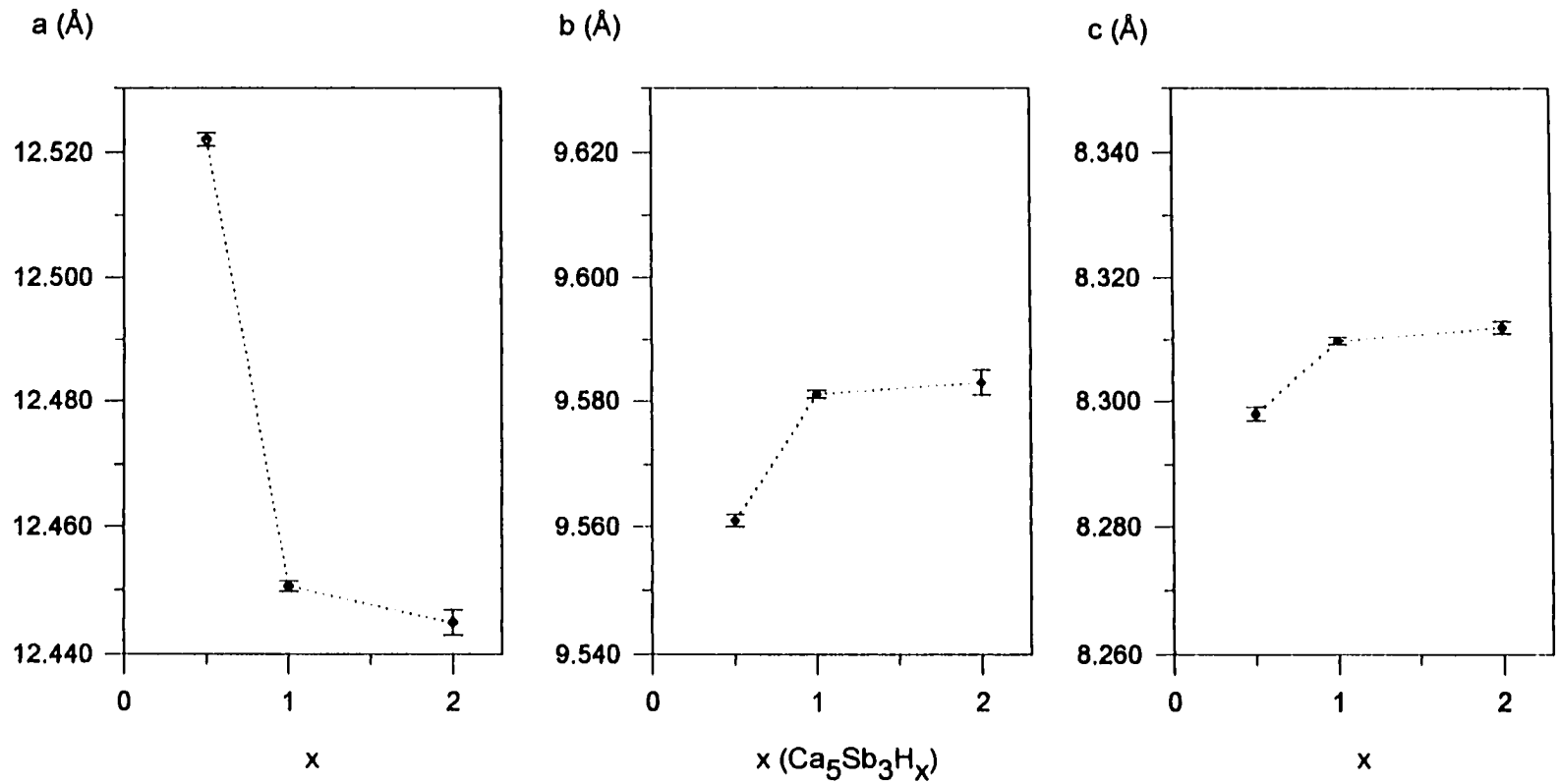

Figure III-11. Graphical representation of the changes in lattice parameters of Y-$Ca_5Sb_3H_x$ as a function of hydrogen loaded, x= 0.5, 1.0 and 2.0 (samples D12 to D14). Bars represent the single standard deviations.

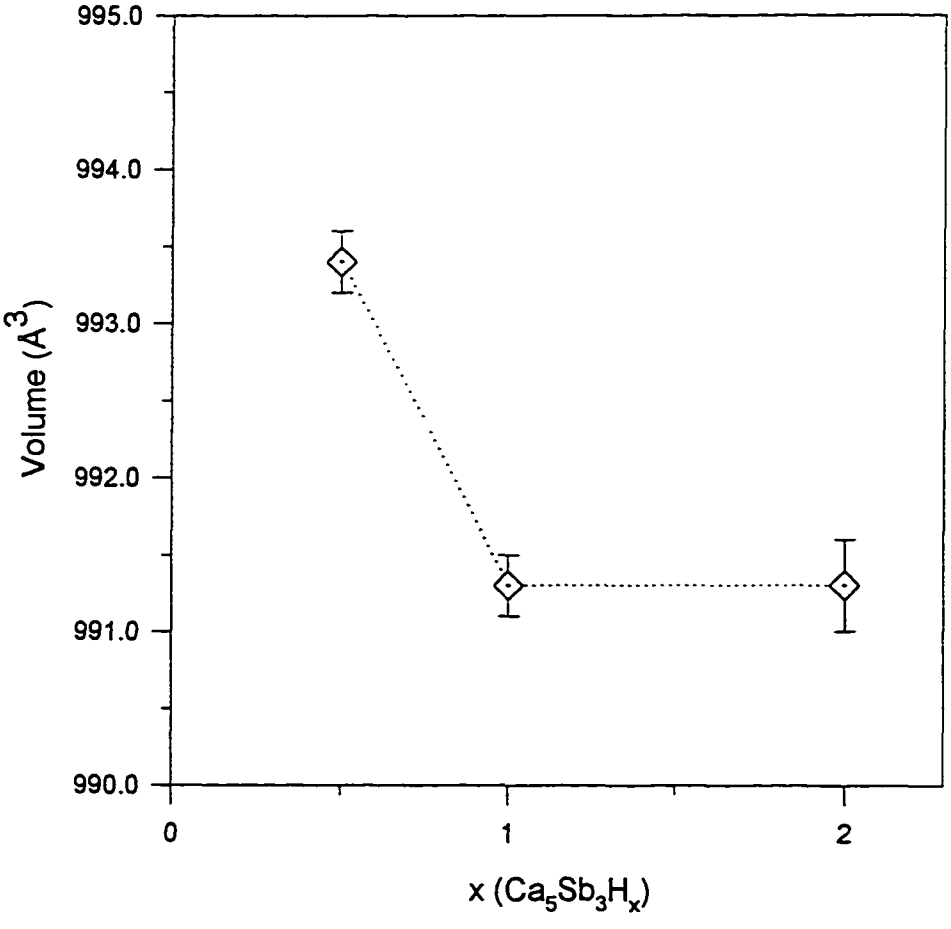

Figure III-12. Graphical representation of the change in cell volume of Y-$Ca_5Sb_3H_x$ as function of loaded hydrogen, x= 0.5, 1.0 and 2.0 (samples D12 to D14). Bars represent the single standard deviations.

highest liquidification temperature at ~1123°C. This latter report is in better agreement with our observations.

In hindsight, the Y-phase yields of reactions D2 and D3 nicely exemplify how much a commercial alkaline-earth metal can be contaminated with hydrogen. Reactions D2 and D3 although carried out under similar experimental conditions, gave different amounts of Y-type product. Thus, it appears that the Ca metal from Ames Lab. is of better quality than that from APL Engineering Labs.

$Yb_5Sb_3H_x$ and $Sr_5Bi_3H_x$

Prior to the initiation of this work two other compounds were reported to be dimorphic with the M and Y structures, Yb_5Sb_3 (that is the parent phase β-Yb_5Sb_3[54]) and Sr_5Bi_3. Results of experiments with hydrogen demonstrated that the Y forms of these compounds are hydrogen-stabilized phases. Table III-9 summarizes the results of significant experiments performed on the $Yb_5Sb_3H_x$ and $Sr_5Bi_5H_x$ systems. As for $Ca_5Sb_3H_x$, reactions in the formal absence of hydrogen gave the M-type structure as major or only product. The Y form was obtained when hydrogen was included in the reactions, with increments in its yield as the availability of hydrogen was increased as well. Single phase products with the Y structure were successfully prepared at compositions $A_5Pn_3H_{1.0}$. Variations of the cell dimension of Y-type phases follow the trend observed for $Ca_5Sb_3H_x$, i.e., reduction of the a-axis and modest increase of b- and c-axes upon hydrogen availability. See Tables III-10 and III-11 for lattice parameters information on $Yb_5Sb_3H_x$ and $Sr_5Bi_3H_x$, respectively.

Annealing a M-Yb_5Sb_3 phase for three weeks at 800°C in sc conditions is enough to transform it to its hydrided form (Y), rxn E15. Analogous observations were previously considered evidence of a phase transition, even though the opposite reaction was never satisfactorily achieved.[49,60] Complete transformation, or dehydrogenation, to the M form is accomplished by heating Y-$Yb_5Sb_3H_x$ at 1100°C under vacuum, rxn E13.

Speculations about a composition dependent transformation M ↔ Y by Steinfink[49] are clarified with the results of dv experiments E16 to E18, loaded $Yb_{4+y}Sb_3$; y= 0.4, 1.0 and 1.8. He observed that alkaline-earth-metal-rich reactions favored the formation of

Table III-9. Distribution of products for reactions $Sr_5Bi_3(H,F)_x$ and $Yb_5Sb_3H_x$.

Rxn. No.	Loaded Composition[a]	Conditions[b]		Product Distribution[c]
E3	Yb_5Sb_3	i	dv	M ~95%, T ~5%
E5	Yb_5Sb_3	i	sc	Y ~95%, T ~5%
E8	$Yb_5Sb_3H_{0.0}$	i	sc	M ~90%, T ~8%, Y ~2%
E9	$Yb_5Sb_3H_{0.5}$	i	sc	Y ~97%
E10	$Yb_5Sb_3H_{1.0}$	i	sc	Y ~100%
E11	$Yb_5Sb_3H_{2.0}$	i	sc	Y ~100%
E13	Rxn E10	i	dv	M ~98%, T ~2%
E15	Yb_5Sb_3	ii	dv/sc	Y ~100%
E16	Yb_5Sb_3	iii	dv	M ~95%, T ~5%
E17	$Yb_{5.8}Sb_3$	iii	dv	M ~100% (+ Yb metal)
E18	$Yb_{4.4}Sb_3$	iii	dv	T ~95%, M ~5%
H2	Sr_5Bi_3	i	dv	M ~95%, T ~2%, Ox
H4	Sr_5Bi_3	i	sc	Y ~97%, Ox
H7	$Sr_5Bi_3H_{0.0}$	i	sc	M ~95%, Y ~3%, Ox
H8	$Sr_5Bi_3H_{0.5}$	i	sc	Y ~55%, M ~43%, Ox
H9	$Sr_5Bi_3H_{1.0}$	i	sc	Y ~90%, T ~8%, Ox
H10	$Sr_5Bi_3H_{2.0}$	i	sc	Y ~97%, T ~2%, Ox
HF1	Sr_5Bi_3F	i	dv	Y ~98%, SrF_2 ~2%

[a] Reactions denoted $A_5Pn_3H_{x.0}$ were loaded with dehydrogenated A metals.
[b] Conditions: i) Reaction at 1100°C for 4h then 10°C/h to 650°C.
ii) Quenched from 1100°C then annealed at 800°C for 21 days.
iii) Similar to (i) but cooled at 4°C/h to 650°C.
sc= Reaction in a sealed fused silica container.
dv= Reaction under dynamic vacuum.
[c] Estimated from Guinier powder patterns. M= Mn_5Si_3-type, Y= β-Yb_5Sb_3-type, T= $Ca_{16}Sb_{11}$-type, Ox= Sr_4Bi_2O (anti-K_2NiF_4-type)

Table III-10. Lattice dimensions of the $Yb_5Sb_3H_x$ compounds.

Rxn No.	Loaded Comp.[a]	Str.Type/ Conds.[b]	a (Å)	b (Å)	c (Å)	Vol.(Å^3)	c/a	c/b	Ref.
	Yb_5Sb_3	M/sc	8.995		6.870	481.4	0.764		49
	Yb_5Sb_3	M/sc	9.0344(2)		6.9112(4)	488.52(4)	0.765		60
E3	Yb_5Sb_3	M/dv	9.0314(4)		6.9024(7)	487.58(7)	0.764		
E8	$Yb_5Sb_3H_{0.0}$	M/sc	9.0292(4)		6.8985(7)	487.06(7)	0.764		
E13	Rxn E10	M/dv	9.0350(5)		6.9049(6)	488.12(7)	0.764		
E16	Yb_5Sb_3	M/dv	9.0357(4)		6.9047(7)	488.21(7)	0.764		
E17	$Yb_{5.8}Sb_3$	M/dv	9.0366(6)		6.9044(9)	488.27(9)	0.764		
	Yb_5Sb_2	Y/sc	12.32	9.60	8.32	984.0	0.675	0.867	49
	Yb_5Sb_3	Y/sc	12.398(2)	9.562(2)	8.246(2)	977.6(4)	0.665	0.862	54
E5	Yb_5Sb_3	Y/sc	12.408(2)	9.5807(7)	8.2649(5)	982.5(2)	0.666	0.862	
E9	$Yb_5Sb_3H_{0.5}$	Y/sc	12.408(1)	9.5795(4)	8.2639(5)	982.2(1)	0.666	0.863	
E10	$Yb_5Sb_3H_{1.0}$	Y/sc	12.3756(9)	9.5938(4)	8.2729(4)	982.24(4)	0.668	0.862	
E11	$Yb_5Sb_3H_{2.0}$	Y/sc	12.374(2)	9.5942(8)	8.2739(7)	982.3(2)	0.669	0.862	

[a] Reactions denoted $Yb_5Sb_3H_{x.0}$ were loaded with dehydrogenated Yb metal.
[b] Cells indexed for M= Mn_5Si_3-type and Y= β-Yb_5Sb_3-type structures.
Conditions: dv = reaction in dynamic vacuum and; sc = reaction in a sealed container.

Table III-11. Lattice dimensions of the $Sr_5Bi_3(H,F)_x$ compounds.

Rxn No.	Loaded Comp.[a]	Str.Type/ Conds.[b]	a (Å)	b (Å)	c (Å)	Vol.(Å^3)	c/a	c/b	Ref.
	Sr_5Bi_3	M/sc	9.63(1)		7.63(2)	614(2)	0.792		58
	Sr_5Bi_3	M/sc	9.651(2)		7.523(5)	606.8(5)	0.779		50
H2	Sr_5Bi_3	M/dv	9.6554(6)		7.5321(8)	608.1(1)	0.781		
H7	$Sr_5Bi_3H_{0.0}$	M/sc	9.647(1)		7.523(2)	606.4(2)	0.780		
H8	$Sr_5Bi_3H_{0.5}$	M/sc	9.654(1)		7.527(2)	607.5(2)	0.780		
	Sr_5Bi_3	Y/sc	13.370	10.233	8.890	1216.3	0.665	0.869	47
H4	Sr_5Bi_3	Y/sc	13.351(3)	10.234(3)	8.885(2)	1214.1(6)	0.665	0.868	
H8	$Sr_5Bi_3H_{0.5}$	Y/sc	13.393(3)	10.230(1)	8.874(1)	1215.8(4)	0.663	0.867	
H9	$Sr_5Bi_3H_{1.0}$	Y/sc	13.356(2)	10.233(2)	8.875(2)	1213.0(2)	0.664	0.867	
H10	$Sr_5Bi_3H_{2.0}$	Y/sc	13.359(4)	10.227(4)	8.873(3)	1212.4(8)	0.664	0.868	
HF1	Sr_5Bi_3F	Y/dv	13.3408(7)	10.2780(5)	8.9316(4)	1224.7(1)	0.669	0.869	

[a] Reactions denoted $Sr_5Bi_3H_{x.0}$ were loaded with dehydrogenated Sr metal.
[b] Cells indexed for M= Mn_5Si_3-type and Y= β-Yb_5Sb_3-type structures.
Conditions: dv= reaction in dynamic vacuum, sc= reaction sealed container.

the orthorhombic phase; however, in actuality more hydrogen impurity was being provided. Products of reaction E16, loaded Yb_5Sb_3, give essentially the hexagonal phase, with traces of $Yb_{16}Sb_{11}$. The formation of the T phase was probably caused by loss of Yb metal that wetted the Ta walls and could not be recovered. Limitations imposed by the dv method impeded us from applying long heating cycles to the samples, which may have allowed better equilibration of the products. A Yb-metal-rich reaction, E17 ($Yb_{5.8}Sb_3$) yielded, according to its Guinier patterns, the M phase as only product. Such a result agrees with the notion that Yb_5Sb_3 is the Yb-richest compound in the Yb–Sb phase diagram. Consequently, the product of E17 is actually a mixture of M-Yb_5Sb_3 and Yb metal that was hard to recover from the Ta walls, and could not be observed in the powder pattern. The Yb-poor reaction, E18 ($Yb_{4.4}Sb_3$) yielded $Yb_{16}Sb_{11}$ as the major product. Importantly, the finding of the tetragonal phase has in many studies been obscured by the presence of hydrogen impurities. A recent revision to the Yb–Sb phase diagram by Abdusalyamova[70] continues to inaccurately consider the M and Y structures to be related by a temperature dependent transformation and lacks the $Yb_{16}Sb_{11}$ phase.

Solution to the structure of a crystal from E17 indicates that the hexagonal phase is stoichiometric, with refined formula $Yb_{5.00(2)}Sb_3$. Tables III-7 and III-8 include the crystallographic and refined data of M-Yb_5Sb_3. Examination of the Yb–Sb interatomic distances, 3.09 – 3.28 Å, suggests that the Yb ions are in divalent oxidation state, as the sum of crystal radii of Yb^{2+} (1.00 Å, CN=6)[62] and Sb^{3-} (2.17 Å)[71] is ~3.17 Å. Accordingly, the effective magnetic moment (μ_{eff} =) of 0.81(1) and 0.77(1) BM for samples E3 and E17, respectively, support the divalent oxidation state for the rare-earth ion, since a moment of ~4.54 BM is expected for the free Yb^{3+} ion.[72] Figure III-13 depicts the temperature dependence of the magnetic susceptibilities (χ) measured at 3 Tesla for samples E3 and E17 after core and sample holder corrections. The effective magnetic moments were calculated by linear regression from $1/\chi$ vs. T plots for T > 100K. The presence of Yb metal traces in E17 could account for the observed weak temperature dependence and higher magnetic susceptibility values. The use of nonlinear fits to χ vs. T curves for both samples resulted in a neglectable temperature independent term to χ.

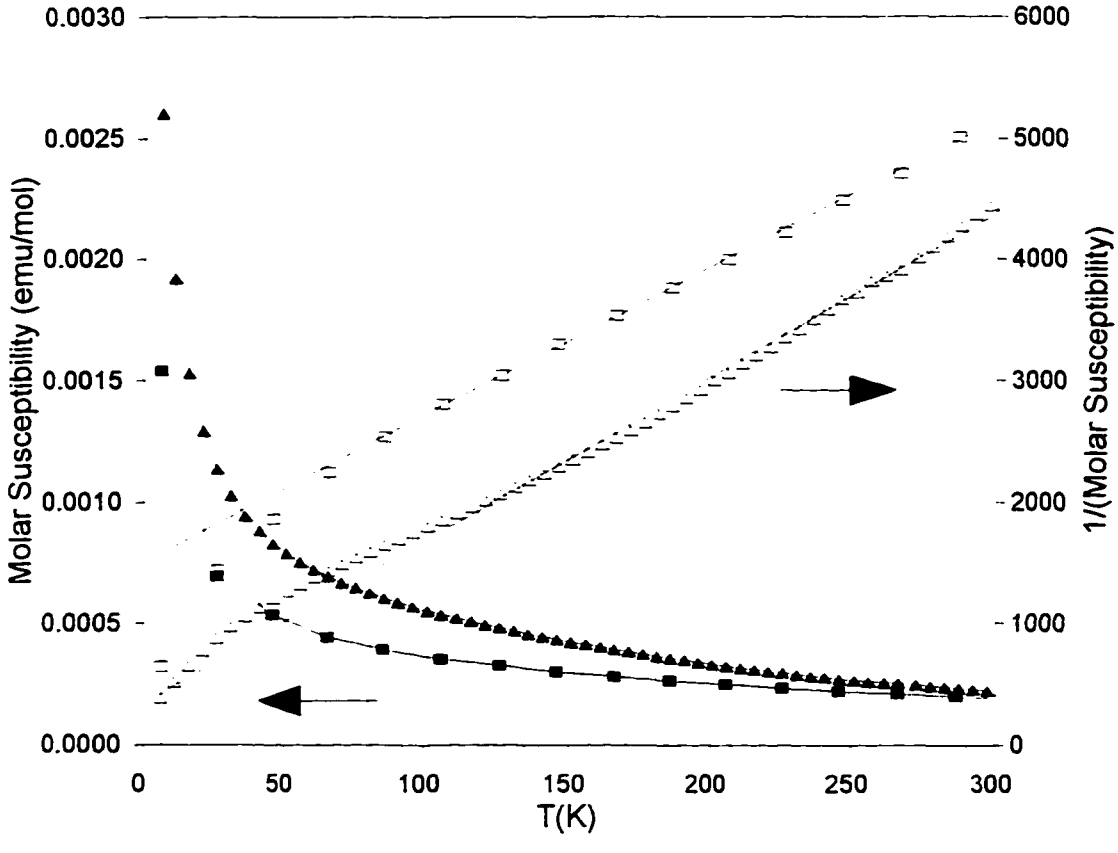

Figure III-13. Temperature dependence of the molar susceptibility (χ) at 3 Tesla of samples E3 (■) and E17 (▲), loaded Yb_5Sb_3 and $Yb_{5.8}Sb_3$ respectively. Solid symbols correspond to χ vs. T plots and empty symbols to $1/\chi$ vs. T. The lines are linear fits for T > 100K.

The Yb ions in Y-$Yb_5Sb_3H_x$ are believe to be in a divalent state as well, because the ratio of the cell volumes of Y and M phases is about two, $V_{Y\text{-}cell}/V_{M\text{-}cell}$= 2.06. The orthorhombic cell contains, without hydrogen, twice as many atoms as the hexagonal one; therefore, a ratio of approximately two between their cell volumes is reasonable if the volumes contribution of the ions remain invariant. The constrictive effect of H^- in the Y-form would give a deviation in volumes in the direction found.

Interestingly and in comparison with $Ca_5Sb_3H_x$, the yield of Y-$Sr_5Bi_3H_x$, as inferred from the data in Tables III-9 and III-11, increases quite proportionally to the amount of hydrogen loaded, see Figure III-14. Variations in yields in these two systems are certainly related to the hydrogen homogeneity range of the compounds. The ternary $Ca_5Sb_3H_x$ can be stabilized with smaller quantities of hydrogen than $Sr_5Bi_3H_x$. Size and electronic requirements must play important roles on the minimum amount of hydrogen required to stabilize these phases.

$Ca_5Bi_3H_x$

To demonstrate that Y-$Ca_5Bi_3H_x$ is a hydrogen-stabilized compound demanded additional experimental efforts. The extraordinary ability of this phase to pick up hydrogen misguided us to think of it as an actual binary compound. Experiments under dynamic vacuum, that in most other systems gave M-A_5Pn_3, resulted in products with the Y structure, rxns F3 and F7 in Table III-12. Conscientious evaluation of the powder pattern of these samples revealed the presence of M-Ca_5Bi_3 in very low yields. Therefore, it was clear that traces of hydrogen in the system were sufficient to stabilize the orthorhombic phase.

In an effort to reduce the hydrogen availability, the reactions between Ca and Bi were carried out in the indirect presence of yttrium metal. The tantalum reaction container was enveloped in a second Ta container along with Y metal as a hydrogen getter. The product of this reaction, F11, exhibited a modest increment in the yield of M-Ca_5Bi_3 to ~ 30%. Unanticipatedly, Y-$Ca_5Bi_3H_x$ seems to be a better hydrogen-getter than Y metal. It was necessary to quench the reactions from 1100°C to retain most of the product in the hexagonal form, rxn F5. Cell dimensions of M-type products, as indicated

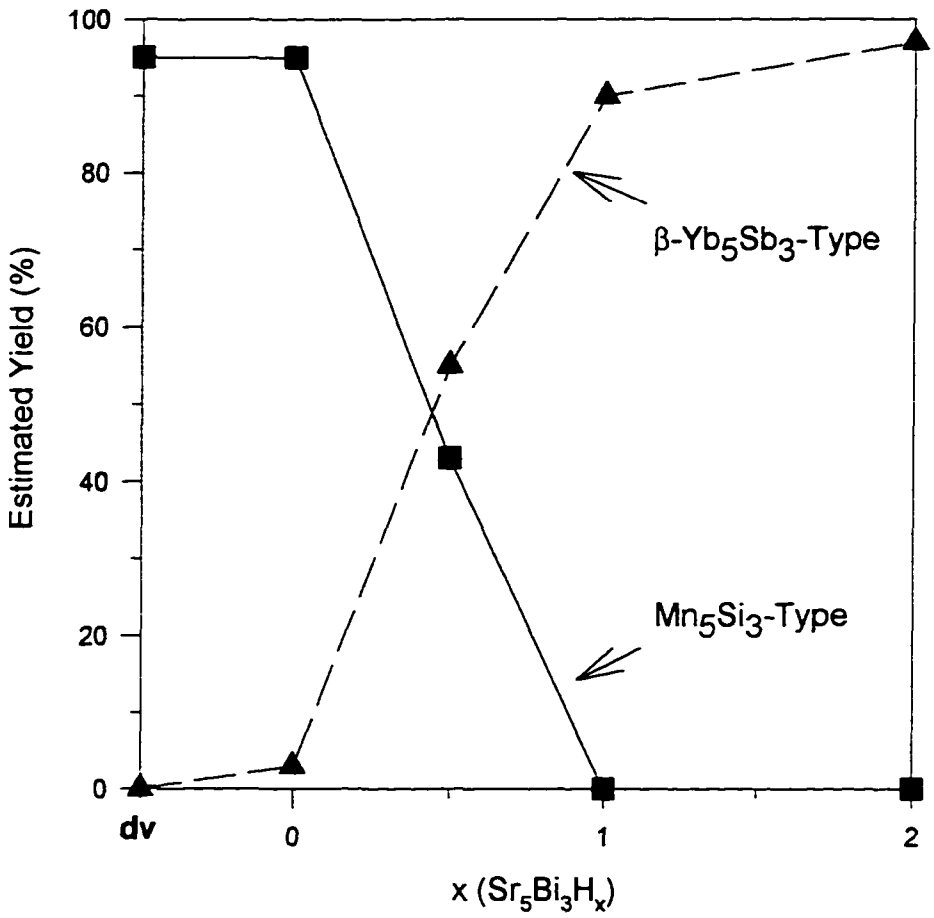

Figure III-14. Graphical representation of the estimated product distribution of reactions $Sr_5Bi_3H_x$, x= 0.0, 0.5, 1.0 and 2.0 (H7 to H10). Data labeled as dv on the abscissas is from sample H2.

Table III-12. Distribution of products for reactions $Ca_5Bi_3(H,F)_x$.

Rxn. No.	Loaded Composition[a]	Conditions[b]		Product Distribution[c]
F3	Ca_5Bi_3	i	dv	Y ~95%, M ~5%
F4	Ca_5Bi_3	i	sc	Y ~85%, T ~10%, Ox
F5	Ca_5Bi_3	ii	dv	M ~90%, Y ~8%, T ~2%
F6	Ca_5Bi_3	iii	dv/sc	Y ~97%, T ~3%
F7	$Ca_5Bi_3H_{0.0}$	i	sc	Y ~92%, M ~6%, T ~2%
F8	$Ca_5Bi_3H_{0.5}$	i	sc	Y ~98%, T ~2%
F9	$Ca_5Bi_3H_{1.0}$	i	sc	Y ~94%, T ~5%, Ox
F10	$Ca_5Bi_3H_{2.0}$	i	sc	Y ~95%, T ~3%, Ox
F11	Ca_5Bi_3	iv	dv	Y ~70%, M ~30%
F13	Rxn F7	v	sc	T ~95%, Ox
F14	Rxn F7	vi	dv	T ~95%, Ox
F16	Ca_5Bi_3	vii	dv	T ~85%, Y ~12%, Ca-metal ~3%
FD2	$Ca_5Bi_3D_x$	i	dg	Y ~100%
FF2	Ca_5Bi_3F	i	dv	Y ~90%, T ~8%, CaF_2 ~2%

[a] Reactions denoted $Ca_5Bi_3H_{x.0}$ were loaded with dehydrogenated Ca metal.

[b] Conditions:
- i) Reaction at 1100°C for 2h then 10°C/h to 650°C.
- ii) Quenched from 1100°C in an ice-water bath.
- iii) Quenched from 1100°C in an ice-water bath, then annealed 850°C for 14 days.
- iv) Heating conditions as (i), Ta-reaction container enveloped in a second container along with Y metal.
- v) Reaction at 1150°C for 2h then quenched to RT. Reaction container encapsulated in a second container with Y metal.
- vi) Reaction at 1150°C for 2h then 10°C/h to 650°C.
- vii) Reaction in a high temperature furnace at 1300°C for 6h then 8°C/h to 600°C, followed for 80°C/h to RT.
- sc= Reaction in a sealed fused silica container.
- dv= Reaction under dynamic vacuum.
- dg= Reaction under constant pressure of deuterium gas.

[c] Estimated from Guinier powder patterns. M= Mn_5Si_3-type, Y= β-Yb_5Sb_3-type, T= $Ca_{16}Sb_{11}$-type, Ox= Ca_4Bi_2O (anti-K_2NiF_4-type) structures.

in Table III-13, are consistently reproducible, while those of the Y-type decrease ~ 0.93 and ~1.01% in their cell volume from low, rxn F3, to high hydrogen content reactions, rxn F10, and according to Hurng's report, respectively.

Complete conversion of M-Ca_5Bi_3 to Y-$Ca_5Bi_3H_x$ is achieved by simply annealing the hexagonal compound in a sealed container, i.e., the slow hydrogenation reaction F6. Attempts to dehydrogenate Y-$Ca_5Bi_3H_x$ by heating the compound at 1150°C under vacuum failed, forming $Ca_{16}Bi_{11}$ (T) in high yields instead (rxn F14). Quenching a sample with the Y form from 1150°C resulted in formation of the T phase as well, rxn F13. Traces of Ca_4Bi_2O were observed in both F13 and F14 products. The presence of the oxide suggest that decomposition of Y-$Ca_5Bi_3H_x$ (F7) occurred during its handling in the dry-box or O_2 in vacuum. Consequently, the loss of calcium in these reactions forced the systems to form the neighboring calcium-deficient phase. On the other hand, the results of F13 and F14 can also be interpreted as contradictory to the information reported by Smirnov and Rudnichenko[73] for the Ca–Bi phase diagram in 1963. They reported that Ca_5Bi_3 melts congruently at ~1350°C. However, our results suggest that a peritectic was reached at near 1150°C instead. In support of this last argument, a reaction carried at 1300°C and under dv conditions, rxn F16, gave the T-type phase and Y-$Ca_5Bi_3H_x$ as major and minor products, respectively. The Ca–Bi phase diagram revisited by Notin and coworkers[69] in 1995 partially agrees with our results. They report that a phase ~Ca_3Bi_2, probably $Ca_{16}Bi_{11}$ misassigned, melts congruently at 1356°C. Unfortunately, they still fail to report any peritectic near 1150°C for Ca-richer compositions. Interestingly, Hösel's original report[75] on the Ca–Bi diagram in 1962 is in better concordance with our observations than the later reports.

To further prove that Y-$Ca_5Bi_3H_x$ is a hydrogen-stabilized phase, powder neutron diffraction studies were performed on the deuteride $Ca_5Bi_3D_x$. This deuterium derivative was prepared in a two-step reaction consisting first of the reaction between the elements in absence of hydrogen, dv conditions, and then reaction with deuterium gas (see the experimental section). The final product, according to its Guinier powder pattern, was a single Y-phase, rxn FD2. Neutron scattering data were collected on a ~2.8 g sample of deuteride at room temperature for ~20 hours at the ORNL neutron facility. The results of

Table III-13. Lattice dimensions of $Ca_5Bi_3(H,F)_x$ compounds.

Rxn No.	Loaded Comp.[a]	St.Type/ Conds.[b]	a (Å)	b (Å)	c (Å)	Vol.(Å^3)	c/a	c/b	Ref.
F3	Ca_5Bi_3	M/dv	9.172(1)		7.145(2)	520.6(2)	0.779		
F5	Ca_5Bi_3	M/dv	9.1757(3)		7.1444(4)	520.93(4)	0.779		
	Ca_5Bi_3	Y/sc	12.722(8)	9.666(6)	8.432(6)	1037(2)	0.663	0.872	74
	Ca_5Bi_3	Y/sc	12.766(1)	9.706(2)	8.437(2)	1045.4(5)	0.661	0.869	50
	Ca_5Bi_3	Y/sc	12.764(4)	9.710(8)	8.430(6)	1045(1)	0.660	0.868	56
F3	Ca_5Bi_3	Y/dv	12.7729(7)	9.6921(5)	8.4326(5)	1043.9(1)	0.660	0.870	
F4	Ca_5Bi_3	Y/sc	12.6145(8)	9.7126(5)	8.4420(5)	1034.3(1)	0.669	0.869	
F6	Ca_5Bi_3	Y/dv/sc	12.718(1)	9.6993(7)	8.4315(5)	1040.1(1)	0.663	0.869	
F11	Ca_5Bi_3	Y/dv	12.769(1)	9.6917(7)	8.4326(6)	1043.6(1)	0.660	0.870	
F7	$Ca_5Bi_3H_{0.0}$	Y/sc	12.7602(7)	9.6924(5)	8.4330(4)	1042.97(9)	0.661	0.870	
F8	$Ca_5Bi_3H_{0.5}$	Y/sc	12.6972(7)	9.7036(5)	8.4334(4)	1039.06(9)	0.664	0.869	
F9	$Ca_5Bi_3H_{1.0}$	Y/sc	12.609(1)	9.7141(8)	8.4443(7)	1034.3(2)	0.670	0.869	
F10	$Ca_5Bi_3H_{2.0}$	Y/sc	12.611(2)	9.714(1)	8.442(1)	1034.2(2)	0.669	0.869	
FD2	$Ca_5Bi_3D_x$	Y/dv/sc	12.608(1)	9.7078(9)	8.4398(8)	1033.0(1)	0.669	0.869	
FD2[c]	$Ca_5Bi_3D_{0.93(3)}$	Y/dv/sc	12.6068(4)	9.7070(3)	8.4384(2)	1032.65(4)	0.669	0.869	
	Ca_5Bi_3F	Y/sc	12.602(2)	9.771(2)	8.501(2)	1046.8(6)	0.675	0.870	50
FF2	Ca_5Bi_3F	Y/dv	12.6974(8)	9.7276(6)	8.4547(7)	1044.3(1)	0.666	0.869	

[a] Reactions denoted $Ca_5Bi_3H_{X.0}$ were loaded with dehydrogenated Ca metal.
[b] Cells indexed for M= Mn_5Si_3-type and Y= β-Yb_5Sb_3-type structures; Conds: dv= dynamic vacuum, sc= sealed container.
[c] Neutron diffraction data.

the structural refinement are given in Tables III-14 and III-15, where the refined crystallographic atom positions for Y-Ca_5Bi_3F[50] are included in Table III-15 for reference purposes. The final fit to the experimental neutron diffraction histogram is given in Figure III-15, where the lower curve represents the difference between calculated and observed values.

The results of the final refinement confirm that $Ca_5Bi_3D_{0.93(3)}$ is isotypic with Ca_5Sb_3F, with statistics; R_p/R_{wp} and reduced-χ^2 5.37/6.36% and 1.210, respectively. They also indicate that hydrogen (deuterium) is present and located in the same interstitial position that Hurng reported for F^- in Y-Ca_5Bi_3F. Removal of hydrogen from the structural solution gave residuals of R_p/R_{wp} and reduced-χ^2 7.72/9.43% and 2.658, respectively, as well as several unaccounted peaks in the final histogram. This indicated that hydrogen is indeed present in the structure. The hydrogen is located in a tetrahedral cavity formed by atoms Ca(1), Ca(3) and Ca(4). Interatomic distances Ca–D, d= 2.24 to 2.30 Å (d_{ave} = 2.265 Å), are in good agreement with the distance anticipated from the sum of crystal radii for Ca^{2+} and H^- of ~2.24 Å (H^- radii ~1.10 Å).[57] Importantly, the neutron data refined lattice parameters are equivalent to those calculated from Guinier powder patterns, see Table III-13.

Lastly, it is interesting to notice that one can, grossly, guesstimate how much hydrogen contaminant was present in Y-$Ca_5Bi_3H_x$ phases in past reports by comparison with the cell volumes of samples F7 to F10, and following the approach used for sample A11, $Ba_5Sb_3H_{\sim 0.7}$. Hence, Hurng's[50] and Wolfe's[56] cell volumes suggest products that had a low hydrogen content (x ~0.05) while Martinez-Ripoll's[74] had a high content (x ~0.6), Table III-13.

Other $A_5Pn_3H_x$ systems

After recognizing the effect of hydrogen in the $Ba_5Sb_3H_x$, $(Ca,Yb)_5Sb_3H_x$ and $(Ca,Sr)_5Bi_3H_x$ systems, it was imperative to establish whether other systems behaved similarly under presence of hydrogen. Consequently, the study was extended to other alkaline-earth and divalent-rare-earth metal pnictides, especially for $Eu_5(Sb,Bi)_3$ and Yb_5Bi_3 because these have been reported with solely the Y structure. Results of

Table III-14. Neutron crystallographic data of $Ca_5Bi_3D_{0.93(3)}$ compound.

	$Ca_5Bi_3D_{0.93(3)}$
Sample from rxn.	FD2
Space group	Pnma (#62)
Lattice parameters	
a (Å)	12.6068(4)
b (Å)	9.7070(3)
c (Å)	8.4384(2)
Volume ($Å^3$)	1032.65(4)
Density calc. (g/cm^3)	5.334
Experimental temperature (K)	298
Neutron wavelength (Å)	1.4177
Refined 2θ region (°)	10 – 140
Total number of points	2474
Number of variables	31
R_p (%)	5.37
R_{wp} (%)	6.36
Reduced χ^2	1.210
Final maximum atom shift	0.00

representative reactions between alkaline-earth (Ca, Sr, Ba) or divalent-rare-earth metals (Sm, Eu, Yb) and the pnictogens (As, Sb, Bi) in absence and presence of hydrogen or fluorine (as AH_2 or AF_2) are given in Table III-16. Experiments with variable hydrogen composition were limited to a few systems.

In general, the reactions with arsenic, with exception of the Ba–As and Sm–As combinations, form phases with the M-type structures. These hexagonal compounds can take up hydrogen without change in their structure type, as noted from variations in their dimensions reported in Table III-17. Cell parameters of selected reports are included this

Table III-15. Refined neutron data of $Ca_5Bi_3(D,F)$, atom positions, isotropic thermal parameters and important interatomic distances.

Atom	x	y	z	U_{iso}·100	Occupancy
Ca_5Bi_3D					
Bi(1)	-0.0187(4)	1/4	0.4192(7)	0.81(12)	1.00
Bi(2)	0.1706(3)	-0.0178(3)	0.0722(5)	0.79(8)	1.00
Ca(1)	0.0724(5)	0.0429(7)	0.6968(7)	1.39(16)	1.00
Ca(2)	0.2285(8)	1/4	0.3208(12)	1.68(26)	1.00
Ca(3)	0.0099(7)	1/4	0.0337(9)	1.02(21)	1.00
Ca(4)	0.2834(8)	1/4	0.8555(12)	1.11(21)	1.00
D	0.1043(6)	1/4	0.8053(9)	1.22(26)	0.93(3)
Ca_5Bi_3F[a]				(B_{eq},Å^2)	
Bi(1)	-0.0188(1)	1/4	0.4171(2)	1.16(5)	1.00
Bi(2)	0.17092(7)	-0.01882(8)	0.0766(1)	1.28(3)	1.00
Ca(1)	0.0722(4)	0.0433(4)	0.6939(6)	1.5(2)	1.00
Ca(2)	0.2300(6)	1/4	0.3209(8)	1.5(3)	1.00
Ca(3)	0.0077(6)	1/4	0.0317(9)	1.4(3)	1.00
Ca(4)	0.2835(6)	1/4	0.8583(9)	1.5(3)	1.00
F	0.105(2)	1/4	0.803(3)	1.7(3)	0.98(5)

Important interatomic distances (Å).

Atom(1) – Z	Ca_5Bi_3D	Ca_5Bi_3F[a]
Ca(1) – Z (2x)	2.245(8)	2.25(1)
Ca(3) – Z (1x)	2.27(1)	2.30(2)
Ca(4) – Z (1x)	2.30(1)	2.29(3)

[a] Taken from ref. 50.

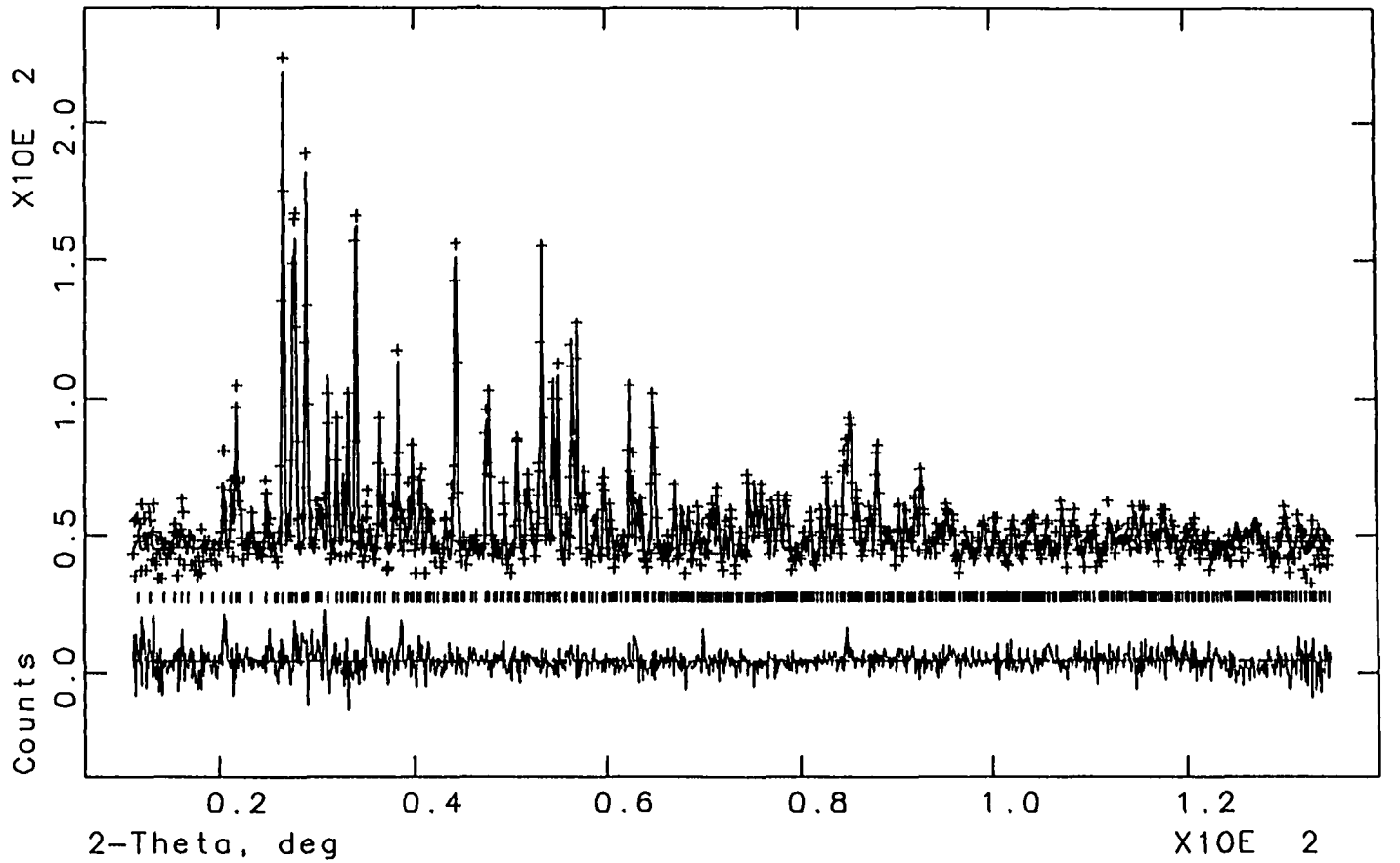

Figure III-15. Powder neutron diffraction pattern of Y-Ca_5Bi_3D. Lines and points represent the calculated and observed values of the profiles, respectively, the bottom curve indicates the difference between them.

Table III-16. Distribution of products for reactions $A_5Pn_3(H,F)_x$.

Rxn. No.	Loaded Composition[a]	Conditions[b]		Product Distribution[c]
AS1	Ca_5As_3	i	dv	M ~95%, UN
AS14	$Ca_5As_3H_{2.0}$	i	sc	M ~95%, T ~5%
AS2	Sr_5As_3	i	dv	M ~75%, UN
AS15	$Sr_5As_3H_{2.0}$	i	sc	M ~50%, T ~40%
G2	Sr_5Sb_3	i	dv	M ~95%, T ~3%, Ox
G9	$Sr_5Sb_3H_{0.0}$	i	sc	M ~100%
G10	$Sr_5Sb_3H_{0.5}$	i	sc	Y ~60%, M ~40%
G11	$Sr_5Sb_3H_{1.0}$	i	sc	Y ~99%, T ~1%
G12	$Sr_5Sb_3H_{2.0}$	i	sc	Y ~96%, T ~4%
GF2	Sr_5Sb_3F	i	dv	Y ~95%, T ~3%, SrF_2 ~2%
AS3	Ba_5As_3	i	dv	ATP ~100%
AS16	$Ba_5As_3H_{2.0}$	i	sc	ATP ~100%
M3	Ba_5Bi_3	i	dv	M ~95%, Ox
M7	$Ba_5Bi_3H_{2.0}$	i	sc	M ~85%, T ~10%, Ox
RE16	Sm_5As_3	i	dv	ATP ~100%
RE13	$Sm_5As_3H_{2.0}$	i	sc	N ~100%
RE17	Sm_5Sb_3	ii	dv	M ~80%, ATP ~20%
RE19	$Sm_5Sb_3H_{2.0}$	ii	sc	M ~95%, ATP ~5%
RE18	Sm_5Bi_3	ii	dv	M ~30%, ATP ~65%
RE20	$Sm_5Bi_3H_{2.0}$	ii	sc	Y ~95%, ATP ~5%

Table III-16. Continued

Rxn. No.	Loaded Composition[a]	Conditions[b]		Product Distribution[c]
AS5	Eu_5As_3	i	dv	M ~98%, T ~2%
AS18	$Eu_5As_3H_{2.0}$	ii	sc	M ~5%, T ~95%
RE7	Eu_5Sb_3	i	dv	M ~98%, Ox
RE9	$Eu_5Sb_3H_{2.0}$	i	sc	Y ~98%, Ox
RE8	Eu_5Bi_3	i	dv	M ~97%, Ox
RE9	$Eu_5Bi_3H_{2.0}$	i	sc	Y ~97%, Ox
AS28	Yb_5As_3	iii	dv	M ~70%, UN
AS17	$Yb_5As_3H_{2.0}$	ii	sc	M ~35%, NC ~15%, UN
P1	Yb_5Bi_3	ii	dv	Y ~75%, M ~25%
P3	Yb_5Bi_3	iv	dv	M ~85%, Y ~15%
P4	Yb_5Bi_3	ii	sc	Y ~96%
P5	$Yb_5Bi_3H_{0.0}$	ii	sc	Y ~90%, M ~7%
P6	$Yb_5Bi_3H_{0.5}$	ii	sc	Y ~95%
P7	$Yb_5Bi_3H_{1.0}$	ii	sc	Y ~98%
P8	$Yb_5Bi_3H_{2.0}$	ii	sc	Y ~96%

[a] Reactions denoted $A_5Pn_3H_{x.0}$ were loaded with dehydrogenated A metals.

[b] Conditions: i) Reaction at 1100°C for 2h then 10°C/h to 650°C.
ii) Same as (i) but reaction temp. 1150°C.
iii) Reaction at 1300°C in a high temperature furnace, then 80°C/h to 600°C.
iv) Quenched from 1100°C.
sc= Reaction in a sealed fused silica container.
dv= Reaction under dynamic vacuum.

[c] Estimated from Guinier powder patterns. M= Mn_5Si_3-type, Y= β-Yb_5Sb_3-type, T= $Ca_{16}Sb_{11}$-type, ATP= anti-Th_3P_4-type, NC= NaCl-type, Ox= A_4Pn_2O (anti-K_2NiF_4-type) structures, UN= Unidentified phase.

Table III-17. Lattice dimensions of $A_5Pn_3(H,F)_x$ compounds.

Rxn No.	Loaded Comp.[a]	Str.Type/ Conds.[b]	a (Å)	b (Å)	c (Å)	Vol.(Å^3)	c/a	c/b	Ref.
	Ca_5As_3	M/sc	8.43		6.75	415.4	0.801		77
	Ca_5As_3	M/sc	8.479		6.844	426.1	0.807		47
AS1	Ca_5As_3	M/dv	8.4885(3)		6.8436(5)	427.05(4)	0.806		
AS14	$Ca_5As_3H_{2.0}$	M/sc	8.4412(8)		6.774(3)	418.0(2)	0.802		
	Sr_5As_3	M/sc	8.942		7.355	509.3	0.822		78
AS2	Sr_5As_3	M/dv	8.930(3)		7.333(7)	506.5(6)	0.821		
AS15	$Sr_5As_3H_{2.0}$	M/sc	8.917(4)		7.302(6)	502.8(6)	0.819		
	Sr_5Sb_3	M/sc	9.496(5)		7.422(5)	579.6(7)	0.782		79
	Sr_5Sb_3	M/sc	9.5037(5)		7.4095(8)	579.6(1)	0.780		50
G2	Sr_5Sb_3	M/dv	9.510(1)		7.426(2)	581.6(2)	0.781		
G9	$Sr_5Sb_3H_{0.0}$	M/sc	9.5035(5)		7.4108(7)	579.6(1)	0.780		
G10	$Sr_5Sb_3H_{0.5}$	M/sc	9.510(3)		7.422(4)	581.4(5)	0.780		
	Sr_5Sb_3	Y/sc	13.173(6)	10.101(7)	8.734(4)	1162(2)	0.663	0.865	48
G10	$Sr_5Sb_3H_{0.5}$	Y/sc	13.236(5)	10.114(5)	8.745(4)	1170.6(3)	0.662	0.865	
G11	$Sr_5Sb_3H_{1.0}$	Y/sc	13.206(2)	10.107(2)	8.751(1)	1168.0(3)	0.662	0.866	
G12	$Sr_5Sb_3H_{2.0}$	Y/sc	13.205(2)	10.108(2)	8.750(1)	1168.0(3)	0.662	0.866	

Table III-17. Continued

Rxn No.	Loaded Comp.[a]	Str.Type/ Conds.[b]	a (Å)	b (Å)	c (Å)	Vol.(Å^3)	c/a	c/b	Ref.
GF2	Sr_5Sb_3F	Y/dv	13.215(2)	10.145(1)	8.7898(6)	1178.5(3)	0.665	0.866	
	Ba_5As_3	M/sc	9.49		7.90	616.1	0.832		76
AS3	Ba_5As_3	ATP/dv	9.9646(5)			989.4(1)	1.000		
AS16	$Ba_5As_3H_{2.0}$	ATP/sc	9.9493(8)			984.9(3)	1.000		
	Ba_5Bi_3	M/sc	10.10		7.78	687.3	0.770		47
	Ba_5Bi_3	M/sc	10.13(1)		7.79(2)	692(2)	0.769		58
	Ba_5Bi_3	M/sc	10.098(2)		7.768(3)	686.0(4)	0.769		50
M3	Ba_5Bi_3	M/dv	10.1556(2)		7.8912(2)	704.84(2)	0.777		
M7	$Ba_5Bi_3H_{2.0}$	M/sc	10.096(1)		7.766(2)	685.4(3)	0.769		
RE16	SmAs	ATP/dv	8.8361(2)			689.90(4)	1.000		
	$Sm_{0.988}As_{0.988}$[c]	NC/sc	5.9205(4)			206.75(8)	1.000		80
	$Sm_{0.980}As_{0.925}$[c]	NC/sc	5.9131(4)			206.53(4)	1.000		80
	$Sm_{0.996}As_{0.800}$[c]	NC/sc	5.9097(2)			206.39(4)	1.000		80
RE13	$Sm_5As_3H_{2.0}$	NC/sc	5.9076(3)			206.18(3)	1.000		

Table III-17. Continued

Rxn No.	Loaded Comp.[a]	Str.Type/ Conds.[b]	a (Å)	b (Å)	c (Å)	Vol.(Å^3)	c/a	c/b	Ref.
	Sm_5Sb_3	M/sc	9.100		6.40	459.0	0.703		81
	Sm_5Sb_3	M/sc	8.99		6.38	446.5	0.710		82
	Sm_5Sb_3	M/sc	9.18		6.40	467.1	0.697		83
RE17	Sm_5Sb_3	M/dv	9.113(2)		6.381(2)	458.9(2)	0.700		
RE19	$Sm_5Sb_3H_{2.0}$	M/sc	9.1043(4)		6.3451(5)	455.47(6)	0.697		
	Sm_5Bi_3	M/sc	9.30		6.48	485.4	0.697		84
RE18	Sm_5Bi_3	M/dv	9.268(3)		6.456(3)	480.2(3)	0.697		
RE20	$Sm_5Bi_3H_{2.0}$	Y/sc	13.1252(8)	10.1418(6)	8.7613(5)	1166.2(1)	0.667	0.864	
	Eu_5As_3	M/sc	8.8526(3)		7.0376(4)	477.64(7)	0.795		85
	Eu_5As_3	M/sc	8.8646(9)		7.0811(4)	481.9(2)	0.799		86
AS5	Eu_5As_3	M/dv	8.866(2)		7.057(3)	480.5(3)	0.796		
RE7	Eu_5Sb_3	M/dv	9.4183(4)		7.2124(4)	554.06(8)	0.766		
	Eu_5Sb_3	Y/sc	12.983(5)	10.003(4)	8.632(3)	1121.0(6)	0.665	0.863	87
RE9	$Eu_5Sb_3H_{2.0}$	Y/sc	12.994(2)	10.016(1)	8.6302(8)	1123.2(3)	0.664	0.862	

Table III-17. Continued

Rxn No.	Loaded Comp.[a]	Str.Type/ Conds.[b]	a (Å)	b (Å)	c (Å)	Vol.(Å^3)	c/a	c/b	Ref.
RE8	Eu_5Bi_3	M/dv	9.5551(3)		7.3256(5)	579.22(5)	0.767		
	Eu_5Bi_3	Y/sc	13.152(2)	10.122(1)	8.754(1)	1165.4(2)	0.666	0.865	87
RE10	$Eu_5Bi_3H_{2.0}$	Y/sc	13.158(2)	10.140(1)	8.752(1)	1167.8(3)	0.665	0.863	
	Yb_5As_3	M/sc	8.480		6.671	415.4	0.787		88
AS28	Yb_5As_3	M/dv-ht	8.4879(4)		6.7116(6)	418.76(6)	0.791		
AS17	$Yb_5As_3H_{2.0}$	M/sc	8.4438(8)		6.5825(8)	406.44(9)	0.780		
P1	Yb_5Bi_3	M/dv	9.1866(2)		7.0401(5)	514.54(6)	0.766		
P3	Yb_5Bi_3	M/dv-q	9.1852(2)		7.0391(4)	514.31(4)	0.766		
	Yb_5Bi_2[c]	Y/sc	12.36	9.66	8.28	988.6	0.670	0.857	89
P4	Yb_5Bi_3	Y/sc	12.638(4)	9.722(2)	8.407(2)	1033.0(5)	0.665	0.865	
P5	$Yb_5Bi_3H_{0.0}$	Y/sc	12.660(2)	9.714(1)	8.4067(6)	1033.9(2)	0.665	0.865	
P6	$Yb_5Bi_3H_{0.5}$	Y/sc	12.592(3)	9.730(2)	8.409(1)	1030.2(4)	0.668	0.864	
P7	$Yb_5Bi_3H_{1.0}$	Y/sc	12.560(1)	9.7369(6)	8.4104(4)	1028.5(1)	0.670	0.864	
P8	$Yb_5Bi_3H_{2.0}$	Y/sc	12.459(5)	9.737(2)	8.414(2)	1028.1(2)	0.675	0.864	

[a] Reactions denoted $A_5Pn_3H_{x.0}$ were loaded with dehydrogenated A metals.
[b] Powder patterns indexed for M= Mn_5Si_3-type, Y= β-Yb_5Sb_3-type, ATP= a-Th_3P_4-type, NC= NaCl-type.
Conditions: dv= dynamic vacuum, sc= sealed container, q= reaction quenched, ht= high temperature furnace used.
[c] Reported composition.

table as well. Single crystal data for $Sr_5As_3H_x$, $Sm_5Sb_3H_x$, Eu_5Sb_3 and Eu_5Bi_3 in the M-type structure are given in Tables III-18 and III-19. Important interatomic distances of these compounds are listed in Table III-20. The structures of $Ca_5As_3H_x$, Eu_5Sb_3 and Eu_5Bi_3 present the characteristic, and already mentioned, features of the hexagonal Mn_5Si_3 and will not be discussed further.

In 1968, Better[76] reported the single crystal x-ray structure of M-Ba_5As_3 with sparse information on how the compound was prepared. Attempts to reproduce this phase by reacting Ba metal and As in either absence or presence of hydrogen failed, rxns AS3 and AS16 respectively. Products with the cubic anti-Th_3P_4-type structure (ATP) were identified instead. The cubic barium arsenide is the first time observed. It is probable that the hexagonal barium arsenide may characteristically be stabilized by heavy atom impurities like oxygen or chloride; however, no additional experiments were performed to confirm this supposition.

Solution to the x-ray single crystal structure of AS3 confirmed the powder pattern assignment and gave a formula of $Ba_4As_{2.8(1)}$ for the compound. Such a formula is agreement with that expected for a valence compound, $Ba_4As_{2.67}$. Fractional occupancy of the pnictide site, as previously discussed, is characteristic of alkaline-earth-metal pnictides with the ATP-type structure.[64,65] Crystallographic and refined data information for $Ba_4As_{2.8(1)}$ are given in Tables III-21 and III-22. Important interatomic distances are listed in Table III-23, where the two sets of As–Ba distances, d= 3.283(1) and 3.629(1) Å, correspond to center-to-edge in the octaverticon polyhedra, see Figure III-9.

Substitution of hydrogen in the structure probably occurs in the tetrahedral interstitial sites (at 7/8, 0, 1/4), because the cell volume decreases ~0.46% from the binary (AS3) to the ternary hydride (AS16), see Table III-16. Consequently, and based on simple electron counts, a composition $Ba_4As_{2.5}H_{0.5}$ is probable for AS16, i.e., a Zintl or valence compound.

The other combination that did not form any A_5Pn_3 phases is Sm–As, of course, under the set of experimental conditions followed. Reactions between the elements in the absence (RE16) and presence of hydrogen (RE13) give products with the ATP and NaCl-type structures, respectively. Calvert and coworkers[80] prepared the NaCl-type

Table III-18. Crystallographic Data for M-$A_5Pn_3H_x$.

	$Sr_5As_3H_x$	$Sm_5Sb_3H_x$	Eu_5Sb_3	Eu_5Bi_3
Crystal from rxn.	AS15	RE19	RE7	RE8
Space Group	$P6_3/mcm$ (#163)	$P6_3/mcm$	$P6_3/mcm$	$P6_3/mcm$
Lattice parameters[a]				
a (Å)	8.917(4)	9.1043(4)	9.4183(4)	9.5551(3)
c (Å)	7.302(6)	6.3451(5)	7.2124(8)	7.3256(5)
Volume ($Å^3$)	502.8(6)	455.47(6)	554.06(8)	579.22(5)
Z	2	2	2	2
Density calc. (g/cm^3)	4.385	8.153	6.743	7.951
Diffractometer	Rigaku AFC6R	Rigaku AFC6R	Rigaku AFC6R	Rigaku AFC6R
Collected octants	h,±k,l	h,±k,±l	±h,k,±l	±h,k,±l
Scan type	ω-2θ	ω-2θ	ω-2θ	ω-2θ
Transmission range	0.680–1.272	0.929–1.122	0.909–1.097	0.719–1.218
Absorption coeff. (cm^{-1})	352.7	405.7	350.9	719.0
Number of reflections				
Measured	1013	1733	2073	2199
Independent (observed[b])	213(148)	218(173)	182(177)	247(187)
R_{ave} (%)	9.08(obs[b])	2.88	3.64(obs[b])	5.97
No. of refined variables	12	12	12	12
R/R_w (%)	2.5/2.6	1.7/2.0	1.8/2.4	1.6/1.9
Goodness of fit	1.339	1.511	1.393	1.158
Secondary ext.coeff. ($x10^{-7}$)	11(1)	6.3(5)	1.5(4)	6.0(2)
Max./min. peak in ΔF map ($e^- Å^{-3}$)	0.73/-1.21	1.99/-1.12	1.34/-1.61	1.51/-1.39

[a] Lattice parameters calculated from Guinier powder patterns.
[b] Observed reflections; $I \geq 3.00\sigma_I$.

Table III-19. Refined positional and thermal parameters for $A_5Pn_3H_x$ phases in the Mn_5Si_3 structure type.

Atom	x	y	z	$B_{eq}(Å^2)$	U_{11}	U_{22}	U_{33}	U_{12}	U_{13}	U_{23}
	$Sr_5As_3H_x$ (AS15)									
Sr(1)	1/3	2/3	0	1.01(4)	0.0155(6)	U_{11}	0.0074(8)	$½U_{11}$	0	0
Sr(2)	0.2499(1)	0	1/4	1.65(8)	0.0108(7)	0.0077(7)	0.043(1)	$½U_{22}$	0	0
As	0.6085(1)	0	1/4	0.81(7)	0.0079(6)	0.0080(8)	0.0147(8)	$½U_{22}$	0	0
(H	0	0	0)							
	$Sm_5Sb_3H_x$ (RE19)									
Sm(1)	1/3	2/3	0	0.40(2)	0.0059(3)	U_{11}	0.0034(4)	$½U_{11}$	0	0
Sm(2)	0.24958(7)	0	1/4	0.65(4)	0.0088(3)	0.0046(4)	0.0099(4)	$½U_{22}$	0	0
Sb	0.61285(8)	0	1/4	0.45(4)	0.0055(4)	0.0048(5)	0.0067(5)	$½U_{22}$	0	0
(H	0	0	0)							
	Eu_5Sb_3 (RE7)									
Eu(1)	1/3	2/3	0	1.12(3)	0.0181(4)	U_{11}	0.0063(5)	$½U_{11}$	0	0
Eu(2)	0.25381(9)	0	1/4	1.50(5)	0.0161(4)	0.0125(5)	0.0274(6)	$½U_{22}$	0	0
Sb	0.6104(1)	0	1/4	0.93(6)	0.0119(5)	0.0110(7)	0.0122(6)	$½U_{22}$	0	0
	Eu_5Bi_3 (RE8)									
Eu(1)	1/3	2/3	0	1.12(2)	0.0185(3)	U_{11}	0.0056(5)	$½U_{11}$	0	0
Eu(2)	0.2517(1)	0	1/4	1.68(4)	0.0186(3)	0.0122(4)	0.0309(5)	$½U_{22}$	0	0
Bi	0.60957(6)	0	1/4	0.96(3)	0.0127(2)	0.0107(3)	0.0126(3)	$½U_{22}$	0	0

Table III-20. Interatomic distances (Å) in $A_5Pn_3H_x$ phases with Mn_5Si_3-type structure.

Atom(1) – Atom(2)	$Sr_5As_3H_x$	$Sm_5Sb_3H_x$	Eu_5Sb_3	Eu_5Bi_3
Pn – A(1) (6x)	3.301(1)	3.2372(3)	3.4241(3)	3.4725(2)
Pn – A(2) (2x)	3.061(2)	3.0948(6)	3.2260(7)	3.2756(5)
Pn – A(2) (1x)	3.198(2)	3.3072(9)	3.359(1)	3.419(1)
Pn – A(2) (2x)	3.863(3)	3.4108(4)	3.8263(6)	3.8952(4)
Pn – Pn (2x)	4.132(3)	3.7798(8)	4.163(1)	4.2191(6)
A(1) – A(1) (2x)	3.651(3)	3.1725(3)	3.6062(4)	3.6628(3)
A(1) – A(2) (6x)	3.865(2)	3.8238(4)	4.0024(5)	4.0732(6)
A(2) – A(2) (2x)	3.859(3)	3.936(1)	4.140(1)	4.166(2)
A(2) – A(2) (4x)	4.277(3)	3.9024(4)	4.3265(6)	4.3819(6)

phase by reaction between the elements and subsequent annealing in closed silica containers. They also mentioned that the Sm_4As_3 in the ATP-type structure can be prepared by arc-melting the elements. Because of the high temperature that is reached through the arc-melting technique, the participation of hydrogen in these reactions is probably diminished. On the other hand, hydrogen in plausible amounts account for the quantitative formation of the NaCl-type phase in reaction RE13 with $Sm_5As_3H_{2.0}$ stoichiometry. Cell dimensions of these phases decrease as the compounds become arsenic deficient, see Table III-17. The cell volume of sample RE13, loaded $Sm_5As_3H_{2.0}$, is ~0.66% smaller than the compound reported by Calvert[80] et al. as stoichiometric, $Sm_{0.988}As_{0.988}$, and also those arsenic-deficient. Therefore, the arsenic vacancies in Sm–As compounds with NaCl-type structure are probably filled with hydride ions.

Calvert and Taylor[89,90,91] have shown a rich structural chemistry of the europium arsenides. They found that two phases exist at approximately the Eu_5As_3 composition, a low temperature phase with the M-type cell and a high temperature phase with the Ca_5Pb_3-type (a supercell deformation ,$\sqrt{3}$a ,$\sqrt{3}$a, c, of the M structure). The latter phase was solely observed when excess Eu reactions were loaded. Thus, because the

Table III-21. Crystallographic Data for $A_5Pn_3H_x$ phases.

	$Ba_4As_{2.8(1)}$	$Sm_5Bi_3H_x$	$Yb_5Bi_3H_x$
Crystal from rxn.	AS3	RE20	P5
Space Group	$I\bar{4}3d$(#220)	Pnma(#62)	Pnma
Lattice parameters[a]			
a (Å)	9.9646(5)	13.1252(8)	12.660(2)
b (Å)		10.1418(6)	9.714(1)
c (Å)		8.7613(5)	8.4067(6)
Volume ($Å^3$)	989.4(1)	1166.2(1)	1033.9(2)
Z	4	4	4
Density calc. (g/cm^3)	5.203	7.859	9.592
Diffractometer	Rigaku AFC6R	Rigaku AFC6R	Rigaku AFC6R
Collected octants	±h,k,l	h,±k,±l	h,±k,l
Scan type	ω-2θ	ω-2θ	ω-2θ
Transmission range	0.796–1.353	0.684–1.262	0.710–1.218
Absorption coeff. (cm^{-1})	255.8	697.7	953.0
Number of reflections			
Measured	747	4378	2057
Independent (observed[b])	139(45)	1227(776)	1079(586)
R_{ave} (%)	10.8	8.70	9.26
No. of refined variables	8	44	44
R/R_w (%)	2.1/2.3	2.7/3.0	4.3/5.4
Goodness of fit	0.720	1.363	1.849
Secondary ext.coeff. ($x10^{-7}$)	0.00	1.3(4)	1.87(6)
Max./min. peak in ΔF map ($e^- Å^{-3}$)	0.71/-0.74	2.04/-2.17	3.69/-3.12

[a] Lattice parameters calculated from Guinier powder patterns.
[b] Observed reflections; $I \geq 3.00\sigma_I$.

Table III-22. Refined positional and thermal parameters of $A_5Pn_3H_x$ phases.

Atom	x	y	z	B_{eq}(Å^2)	U_{11}	U_{22}	U_{33}	U_{12}	U_{13}	U_{23}
	$Ba_4As_{2.8(1)}$ (AS3, a-Th_3P_4-type)									
Ba	0.0673(1)	x	x	1.587(1)	0.0201(1)	U_{11}	U_{11}	0.0000(5)	U_{12}	U_{12}
As	3/8	0	1/4	1.4(2)	0.020(3)	U_{11}	0.014(5)	0	0	0
	$Sm_5Bi_3(H_x)$ (RE20, β-$Yb_5Sb_3H_x$-type)									
Sm(1)	0.2285(1)	1/4	0.3204(2)	0.85(6)	0.0078(9)	0.0150(8)	0.0097(7)	0	-0.0009(6)	0
Sm(2)	0.2876(1)	1/4	0.8501(2)	0.85(6)	0.0073(8)	0.0150(8)	0.0092(7)	0	-0.0032(6)	0
Sm(3)	0.5058(1)	1/4	0.4662(1)	0.77(6)	0.0093(8)	0.0116(7)	0.0082(6)	0	-0.0007(6)	0
Sm(4)	0.07379(9)	0.0418(1)	0.6951(1)	0.99(4)	0.0187(6)	0.0071(5)	0.0118(5)	0.0003(4)	-0.0050(4)	-0.0012(4)
Bi(1)	0.98334(8)	1/4	0.4209(1)	0.59(4)	0.0091(6)	0.0055(5)	0.0079(4)	0	0.0028(4)	0
Bi(2)	0.17053(6)	0.98568(7)	0.06950(8)	0.67(3)	0.0094(4)	0.0078(4)	0.0085(3)	0.0013(3)	-0.0020(3)	-0.0004(3)
	$Yb_5Bi_3(H_x)$ (P5, β-$Yb_5Sb_3H_x$-type)									
Yb(1)	0.2299(3)	1/4	0.3180(4)	0.8(1)	0.009(2)	0.013(2)	0.007(2)	0	-0.003(1)	0
Yb(2)	0.2900(3)	1/4	0.8476(4)	0.9(1)	0.010(2)	0.013(2)	0.012(2)	0	0.001(1)	0
Yb(3)	0.5051(3)	1/4	0.4656(4)	0.7(1)	0.007(2)	0.011(2)	0.008(2)	0	0.001(2)	0
Yb(4)	0.0744(2)	0.0438(2)	0.6945(3)	0.87(7)	0.014(1)	0.010(1)	0.010(1)	0.001(1)	-0.005(1)	-0.001(1)
Bi(1)	0.9834(2)	1/4	0.4212(3)	0.5(1)	0.009(1)	0.004(1)	0.006(1)	0	0.001(1)	0
Bi(2)	0.1713(1)	0.9871(2)	0.0657(2)	0.59(7)	0.0061(8)	0.0076(9)	0.009(1)	0.0009(9)	-0.0020(8)	-0.0030(8)

Table III-23. Interatomic distances in $Ba_4As_{2.8(1)}$.

Atom – Atom	Distance (Å)
As – As (8x)	4.6605(2)
As – Ba (4x)	3.283(1)
As – Ba (4x)	3.629(1)
Ba – Ba (3x)	3.880(1)
Ba – Ba (2x)	4.3148(2)
Ba – Ba (6x)	4.713(1)

experimental conditions they followed unavoidably allow hydrogen in the reactions, i.e., closed silica containers and long annealing periods, it is possible that the supercell could be a hydrogen-stabilized phase. Results of our experiments show that M-type products are formed for reactions in the absence of hydrogen (AS5) because no superlattice reflections were observed in the powder patters. When Eu and As in 5:3 proportions were reacted in presence of hydrogen (AS18) a $Eu_{16}As_{11}$ phase with the $Ca_{16}Sb_{11}$-type structure was formed in high yield, with a small fraction of the M-type phase in the product as well. Additional reactions in the presence of hydrogen resulted in mixture of T and M phases, the latter in very low yield. These results are consistent with the assumption that Eu was removed from the system, probably as unseen EuH_2, driving the reaction to the neighboring Eu-deficient phase. Suspicions about the possible stabilization of the T phase by hydrogen were eliminated after the compound was duplicated in high yield in a reaction under continuous vacuum.

Problems in achieving high yields of ytterbium arsenides at temperatures below 1150°C were caused by an incomplete reaction of the rare-earth metal. It was necessary to increase the reaction temperature to 1300°C to get acceptable yields of the M-phase, rxn AS28, Table III-15. Part of the product of AS28 could not be identified with any other binary in the Yb–As system. It is possible, however, that some of the unassigned lines in the pattern of AS28 may be related to a distortion of M-Yb_5As_3 basic structure. Attempts

to solve the structure in the normal Mn_5Si_3-type were not totally successful. Splitting of the Yb(2) atom position was necessary to achieve a decent solution, R/R_w = 2.9/3.1 %, with large anisotropy in the thermal parameters for the Yb atoms. Axial Polaroid photos did not show evidence of a superstructure. Reactions in presence of hydrogen gave multi-phase products that included, in low yield, the M-type structure, rxn AS17, and other phases that could not be identified. Variations in the cell dimensions between AS28 (Yb_5As_3 loaded) and AS17 ($Yb_5As_3H_x$) show that hydrogen is taken up by the hexagonal M compound.

Other phases originally reported to adopt the Y structure, Sr_5Sb_3,[48] Eu_5Sb_3, Eu_5Bi_3[87] and Yb_5Bi_3,[89] are hydrogen stabilized-compounds as well. They form only when reactions between the elements are carried out in presence of hydrogen; phases with the M-type structure are obtained otherwise. The M-$Eu_5(Sb,Bi)_3$ phases were observed for first time, and their single crystal x-ray structure solutions and results are given in Tables III-18, III-19 and III-20.

The estimated product distribution of reactions G9 to G12 with variable hydrogen content, $Sr_5Sb_3H_x$, are comparable to those of $Sr_5Bi_3H_x$ and different from the $Ca_5Sb_3H_x$ and $Ca_5Bi_3H_x$ systems, compare Figures III-10 and III-14. Such a variety of results is an indication that atom sizes are highly influential on the stability of the orthorhombic phase. Thus, Y-type phases that involve small alkaline-earth metals and large pnictides probably have wider hydrogen homogeneity ranges and, consequently, are stabilized with smaller quantities of hydrogen, i.e. $Ca_5Bi_3H_x$ versus $Sr_5Sb_3H_x$.

Rehr and Kauzlarich[48] reported in 1994 the single crystal structure of Y-$Sr_5Sb_3(H_x)$ as a new binary in the Sr–Sb system. They were unable to reproduce the phase in high yield, despite the fact that they were told about the stabilizing effects of hydrogen in this system.[93] They collected the crystal from a reaction intended to prepare $Sr_{14}MnSb_{11}$. Therefore, at least the Sr metal they used was heavily contaminated with hydrogen.

Europium in M-Eu_5Sb_3 (sample RE7) and M-Eu_5Bi_3 (RE8) has a divalent oxidation state according to the calculated effective magnetic moments (μ_{eff}). Temperature dependencies of the magnetic susceptibility of samples RE7 and RE8 reveal, as

depicted in Figure III-16, a Curie-Weiss behavior above 150K. Effective moments of μ_{eff}= 19.1(3) and 16.9(2) BM were calculated for Eu_5Sb_3 and Eu_5Bi_3, respectively, from $1/\chi$ versus T plots. The single ion calculated contributions ($\mu_{eff}/(5)^{1/2}$) are 8.56 BM for the antimonide and 7.57 BM for the bismuthide, while the free ion Eu^{2+} (Gd^{3+}) theoretical effective moment is 7.94 BM.[94] Weiss constants (θ) for both compounds were calculated to be ~101K. Europium ions in the orthorhombic hydrides are believed to be in a divalent oxidation state on the basis of their cell volume ratios $V_{Y\text{-}cell}/V_{M\text{-}cell}$ = 2.0 as well.

After M-Ca_5Bi_3, M-Yb_5Bi_3, was the second most difficult phase to be prepared in high yield. As in the case of the Ca derivative, it was necessary to quench the reactions from the high temperature in order to retain most of the hexagonal phase, rxns P1 to P8. The comparable sizes of Ca^{2+} and Yb^{2+} ions, with crystal radii of 1.14 and 1.16 Å respectively (CN=6),[62] decisively account for the parallel chemistry between these two systems. Ytterbium ions in Y-$Yb_5Bi_3H_x$, and M-Yb_5Bi_3, are assumed to be in a divalent oxidation state, because their cell volume ratios (Y/M) are nearly two. The structural refinement of a crystal from reaction P5, loaded $Yb_5Bi_3H_{0.0}$, gives a composition of $Yb_{4.99(2)}Bi_{3.00(1)}(H_x)$ for the orthorhombic form. Speculations about the nonstoichiometry of the Y-$Yb_5Bi_3H_x$ phase, formulated as Yb_5Sb_2 by Maksudova,[89] are consequently proved inaccurate. Maskudovas's formulation was justified by the need of excess Yb metal, i.e., hydrogen contaminant source to accomplish higher yields of the Y phase. Crystallographic and refined data of the $Yb_5Bi_3(H_x)$ structure are given in Tables III-21, III-22; selected interatomic distances are reported in Table III-24.

The Sm compounds display a distinctive chemistry from those observed for divalent metals. Antimonides of samarium crystallize in the M-type structure whether hydrogen is present or not. A cell volume decrement of ~0.75% from reaction RE17 (loaded Sm_5Sb_3) to RE19 ($Sm_5Sb_3H_{2.0}$) indicates that some hydrogen is bound in the compound. The Sm ions in these compounds seem to be in a trivalent oxidation state, as one can deduce from their c/a-ratios of 0.700 for RE17 and 0.697 for RE19. All the compounds of dispositive cations with the M-type structures studied to the moment have c/a axial ratios larger than 0.760 (specifically 0.766 to 0.820). On the other hand, trivalent rare-earth-metal pnictides with the same structure type have c/a ratios of about

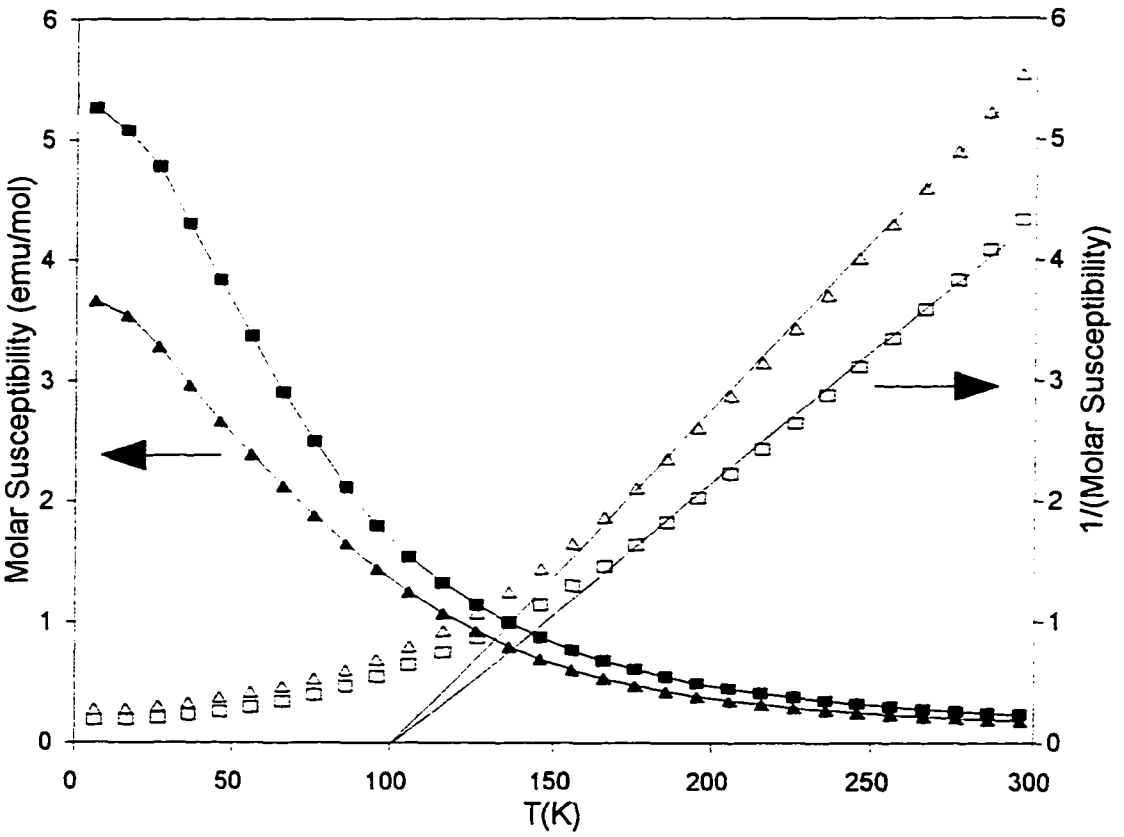

Figure III-16. Temperature dependence of the molar susceptibilities (χ) at 3 Tesla of M-Eu_5Sb_3 (■) and M-Eu_5Bi_3 (▲). Solid symbols correspond to χ vs. T plots and empty symbols to $1/\chi$ vs. T; linear fit for T > 150K.

Table III-24. Interatomic distances (Å) in $A_5Bi_3H_x$ compounds with the β-$Yb_5Sb_3H_x$-type structure.

Atom(1) – Atom(2)	$Sm_5Bi_3H_x$	$Yb_5Bi_3H_x$	Atom(1) – Atom(2)	$Sm_5Bi_3H_x$	$Yb_5Bi_3H_x$
Bi(1) – Bi(2) (2x)	4.768(2)	4.595(3)	Bi(2) – A(4) (1x)	3.562(2)	3.410(3)
Bi(2) – Bi(2) (1x)	4.649(2)	4.483(4)	Bi(2) – A(4) (1x)	3.825(2)	3.719(3)
Bi(2) – Bi(2) (1x)	4.781(3)	4.606(4)	A(1) – A(2) (1x)	4.192(4)	4.027(5)
Bi(1) – A(1) (1x)	3.345(3)	3.238(5)	A(1) – A(2) (1x)	4.706(4)	4.517(5)
Bi(1) – A(1) (1x)	3.950(3)	3.788(5)	A(1) – A(3) (1x)	3.850(4)	3.699(5)
Bi(1) – A(2) (1x)	3.255(3)	3.126(5)	A(1) – A(3) (1x)	3.858(4)	3.712(5)
Bi(1) – A(3) (1x)	3.406(3)	3.263(4)	A(1) – A(4) (2x)	4.081(3)	3.920(3)
Bi(1) – A(4) (2x)	3.217(2)	3.103(3)	A(1) – A(4) (2x)	4.403(3)	4.231(4)
Bi(1) – A(4) (2x)	3.413(2)	3.259(3)	A(2) – A(3) (1x)	4.040(4)	3.934(5)
Bi(2) – A(1) (1x)	3.496(2)	3.348(3)	A(2) – A(3) (1x)	4.413(4)	4.210(5)
Bi(2) – A(1) (1x)	3.549(2)	3.402(3)	A(2) – A(4) (2x)	3.766(3)	3.622(4)
Bi(2) – A(2) (1x)	3.472(2)	3.341(3)	A(2) – A(4) (2x)	4.326(3)	4.135(4)
Bi(2) – A(2) (1x)	3.640(2)	3.485(3)	A(2) – A(4) (2x)	4.604(3)	4.427(4)
Bi(2) – A(3) (1x)	3.446(2)	3.317(3)	A(3) – A(4) (2x)	3.751(3)	3.598(4)
Bi(2) – A(3) (1x)	3.461(2)	3.319(3)	A(3) – A(4) (2x)	3.935(3)	3.789(3)
Bi(2) – A(4) (1x)	3.541(2)	3.398(3)	A(4) – A(4) (1x)	4.021(4)	3.869(5)

0.700. A section is devoted to RE_5Pn_3 later in this chapter.

Refinement of the $Sm_5Sb_3H_x$ structure, RE19, demonstrate that this electron-rich phase is stoichiometric, $Sm_{5.000(8)}Sb_{2.99(1)}(H_x)$, and no heavy atoms are present in the interstitial position. Crystallographic and refined data information are given in Tables III-18 to III-20. The Sm–Sm interatomic distances in the linear array of Sm(1) ions are much smaller, 3.1725(3) Å, than the distances in the trigonal prismatic Sm(2) arrangement, d_{ave} = 3.914 Å. The short contacts in the linear array are suggestive of Sm ions in the trivalent state, judging from the Sm metallic radii, 1.804 Å after Pauling.[61] However, the larger Sm–Sm distances in the confacial chain are allusive of divalent Sm.

Magnetic susceptibility measurements at 3 Tesla as function of temperature (6 - 300K) on Sm_5Sb_3 and $Sm_5Sb_3H_x$ exhibit a rather complex behavior, delineated in Figure III-17, and do not follow a Curie-Weiss law. In a brief report, Abdusalyamova[95] mentions, without showing any data, that M-Sm_5Sb_3 departure from the law is perhaps because of a mixed valence for samarium. The molar susceptibility of Sm_5Sb_3 (RE17) is nearly temperature independent from room temperature to about 175K where it starts to increase to a maximum at ~140K, the first magnetic transition. As the temperature is further decreased, the susceptibility continues to increase to reach another maximum at ~100K, the second transition, followed by a slow fall of the susceptibility. Field-dependent magnetization measurements at 140, 100 and 6K, upper part of Figure III-18, show that antiferromagnetic and ferromagnetic states are contributing to the observed transitions. The field dependence isotherm at T=140K presents a small hysteresis with a saturation field of 25 kOe, suggesting that the first magnetic transition in RE17 is largely from an antiferromagnetic ordering in the structure. The field dependence curves at 100K show a large hysteresis in the magnetization, with saturation fields of ~53 kOe, indicating that the second transition has a large ferromagnetic contribution. This ferromagnetic state seems to continue at lower temperatures, because the isotherm at 6K presents similar characteristics to that of 100K.

The presence of hydrogen in M-Sm_5Sb_3 causes drastic changes on its magnetic behavior as observed from the magnetic susceptibility measurements of $Sm_5Sb_3H_x$ (RE19). Parallel to RE17, two magnetic transitions appear to occur in sample RE19,

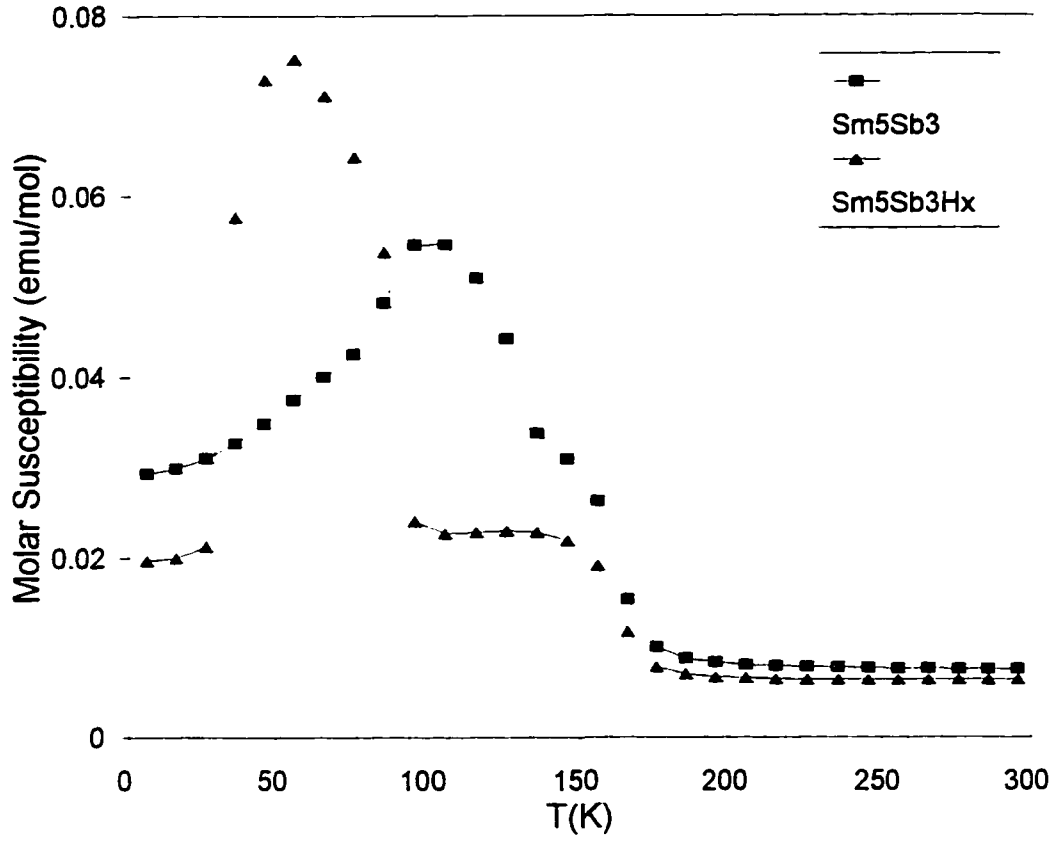

Figure III-17. Temperature dependence of the molar susceptibilities (χ) at 3 Tesla of Sm_5Sb_3 (■) and $Sm_5Sb_3H_x$ (▲).

I)

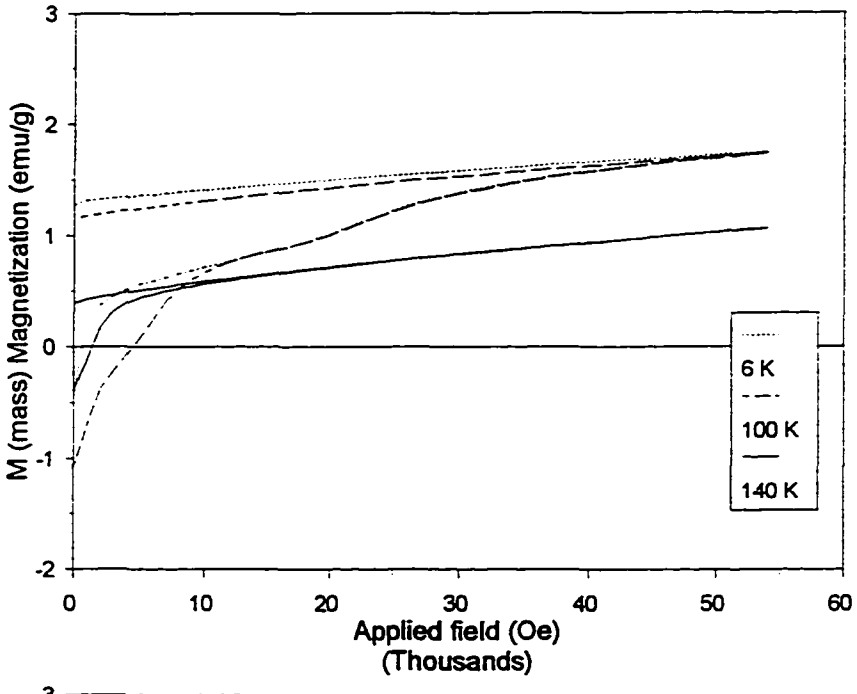

II)

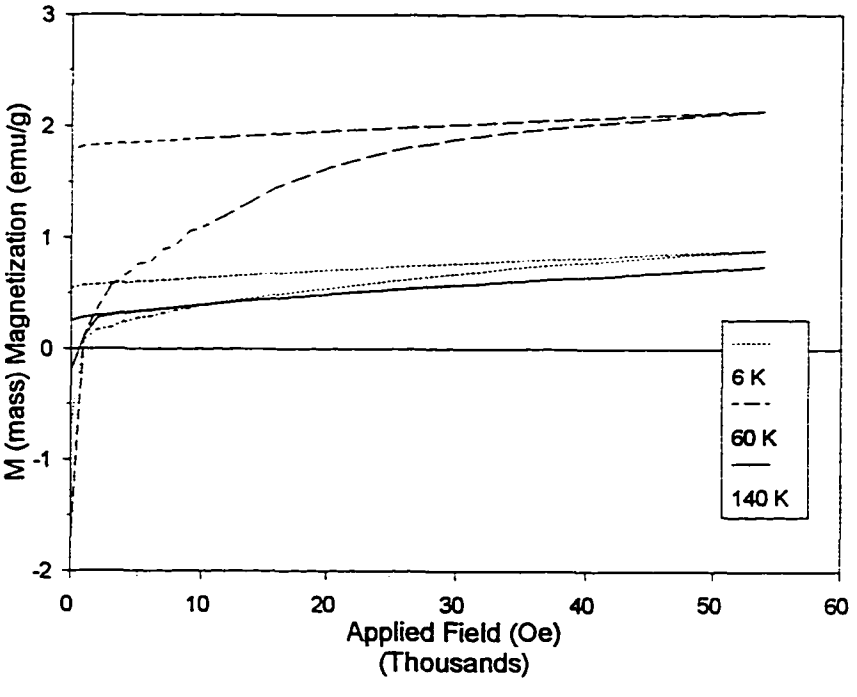

Figure III-18. Field dependence of the magnetizations of (I) Sm_5Sb_3 at 6, 100 and 140K and (II) $Sm_5Sb_3H_x$ at 6, 60 and 140K.

although the second transition temperature switches to ~60K followed by a rapid drop in the susceptibility to nearly temperature-independent values at ~25K. Field-dependent magnetization curves in lower part of Figure III-18 suggest that the second transition at ~60K is still largely due to ferromagnetic interactions. These ferromagnetic states, however, seem to decay as their contribution at 6K is greatly diminished.

Whereas a precise interpretation of the magnetic behavior of Sm_5Sb_3 and $Sm_5Sb_3H_x$, requires at least a combination of magnetic and single-crystal neutron diffraction studies that are beyond the scope of this work, Abdusalyamova[95,96] and Yakinthos[97,98] in their magnetic studies on rare-earth-metal antimonides have shown that several M-RE_5Sb_3 phases present one magnetic transition at low temperatures. Such transitions have been rationalized in terms of magnetic spirals and sublattice interactions within the compounds; the reader is referred to the original work for more details.

Bismuthides of samarium form the M and Y structures when in absence and presence of hydrogen, respectively, rxns RE18 and RE20. The Y-$Sm_5Bi_3H_x$ structure is its first observation. Samarium ions in the M-Sm_5Bi_3 are in a trivalent state as presumed from its lattice parameters, c/a= 0.697 (see Table III-16). On the other hand, the cell volume ratio between the Y and M phases, $V_{Y\text{-}cell}/V_{M\text{-}cell}$= 2.43, suggests that Sm in the Y-type phase is in a different oxidation state. In actuality, the effective magnetic moment of the Y-$Sm_5Bi_3H_x$, μ_{eff}=9.75(1) BM, corresponds to a saturation moment of 4.36 BM per Sm while the usual $Sm^{2+}(Eu^{3+})$ moments of 3.3 – 3.5 BM are observed.[94] The effective moment calculated from $1/\chi$ versus T curves is larger than the anticipated for the free ion perhaps because no correction for the second phase in the sample, Sm_4Bi_3 in the ATP-type structure, was applied. As shown in Figure III-19, $Sm_5Bi_3H_x$ (RE20) displays a much less complex magnetic behavior than the corresponding antimonides. Solution to the structure of Y-$Sm_5Bi_3H_x$ evidences the full stoichiometry of the compound as $Sm_{4.98(2)}Bi_{3.00(1)}(H_x)$. Interatomic Sm–Sm distances in this compound agree with those for divalent Sm ions, minimum $d_{Sm\text{–}Sm}$= 3.75 Å, and in support of the magnetic data information. Crystallographic and refined data of the new Y phases are consolidated in Tables III-21, III-22 and III-24.

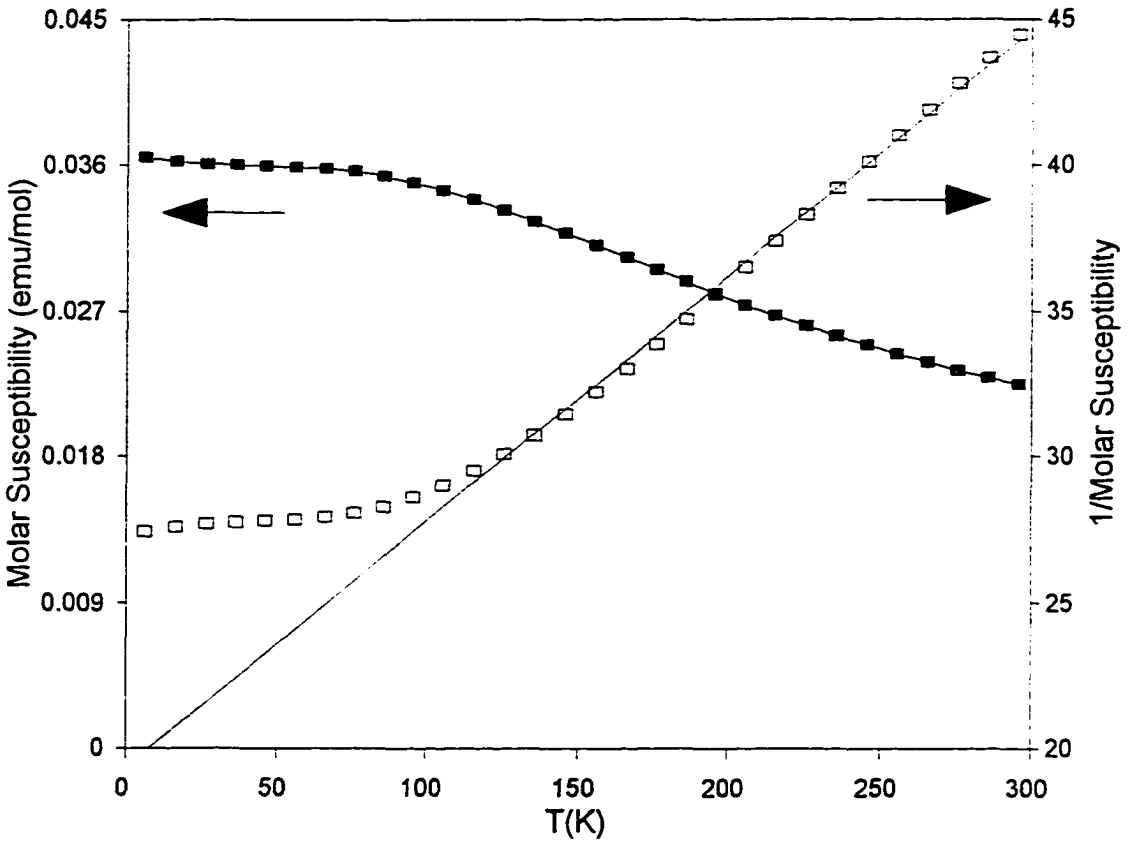

Figure III-19. Temperature dependence of the molar susceptibilities (χ) at 3 Tesla of Y-$Sm_5Bi_3H_x$, (■) for χ vs. T plot and (▫) for $1/\chi$ vs. T; linear fit for T>100K.

Electrical resistivity and magnetic properties

In an attempt to delineate the properties of the Ae_5Pn_3H compounds based on the Zintl ideas, the electrical resistivity and magnetic susceptibility of selected samples were measured as function of the temperature. The resistivity measurements were done by the electrodeless Q method in a temperature range of ~100 to 298K and the susceptibility measurements were made with a SQUID magnetometer at 3 Tesla and from 6 to 300K (see experimental part for details). Results of these measurements are summarized in Tables III-25 and III-26, where effective moments (μ_{eff}) and Weiss constants (θ) values based on Curie-Weiss fits are given as a means of quantifying the temperature dependencies.

Ternary hydrides with Zintl compositions and structures, Ae_5Pn_3H, are anticipated to display semiconducting and diamagnetic behaviors. However, as depicted in Figure III-20 the molar susceptibilities of samples D14 and G12, loaded $Ca_5Sb_3H_{2.0}$ and $Sr_5Sb_3H_{2.0}$ respectively, are temperature-independent paramagnetic. Such a paramagnetic behavior is characteristic of metallic systems. These samples were single Y-type phase products according to their Guinier powder patterns. The effect of paramagnetic impurities as probable cause of these magnetic behaviors can conceivably be ruled out, because no significant variations are observed in the susceptibilities after subtraction of the probable impurity contribution to the original data; the data plotted in Figure III-20 already include this correction. The impurity contribution to the signal was calculated from the intercept at zero field of the magnetization vs. field curve at 300K for each sample.[99] This magnetic impurity contribution ($M = 8.5 \times 10^{-5}$ emu for D14) was then subtracted from the total signal before sample holder and diamagnetic core corrections were applied. Importantly, the diamagnetic core correction applied to D14 was larger than the actual signal for the sample, $\chi_{diam.corr.} = -1.37 \times 10^{-4}$ emu/mol. Consequently, the molar susceptibility of D14 became positive after corrections, i.e, the sample is nearly diamagnetic.

The temperature-independent paramagnetism of D14 and G12 can be rationalized in terms of a possible off-stoichiometry of the ternary hydrides $Ae_5Pn_3H_x$, where $x < 1$. Although, these samples D14 and G12 were prepared in an excess of

Table III-25. Properties of $(Ca,Sr)_5(Sb,Bi)_3(F,H_x)$ compounds with the Y-type structure.

Rxn. No.	Compound	Electrical properties[a]		Magnetic measurements			Ref.
		ρ_{298K} ($\mu\Omega$·cm)	$[\partial\rho/\rho_o\partial T]\cdot 100$ (K^{-1})	Interpreted Behavior[b]	$\chi_M x10^{-6}$ @298K (emu/mol)	μ_{eff}(BM)/θ(K)[c]	
D11	$Ca_5Sb_3H_{\sim 1}$	—	—	PP	17[d]	—	
G12	$Sr_5Sb_3H_{\sim 1}$	—	—	PP	62[d]	—	
	$Ca_5Bi_3H_{\sim 0.05}$[e]	251[f]	0.28[f]	—	—	—	56
DF1	Ca_5Sb_3F	>1000[g]	—	PCW	370	1.31(6)/-310	
FF2	Ca_5Bi_3F	>1050[g]	—	PCW	548	1.83(4)/-469	
	Ca_5Bi_3F	~3.4 x 10^{5} (I)	(E_g= 0.07 eV)[f]	—	—	—	56
GF2	Sr_5Sb_3F	>1600[g]	—	PCW	473	1.46(6)/-287	
HF1	Sr_5Bi_3F	148	0.31(3)	PP	391	—	

[a] Electrical resistivity measured by the electrodeless Q Method at 34 MHz in a temperature range ~100–298K unless noted.
[b] Interpreted behavior of the molar susceptibilities vs. temperature after core and sample holder corrections; PP= Pauli Paramagnetic, PCW= Paramagnetic Curie-Weiss.
[c] Effective moment (μ_{eff}) and Weiss constant (θ) calculated from linear fit of $1/\chi$ vs. T plots; for T >100K.
[d] Molar susceptibility values include a correction for paramagnetic impurities in addition to standard corrections, ref. 99.
[e] Hydrogen content in Wolfe's sample was estimated from the cell volume reported for the phase, see main text.
[f] Electrical resistivity measurements made by the four-probe method on a compressed polycrystalline sample, ref. 56.
[g] Because no changes in the Q signal were observed for this sample, the electrical resistivity was calculated from the minimum estimated reading on the Q meter.

Table III-26. Magnetic measurements on several compounds with the M-type structure.

Rxn. No.	Loaded Composition	Magnetic Information		
		Interpreted Behavior[a]	μ_{eff}(BM)/θ(K)[b]	$\chi_{M(298K)} \times 10^{-6}$ (emu/mol)
AS1	Ca_5As_3	PP	—	77
AS14	$Ca_5As_3H_{2.0}$	D	—	-68
D6	Ca_5Sb_3	PCW	0.65(3)/-114	125
G2	Sr_5Sb_3	PCW	1.24(2)/-203	378
H2	Sr_5Bi_3	PCW	1.20(1)/-332	286
A19	Ba_5Sb_3	PCW	1.59(1)/-251	574
A26	$Ba_5Sb_3H_{0.0}$	D	—	-20
A27	$Ba_5Sb_3H_{0.5}$	PP	—	93
A28	$Ba_5Sb_3H_{1.0}$	PP	—	96
A29	$Ba_5Sb_3H_{2.0}$	PP	—	88
M2	Ba_5Bi_3	PCW	1.53(2)/-261	522
E3	Yb_5Sb_3	PCW	0.81(1)/-125	195

[a] Interpreted behavior of the molar susceptibilities after corrections: D= Diamagnetic; PP= Pauli Paramagnetic; PCW= Paramagnetic Curie-Weiss.
[b] Effective moment (μ_{eff}) and Weiss constant (θ) calculated from a linear fit of $1/\chi$ vs. T plots; for T >50K.

hydrogen, one cannot claim that the valence composition was achieved, because no direct hydrogen quantifications were performed. Therefore, it is possible that deficiency of hydrogen may generate unoccupied states in the orbital bands near the Fermi level, that combined with appropriate electronic interactions between ions may lead to electron mobility throughout the compound. Extended Hückel band calculations on the Y-$Ca_5Bi_3H_y$ (y=0, 0.5, 1.0) models suggest that fractional occupancy of hydrogen atoms in the structure may lead to poor electrical conductive systems. Calculations on the $Ca_5Bi_3H_y$ models were selected because of the complete structural data available for the ternary

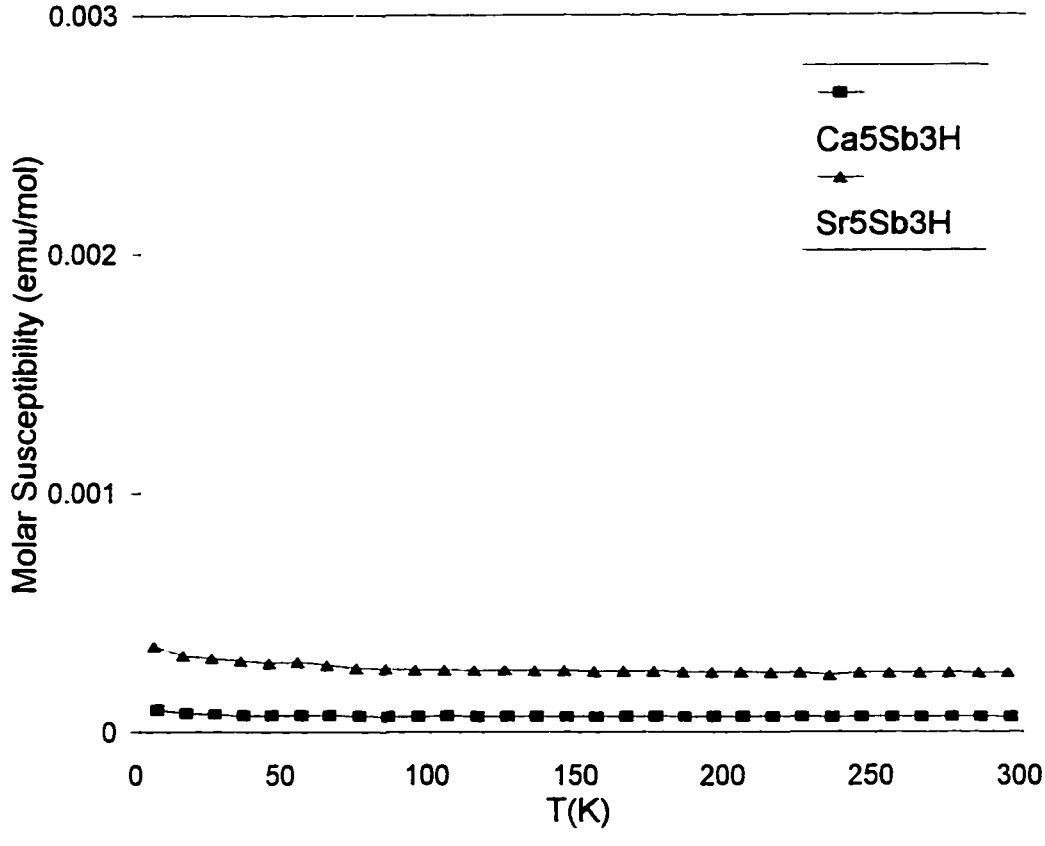

Figure III-20. Temperature dependence of the molar susceptibilities (χ) at 3 Tesla of samples D14 (■) and G12 (▲) with the Y-type structure, loaded $Ca_5Sb_3H_{2.0}$ and $Sr_5Sb_3H_{2.0}$, respectively.

hydride. The calculations for the Ca–Sb and Sr–Sb model combinations give equivalent results to Ca–Bi. The left of Figure III-21 shows the DOS (Density of States) plot for the ideal Y-Ca_5Bi_3, where the shaded area corresponds to the total Bi atoms contribution to the system; s and p atomic states are at ~ -16 and -9 eV, respectively. According to these calculations a hypothetical Y-Ca_5Bi_3 phase would be a metallic conductor, since the Fermi level (ε_F) at -3.32 eV (for a $100e^-$ and 50 k-point calculation) falls within an energy band in a region of a substantial DOS. This band is fundamentally formed by the Ca atoms that define the tetrahedral cavity where hydrogen can be located, specifically Ca(1), Ca(3) and Ca(4). The COOP (crystal orbital overlap population) curves for Ca–Bi and Ca–Ca contacts, below 4.0 and 4.3 Å, respectively, are depicted on the right of Figure III-21. These curves indicate that Ca–Bi antibonding and Ca–Ca bonding interactions occurs at the Fermi level; Bi–Bi interactions are negligible since the Bi atoms separations are large, $d_{Bi-Bi} > 4.4$ Å. The destabilizing effect of the antibonding Ca–Bi interactions at the Fermi level are somewhat diminished by the bonding interactions below the level. According to calculations for Y-$Ca_5Bi_3H_{0.5}$, the orbitals involved in the Ca–Ca bonding interaction are used to bind the interstitial atom, when present; see center plot of Figure III-22. Presence of hydrogen in the compound provokes the formation and diminution of the bands at -14 and -3 eV, respectively. The former band is primarily due to hydrogen and the latter to Ca–Ca interactions. The calculations on Y-$Ca_5Bi_3H_{0.5}$ also suggest that the fractional occupancy of hydrogen would still lead to a metallic-like compounds, which is in good agreement with the electrical resistivity measurements performed by Wolfe[56] on a polycrystalline compressed sample of Y-$Ca_5Bi_3(H_{\sim 0.05})$ by the four-probe method, see Table III-25. He, of course, was unaware of the presence and effects of hydrogen in this compound. His resistivity measurements indicated that the bismuthide is a poor metallic conductor with a temperature coefficient of ($[\partial\rho/\rho_o\partial\cdot T]100 \approx$) 0.28% K^{-1} and electrical resistivity of (ρ_{298K}) 251 μΩ·cm. Bismuth metal has an electrical resistivity of ρ= 106.8 μΩ·cm at room temperature.[100] The hydrogen content in Wolfe's sample was estimated from the cell volume he reported for the phase, see Table III-13; a similar approach was used for sample A11, $Ba_5Sb_3H_{\sim 0.7}$.

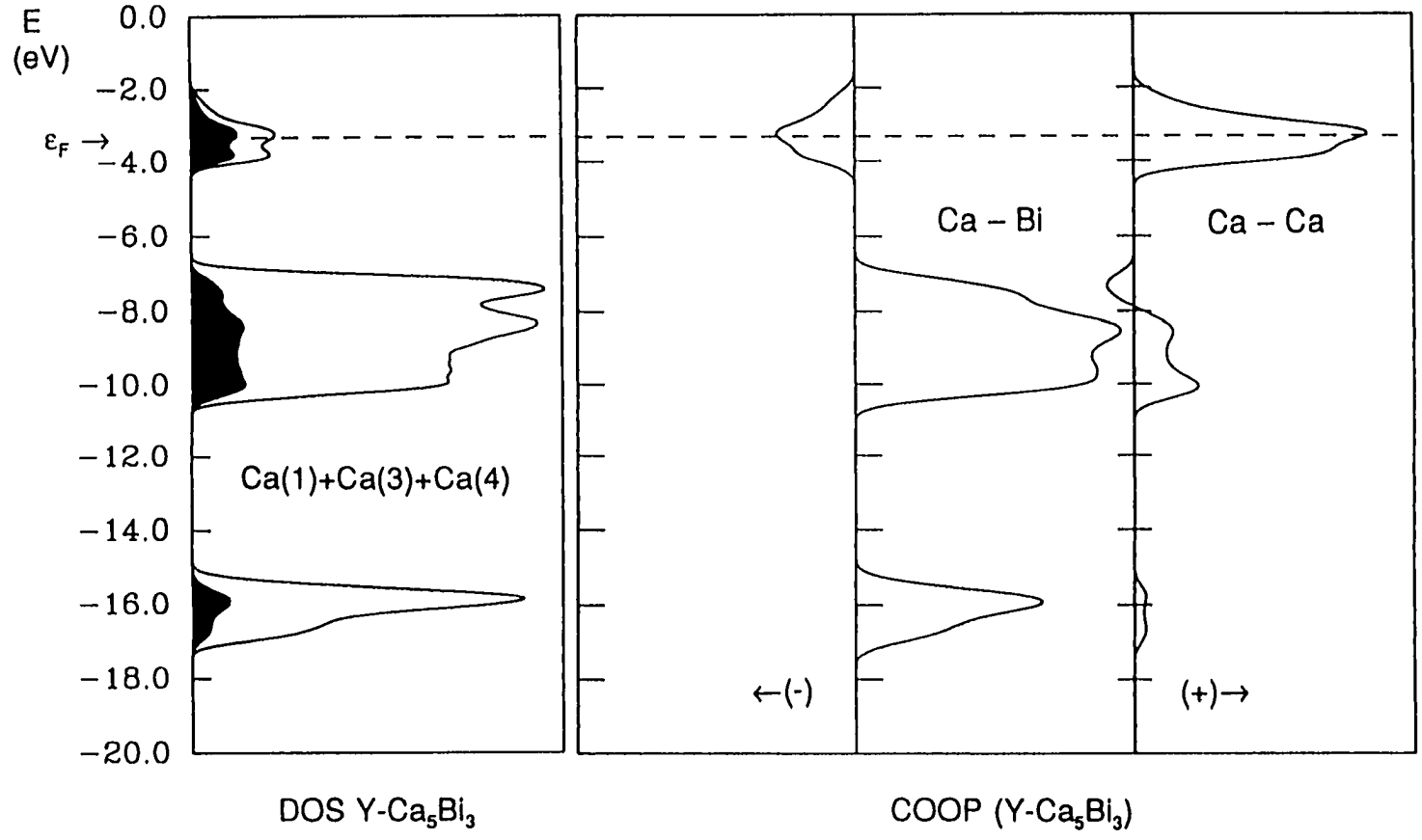

Figure III-21. Graphical results of the Extended Hückel-MO band calculations for Ca_5Bi_3 with the Y-type structure.(I) Total DOS (Density of States) of Y-Ca_5Bi_3 with the Ca(1), Ca(3) and Ca(4) total atomic orbital projection shaded; (II) COOP (crystal orbital overlap population) curves for the averaged Ca–Bi and Ca–Ca interaction. Dashed lines signify the Fermi levels (ε_F).

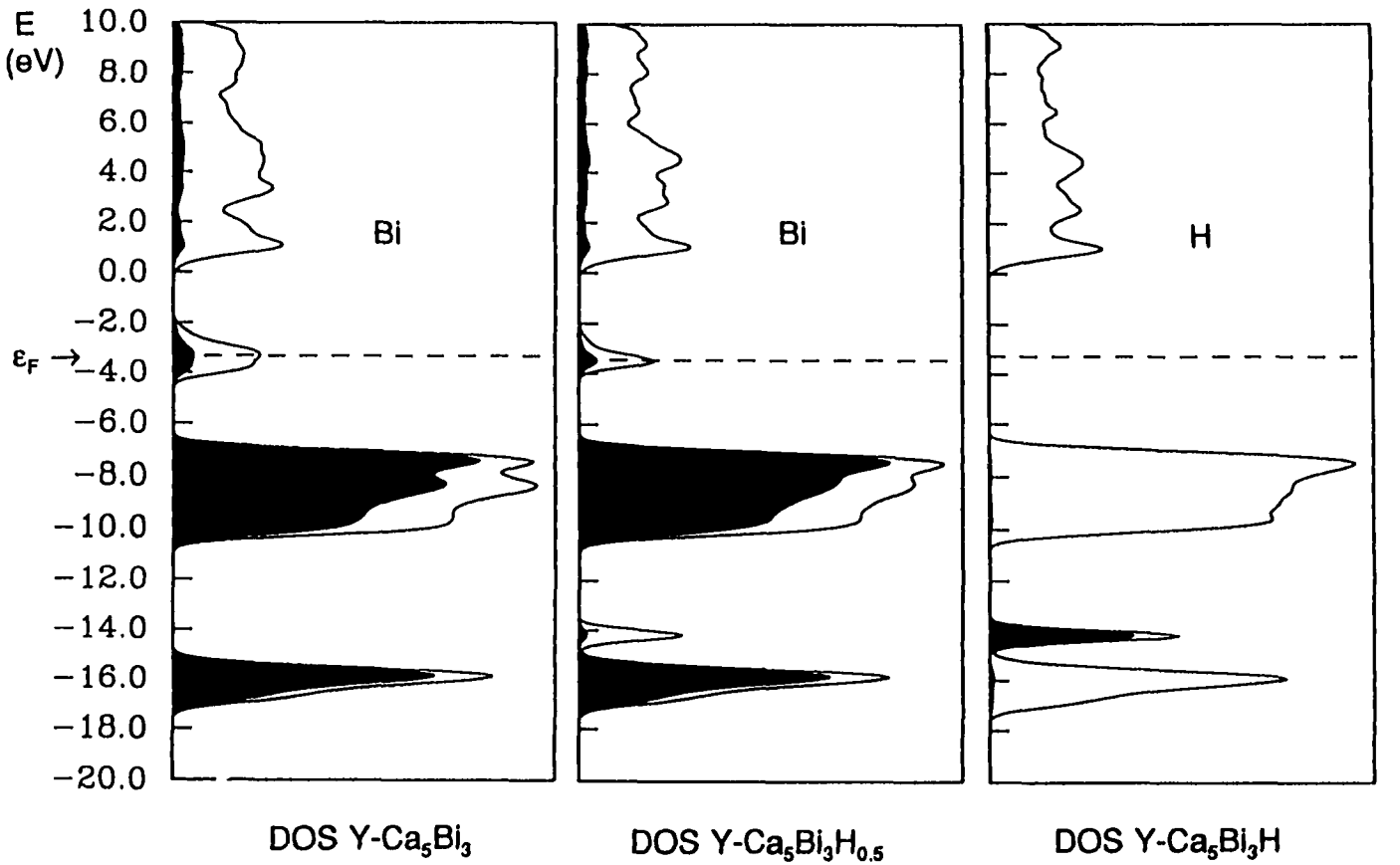

Figure III-22. Total DOS (Density of States) for (I) Y-Ca_5Bi_3 with the Bi atomic orbital projection shaded; (II) Y-$Ca_5Bi_3H_{0.5}$; Bi projection shaded; (III) Y-Ca_5Bi_3H; H projection. Dashed lines signify the Fermi energy levels (ε_F).

The results of calculations for the fully hydrided compound Y-Ca_5Bi_3H, as one would have predicted from simple electron counts, suggest the phase would be a semiconductor or insulator, because the Fermi energy level lies within an energy gap, ε_F= -3.28 eV (for a 104e^- and 50 k-point calculation). Of course, these calculations tend to overestimate the energy gap. Overall, the results of the theoretical calculations discussed above suggest that hydrogen deficiencies in samples D14 and G12 may be responsible for their metallic-like behavior. However, it is still not clear how the electron mobility occurs in systems with nearly stoichiometric hydrogen, Y-$Ae_5Pn_3H_{\sim 1}$.

The electrical resistivity measurements on samples DF1, GF2 and FF2, Ca_5Sb_3F, Sr_5Sb_3F and Ca_5Bi_3F, respectively, indicate that these fluorides are either semiconductors or insulators because of their high resistivity at room temperature. The resistivity values quoted in Table III-25 correspond to estimates based on the minimum readable Q signals for these samples, and in agreement with the Q measurements, these sample had a infinity resistance (Ω) according to two-probe readings made with a Hewlett-Packard multimeter during their handling in the glove-box. The molar susceptibilities measurements of these fluorides as depicted in Figure III-23 show some temperature dependence, i.e., Curie-Weiss behavior. Although, these results seem to contradict the resistivity measurements, they could be rationalized in terms of defects in their structures. Presence of impurities can also be blamed for these results, because as proven by Spedding and coworkers[101,102] minor quantities of ferromagnetic impurities, <0.01 at.% of Gd or Fe, are able to make the molar susceptibilities of Sc, Y and La metals appear Curie-Weiss down to 20K. However, corrections to the susceptibilities of sample GF2, Sr_5Sb_3F for ferromagnetic impurities do not result in a significant change in temperature dependence of the signal, that is, effective moments of 1.46(6) and 1.29(4) BM are calculated from the $1/\chi$ vs. T curves (T > 100K) before and after correction. The correction for paramagnetic impurities was done following the approach used for samples D14 and G12 (see above). Therefore, the presence of defects in the structure as F^- deficiency could be blamed for the unexpected magnetic behaviors. Empty fluoride sites may act as electron traps that could prompt the temperature dependence of the molar susceptibility. The possible F^- deficiency in samples DF1 and FF2 was already

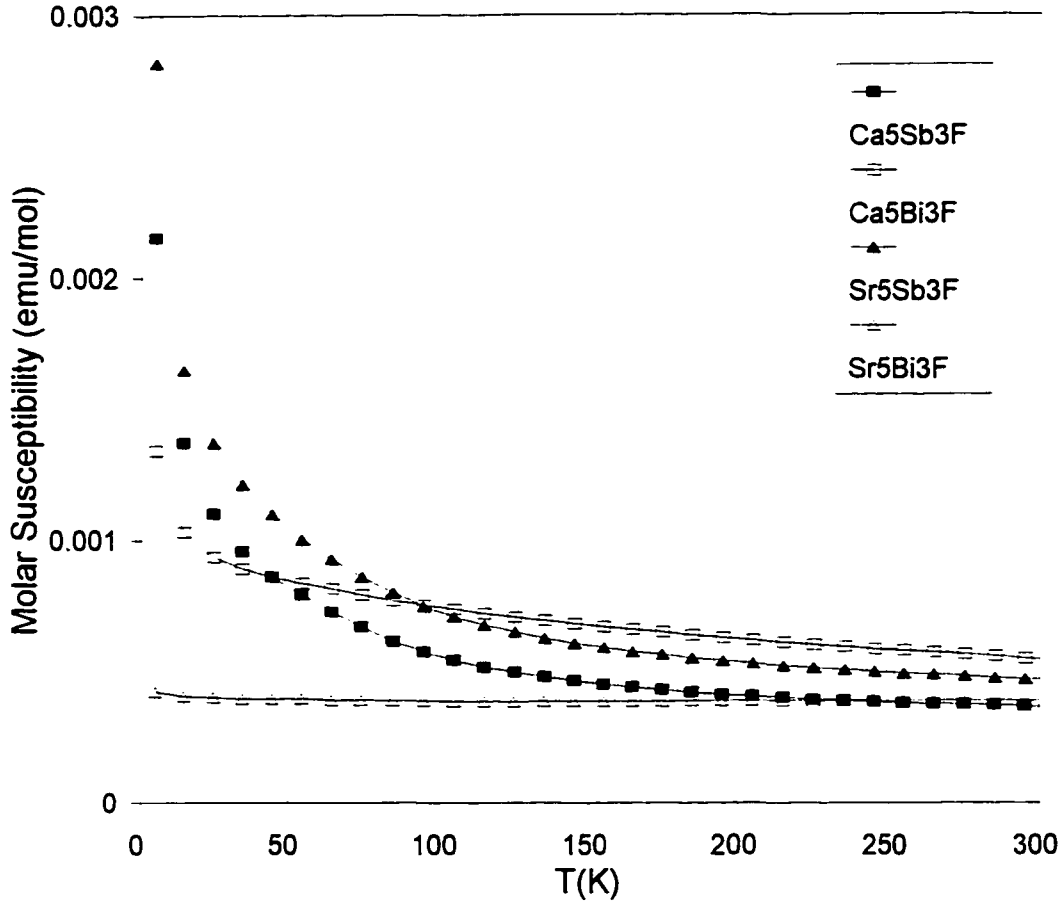

Figure III-23. Temperature dependence of the molar susceptibilities (χ) at 3 Tesla of ternary fluorides with the Y-type structure; $Ca_5Sb_3F_x$ (▪), $Ca_5Bi_3F_x$ (▫), $Sr_5Sb_3F_x$ (▲) and $Sr_5Bi_3F_x$ (△).

inferred from their smaller lattice parameters from those reported by Hurng for the equivalent phases, see data in Tables III-6 and III-13. Significantly, and in a gross comparison to our case, magnetic measurements have been used to monitor and quantify the effect oxygen defects in copper oxide superconductors.[103]

From the Y-Ae_5Pn_3F phases prepared in this work, Y-Sr_5Bi_3F (sample HF1) presented, as shown in Figure III-23, an unexpected temperature-independent paramagnetism, that is characteristic of metallic compounds. The electrical resistivity measurements on the sample, shown in Figure III-24 are supportive of the magnetic results. A positive temperature dependence of the electrical resistivity was observed for Y-Sr_5Bi_3F with a calculated the temperature coefficient and room temperature resistivity of a poor metal, 0.31(3)% K^{-1} and ~148 μΩ·cm, respectively. Therefore, we can reasonably assert that Y-Ca_5Sb_3F, Y-Sr_5Sb_3F and Y-Ca_5Bi_3F are Zintl phases, because their properties conform to anticipations based on the Zintl ideas, and in agreement with Wolfe's four-probe resistivity measurements on Y-$Ca_5Bi_3F_{1.0(1)}$, a semiconductive phase with gap energy of ~0.07 eV.[56] The phase Y-Sr_5Bi_3F, although structurally a Zintl phase, deviates from its expected properties. This is probably an indication that an incomplete electron transfer from the electropositive to the electronegative atoms may indeed occur.

Studies of M-$Ae_5Pn_3H_x$ compounds were limited to magnetic measurements and are given in Table III-26. Hence, shown in Figure III-25 are the temperature dependencies of the molar susceptibilities of M-Ca_5As_3 (sample AS3) and Ca_5As_5H (AS15). Conforming to anticipation, the former compound is Pauli paramagnetic and the latter is diamagnetic, or a Zintl phase. Presence of paramagnetic impurities in both compounds could be blamed for the tail below 50K.

The susceptibilities of compounds prepared under dv conditions M-$(Ca,Sr,Ba)_5Sb_3$ and M-$(Sr,Ba)_3Bi_5$, as pictured in Figure III-26, are paramagnetic and quite temperature-dependent. Such behaviors are comparable to the slight temperature-dependent Pauli spin paramagnetism observed in several metallic systems.[104] The room temperature molar susceptibilities of these phases are at least ten-fold of those reported by Collings[105] for the alkali metals Na, K and Rb, i.e., one-electron metals. Interestingly, there seem to be a trend in the magnetic behavior of these compounds, that is, their

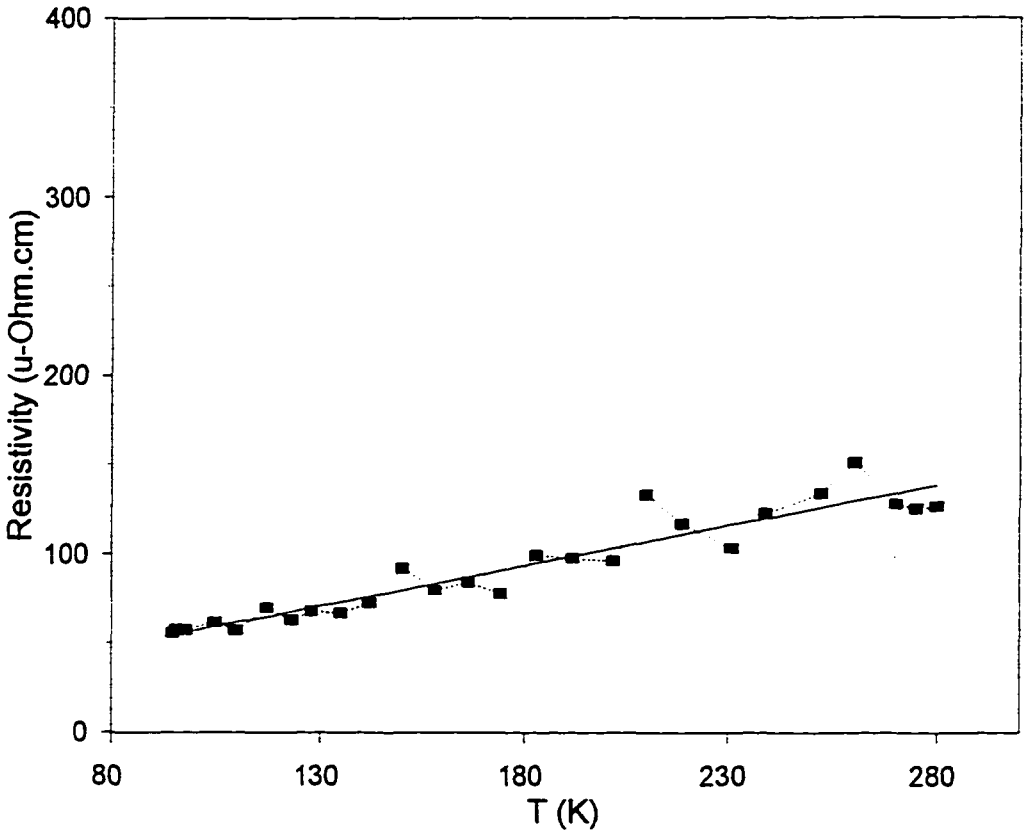

Figure III-24. Temperature dependence of the electrical resistivity (μΩ·cm) for sample HF1, Y-Sr_5Bi_3F measured by the Q method. The temperature coefficient calculated from the slope of the ρ versus T curve is 0.31(3)% K^{-1}.

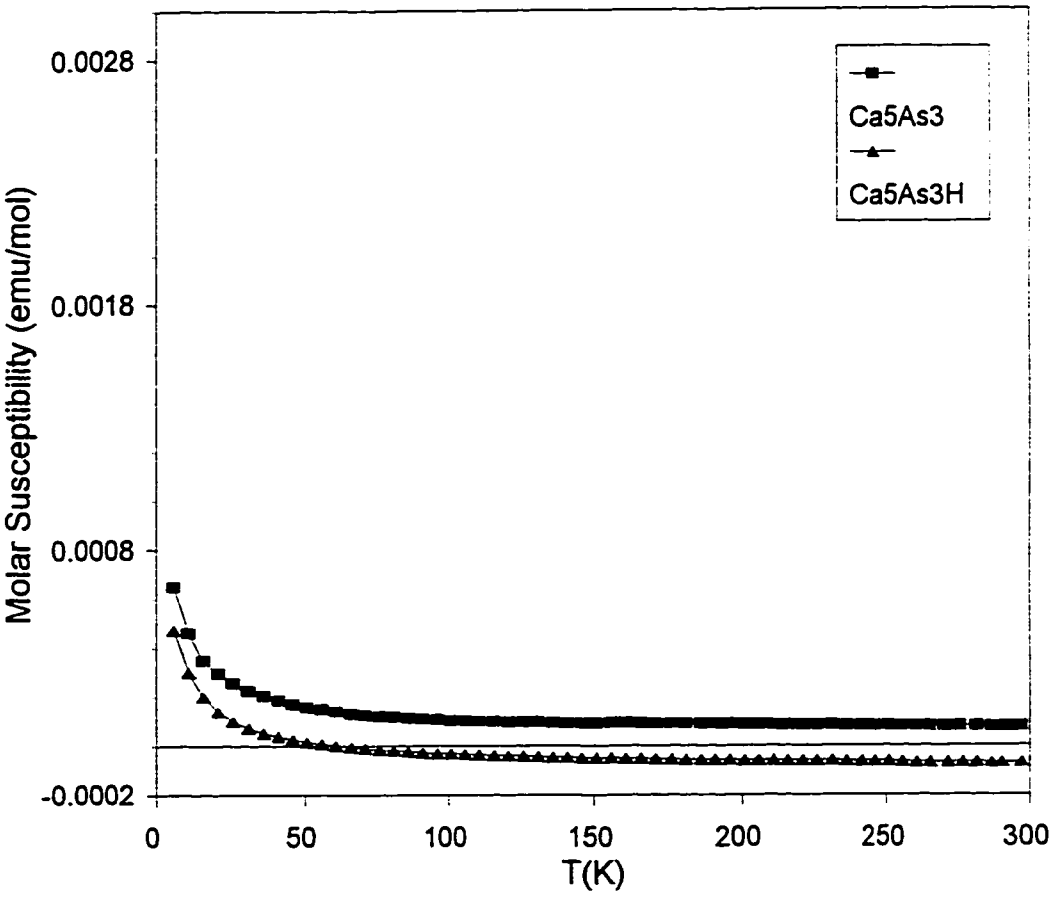

Figure III-25. Temperature dependence of the molar susceptibilities (χ) at 3 Tesla of samples AS1 (■) and AS14 (▲) with the M-type structure, loaded Ca_5As_3 and $Ca_5As_3H_{2.0}$, respectively.

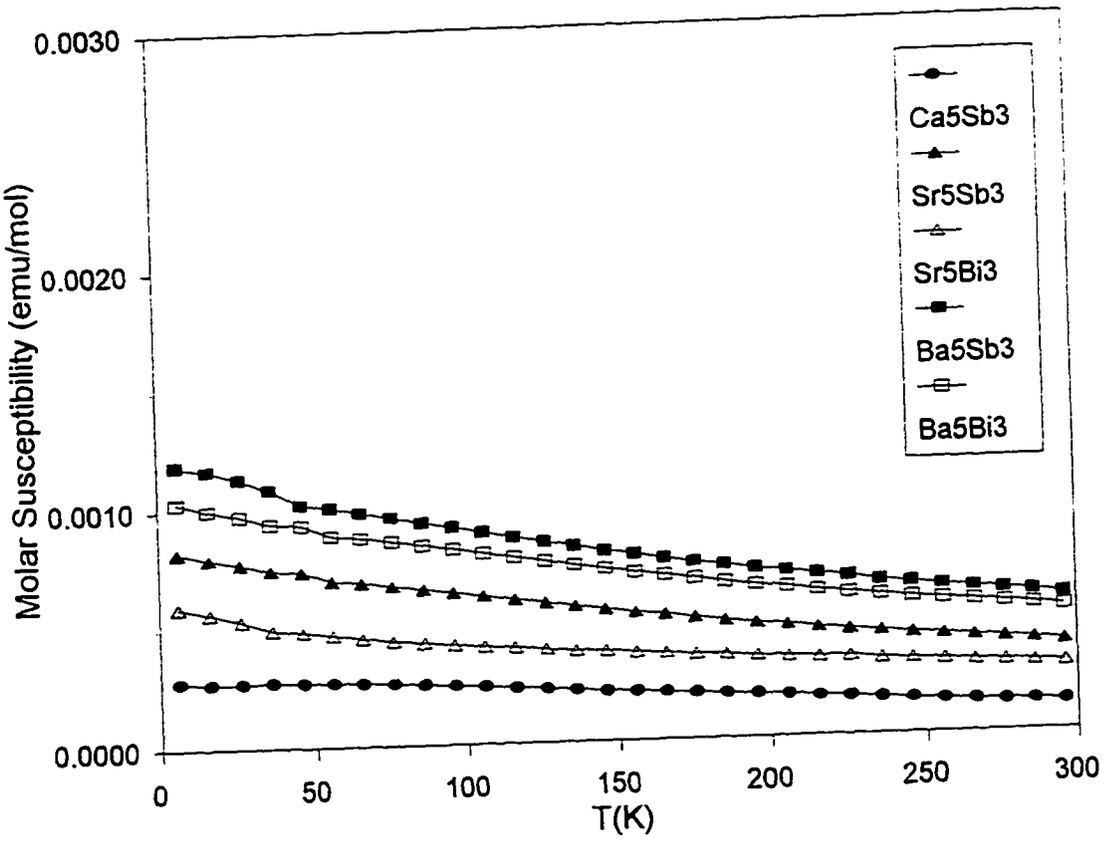

Figure III-26. Temperature dependence of the molar susceptibilities (χ) at 3 Tesla of several M-Ae_5Pn_3 samples prepared under dynamic vacuum conditions.

molar susceptibility becomes more temperature-dependent (or more Curie-Weiss) as the size of the alkaline-earth metal ion increases. Thus, compounds with large cations are more Curie-Weiss, M-Ba_5Sb_3 μ_{eff}= 1.59(1) BM, than for small cations, M-Ca_5Sb_3 μ_{eff}= 0.65(3) BM. Additionally, the moment of the antimonides is higher than that of the bismuthides, μ_{eff}= 1.53(2) BM for M-Ba_5Bi_3. It is also possible that particulars of the states near the Fermi level, as f(ΔDOS/ΔT), could be responsible for the observed paramagnetic Pauli temperature-dependencies.[104] The influence of paramagnetic impurities in these samples were disregarded because the field-dependent magnetization curves of M-Ba_5Sb_3 at 6 and 300K were linear and with an intercept at nearly zero.

The effects of hydrogen on the magnetic behavior of M-Ba_5Sb_3 phases can be appreciated in Figure III-27. Samples with high hydrogen content, A28 and A29 (loaded $Ba_5Sb_3H_{1.0}$ and $Ba_5Sb_3H_{2.0}$) are essentially Pauli or temperature-independent paramagnetic. Such a Pauli behavior is conceivable if the hydrogen content in these samples is near stoichiometric, $Ba_5Sb_3H_{<1}$, in concordance with the results of the already discussed Y-$(Ca,Sr)_5Sb_3H_{<1}$ compounds. Fully hydrogenated phases, in principle, would be semiconductive and diamagnetic in parallel to the ternary halide Ba_5Sb_3Cl that has a calculated energy gap of ~0.09 eV.[56] Importantly, elimination of the diamagnetic core correction (χ= -2.11 x 10^{-4} emu/mol) to the susceptibilities of samples A26, A27, A28 and A29, loaded $Ba_5Sb_3H_x$; x=0.0, 0.5, 1.0 and 2.0, respectively, results in diamagnetic behaviors for all, that are in support of Wolfe's calculated gap energy for M-$Ba_5Sb_3(H_{\sim 0.7})$, E_g = 0.03 eV.

Extended Hückel band calculations on M-$Ba_5Sb_3H_{1.0}$ confirm the expectations that these valence compounds should be semiconductors. Pictured on the left of Figure III-28 is the total DOS of Ba_5Sb_3H where the shaded area corresponds to the Sb total orbital projection (s and p states at ~ -19, -12 and the hydride band at -14 eV). The calculations indicate that most of the occupied states below the Fermi energy (ε_F) at -4.62 eV (for a $52e^-$ and 30 k-point calculation) belong to the more electronegative atoms. The gap energy for this hydride is overestimated. The center plot of Figure III-28 shows the total DOS for M-Ba_5Sb_3, where the shaded areas correspond to the orbital projection of Ba(2)

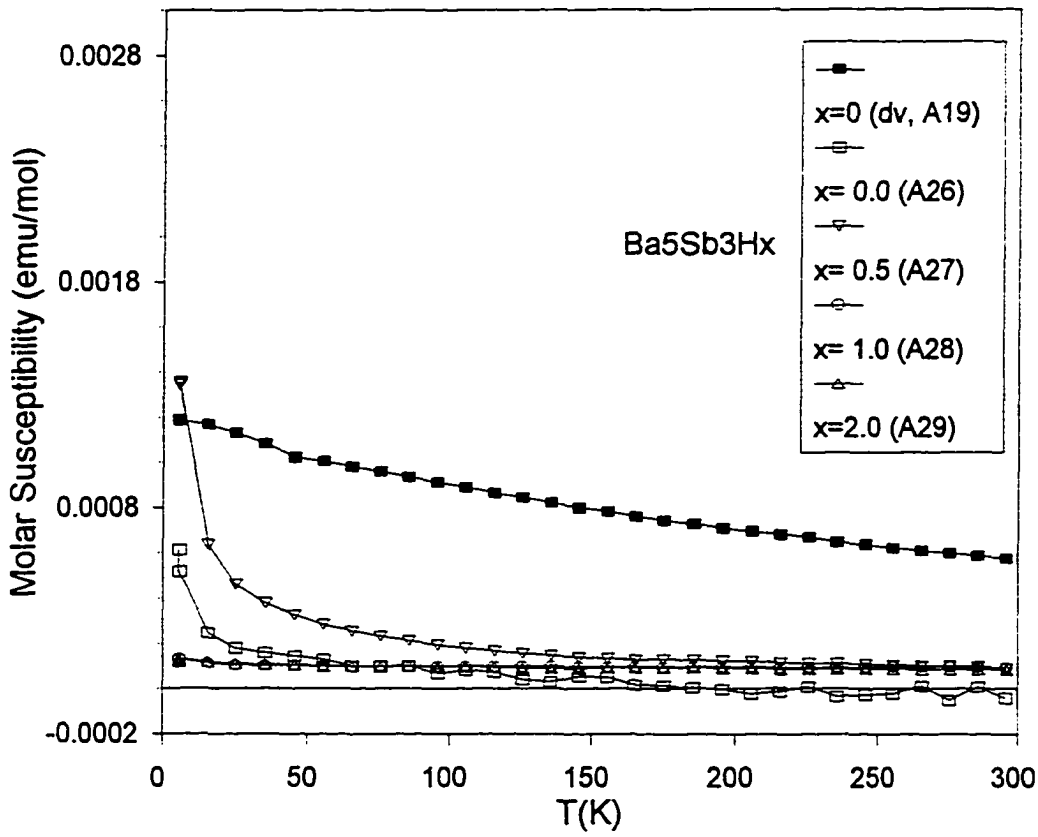

Figure III-27. Temperature dependence of the molar susceptibilities (χ) at 3 Tesla of M-$Ba_5Sb_3H_x$ prepared under dynamic vacuum, sample A19, and under sealed silica container conditions, samples A16, A27, A28 and A29 loaded for x=0.0, 0.5, 1.0 and 2.0 respectively.

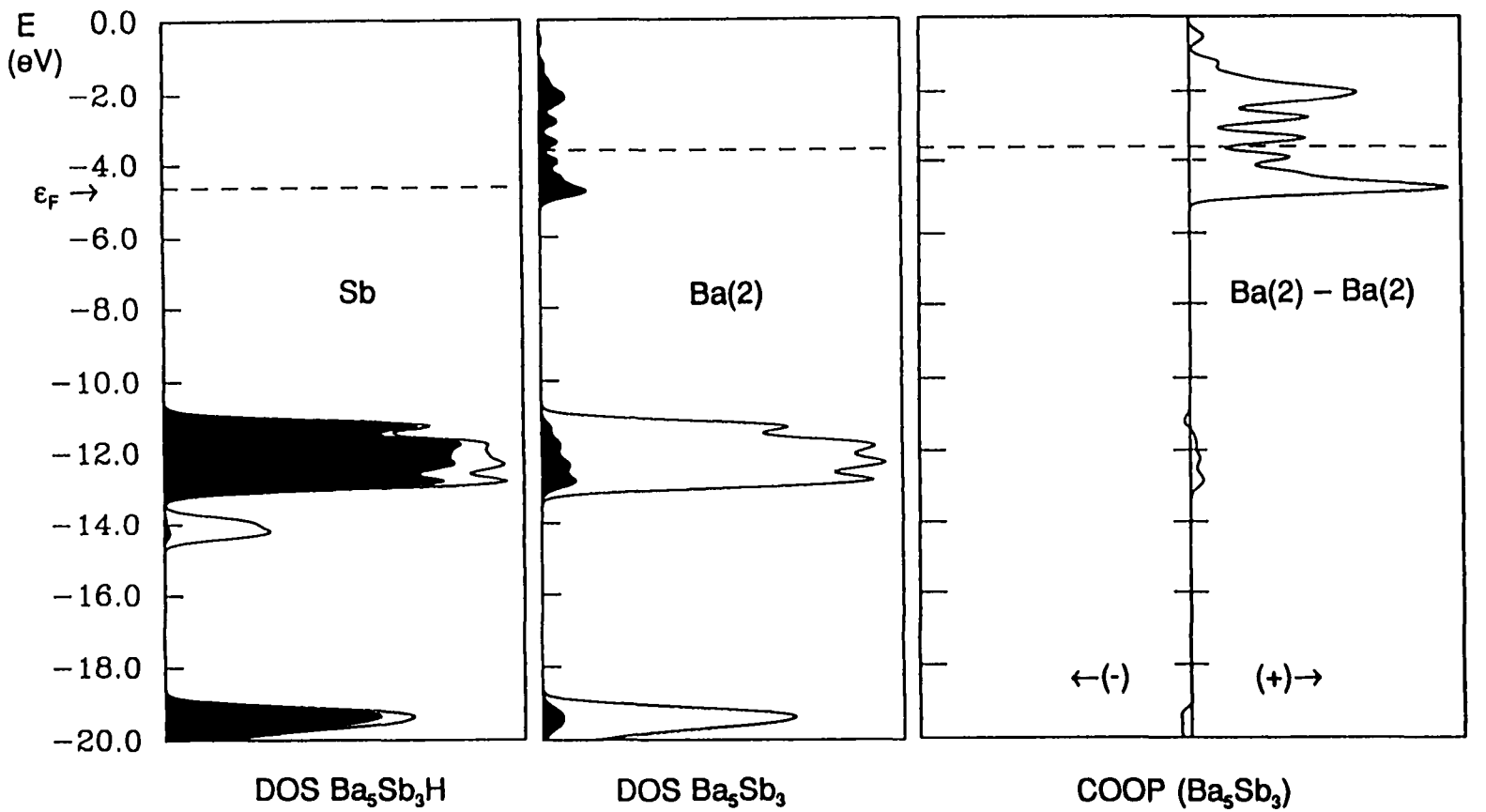

Figure III-28. Graphical results of the Extended Hückel-MO band calculations for Ba_5Sb_3H and Ba_5Sb_3 with the M-type structure.(I) Total DOS (Density of States) of Ba_5Sb_3H with the Sb atomic orbital projection shaded; (II) Total DOS of Ba_5Sb_3 with the Ba(2) orbital projection shaded, and (III) COOP (crystal orbital overlap population) for the Ba(2)–Ba(2) interaction in Ba_5Sb_3. Dashed lines signify the Fermi levels (ε_F).

in the infinite confacial antiprismatic arrangement. Results of the calculations on the binary M-Ba_5Sb_3 show a significant contribution of the p-states of Ba(2) atoms occur at the Fermi level (ε_F= -3.61 eV for 52e^- and 30-k point calculation), which according to the COOP curves, right of Figure III-28, are Ba(2)–Ba(2) bonding interactions near and below the Fermi level. The Ba(1) atoms contribution in M-Ba_5Sb_3, not shown in the plot, lies in the bands at -12 and -19 eV. Consequently, based on the results of these calculations, it is reasonable to suppose that the electrons could be partially localized on the states created by the Ba(2)–Ba(2) interactions. In other words, the empty interstitial cavities may act as electron traps. This is consistent with the changes in magnetic behavior for samples A26 to A29, where the Curie-Weiss behavior or temperature-dependence is more pronounced for samples with relatively large hydrogen deficiency, A26 and A27, than those that probably have reached saturation or the number of electron traps have decreased, A28 and A29. The electron trapping in other M-Ae_5Pn_3 compounds is probably diminished by a less effective bonding interaction between cations at the Fermi level. Moreover, a larger participation of the pnictide may also contribute to the less pronounced electron trapping in the bismuthides. Energy band calculations would probably illuminate better on these suppositions, although arguments of electron localization in orbital states conformed by cation–cation interactions are not new, Yee and Hughbanks[106] invoked pairing of electrons in valence band orbitals Gd–Gd bonding orbitals to explain the semiconducting properties of Gd_2Cl_3, an otherwise electron rich compound.

The Zintl concept, on its more basic form, relies on the idea that the electropositive element donates all its electrons to the anionic network. Indiscriminate use of such assumption would implicate that properties of isotypic and isoelectronic systems should be very similar. Hence, the properties of all M-Ae_5Pn_3H and Y-Ae_5Pn_3(F,H) compounds should be those of semiconductive materials. In actuality, and as inferred from our results, the electron transfer would vary depending upon the specific combination of metals. The electrical and magnetic properties of intermetallic phases that structurally qualify as Zintl compounds would be better predicted for combination of elements from the lighter part of the periodic table, e.g., M-Ca_5As_3H, than for heavier

elements, e.g., Y-Sr_5Bi_3F. Nonetheless, most of the compounds that achieve a valence composition can reasonably be called Zintl phases, i.e., Y-$Ca_5(Sb,Bi)_3(H,F)_{-1}$, Y-$Sr_5Sb_3F_{-1}$, M-$Ca_5As_3H_{-1}$, M-$Ba_5Sb_3H_{-1}$.

Trivalent rare-earth-metal pnictides

The results of our work on alkaline-earth, and certain rare-earth, metal pnictides and hydrogen unambiguously demonstrate that compounds with the actual ternary β-Yb_5Sb_3-type structure (Ca_5Sb_3F) are hydrogen stabilized. The results also strongly suggest that such a structure type is characteristic of divalent metal systems. However, in partial contradiction to our observations, Fornasini and Borzone[107] characterized the Er_5Sb_3 phase in the Y-type structure by single crystal diffraction; Er is a typical trivalent rare-earth metal. Their report was also conflicting with the knowledge that trivalent rare-earth metal antimonides and bismuthides, $RE_5(Sb,Bi)_3$ crystallize in either the M and or the Y_5Bi_3 (YB) structure types, where Gd_5Bi_3 and Tb_5Bi_3 have been found to be dimorphic, with the orthorhombic YB structure as high temperature phase.[108] Therefore, it seemed apparent that Fornasini's Y-Er_5Sb_3 should have formed in the YB-type structure instead.

Calvert and coworkers[109] determined the structure of Y_5Bi_3 (sp.gr. # 62, Pnma, Z=4) and noticed its remarkable resemblance with Steinfink's[54] β-Yb_5Sb_3 (Y). Such a resemblence can be appreciated in Figure III-29 where both structure types have been drawn in their equivalent [001] and [100] projections. Both Y and YB structures occur in the space group No. 62 but their a- and c-axis are interchanged. Thus, the YB structure can be described, similarly to the Y-type, with six-member hexagonal rings of edge-sharing BiY_6 or $SbYb_6$ trigonal prisms. The hexagonal channels are further filled by two Y(Yb) atoms near y=0,1/2 and two Bi(Sb) atoms (per cell) at y= 1/4,3/4. Notwithstanding, Calvert et al. noticed that the major difference between these two structures was on the planes at y= 0, 1/2. Subsequently, Garcia and Corbett[110] more clearly illustrated this difference by the way the atoms in these planes buckle. On the other hand, based on our present knowledge about the Y-type structure, we have identified that the difference in buckling is motivated by the interstitial atom in the Y structure. Figure III-30 depicts

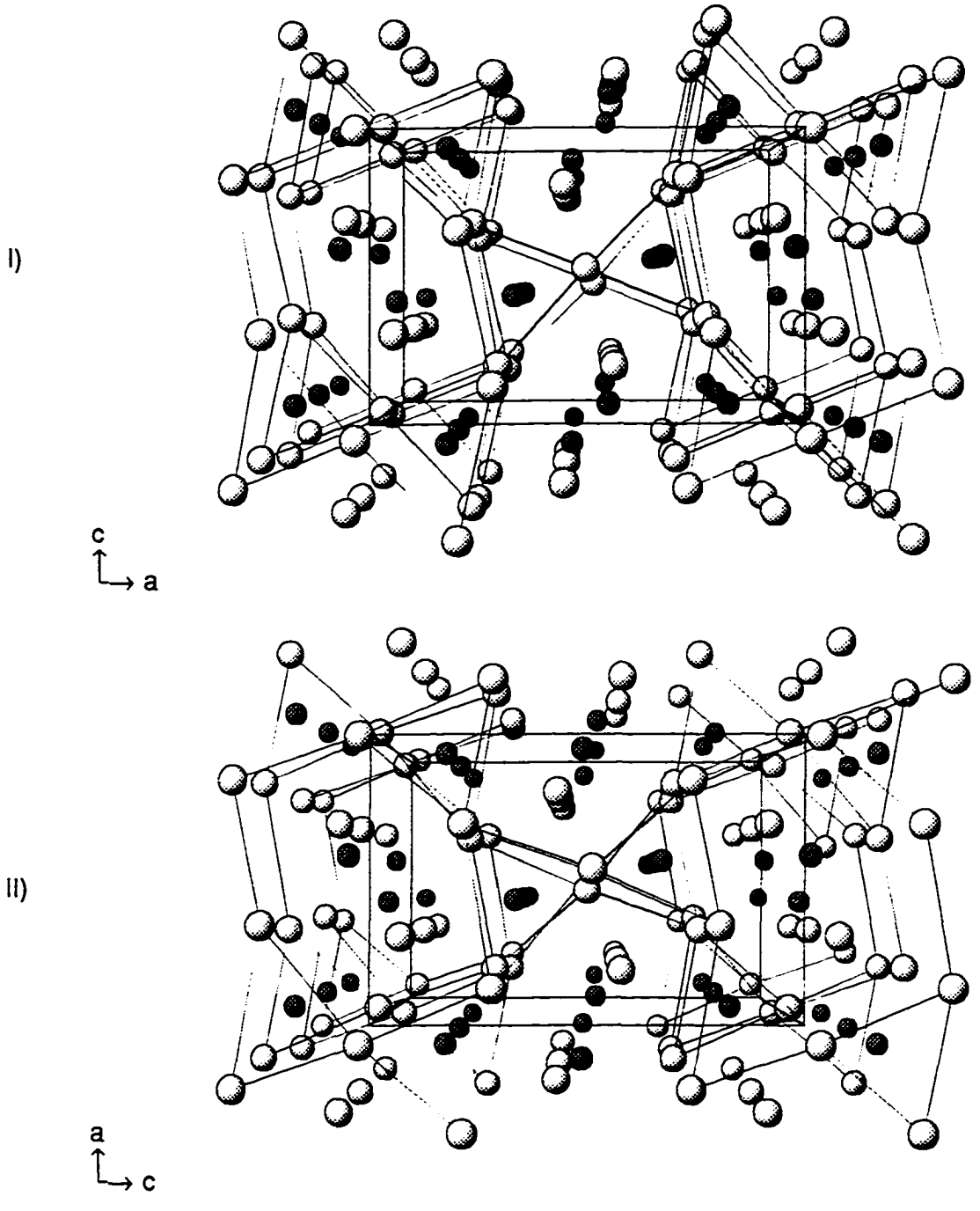

Figure III-29. The [010] perspective of the (I) Y_5Bi_3 and (II) β-Yb_5Sb_3 structure types. Large and small spheres represent cations (Y, Yb) and anions (Bi, Sb), respectively. Lines between atoms highlight the edge sharing trigonal prismatic arrangements that form the hexagonal channels of Y or Yb atoms.

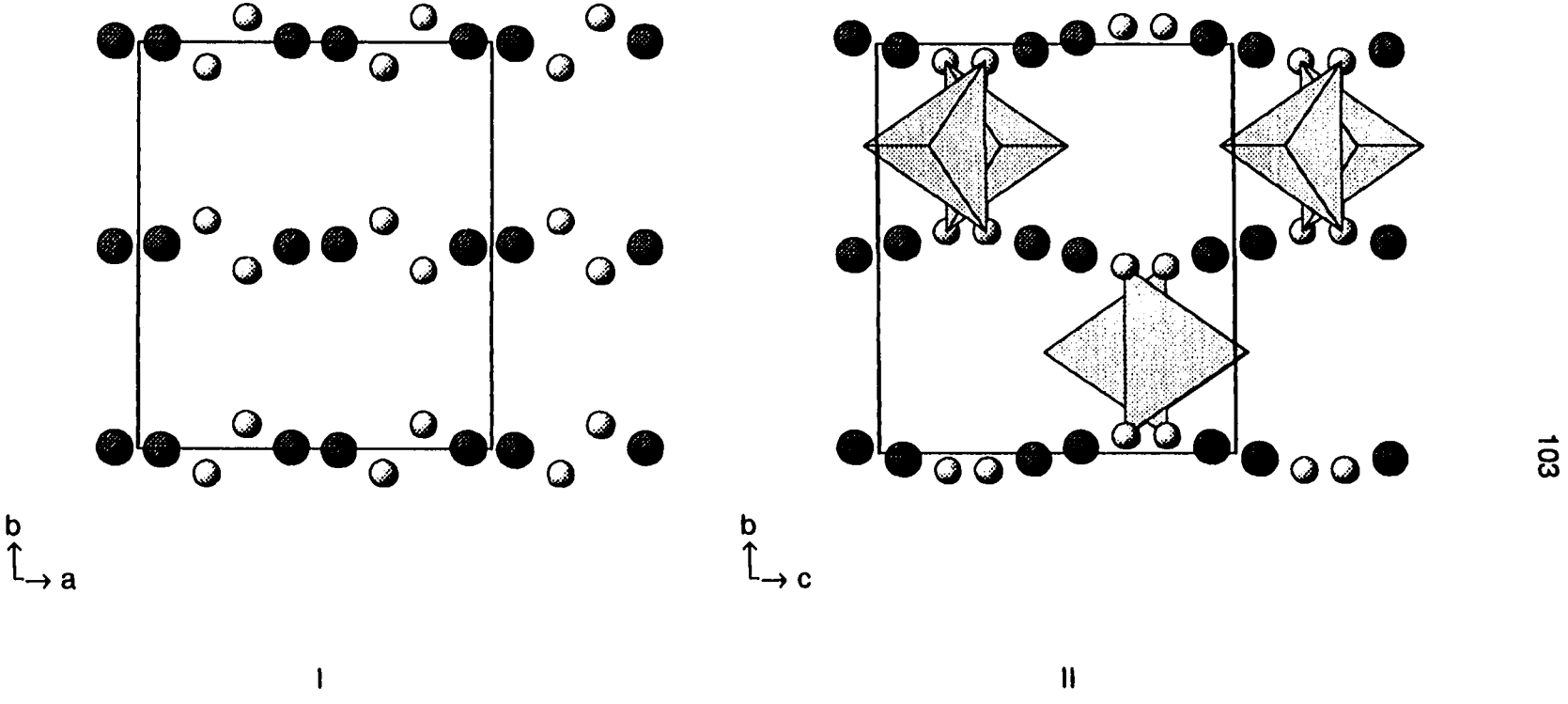

Figure III-30. Details of the (I) Y_5Bi_3 and (II) pseudo β-Yb_5Sb_3 (Ca_5Sb_3F) structure types on their (001) and (100) projections, respectively. The difference between these structure can be appreciated in the buckling of the layers at y= 0 and 1/2 caused by the interstitial atom in the latter structure type, H(F). Shaded tetrahedra highlight the position of the hydride interstices in the structure of the antimonide. Large spheres represent anions (Bi, Sb) and small ones cations (Y, Yb). For clarity other atoms at y= 1/4 and 3/4 are not included in the picture.

details of the [001] and [100] projections of the YB and Y structures, respectively, where it can be appreciated that the difference in buckling of the layers at $y \approx 0, 1/2$ is motivated by the interstitial atom in the Y structure, highlighted on the right of Figure III-30 as shaded tetrahedra. Because of these slight perturbations, one cannot easily discriminate between the two structure types by powder patterns, wherefore single crystal work is necessary to make reliable structural assignments. The large similarities between these structure motivated the editors of "Pearson's Handbook of Crystallographic Data"[24] to classify both structures under the earlier Y-type. They refer the YB structure as the Y-type in a nonstandard crystallographic setting ($\bar{c}ba$), which in fact is not accurate.

The discrepancy between Fornasini's report and our observations about the divalent metal systems, as well as the fact that compounds with the YB structure are only well documented for trivalent rare-earth and some transition metal pnictides, i.e. Y_5Bi_3,[109] $(Gd,Tb,Dy,Ho,Er,Tm)_5Bi_3$,[111] β-V_5As_3[112] and Zr_5Sb_3,[110] motivated us to revisit the crystallographic work on Er_5Sb_3. Therefore, several reactions between typical trivalent metals (Y, La, Gd, Tb, Dy, Ho, Er and Tm) and pnictogens (As, Sb and Bi) were performed. In an attempt to investigate whether hydrogen may be involved in the suspected transformation YB $\leftrightarrow$ M in Gd_5Bi_3 and Tb_5Bi_3, a few reactions in presence of hydrogen and fluorides were carried out on the former system. The reactions with fluorides were partially extended to Y and La systems. Because of the high melting points of some of these metals, the reactions were carried out in either an induction or a high temperature furnace. Both types of furnaces work under a high vacuum regime (see the experimental part for details).

Arsenides

Reactions between rare-earth metals and arsenic (loaded RE_5As_3, RE= Y, La, Gd, Tb, Dy, Ho, Er, Tm) gave, in concordance with their respective phase diagrams, products with the NaCl-type structure.[108] Results of these reactions are not included in tables or commented on further in this work.

Antimonides

The reaction between Sb and any of Gd, Tb, Dy or Ho metals, as indicated in Table III-27, gave products with the M-type structure. The Guinier lattice parameters of these phases did not differ significantly from previous reports, see Table III-28. However, most of the phases in the original reports were prepared by arc melting techniques, where the participation of hydrogen is reduced. The reactions to prepare Tm_5Sb_3 and Er_5Sb_3 gave products that after careful evaluation to their powder patterns were assigned to the YB-type structure. The hexagonal M form was not observed in these last reactions. To eliminate ambiguities about the assertion of the structural assignments on Tm_5Sb_3 and Er_5Sb_3, single crystal x-ray work was realized.

A crystal from reaction X19, loaded Er_5Sb_3, was mounted in the diffractometer RIGAKU AFC6R and data were collected on an orthorhombic cell setting based on 25 indexed refections found by the SEARCH subroutine. Systematic absences for h+k=2n+1 and l=2n+1 of the hk0 and h0l reflections sets, respectively, suggested the space groups $Pc2_1n$ (#33) and Pcmn (#62) as most probable solutions to the structure. The standard setting of the latter space group, Pnma, was selected to solve the structure. The atom position reported by Fomasini for Er_5Sb_3 with the Y-type structure, Pnma setting, were then used as initial model. Convergence on the atomic positions refined to residuals (R/R_w) of 46 and 51%, and 51 violations with $I > 4\sigma_I$ out of 752 observed reflections ($I > 3\sigma_I$) for the 0kl (k+l=2n) and hk0 (h=2n) conditions evidenced the incorrectness of the initial model; therefore it was abandoned. Refinement of the atomic positions based on the YB structure converged to residuals (R/R_w) of 11 and 13%, suggesting the better fit of the model. The final anisotropic refinement confirmed that Er_5Sb_3 is isotypic with Y_5Bi_3, final residuals R/R_w= 3.4/4.1%. Tables III-29 and III-30 comprise the crystallographic and refined data information of Er_5Sb_3. The RE–RE interatomic distances in this structure, listed in Table III-31, indicate that the Er ions are in a trivalent state. The short Er–Er contacts, below 3.5 Å, are shorter than the sum of metallic radii of the element (2x1.762= 3.524 Å).[61] The cell dimensions of YB-Er_5Sb_3 products, rxns X18 and X19, were consistently reproducible, supporting the refinement results for a composition $Er_{5.00(2)}Sb_{2.99(1)}$. The binary Tm_5Sb_3 crystallizes in the YB-type

Table III-27. Distribution of products for reactions RE_5Sb_3 involving trivalent RE metals.

Rxn. No.	Loaded Composition	Conditions[a]		Product Distribution[b]
XF5	Y_5Sb_3F	i	dv/HTF	Y ~65%, M ~30%, N ~5%, YF_3 ~5%
XF13	Y_5Sb_3F	ii	dv/HTF	M ~70%, N~20%, YF_3 ~10%
XF6	$Y_5Sb_3F_2$	i	dv/HTF	Y ~75%, M ~15%, N ~5%, YF_3 ~5%
XF14	La_5Sb_3F	ii	dv/HTF	ATP ~90%, LaF_3 ~10%
X15	Gd_5Sb_3	ii	dv/HTF	M >95%, UN
X5	$Gd_5Sb_3H_{4.5}$	iii	sc	ATP ~50%, N ~40%, UN
XF2	Gd_5Sb_3F	iii	dv	ATP ~70%, M ~20%, GdF_3 ~10%
RE2	Tb_5Sb_3	iii	dv	M ~20% + unreacted material
X17	Dy_5Sb_3	ii	dv/HTF	M ~100%
X22	Ho_5Sb_3	ii	dv/HTF	M ~50%, N ~50%
X18	Er_5Sb_3	iv	dv/HTF	YB ~95%
X19	Er_5Sb_3	ii	dv/HTF	YB >95%
X13	Tm_5Sb_3	i	dv/HTF	YB ~65%, N ~30%, UN
X20	Tm_5Sb_3	iv	dv/HTF	YB ~95%, N ~5%
X21	Tm_5Sb_3	ii	dv/HTF	YB ~85%, ATP ~15%
X12	Y_5Bi_3	v	dv/IF	YB >>95%
XF12	Y_5Bi_3F	ii	dv/HTF	YB ~80%, N ~15%, YF_3 ~5%
X1	La_5Bi_3	v	dv/IF	ATP ~95%, SS ~5%
XF15	La_5Bi_3F	ii	dv/HTF	ATP ~90%, LaF_3 ~10%
X2	Gd_5Bi_3	iii	dv	M ~90%, ATP ~10%
X4	Gd_5Bi_3	i	dv/IF	YB ~90%, ATP ~10%
X7	Gd_5Bi_3	v	dv/HTF	M ~95%, ATP ~5%
X16	Gd_5Bi_3	ii	dv/HTF	M ~95%, ATP ~5%
X6	$Gd_5Bi_3H_{4.5}$	iii	sc	YB ~40%, N ~40%, Gd-Metal
XF9	Gd_5Bi_3F	ii	dv/HTF	M ~95%, GdF_3 ~5%

Table III-27. Continued

Rxn. No.	Loaded Composition	Conditions[a]		Products Distribution[b]
X8	Tb_5Bi_3	v	dv/IF	YB ~100%
X9	Dy_5Bi_3	v	dv/IF	YB ~100%
X10	Ho_5Bi_3	v	dv/IF	YB ~90%, N ~10%
X11	Er_5Bi_3	v	dv/HTF	YB ~90%, N ~10%

[a] Conditions: i) Metals heated to 1400°C for 2h then 100°C/h to 1300°C, kept at that temperature for ~12h, followed by slow cooling to RT at ~18°C/h.
ii) Reaction 1400°C for 4h, then decreased to 650°C at 10°C/h after which the furnace was turned off.
iii) Reactions carried in a vacuum line at 1200°C for 6h then 10°C/h to 650°C and 50°C/h to RT.
iv) Reaction at 1300°C for 10h then 8°C/h to 600°C and 100°C/h to RT.
v) Reactions at 1500°C in the induction furnace for 1h, then 100°C/h to 900°C, subsequently the furnace power was turned off.
sc = Reaction in a sealed fused silica container.
dv = Reaction under dynamic vacuum.
HTF = High temperature furnace was used.
IF = Induction furnace was used

[b] Estimated from Guinier powder patterns. M= Mn_5Si_3-type, YB= Y_5Bi_3-type, N= NaCl-type, ATP= anti-Th_3P_4-type, SS= $SmSb_2$-type, UN= Unidentified lines.

structure as well. This new antimonide according to its structural refinement is a stoichiometric compound as well, $Tm_{5.00(1)}Sb_{2.988(6)}$, and judging from the RE–RE short contacts, < 3.5 Å, it involves trivalent Tm ions. Tables III-29, III-30 and III-31 summarize the crystallographic and structural information of this compound.

In an effort to eliminate doubts about the trivalent state of the Tm and Er compounds, the molar susceptibility of samples X18 and X20, Er_5Sb_3 and Tm_5Sb_3, respectively, were measured as function of the temperature. These antimonides are ferromagnetic and as depicted in Figure III-31 display a Curie-Weiss behavior above 50K. Néel and Weiss temperatures were calculated as (T_N ~) 26, 34 K and (θ ~) 0.3, 1.2 K for the Er and Tm compounds, respectively. Effective magnetic moments 22.28(1) and

Table III-28. Lattice dimensions of products of reactions $RE_5(Sb,Bi)_3(H,F)_x$.

Rxn No.	Loaded Composition	Str.Type/ Conds.[a]	a (Å)	b (Å)	c (Å)	Vol.(Å^3)	c/a	a/b	Ref.
	Y_5Sb_3	M/AM	8.9114(5)		6.2960(6)	433.00(7)	0.706		113
XF13	Y_5Sb_3F	M/HTF	8.9118(4)		6.2954(6)	433.00(6)	0.706		
XF5	Y_5Sb_3F	Y/HTF	11.869(1)	9.2317(8)	8.1034(7)	887.9(1)	0.683	0.878[b]	
XF6	$Y_5Sb_3F_{2.0}$	Y/HTF	11.8701(9)	9.2326(6)	8.1043(4)	888.2(1)	0.683	0.878[b]	
	Y_5Bi_3	YB/AM	8.1895(4)	9.4202(4)	11.9753(6)	923.85(9)	0.684[c]	0.869	109
X12	Y_5Bi_3	YB/IF	8.201(1)	9.4296(8)	11.983(1)	926.7(2)	0.684[c]	0.870	
XF12	Y_5Bi_3F	YB/HTF	8.1920(8)	9.4282(5)	11.9786(9)	925.2(1)	0.684[c]	0.869	
	La_5Sb_3	M/IF	9.428		6.618	509.4	0.702		114
	La_4Sb_3	ATP/IF	9.649(1)			898.4(4)	1.000	1.000	115
XF14	La_5Sb_3F	ATP/HTF	9.6495(2)			898.49(6)	1.000	1.000	
	La_4Bi_3	ATP/AM	9.790(2)			938.3(2)	1.000	1.000	116
	La_4Bi_3	ATP/sc	9.786(1)			937.1(1)	1.000	1.000	117
	La_5Bi_3	M/sc	9.6585(7)		6.6970(5)	541.0(8)	0.693		111
X1	La_5Bi_3	ATP/IF	9.7894(7)			938.1(2)	1.000	1.000	
XF15	La_5Bi_3F	ATP/HTF	9.7923(3)			938.97(8)	1.000	1.000	

Table III-28. Continued

Rxn No.	Loaded Composition	Str.Type/ Conds.[a]	a (Å)	b (Å)	c (Å)	Vol.(Å^3)	c/a	a/b	Ref.
	Gd_4Sb_3	ATP/AM	9.224(5)			784.8(4)	1.000	1.000	118
	Gd_5Sb_3	M/AM	8.975(4)		6.343(3)	442.5(2)	0.707		119
	Gd_5Sb_3	M/AM	8.970		6.366	441.5	0.706		120
X15	Gd_5Sb_3	M/HTF	9.0173(3)		6.3242(3)	445.33(4)	0.701		
XF2	Gd_5Sb_3F	M/HTF	9.0252(7)		6.3239(5)	446.10(8)	0.701		
X5	$Gd_5Sb_3H_{4.5}$	ATP/sc	9.234(1)			787.3(3)	1.000	1.000	
XF2	Gd_5Sb_3F	ATP/HTF	9.236(1)			787.8(4)	1.000		
	Gd_5Bi_3	M/AM	9.182(8)		6.426(7)	469.2(9)	0.700		117
	Gd_5Bi_3	M/sc	9.1580(9)		6.4186(6)	466.20(9)	0.701		118
	Gd_5Bi_3	YB/sc	8.2267(8)	9.531(1)	12.081(1)	947.3(3)	0.681[c]	0.863	118
X2	Gd_5Bi_3	M/dv	9.1781(5)		6.4042(7)	467.19(7)	0.698		
X7	Gd_5Bi_3	M/HTF	9.1807(9)		6.406(1)	467.6(1)	0.698		
X16	Gd_5Bi_3	M/HTF	9.1808(9)		6.4007(4)	466.99(4)	0.697		
XF9	Gd_5Bi_3F	M/HTF	9.1808(9)		6.4060(8)	467.6(1)	0.698		
X4	Gd_5Bi_3	YB/IF	8.269(2)	9.550(2)	12.095(2)	955.1(4)	0.684[c]	0.866	
X6	$Gd_5Bi_3H_{4.5}$	YB/sc	8.248(2)	9.583(2)	12.090(4)	955.7(4)	0.682[c]	0.861	
	Tb_5Sb_3	M/AM	8.920(3)		6.304(3)	434.3(3)	0.707		119

Table III-28. Continued

Rxn No.	Loaded Composition	Str.Type/ Conds.[a]	a (Å)	b (Å)	c (Å)	Vol.(Å^3)	c/a	a/b	Ref.
	Tb_5Bi_3	M/sc	9.101(2)		6.365(2)	456.6(2)	0.699		111
	Tb_5Bi_3	YB/sc	8.1993(8)	9.4759(9)	11.999(1)	932.3(1)	0.683[c]	0.865	111
X8	Tb_5Bi_3	YB/IF	8.1964(6)	9.4799(9)	11.9984(8)	932.3(1)	0.683[c]	0.865	
	Dy_5Sb_3	M/AM	8.868		6.263	426.5	0.706		121
	Dy_5Sb_3	M/AM	8.870(4)		6.266(3)	427.0(4)	0.706		119
X17	Dy_5Sb_3	M/HTF	8.9023(5)		6.2577(5)	429.49(6)	0.703		
	Dy_5Bi_3	YB/sc	8.1603(4)	9.4214(4)	11.9341(6)	917.5(1)	0.684[c]	0.866	111
X9	Dy_5Bi_3	YB/IF	8.1615(9)	9.4327(7)	11.9294(7)	918.4(1)	0.684[c]	0.865	
	Ho_5Sb_3	M/AM	8.851(2)		6.234(2)	422.9(2)	0.704		119
X22	Ho_5Sb_3	M/HTF	8.8573(3)		6.2277(4)	423.11(4)	0.703		
	Ho_5Bi_3	YB/sc	8.1328(5)	9.3820(6)	11.8744(7)	906.0(1)	0.685[c]	0.867	111
X10	Ho_5Bi_3	YB/IF	8.130(1)	9.3812(9)	11.873(1)	905.5(2)	0.685[c]	0.867	
	Er_5Sb_3	Y/IF	11.662(1)	9.136(1)	8.007(1)	853.4(2)	0.687	0.876[b]	107
X18	Er_5Sb_3	YB/HTF	7.966(1)	9.177(2)	11.661(1)	852.4(2)	0.683[c]	0.868	
X19	Er_5Sb_3	YB/HTF	7.9646(9)	9.176(1)	11.662(1)	852.2(2)	0.683[c]	0.868	

Table III-28. Continued

Rxn No.	Loaded Composition	Str.Type/ Conds.[a]	a (Å)	b (Å)	c (Å)	Vol.(Å^3)	c/a	a/b	Ref.
	Er_5Bi_3	YB/sc	8.0930(4)	9.3402(5)	11.8134(6)	892.98(9)	0.685[c]	0.866	111
X11	Er_5Bi_3	YB/IF	8.103(1)	9.3481(8)	11.810(1)	894.6(2)	0.686[c]	0.867	
X13	Tm_5Sb_3	YB/dv	7.9260(8)	9.136(2)	11.609(1)	840.6(2)	0.683[c]	0.867	
X20	Tm_5Sb_3	YB/HTF	7.9262(5)	9.1375(8)	11.6013(7)	840.2(1)	0.683[c]	0.867	
X21	Tm_5Sb_3	YB/HTF	7.9289(5)	9.1382(7)	11.6026(6)	840.68(9)	0.683[c]	0.868	
	Tm_5Bi_3	YB/sc	8.0645(7)	9.3055(8)	11.758(1)	882.4(2)	0.686[c]	0.867	111

[a] Powder patterns indexed for M= Mn_5Si_3-type, YB= Y_5Bi_3-type, Y= β-Yb_5Sb_3-type, ATP= a-Th_3P_4-type.
Conditions: AM= Sample arc melted.
IF= Induction furnace.
HTF= High temperature furnace.
dv= dynamic vacuum.
sc= sealed container.

[b] Denotes $(a/b)^{-1}$.

[c] Denotes $(c/a)^{-1}$.

Table III-29. Crystallographic Data of $(Er,Tm)_5Sb_3$.

	Er_5Sb_3	Tm_5Sb_3
Crystal from rxn.	X19	X20
Space Group	Pnma(#62)	Pnma
Lattice parameters[a]		
a (Å)	7.9646(9)	7.9262(5)
b (Å)	9.176(1)	9.1375(6)
c (Å)	11.662(1)	11.6013(7)
Volume ($Å^3$)	852.2(2)	840.2(1)
Z	4	4
Density calc. (g/cm^3)	9.363	9.564
Diffractometer	Rigaku AFC6R	Rigaku AFC6R
Collected octants	h,k,±l	h,k,±l
Scan type	ω-2θ	ω-2θ
Transmission range	0.563–1.128	0.713–1.203
Absorption coefficient (cm^{-1})	586.7	622.6
Number of reflections		
Measured	2082	2060
Independent (observed[b])	1115(752)	1105(774)
R_{ave} (%)	5.15	3.77
No. of refined variables	44	44
R/R_w (%)	3.4/4.1[c]	2.3/3.0[c]
Goodness of fit	1.488	1.187
Secondary ext. coeff. (x 10^{-7})	6.7(2)	3.9(1)
Max./min. peak in ΔF map ($e^- Å^{-3}$)	2.51/-4.27	1.81/-2.29
Refined Formula	$Er_{5.00(2)}Sb_{2.99(1)}$	$Tm_{5.00(1)}Sb_{2.988(6)}$

[a] Lattice parameters calculated from Guinier powder patterns.
[b] Observed reflections; $I \geq 3\sigma_I$.
[c] Take-off angle for refinement θ= 4°.

Table III-30. Refined positional and thermal parameters of $(Er,Tm)_5Sb_3$ phases in the Y_5Bi_3-type structure.

Atom	x	y	z	$B_{eq}(Å^2)$	U_{11}	U_{22}	U_{33}	U_{12}	U_{13}	U_{23}
Er_5Sb_3 (X19)										
Er(1)	0.4709(1)	1/4	0.49047(9)	0.48(4)	0.0044(5)	0.0066(5)	0.0073(5)	0	0.0005(4)	0
Er(2)	0.3146(1)	1/4	0.22051(8)	0.55(4)	0.0047(5)	0.0091(6)	0.0070(5)	0	-0.0009(4)	0
Er(3)	0.1457(1)	1/4	0.71314(8)	0.64(4)	0.0084(5)	0.0099(6)	0.0060(5)	0	-0.0002(4)	0
Er(4)	0.19490(9)	0.55879(8)	0.43952(6)	0.54(3)	0.0046(4)	0.0066(4)	0.0093(3)	-0.0003(3)	0.0007(3)	-0.0002(3)
Sb(1)	0.0862(2)	1/4	0.4593(1)	0.53(6)	0.0056(7)	0.0065(7)	0.0079(7)	0	-0.0003(6)	0
Sb(2)	0.0661(1)	0.9968(1)	0.17329(9)	0.53(4)	0.0062(5)	0.0057(6)	0.0084(5)	-0.0001(4)	-0.0011(4)	-0.0006(4)
Tm_5Sb_3 (X20)										
Tm(1)	0.4714(1)	1/4	0.49068(7)	0.24(3)	0.0021(4)	0.0036(4)	0.0032(4)	0	0.0005(3)	0
Tm(2)	0.3140(1)	1/4	0.22017(7)	0.35(3)	0.0040(4)	0.0064(4)	0.0028(4)	0	-0.0000(3)	0
Tm(3)	0.1456(1)	1/4	0.71361(7)	0.42(3)	0.0062(4)	0.0073(4)	0.0026(4)	0	-0.0003(3)	0
Tm(4)	0.19483(7)	0.55981(6)	0.43938(5)	0.30(2)	0.0032(3)	0.0025(3)	0.0056(3)	-0.0006(2)	0.0010(2)	0.0002(2)
Sb(1)	0.0871(2)	1/4	0.4591(1)	0.25(4)	0.0027(6)	0.0032(6)	0.0034(5)	0	-0.0012(5)	0
Sb(2)	0.0660(1)	0.9971(1)	0.17354(7)	0.32(3)	0.0047(4)	0.0030(4)	0.0045(4)	-0.0005(3)	-0.0012(3)	0.0006(3)

Table III-31. Interatomic distances in the $(Er,Tm)_5Sb_3$ compounds with the Y_5Bi_3 structure type, (Å).

Atom(1) – Atom(2)	Er_5Sb_3	Tm_5Sb_3	Atom(1) – Atom(2)	Er_5Sb_3	Tm_5Sb_3
Sb(1) – Sb(2) (2x)	4.067(2)	4.043(1)	Sb(2) – A(4) (1x)	3.310(1)	3.290(1)
Sb(2) – Sb(2) (2x)	4.363(2)	4.341(1)	Sb(2) – A(4) (1x)	3.373(1)	3.362(1)
Sb(2) – Sb(2) (1x)	4.177(2)	4.161(2)	A(1) – A(2) (1x)	3.386(1)	3.377(1)
Sb(2) – Sb(2) (2x)	4.3658(9)	4.3421(7)	A(1) – A(2) (1x)	3.681(2)	3.655(1)
Sb(1) – A(1) (1x)	3.086(2)	3.067(2)	A(1) – A(3) (1x)	3.668(2)	3.654(1)
Sb(1) – A(2) (1x)	3.012(2)	3.002(1)	A(1) – A(3) (1x)	3.726(2)	3.698(1)
Sb(1) – A(2) (1x)	3.326(2)	3.304(1)	A(1) – A(4) (2x)	3.291(1)	3.2679(9)
Sb(1) – A(3) (1x)	2.999(2)	2.989(1)	A(1) – A(4) (2x)	3.635(1)	3.6294(8)
Sb(1) – A(4) (1x)	2.9717(9)	2.9656(7)	A(2) – A(2) (2x)	4.0413(6)	4.0231(4)
Sb(1) – A(4) (1x)	3.080(2)	3.066(1)	A(2) – A(4) (2x)	3.718(1)	3.6928(8)
Sb(2) – A(1) (2x)	3.101(1)	3.088(1)	A(2) – A(4) (2x)	3.932(1)	3.9209(8)
Sb(2) – A(1) (2x)	3.125(1)	3.112(1)	A(3) – A(3) (2x)	4.0741(6)	4.0521(4)
Sb(2) – A(2) (2x)	3.102(1)	3.082(1)	A(3) – A(4) (2x)	3.415(1)	3.3882(9)
Sb(2) – A(2) (2x)	3.308(1)	3.294(1)	A(3) – A(4) (2x)	3.689(1)	3.668(1)
Sb(2) – A(3) (2x)	3.119(1)	3.103(1)	A(3) – A(4) (2x)	4.285(1)	4.2764(8)
Sb(2) – A(3) (2x)	3.258(1)	3.246(1)	A(4) – A(4) (1x)	3.509(2)	3.476(1)
Sb(2) – A(4) (1x)	3.276(1)	3.262(1)	A(4) – A(4) (1x)	3.577(1)	3.565(1)

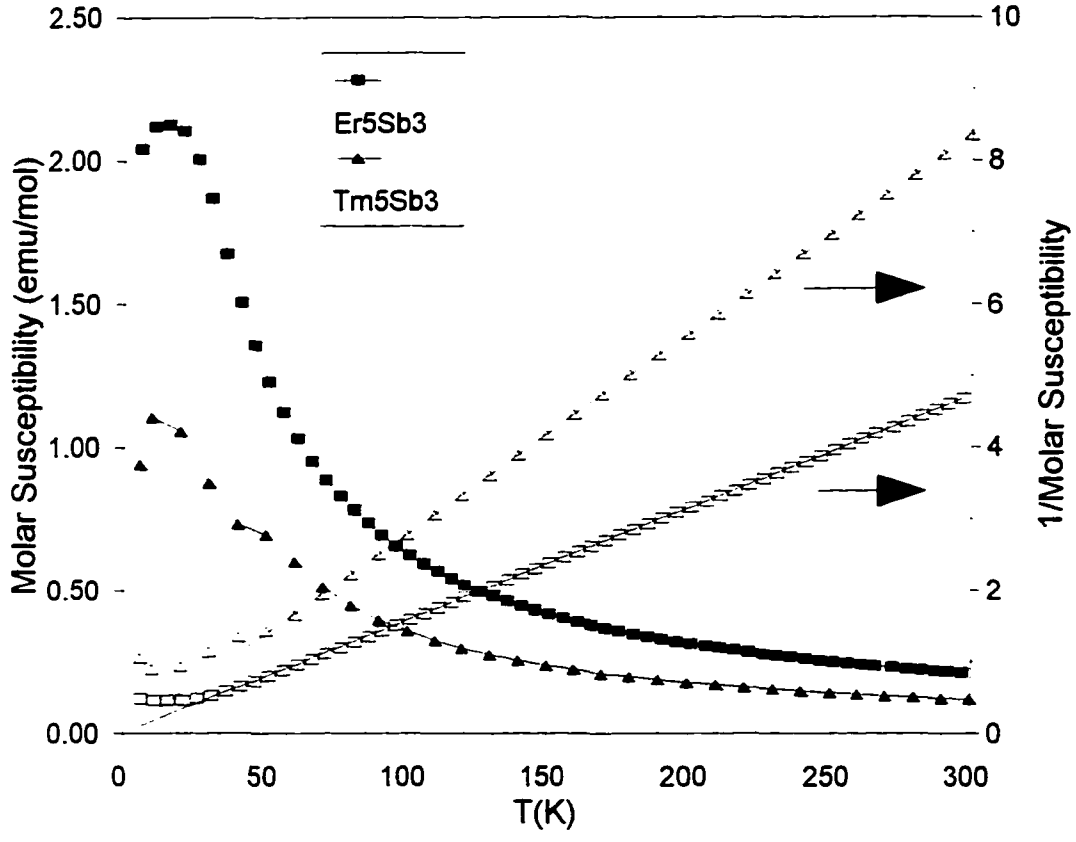

Figure III-31. Temperature dependence of the molar susceptibilities (χ) at 3 Tesla of YB-Er_5Sb_3 (■) and YB-Tm_5Sb_3 (▲). Solid symbols correspond to χ vs. T plots and empty symbols, to $1/\chi$ vs. T; linear fit for T > 50K.

16.90(2) BM corresponded to saturation moments of 9.96 and 7.56 BM per atom for Er_5Sb_3 and Tm_5Sb_3, respectively. These saturation moments are close to the reported values for Er^{3+} (9.58 BM) and Tm^{3+} (7.56 BM) free ions.[72] Yakinthos and Semitelou[98] reported saturation effective moments of 7.2 and 7.6 BM for what they claimed to be M-type Er and Tm antimonides. They did not provide synthetic or structural information in the original report.

Reactions in presence of hydrogen were limited to the Gd_5Sb_3 system, rxn X5 in Table III-27. The major product of this reaction had the cubic ATP-type structure. Such a structure type was identified in reactions with GdF_3 added instead, rxn XF2. Invariability in the cell dimensions of these cubic phases indicated that no substitution of either hydrogen or fluoride resulted. Restrictions in the availability of the rare-earth metal, because of the non-reactivity of GdF_3, led to formation of the neighboring Gd-deficient phase, Gd_4Sb_3. On the other hand, the product with the hexagonal cell (rxns XF2 and X15) show some difference from the dimensions in Parthé's report;[119] ~0.81% cell volume decrement is calculated. This variation is suggestive of hydrogen involvement because he prepared the M-Gd_5Sb_3 sample by arc-melting the elements, controlling the stoichiometry by weight loss monitoring, followed by annealing in closed silica containers. The restricted number of reactions performed in this work prevent us from claiming that hydrogen is uniquely responsible for the observed variation in cell dimensions. Other factors like pnictogen self-substitution in the interstitial sites may occur as well, i.e., stuffed Mn_5Si_3Z structure. In resemblence to the Gd_5Sb_3F system, the reaction to prepare La_5Sb_3F, rxn XF14, gave products with the ATP-type structure.

Unanticipatedly, the reaction between Y metal and Sb in presence of fluorides, when briefly annealed at 1300°C, gave products that were identified as the orthorhombic Y-type structure (rxns XF5 and XF6, loaded Y_5Sb_3F and $Y_5Sb_3F_2$, respectively). Differentiation between the Y and YB structures by powder patterns is quite feasible if knowledge of the patterns features from both structures are available. The significant differences between the patterns will be on the planes that involve a large contribution from the h and l indexes. Invariance in the lattice parameters of products from reactions loaded for different fluoride content, rxns XF5 and XF6, suggest that the ternary halide

forms for a given composition, probably ~Y_5Sb_3F. The results of these reactions suggest that the Y-type structure may not be distinctive of ternary divalent metal systems as initially thought. Nevertheless, unsuccessful attempts to grow single crystals of the target phase prevented us from obtaining conclusive arguments about its structure. Interestingly, when the reactions were carried out at higher temperatures (~1400°C), rxn XF13, the YB-type phase was not observed among the products, instead the M-type was observed. The cell dimensions of this hexagonal phase were the same to those reported by Schmidt and McMasters[113] for the binary M-Y_5Sb_3.

The limited number of experiments performed with the antimonides content us with demonstrating that Fornasini's report about Y-Er_5Sb_3 appears incorrect. Nonetheless, they show that Er_5Sb_3 and Tm_5Sb_3 form in the YB-type structure and that trivalent metal antimonides may form in the Y-type structure when stabilized by fluoride, at least for Y_5Sb_3F. Ternary hydrides with this last structure type may exist, $Er_5Sb_3H_x$. However, Fornasini's Y-Er_5Sb_3 was prepared in hydrogen free conditions, since the reaction was carried out in an induction furnace.

Bismuthides

In agreement with reports by Calvert and Wang[109] the reaction between rare-earth metals and Bi at ~1500°C, RE_5Bi_3 (RE= Y, Tb, Dy, Ho and Er), gave products with the YB-type structure. The phases Gd_5Bi_3 and Er_5Bi_3 showed increments and Y_5Bi_3, a decrement, in their cell volume of about 0.82, 0.18 and -0.31%, respectively, with respect to previous reports, see Table III-28. Because of the limited number of experiments performed, arguments about presence of hydrogen in these phases cannot be made. However, the reaction between Y metal and Bi in presence of YF_3 (rxn XF12) gave products with the YB phase as major product and with negligible variations in its lattice parameters from those of the binary reaction, Y_5Bi_3 (X12). Calvert has suggested based on some experiments with variable loaded compositions that the YB structure may be bismuth-deficient.[111] The reaction for La_5Bi_3 (rxn X1) as well as La_5Bi_3F (XF15) gave products with the ATP-type structure, even though the M-La_5Bi_3 is reported to form.[111] Lattice parameters for these cubic phases did not differ from previous

reports.[116,117]

Some controversy exists about the possible phase transformation YB ↔ M for Gd_5Bi_3.[117,118] It has been reported that Gd-deficient reactions favor the M form and that the YB is generally observed for stoichiometric reaction compositions. Our results indicated that the YB phase was formed when the reactions were carried at high temperatures, ~1500°C (rxn X4). For reactions at lower temperatures, < 1400°C, and in presence or absence of fluoride, rxns X2, X7, X16 and XF9, the major product had the M-type structure with reproducibility of the lattice dimensions. Mixtures of both structure types were never observed under the experimental conditions followed. Unexpectedly, the reaction X6 ($Gd_5Bi_3H_{4.5}$) gave the YB phase among the products. However, because of the experimental set up, i.e., sc conditions, the reaction could not be heated above 1200°C and it did not go to completion. Thus, formation of the orthorhombic YB phase may have been caused by the greater surface contact between Gd formed in the decomposition of powder GdH_3, and Bi. Moreover, the cell volume of products X4 and X6 are equivalent with some variations in their axial lengths. Single crystal work and additional experiments are necessary to extend these observations. Thus, the results from the work on antimonides, and partially the bismuthides, support the assumption that the YB-type structure is not a ternary hydride.

Interpretation of results

While we have not been totally able to prove that the structural report of Y-Er_5Sb_3 is inaccurate, we have been able to establish that the Y_5Bi_3-type structure, as initially suspected, is particular to trivalent metal pnictides. Consequently, we can claim that such a structure type is characteristic of electron-rich binary phases ($5RE^{3+}$, $3Pn^{3-}$) and conceivably should be found in systems that involve tetravalent metals. This claim was already evidenced as authentic by Garcia and Corbett[109] in their work with the Zr_5Sb_3 system. They found that the compound with the YB structure forms stoichiometrically, $Zr_{4.99(1)}Sb_{3.02(3)}$ and that small excess of Sb in the reactions leads to formation of M-type products with partial substitution of Sb atoms in the interstitial sites (stuffed Mn_5Si_3Z-type structure), $Zr_5Sb_3Sb_x$; $0 \le x \le 0.4$, in concordance with an early study by Brauer[122] on

M-$Ti_5P_3P_{0.15}$.

Although the conditions used in several preceding experimental efforts and the current one minimize the participation of hydrogen in the reactions, i.e., through arc melting reactions and dv conditions, the possibility that some ternary trivalent metal pnictides may form in the Y-type structure is still latent, because the results of reactions between Y, Sb and YF_3 are suggestive of this. Therefore, additional experimental work is required to illuminate on this problem.

The phases Er_5Sb_3 and Tm_5Sb_3 are the first examples of trivalent rare-earth metal antimonides that crystallize in the YB-type structure. Size effects seem to play a very important role on the formation of these phases as inferred from the structural map represented in Figure III-32. Such a map was constructed from the ratio of ionic radii of the rare-earth metal ions and pnictides, r^+/r^- (CN=6)[71] placed on the abscissas and the Pauling's electronegativity[61] difference of the elements ($\Delta E = E_{anion} - E_{cation}$ =) on the ordinates. This map can apparently be divided into three regions; (I) the lanthanum compounds in the ATP-type structure; (II) the phases found in the hexagonal M-structure type, where the Gd–Bi combination was used as a point to separate regions II and III, and; (III) the rare-earth-metal pnictides that crystallize in the YB-type structure. The combinations Er–Sb and Tm–Sb are included within region III, which seems to group combinations of small cations and large anions. This map suggest that combinations Ho–Sb and Tb–Bi may form both in the M and YB structures types. Such dimorphism has already been reported for the latter combination.[108] Experiments to test the dimorphism of Ho_5Sb_3 were not performed.

The possibility that electron rich systems may favor the YB-type structure instigates one to doubt about the reliability of assigning Sc_5As_3,[123] Sc_5Sb_3,[124] α-Ti_5P_3,[125,126] Ti_5As_3,[124] Ti_5Sb_3,[124,127] V_5As_3[128] and Cr_5As_3[112,128] to the Y-type structure, because these were primarily done with powder pattern information.

Conclusions About the $A_5Pn_3(H,F)_x$ Systems

We have, through careful and well planned work, been able to demonstrate that hydrogen impurities play a very important role in the chemistry of alkaline-earth-metal

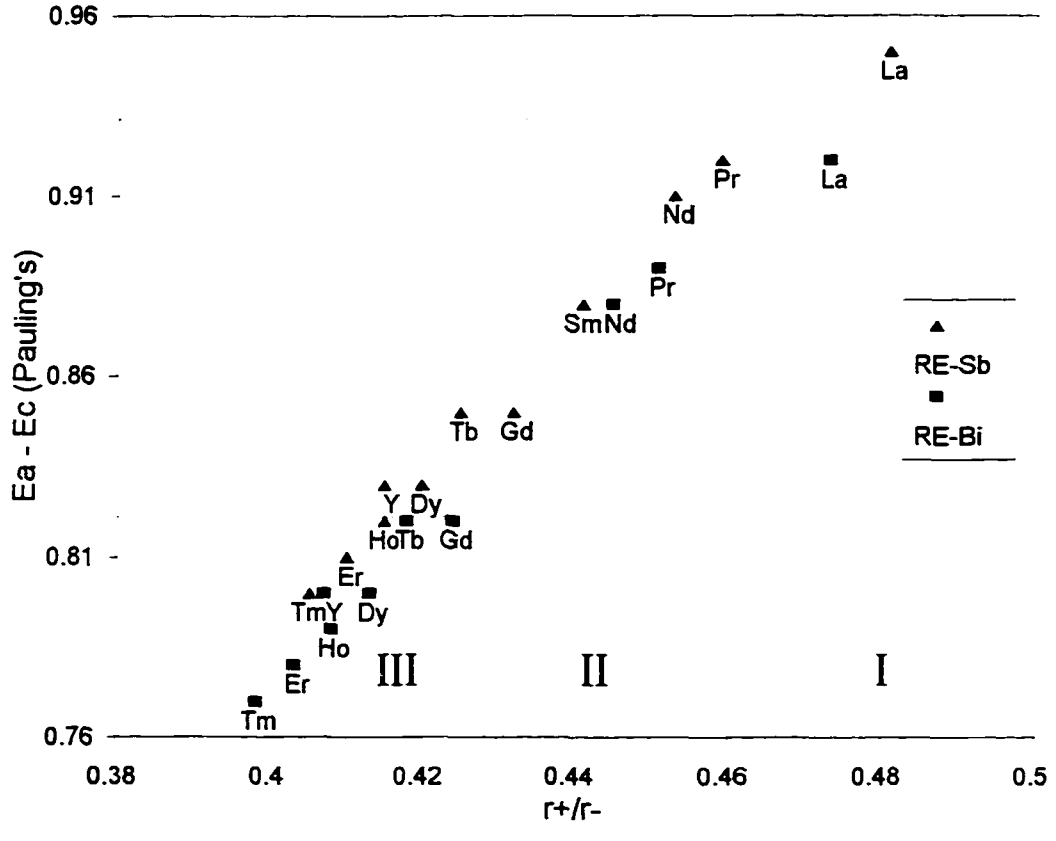

Figure III-32. Structural map of the Pauling's electronegativity difference ($\Delta E = E_a - E_c$) versus crystal radii ratio (r^+/r^-, CN=6) for trivalent metal antimonides (▲) and bismuthides (■). The map is divided in three main regions for RE-Pn combinations that form (I) the anti-Th_3P_4, (II) the Mn_5Si_3 and (III) the Y_5Bi_3 structures types.

and divalent rare-earth-metal pnictides, A_5Pn_3. For instance the previously reported phase transition between M ↔ Y structures in Ca_5Sb_3, Sr_5Bi_3 and Yb_5Sb_3 is nonexistent; the compounds with Y-type structures are hydrogen-stabilized. Other reported examples of phases with this structure are hydrogen-stabilized compounds as well, i.e., $Ca_5Bi_5H_x$, $Sr_5Sb_3H_x$, $Eu_5Sb_3H_x$, $Eu_5Bi_3H_x$ and $Yb_5Bi_3H_x$. In some instances, water from the silica containers provides enough hydrogen to stabilize the orthorhombic phase. The fluoride ion is capable of stabilizing the Y-type structure as well, e.g., in Ca_5Sb_3F, Ca_5Bi_3F, Sr_5Sb_3F and Sr_5Bi_3F phases. Powder neutron diffraction studies on Y-$Ca_5Bi_3D_{0.93(3)}$ indicated that hydrogen (D) is located in the same tetrahedral cavity that Hurng[50] reported for fluoride in Y-$Ca_5Sb_3F_{1.0(1)}$. Table III-32 summarizes the results of identified products from reactions $A_5Pn_3(H,F)_x$, where bold and underlined entries indicate new and previously misidentified phases, respectively. The earlier conclusions that omitted several binaries were understandably obscured by presence of hydrogen impurities. Thus, the M-type structure of Ca_5Bi_3, Eu_5Sb_3, Eu_5Bi_3 and Yb_5Bi_3 were observed for first time. The ternary $Sm_5Bi_3H_x$ phase is a new example of the Y-type structure. The Sm ions in this orthorhombic phase as inferred from its structural and magnetic susceptibility data are in a divalent state. The Eu and Yb ions in antimonides and bismuthides with either the M or Y structures are in a divalent state as well. Consequently, the presence of the third element, hydride or fluoride, is necessary to stabilize the Y-type structure. Additionally, this structure type is characteristic of systems that involve divalent metal ions. Some trivalent metal systems may form in this structure as well, as with Y_5Sb_3F. Importantly, the so-called β-Yb_5Sb_3-type structure should be better referred as Ca_5Sb_3F-type in recognition of the first accurate structural determination by Hurng.[50]

We have additionally been able to prove that the YB-type structure, as initially thought, is characteristic of binary pnictide systems that involve trivalent metal ions. The first two examples of rare-earth-metal antimonides with this structure type are Er_5Sb_3 and Tm_5Sb_3. These phases were characterized by single crystal x-ray diffraction and magnetic susceptibility measurements. Size or matrix factors play a very important role in the formation of these phases in the YB-type structure. Crystallization of a compound in this structure type is favored by combinations of small cations and large anions.

Table III-32. Products of the reactions in absence (-[H]) and presence of hydrogen or fluoride (+[H,F])[a]. Bold and underlined letters indicate new and previously misidentified phases, respectively.

A\Pn	As		Sb		Bi	
	-[H]	+[H]	-[H]	+[H,F]	-[H]	+[H,F]
Ca	**M**	<u>MH</u>	M[b]	<u>YH</u>,YF	**M**	<u>YH</u>[c],YF
Sr	**M**	<u>MH</u>[b]	M	<u>YH</u>,**YF**	M	<u>YH</u>,**YF**
Ba	**ATP**[b]	**ATPH**	**M**	<u>MH</u>[b],**ATPF**	**M**	<u>MH</u>
Sm	ATP	NH	M	**MH**[b]	M	**YH**[b]
Eu	M	<u>MH</u>	**M**[b]	<u>YH</u>	**M**[b]	<u>YH</u>
Yb	M	<u>MH</u>	M[b]	<u>YH</u>	**M**	<u>YH</u>[b]

[a] Products: M = Mn_5Si_3-type.
MH = Hydrogen-stuffed Mn_5Si_3-type.
YH = Hydrogen-stuffed β-Yb_5Sb_3-type (Ca_5Sb_3F).
YF = Fluoride-stuffed β-Yb_5Sb_3-type (Ca_5Sb_3F).
ATP = anti-Th_3P_4-type.
ATPH = Hydrogen-stuffed anti-Th_3P_4-type.
ATPF = Fluoride-stuffed anti-Th_3P_4-type.
NH = NaCl-type; probably an As deficient and hydrogen stuffed compound.

[b] Phase characterized by single crystal x-ray diffraction.

[c] Phase characterized by powder neutron diffraction on a deuterated sample, $Ca_5Bi_3D_{0.93}$.

In analogy to the trivalent metal systems, binary pnictides that involve tetravalent metal ions are expected to crystallize in the YB-type structure as well.

Our results on the YB-Er_5Sb_3 system are in contradiction with Fornasini's structural report of Y-Er_5Sb_3. We suspect that fluoride impurities may have stabilized the Y-type structure of this trivalent metal compound, in parallel to our results on Y-Y_5Sb_3F. The experimental conditions used by Fornasini to prepare the phase, dv conditions, greatly decrease the availability of hydrogen in the reaction. Fluoride impurities in rare-earth metals are not uncommon; these could come from their manufacturing processes, where rare-earth metals are prepared by the reduction of their corresponding fluorides with alkaline-earth metals.[129]

Matrix effects play a very important role in the structural tendencies of the ternaries $Ae_5Pn_3(H,F)_x$ compounds, where the size of the relative cation seem to be greatly influential. For instance, compounds that involve small cations and large anions favor the Y-type structure. Thus, antimonides and bismuthides of calcium and strontium form the Y-type structure. On the other hand, the combinations of large cations and small anions form in the M-type structure. Hence, arsenides and barium compounds are found only in the hexagonal M form. Nevertheless, the barium arsenides crystallize in the ATP-type structure. Figure III-33 show a structural map for the Ae–Pn combinations constructed from the metallic radii ratio, r+/r- (CN=12) on the abscissa and the difference of Pauling's electronegativities (E_{anion}-E_{cation}) on the ordinate. This map can be divided into two main regions; phases that crystallize in the ATP-type (I) and phases that crystallize in the M-type (II) structures. The second region in the map can be further subdivided into the combinations that upon reaction with hydrogen remain in the M-type (II-a) or form the Y-type (II-b) structures. For clarity purposes the Sm–(P,As) combinations were not included; they form in the NaCl-type structure.

Lack of Y-type phases competing for hydrogen allows the M-type compounds to show a large variation in their cell dimensions as result of their hydrogen intake. Thus, the $Ba_5Sb_3H_x$ and $Ba_5Bi_3H_x$ compounds present cell volume decrements of ~2.45 and 2.84%, respectively, between the phase prepared in hydrogen free conditions (dv) to the possible stoichiometric compositions $Ba_5(Sb,Bi)_3H_{-1}$. The variations of the Guinier cell

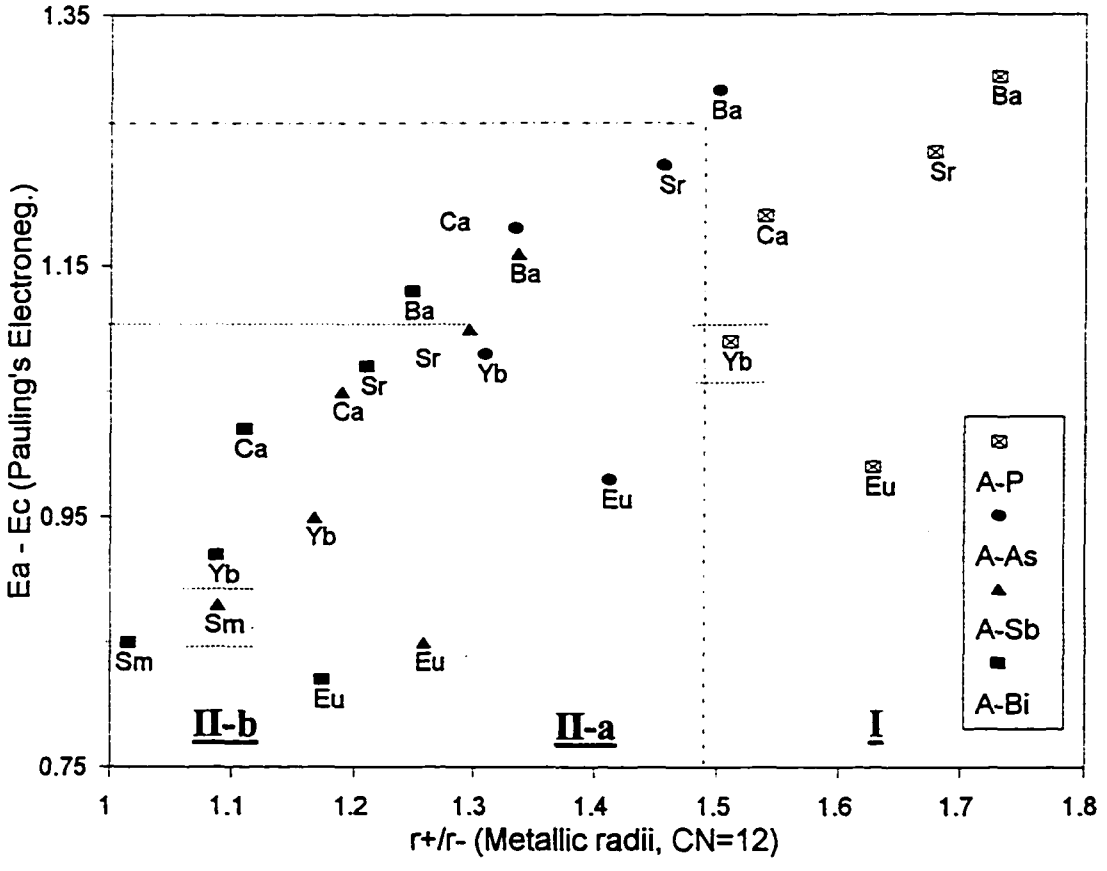

Figure III-33. Structural map of the Pauling's electronegativity difference ($\Delta E = E_a - E_c$) versus metallic radii ratio (r^+/r^-, CN=12) for A–Pn combinations (A= Ca, Sr, Ba, Sm, Eu, Yb; Pn= P, As, Sb, Bi). The map is divided in two main regions for combinations that form (I) the anti-Th_3P_4 and (II) the Mn_5Si_3 structures types. The region (II) is further divided into combinations that upon reaction with hydrogen form the (II-a) hydrogen-stuffed Mn_5Si_3-type and (II-b) the Ca_5Sb_3F (hydrogen-stuffed β-Yb_5Sb_3-type) structures. The combinations Yb–P and Sm–Sb in squares form in the NaCl-type and M-type, respectively.

volumes for M and Y phases prepared in this work are reported in Table III-33. The cell volume decrement for compounds with the M-type structure follow the trend; $Yb_5As_3H_x$ > $Ba_5Bi_3H_x$ > $Ba_5Sb_3H_x$ > $Ca_5As_3H_x$ > $Sm_5Sb_3H_x$ ≈ $Sr_5As_3H_x$ > $Eu_5As_3H_x$ > $Sr_5Sb_3H_x$ > $Sr_5Bi_3H_x$ ≈ $Yb_5Sb_3H_x$ > $Ca_5Sb_3H_x$ ≈ $Ca_5Bi_3H_x$. The large variation between Yb_5As_3 and $Yb_5As_3H_x$ (x ~1) phases is possibly influenced by distortions in the structure of the former.

The largest decrement of cell volume with hydrogen content for phases with the Y-type structure was observed for $Ca_5Bi_3H_x$, ~1.01%. Such a large variation is in concordance with the notion that the phase can be stabilized with low hydrogen contents. Interestingly, this bismuthide turned out to be a better hydrogen getter than Y metal. The trend of cell volume decrements for phases with the Y-structure is; $Ca_5Bi_3H_x$ > $Yb_5Bi_3H_x$ > $Yb_5Sb_3H_x$ ≈ $Ca_5Sb_3H_x$ > $Sr_5Bi_3H_x$ > $Sr_5Sb_3H_x$ > $Eu_5Sb_3H_x$ ≈ $Eu_5Sb_3H_x$. The hydrogen stoichiometry width in either M or Y phases is expected to follow the observed trend in cell volume decrements. Thus, traces of hydrogen are sufficient to stabilize the Y-$Ca_5Bi_3H_x$ phase (a compound formed by the combination of a small cation and a large anion) and large quantities of hydrogen are required to get the Y-$Sr_5Sb_3H_x$ phase in high yields (a combination of a larger cation and smaller anion than the previous example).

Hydrogenated phases ($A_5Pn_3H_x$) can successfully be converted into their dehydrogenated forms (A_5Pn_3) by heating the samples under dynamic vacuum. The opposite reaction is accomplished by the direct reaction between the binary with hydrogen gas or by slow hydrogenation in a closed silica container. The reactions of hydrogenation and dehydrogenation are generalized in Scheme III-1, where the path of reactions on the right pertains to systems that only form the M-type structure, and the part on the left, for systems that form the Y-type structure.

The temperature-dependent paramagnetic susceptibilities of Y-Ca_5Sb_3F, Y-Ca_5Bi_3F and Y-Sr_5Sb_3F suggest partial electron localization in these compounds, because deficiencies in the fluoride sites may act like electron traps in the structure. Nevertheless, the high electrical resistivity of these compounds indicates that they can reasonably be called Zintl phases. Semiconductive and diamagnetic behaviors are expected for stoichiometric phases in concordance with the classical Zintl concepts.

Table III-33. Calculated cell volume decrements for phases $A_5Pn_3H_x$ (%). Several variations were calculated in reference to previously reported cell constants, when reactions for variable hydrogen content were not performed.

A\Pn	As		Sb		Bi	
Str.Type	M[a]	Y[a]	M	Y	M	Y
Ca	2.16	—	0.00	0.48	0.00	1.05[b]
Sr	0.74	—	0.34	0.22	0.28	0.28
Ba	—	(0.46)[c]	2.45	—	2.84	—
Sm	—	(0.28)[d]	0.75	—	—[e]	—
Eu	0.60[f]	—	—[e]	0.20[g]	—[e]	0.21[g]
Yb	3.03	—	0.25	0.50[b]	—[e]	0.56

[a] Cell type: M = Mn_5Si_3-type structure.
Y = β-Yb_5Sb_3-type structure (Ca_5Sb_3F).
[b] In comparison with ref. 50.
[c] Combination does not form either M or Y type structures. Decrement calculated for the anti-Th_3P_4-type structure.
[d] Same as (c), however the decrement was calculated for the NaCl-type structure in comparison to ref. 80.
[e] No variable hydrogen content experiments performed and no available reference values.
[f] In comparison to ref. 85.
[g] In comparison to ref. 87.

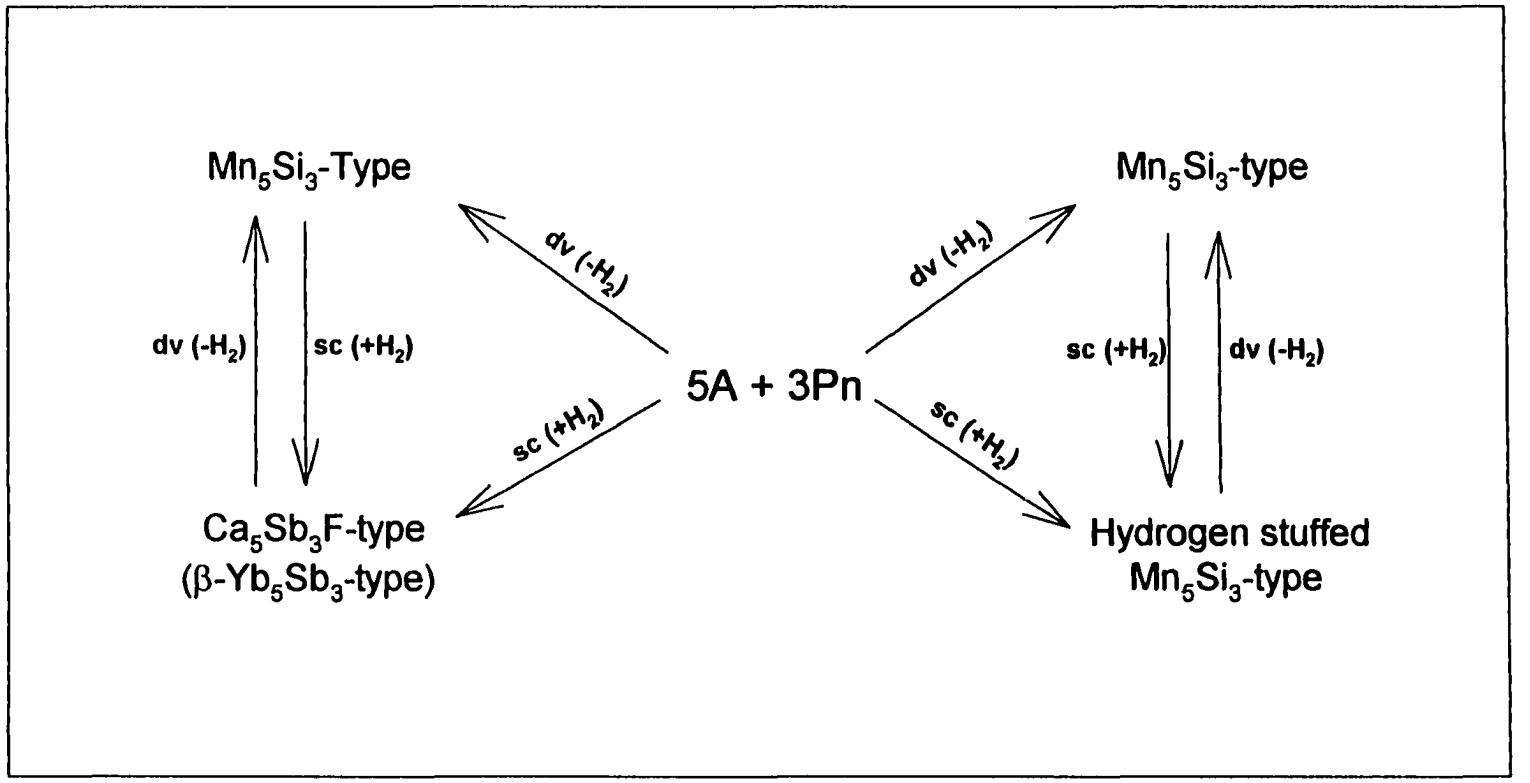

Scheme III-1. Summary of products for reactions of hydrogenation and dehydrogenation of A_5Pn_3 phases (A= Ca, Sr, Ba, Sm, Eu, Yb; Pn= As, Sb, Bi). Reversibility between the reactions of hydrogenation (sc conditions, $+H_2$) and dehydrogenation (dv conditions, $-H_2$) was commonly observed in these systems. For details about the structure type of each specific combination A–Pn see Table III-32 and the main text.

Long range interactions between the heavy pnictides plus band formation could be blamed for the metallic-like properties of Y-Sr_5Bi_3F, although, the exact electrical conductivity mechanism is at this time not well understood.

The temperature-independent paramagnetism of Y-$Ca_5Sb_3H_x$ and Y-$Sr_5Sb_3H_x$ is rationalized in terms of off-stoichiometry hydrogen content, i.e., $x < 1$. EHMO band calculations on the isotypic Y-$Ca_5Bi_3H_x$ (for x=0, 0.5 and 1) suggest that systems with fractional occupancy of hydrogen would be metallic-like, because the Fermi level passes through a band of substantial DOS primarily formed of Ca atoms orbital contributions. Additionally, when the Zintl composition is achieved, Y-Ca_5Bi_3H, the Fermi level passes trough an energy gap and the phase is expected to be semiconducting or insulating. These observations are in agreement with studies reported by Guloy and Corbett[130] for the M-La_5Ge_3Z systems, where according to EHMO band calculations, a band gap forms when the phase reaches the Zintl composition, i.e., M-La_5Ge_3P. The arsenides of calcium comply with their predicted properties. Thus $Ca_5As_3H_{\sim 1}$, a Zintl compound, is diamagnetic and Ca_5As_3, a non-Zintl compound, is Pauli paramagnetic. The small temperature-dependent paramagnetism of M-Ae_5Pn_3 phases seem to be consistent with the temperature dependence spin-paramagnetism observed in metallic systems, that is in agreement with simple electron counts ($5Ae^{2+}$, $3Pn^{3-}$). However, because of the observed trend of temperature dependencies in the susceptibilities of these materials, some electron trapping may occur in the structure. Band calculations on M-Ba_5Sb_3 suggest that the p-orbitals of the Ba(2) atoms have large contributions to the states near the Fermi level. The Ba(2)–Ba(2) bonding interactions implied by the COOP curves conceivably provide the states for localization of free electrons. Less efficient Ae(2)–Ae(2) interactions in the structure of the other M-Ae_5Pn_3 compounds may be accountable for the smaller temperature dependencies of their molar susceptibilities.

Ultimately, the prediction of properties, such as electrical conductivity and magnetic susceptibility, of compounds that qualify structurally as Zintl phases based on the assumption that the electropositive element donates all its electrons to the electronegative framework are apparently inaccurate. This last account is a matter of discussion in recent reviews about Zintl compounds.[15,131] Our results indicate that the

observed properties of some intermetallic compounds will be closer to predictions when elements of the earlier part of the periodic table occur in the compound. The possibility of ferromagnetic impurities in the original reactants as sources of unexpected magnetic behaviors in certain binary and ternary compounds were considered. However, substraction of the magnetic signal from data for selected samples did not modify their overall behaviors.

The effects of hydrogen on the properties of some intermetallic compounds, as exemplified in the Sm_5Sb_3 and $Sm_5Sb_3H_x$ systems, can be quite drastic. The presence of hydrogen in the samarium antimonide provokes, in addition to stronger magnetic signals, a notable shift in the magnetic transition temperatures and possibly internal spin–spin interactions as well. Therefore, the studies of compounds in which inadvertent impurities like hydrogen are present may lead to inaccurate and deceptive results and arguments.

The particularly pervasive hydrogen impurities in divalent metals certainly merit extra thought and precautions regarding possible effects of hydrogen on compound stability. For instance, the mixed pnictide $Ca_5As_{1.6}Sb_{1.4}$ recently reported by Carrillo-Cabrera and von Schnering[132] in the Y-type structure, is undoubtedly a hydrogen-stabilized phase. Our previous results conclusively support this assertion. Involvement of hydrogen in the chemistry of intermetallic compounds is not limited to $A_5Pn_3H_x$ systems, as we will discuss in the next chapter. Several other phases that structurally qualify as Zintl phases are hydrogen-stabilized compounds as well.

$A_{16}Pn_{11}$ Systems

Introduction

The binary $Ca_{16}Sb_{11}$ was serendipidously discovered by Hurng[60] while working with the Ca_5Sb_3 system. This phase was found in unsuccessful reactions with stoichiometries close to Ca_3Sb_2. Old reports based on calorimetric or thermal analysis for such a composition, Ca_3Sb_2, were later associated with the M- and Y- $Ca_5Sb_3(H)$ phases,[70] albeit in the presence of hydrogen. Thus, Hurng demonstrated that $Ca_{16}Sb_{11}$ was the correct formulation of the Ca_3Sb_2 composition. He solved the structure of

$Ca_{16}Sb_{11}$ (T) in the tetragonal space group $P\bar{4}2_1m$ (#113), R/R_w = 3.1/3.8, however, with some highly anisotropic atom positions. In an effort to find a more accurate structural solution, E. Peterson[113] revisited some of the experimental and crystallographic work that led to $Ca_{16}Sb_{11}$. Peterson, through extensive experimentation, confirmed that the new phase was indeed a binary in the Ca–Sb system with a $Ca_{16}Sb_{11}$ composition, and that the most reliable structural solution was in the space group $P\bar{4}2_1m$, R/R_w = 3.1/3.2. Table III-34 gives the refined positional data that Hurng and Peterson reported for $Ca_{16}Sb_{11}$.

Earlier, these solutions were considered as non-equivalent; however, interconversion of one to the other's position set is possible by adding ½, ½, ½ to either's enantiomeric set of positions. Such a claim was confirmed by refining Peterson's original diffraction data for either set of atomic positions separately to achieve equivalent solution statistics. The Sb(1) atom at 0,0,0 in Hurng's solution was split to the 0,0,z positions to achieve the equivalence. Troublesome atom positions in either solution, e.g., $U_{33}/U_{11} > 3$ for Sb(2) and Ca(1) atoms in Hurng's solution and Sb(2), Ca(3) and Ca(6) atoms in Peterson's, prevent us from considering any structural solution as final. Attempts to solve the structure in a lower symmetry space group than that would eliminate the operations generating the $\bar{4}$ in $P\bar{4}2_1m$, or other troublesome positions, did not achieve the ordered structure sought. Unsuccessful refinements in space groups $P42_12$ (#90), P4/m (#83), $P\bar{4}$ (#81), $P2_12_12$ (#18), $P2_122$ (#17), $P2_1/m$ (#11), $P2_1$ (#4), $P\bar{1}$ (#2) and P1(#1) resulted large correlation factors, split atom positions and large anisotropic thermal parameters.

The structure of $Ca_{16}Sb_{11}$ ($Ca_{16}Sb_{11}$-type, $P\bar{4}2_1m$, Z=2) is rather complex and could be described as the linkage of four different polyhedra of calcium atoms that coordinate the antimonys. The confacial stacking of two polyhedra types, distorted square prisms and antiprisms, make infinite chains that run parallel to c, at 0,0,z and ½,½,z. These chains are joined to irregular bicapped trigonal prisms and distorted bicapped square prisms of calcium atoms. Figure III-34 depicts the [001] view of the $Ca_{16}Sb_{11}$ cell, where the lines between atoms do not represent bonds and are drawn as a visual aid to appreciate some structural features. The polyhedra stacking that forms

Table III-34. Atom positions of $Ca_{16}Sb_{11}$ according to the structural solutions in space group $P\bar{4}2_1m$ (#113) by Hurng and Peterson.

Atom	Mult. Wyckoff	Site Symm.	W.-M. Hurng's data[a]			E. Peterson's data[b]		
			x	y	z	x	y	z
Sb(1)	2a/4d[c]	$\bar{4}$/2..[c]	0	0	0	0	0	0.4700(2)[d]
Sb(2)	4d	2..	0	0	0.3490(2)	0	0	0.1503(1)
Sb(3)	4e	..m	0.1267(1)	x + ½	0.0135(2)	0.37300(5)	x + ½	0.48668(9)
Sb(4)	4e	..m	0.1450(1)	x + ½	0.4681(2)	0.35504(5)	x + ½	0.03183(8)
Sb(5)	4e	..m	0.3208(1)	x + ½	0.7382(2)	0.17918(5)	x + ½	0.76210(8)
Sb(6)	4e	..m	0.3364(1)	x + ½	0.2636(2)	0.16402(5)	x + ½	0.23653(7)
Ca(1)	2c	2.mm	0	½	0.287(1)	0	½	0.7862(4)
Ca(2)	2c	2.mm	0	½	0.639(1)	0	½	0.1399(4)
Ca(3)	4e	..m	0.3683(5)	x + ½	-0.0012(7)	0.1313(2)	x + ½	0.5006(3)
Ca(4)	8f	1	0.0884(4)	0.2074(4)	0.4994(5)	0.2922(1)	0.5881(1)	-0.0010(2)
Ca(5)	8f	1	0.2100(5)	0.0752(5)	0.7882(4)	0.4239(2)	0.7095(2)	0.2885(2)
Ca(6)	8f	1	0.2032(5)	0.0711(5)	0.1855(6)	0.0706(2)	0.2034(2)	0.3157(3)

[a] Data from ref. 60.
[b] Data from ref. 133.
[c] Wyckoff sites 2a and $\bar{4}$ for W.M.H. data and 4d and 2.. for E.P. data, respectively.
[d] 50% occupancy.

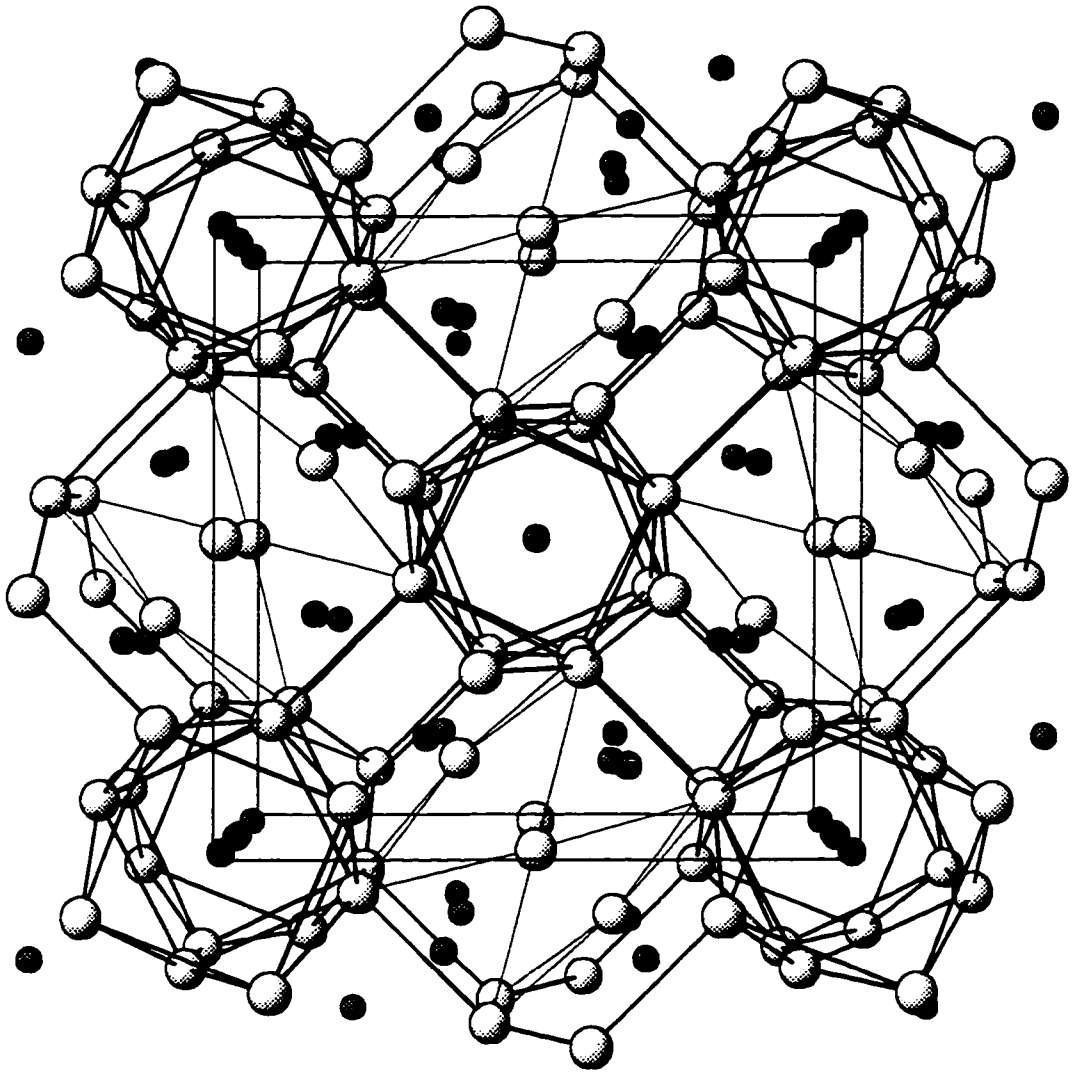

Figure III-34. Projection of the $Ca_{16}Sb_{11}$ structure along [001]. The large clear and small dark spheres represent Ca and Sb atoms, respectively. The lines between atoms do not represent bonds.

the chains and coordinate atoms Sb(1) and Sb(2) are visualized in Figure III-35, where Sb(1) is plotted with its split position. Chains assembled by stacking of square prisms and antiprisms in a 1:2 sequence is unique to the $Ca_{16}Sb_{11}$ structure. This chains are better illustrated in the [110] section of the T structure that is given in Figure III-36. Different stacking sequences of these polyhedra have been observed in other structure types. Thus, a 1:3 sequence is found in the Y_3Rh_2-type,[134] 1:5 in the $Pu_{31}Pt_{20}$[135] and, as it will be described in this work, a 1:6 sequence in the new $Yb_{36}Sn_{23}$ structure type. Chains composed of regular square antiprismatic arrangement of atoms are characteristic of the W_5Si_3-type structure.[136]

The shorter interatomic Sb–Sb contacts in $Ca_{16}Sb_{11}$ are ~3.40 and 3.62 Å for Sb(2)–Sb(2) and $Sb(1)_{split}$–Sb(2), respectively, see Figure III-35. All other Sb–Sb contacts are above 4.04 Å. These short contacts are longer than what typically would be considered a Sb–Sb single bond distance, 2.9 – 3.1 Å.[137,138,139] However, a lack of Sb–Sb bonding interactions in the structure would suggest an electron deficient compound, $16Ca^{2+}$ vs. $11Sb^{3-}$. On the other hand, supposition of a full bond only between Sb(2)–Sb(2) atoms would indicate that $Ca_{16}Sb_{11}$ is an electron-rich compound, $16Ca^{2+}$, $9Sb^{3-}$, Sb_2^{4-}, e^-. Prediction of electrical properties for the binary, based on either electron count, would anticipate a metallic-like compound. Unsuspecting, Wolfe and Peterson demonstrated that the compound is semiconducting between 253 – 293K, with a calculated energy gap of 0.46(2) eV.[56,113]

In an effort to better understand the $Ca_{16}Sb_{11}$ system, we revisited some of the experimental and crystallographic work on this system and extended this to other combinations of alkaline-earth- and divalent rare-earth metals with the pnictogens, $A_{16}Pn_{11}$; A= Ca, Sr, Ba, Eu, Yb; Pn= As, Sb, Bi. Additionally, several experiments were carried out in order to obtain ordered structures by varying the electron availability in $Ca_{16}Sb_{11}$. These changes in electron availability were attempted through ternary reactions $Ca_{16-x}M_xSb_{11}$, M= Na, K, Y, La. Magnetic measurements as function of temperature were made on several samples to determine possible structure–properties relationships.

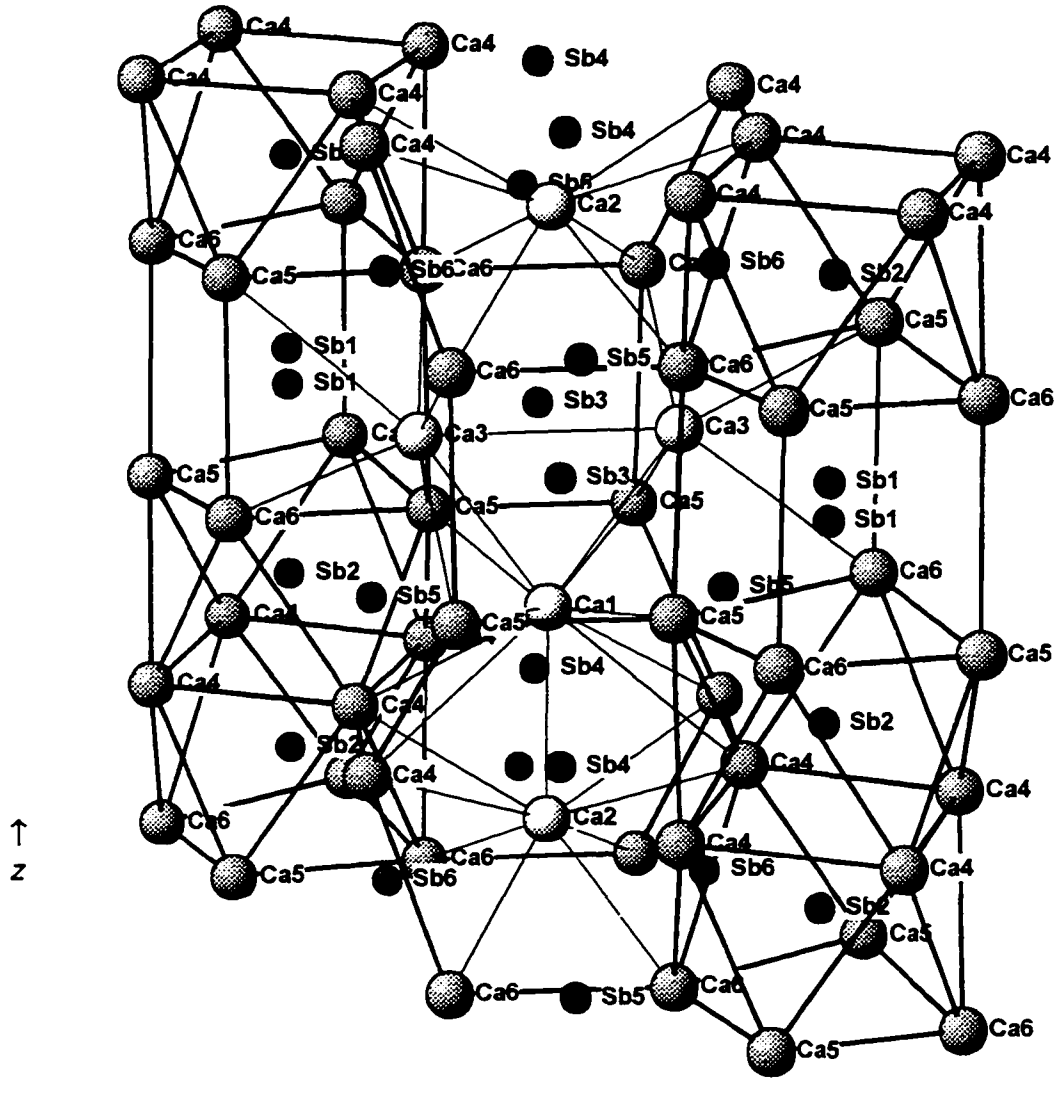

Figure III-35. Perspective section of the $Ca_{16}Sb_{11}$ structure, ca. [010]. Large and small dark spheres represent Ca and Sb atoms, respectively. The Sb(1) atoms are depicted in their split position according to E. Peterson's structural solution. The shorter interatomic Sb–Sb contacts are Sb(2)–Sb(2) and $Sb(2)–Sb(1)_{split}$, ~3.40 and 3.62 Å, respectively. All other d_{Sb-Sb} > 4.04 Å.

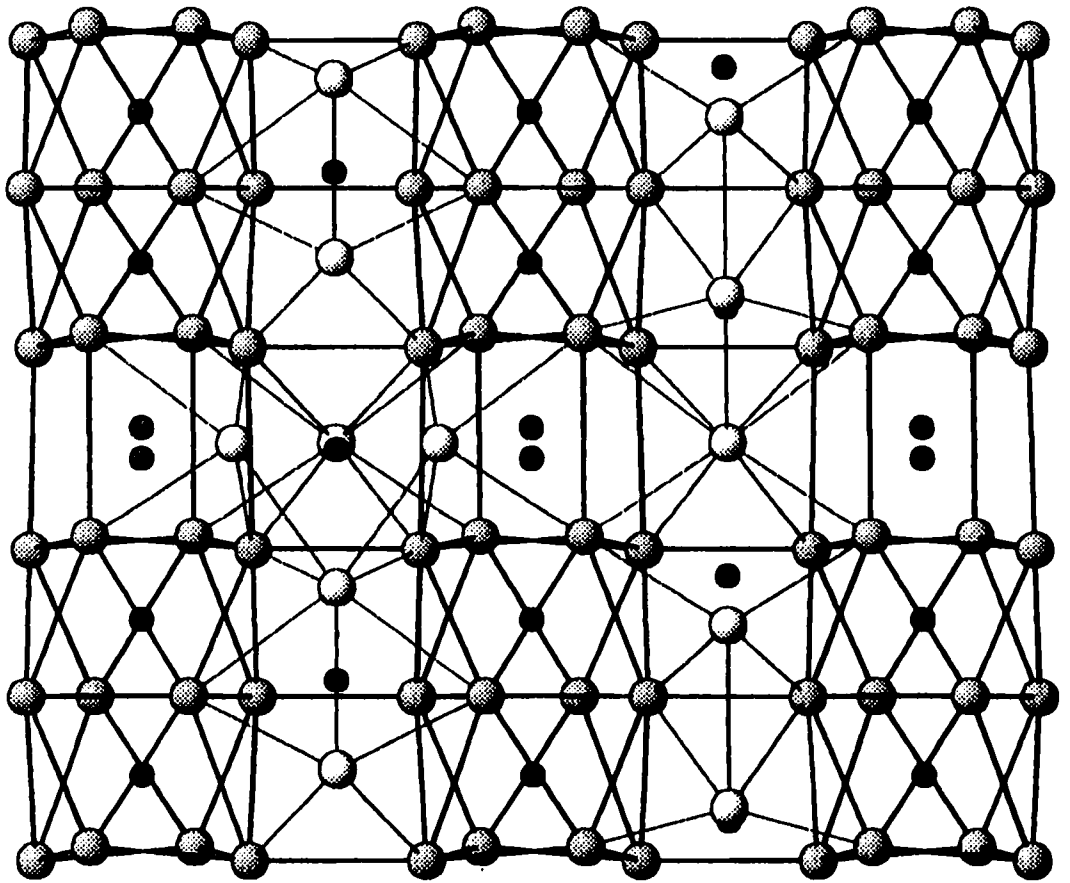

Figure III-36. The [110] partial view of the $Ca_{16}Sb_{11}$ structure. Large and small spheres represent Ca and Sb atoms, respectively. Heavy lines between Ca atoms highlight the distorted square prismatic and antiprismatic arrangements that surround Sb(1) and Sb(2) atoms. The Sb(1) are depicted in their split position according to E. Peterson's positions.

Results and Discussion

$Ca_{16}Sb_{11}$

Reactions at 1100°C between calcium and antimony at the proper stoichiometry give products in high yield with the $Ca_{16}Sb_{11}$-type (T) structure. Table III-35 shows the results of selected reactions carried out under various conditions and in presence of third elements. The obscuring effects of hydrogen in this system can be recognized in reaction C7, where the ternary hydride Y-$Ca_5Sb_3H_x$ formed as second major phase when reagent Ca was used as received. On the other hand, when previously dehydrogenated Ca metal was used as reagent or when the reaction was carried out under dynamic vacuum, rxns C34 and C44, respectively, the T phase was the only product. The cell dimensions of these T phases seem to depend on the history of the sample, because variations in the a and c axes are evident among the samples prepared under sc and dv conditions, which is suggestive of some hydrogen substitution in the samples. However, the cell volumes of these products are not significantly different, see Table III-36. Lack of a clear variation trend in the cell axes and their cell volume equivalence and yields of reactions indicate that the T phases are not hydrogen-stabilized compounds.

Reactions intended to vary the electron availiability in these systems, by including a third element, did not achieve the desired ordered T structures; instead either no reaction occurred or other phases formed. Thus, compositions intended for electron-deficient compounds, $Ca_{16-x}(Na,K)_xSb_{11}$; x=1,2 (rxns C14, C25, C26 and C27), led to a tetragonal phase initially identified as $Ca_{11}Sb_{10}$ in the $Ho_{11}Ge_{10}$-type structure (I4/mmm, #139, Z=4)[140]. This phase was originally believed to be sodium or potassium substituted, $Ca_{11-x}(Na,K)_xSb_{10}$; however, subsequent experimental efforts demonstrated the phase to be a new binary in the Ca–Sb system with an approximated composition $Ca_{11}Sb_{9.16}$ ($Ca_{11}Sb_{9+x}$-type, $P4_2/mnm$, #136, Z=4). The $Ca_{11}Sb_{9+x}$ phase (DH) is a defect variation of $Ca_{11}Sb_{10}$ reported by Eisenmann and coworkers.[137] Because of the large similarities between the $Ca_{11}Sb_{10}$ and $Ca_{11}Sb_9$ structures, they cannot easily be differentiated by Guinier powder patterns. Therefore, exceptional quality patterns were necessary for a reliable identification. In conclusion, the electron deficient compositions failed to form T phases because formation of $(Na,K)Sb_x$ compounds and the oxide Ca_4Sb_2O obviously

Table III-35. Distribution of products for reactions $Ca_{16-x}(Na,K,Y,La)_xSb_{11}$.

Rxn. No.	Loaded Composition	Conditions[a]		Product Distribution[b]
C7	$Ca_{16}Sb_{11}$	i	sc	T ~80%, Y~15%, Ox
C34[c]	$Ca_{16}Sb_{11}$	i	sc	T ~100%
C44	$Ca_{16}Sb_{11}$	i	dv	T ~100%
C27	$Ca_{14}Na_2Sb_{11}$	ii	sc	DH > 90%, $NaSb_x$ + Ox
C25	$Ca_{14}K_2Sb_{11}$	ii	sc	DH > 90%, KSb_x + Ox
C26	$Ca_{15}NaSb_{11}$	ii	sc	DH > 85%, $NaSb_x$ + Ox
C14	$Ca_{15}KSb_{11}$	ii	sc	DH > 90%, KSb_x + Ox
C2	$Ca_{16}NaSb_{11}$	ii	sc	T ~95%, $NaSb_x$ + Ox
C53	$Ca_{16}NaSb_{11}$	ii	dv	T ~95%, $NaSb_x$ + Ox
C18	$Ca_{15}YSb_{11}$	ii	sc	T ~50%, Y ~40%, Y_{metal}~10%
C55	$Ca_{15}YSb_{11}$	iii	dv	T ~60%, ATP ~40%
C19	$Ca_{15}LaSb_{11}$	ii	sc	T ~40%, Y ~45%, La_{metal}~15%
C56	$Ca_{15}LaSb_{11}$	iii	dv	M ~100%
C22	$Ca_{14}Y_2Sb_{11}$	ii	sc	T ~20%, Y ~60%, Y_{metal}~15%, UN
C23	$Ca_{14}La_2Sb_{11}$	ii	sc	T ~15%, Y ~60%, La_{metal}~20%, UN

[a] Conditions: i) Reaction at 1100°C for 2h, then 10°C/h to 650°C, followed by cooling to room temperature.
ii) Reaction at 1100°C for 2–4h, then 20°C/h to 850°C, annealed at 850°C for 15 days, thereafter slowly cooled to room temperature.
iii) Reaction at 1300°C for 4h in a high temperature furnace, then slowly cooled ~15°C/h to 650°C.
sc = Reaction in a sealed fused silica container.
dv = Reaction under dynamic vacuum.

[b] Estimated from Guinier powder patterns. T= $Ca_{16}Sb_{11}$-type, Y= Ca_5Sb_3F-type (formerly β-Yb_5Sb_3-type), DH= Defect-$Ho_{11}Ge_{10}$-type ($Ca_{11}Sb_9$), M= Mn_5Si_3-type, Ox= Ca_4Sb_2O (anti-K_2NiF_4-type), ATP= anti-Th_3P_4-type, UN= Unidentified phase.

[c] Reaction loaded with dehydrogenated Ca metal.

Table III-36. Lattice dimensions of the $Ca_{16-x}(Na,Y,La)_xSb_{11}$ compounds.

Rxn No.	Loaded Comp.	Str.Type/ Conds.[a]	a (Å)	c (Å)	Vol.(Å^3)	c/a	Ref.
	$Ca_{16}Sb_{11}$	T/sc	12.2453(5)	11.323(1)	1697.8(2)	0.925	60
	$Ca_{16}Sb_{11}$	T/sc	12.253(3)	11.313(4)	1698(1)	0.923	133
C7	$Ca_{16}Sb_{11}$	T/sc	12.266(2)	11.288(3)	1698.3(5)	0.920	
C34	$Ca_{16}Sb_{11}$	T/sc	12.2641(4)	11.2966(8)	1699.1(1)	0.921	
C44	$Ca_{16}Sb_{11}$	T/dv	12.2332(4)	11.3463(6)	1698.0(1)	0.927	
C2	$Ca_{16}NaSb_{11}$	T/sc	12.3562(7)	11.085(2)	1692.5(3)	0.897	
C53	$Ca_{16}NaSb_{11}$	T/dv	12.348(1)	11.106(1)	1693.4(3)	0.899	
C18	$Ca_{15}YSb_{11}$	T/sc	12.300(1)	11.237(2)	1699.9(4)	0.914	
C55	$Ca_{15}YSb_{11}$	T/dv	12.2328(9)	11.347(2)	1698.0(4)	0.928	
C19	$Ca_{15}LaSb_{11}$	T/sc	12.306(1)	11.235(2)	1701.4(4)	0.913	
C56	$Ca_{15}LaSb_{11}$	M/dv	9.0449(5)	7.0194(8)	497.32(8)	0.776	
C22	$Ca_{14}Y_2Sb_{11}$	T/sc	12.300(1)	11.241(2)	1700.6(4)	0.913	
C23	$Ca_{14}La_2Sb_{11}$	T/sc	12.316(1)	11.218(2)	1701.6(4)	0.912	

[a] Cells indexed for T= $Ca_{16}Sb_{11}$-type and M= Mn_5Si_3-type.
Conditions: dv= dynamic vacuum and sc= sealed container.

upset the loaded composition. Some details about the new phase $Ca_{11}Sb_9$ (DH) phase and its troublesome crystal structure solution are given in Appendix A at the end of this work.

Reactions intended to be electron precise and that involved sodium as the third element, $Ca_{16}NaSb_{11}$, gave products identified as T-type, rxns C2 and C53. Variation of the lattice parameters of these phases were quite apparent, when compared to those of the binary reactions. Increment of the a/b axes and decrement of c resulted in an averaged cell volume decrement of ~0.33%. Attempts to refine the structure of a crystal from reaction C2 ($P\bar{4}2_1m$, R/R_w= 4.6/6.0), ended in a pathological solution.[141] In addition to the Sb(1) split position, the Sb(2), Ca(1), Ca(2), Ca(3), and Ca(5) positions were considerably anisotropic. Importantly, the refinement did not generate new atoms positions. Careful evaluation of the $Ca_{16}Sb_{11}$ structure indicates a lack of large cavities that may incorporate the sodium ions. Partial substitution of Ca by Na ions in the structure appeared quite possible; however, refinement of the troublesome Ca positions as mixed Na + Ca occupancy led to bad residuals. Solution of the structure in lower space groups gave unacceptable statistics; therefore, the problem was abandoned.

Reactions that involved rare-earth metals Y and La did not achieve the expected structural ordering in the T cell either. When the reactions were heated below 1100°C (rxns. C18, C19, C22 and C23) they were incomplete. Unreacted rare-earth metal, T phase and Y-$Ca_5Sb_3H_x$ were among the products. On the other hand, completion was achieved when the reactions were heated at 1300°C and under dv conditions, rxns C55 and C56. The reaction involving yttrium, C55, gave the T and ATP phases as major and minor products, respectively. The reaction involving lanthanum, C56, gave a single phase product with the hexagonal M-type structure. The lattice parameters of this M phase suggest that some substitution of the Ca sites by La might have occurred, a ~ 0.21% cell volume increment being observed with respect to M-Ca_5Sb_3, see Table III-6. Cell dimensions of the T phases from ternary reactions C18, C19, C22, C23 and C55, as in the case of the binary reactions, seemed to depend on the history of the sample. Phases prepared under dv conditions characteristically had larger c/a ratios than those phases prepared under sc conditions. These cell axes variations were likely caused by

the presence of some hydrogen in the T structure rather than to substitution of either Y or La, albeit their cell volumes are nearly invariant to those of the binary.

In an effort to determine whether T phases prepared under vacuum differed significantly from those prepared under sc conditions, i.e., Hurng's and Peterson's samples, the structure of a crystal from binary C44 was solved. Table III-37 and III-38 summarize the crystallographic and refined data information of $Ca_{16}Sb_{11}$. In concordance with previous structural solutions, the most acceptable refinement was achieved in space group $P\bar{4}2_1m$. Pathologies of the structure are the Sb(1) split-position and for large thermal anisotropies Sb(2), Ca(3) and Ca(6). Figure III-37 depicts a section of the $Ca_{16}Sb_{11}$ structure as refined for C44, where the Sb(1) and Sb(2) atoms environments are detailed. The structural refinement statistics of C44 (R/R_w= 4.3/4.5) indicate that this last solution is not as accurate as Peterson's (R/R_w= 3.1/3.2). However, these results were expected; since the averaging statistics of all reflections collected for C44 (one octant, R_{int}= 6.5%, Laue group 4/mmm), was larger than Peterson's data set average (one quadrant, R_{int}= 4.7%)[133]. Overall, the pathologies in the solution for C44 are split Sb(1) atom position and large thermal anisotropic parameters for Sb(2), Ca(1), Ca(3) and Ca(6) atoms with U_{33}/U_{22} ratios of ~ 4.5, 3.3, 0.17 and 3.0, respectively; Peterson's anisotropic thermal parameters ratios for the same atoms were 3.7, 2.4, 0.45 and 2.6, respectively. Despite the small differences between Peterson's and this work's $Ca_{16}Sb_{11}$ structural solutions, they can be considered as equivalent and trustworthy. Additionally, the structures of phases T-$Ca_{16}Sb_{11}$ prepared either under sc or dv conditions, are equivalent.

Because the presence of superstructures in this system were not considered as a cause of the structural problems, several overexposed precession and Weissenberg layer photographs of several $Ca_{16}Sb_{11}$ crystals were taken. A 2*c* superstructure might have eliminated the need to split the Sb(1) and other troublesome positions. However, these photographs did not evidence the presence of any superstructure in the system. Adversely, a superstructure caused by disorder of only one atom in a 54-atom matrix would have been very difficult to document. On the other hand, the photographs indicated that all the crystals of $Ca_{16}Sb_{11}$, and other $A_{16}Pn_{11}$, were probably multiple,

Table III-37. Crystallographic Data of $Ca_{16}Sb_{11}$.

	$Ca_{16.01(7)}Sb_{10.99(3)}$
Crystal from rxn.	C44
Space group	$P\bar{4}2_1m$ (#113)
Lattice parameters[a]	
a (Å)	12.2332(4)
c (Å)	11.3463(6)
Volume (Å^3)	1698.0(1)
Z	2
Density calc. (g/cm^3)	3.873
Crystal dimensions (mm)	0.25 x 0.04 x 0.04
Diffractometer	Enraf-Nonius CAD4
Collected octants	-h, -k, -l
Scan type	ω-2θ
2θ limit (°)	54
Transmission range	0.869–1.097
Absorption coefficient (cm^{-1})	110.3
Number of reflections	
Measured	4068
Independent (observed[b])	2531(1595)
R_{ave} (%)[c]	6.46
No. of refined variables	77
R/R_w (%)	4.3/4.5
Goodness of fit	1.092
Secondary extinction coefficient	$7(2) \times 10^{-7}$
Max./min. peak in ΔF map. (e$^-$ Å^{-3})	3.21/-2.14

[a] Lattice parameters calculated from Guinier powder patterns.
[b] Observed reflections; $I \geq 3.00\sigma_I$.
[c] Average for all data; $I > 0$.

Table III-38. Refined positional and thermal parameters of $Ca_{16}Sb_{11}$ phase in the $Ca_{16}Bi_{11}$-type structure.

Atom	x	y	z	$B_{eq}(Å^2)$	U_{11}	U_{22}	U_{33}	U_{12}	U_{13}	U_{23}
$Ca_{16}Sb_{11}$ (C44)										
Sb(1)[a]	0	0	0.0306(2)	2.4(2)	0.040(3)	0.025(2)	0.027(3)	0.012(3)	0	0
Sb(2)	0	0	0.3494(1)	1.45(8)	0.010(1)	0.008(1)	0.0375(9)	0.0013(8)	0	0
Sb(3)	0.12662(9)	x + ½	0.0133(1)	1.25(3)	0.0199(5)	U_{11}	0.0080(8)	0.0047(6)	-0.0018(5)	U_{13}
Sb(4)	0.14509(8)	x + ½	0.4689(1)	1.29(4)	0.0114(4)	U_{11}	0.026(1)	-0.0017(6)	-0.0001(4)	U_{13}
Sb(5)	0.32085(8)	x + ½	0.7376(1)	0.94(3)	0.0139(5)	U_{11}	0.0082(8)	-0.0023(6)	-0.0006(5)	U_{13}
Sb(6)	0.33588(8)	x + ½	0.2635(1)	0.79(3)	0.0117(5)	U_{11}	0.0067(7)	-0.0005(6)	0.0009(5)	U_{13}
Ca(1)	0	½	0.2869(6)	1.4(2)	0.010(2)	U_{11}	0.033(4)	-0.001(3)	0	0
Ca(2)	0	½	0.6393(6)	1.6(2)	0.017(2)	U_{11}	0.025(4)	-0.001(3)	0	0
Ca(3)	0.3683(3)	x + ½	-0.0002(4)	2.1(1)	0.036(2)	U_{11}	0.006(2)	0.008(2)	0.000(2)	U_{13}
Ca(4)	0.0880(2)	0.2076(2)	0.4991(3)	1.3(1)	0.017(1)	0.017(1)	0.014(2)	0.001(1)	0.000(2)	0.002(2)
Ca(5)	0.2102(3)	0.0759(3)	0.7882(3)	1.7(2)	0.024(2)	0.018(2)	0.023(2)	0.002(2)	-0.013(2)	-0.013(2)
Ca(6)	0.2034(4)	0.0711(3)	0.1856(4)	2.6(2)	0.037(3)	0.016(2)	0.048(3)	0.008(2)	0.031(2)	0.010(2)

[a] 50% occupancy.

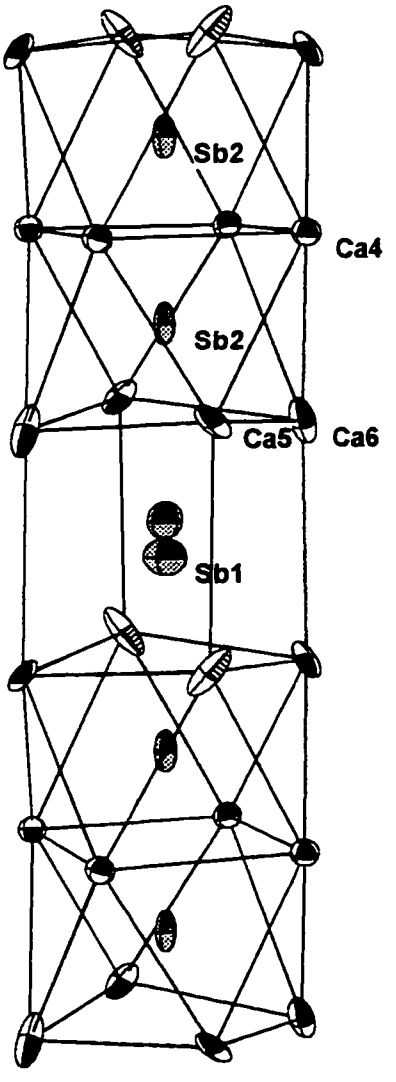

Figure III-37. Detail of the coordination environments of Sb(1) and Sb(2) atoms in $Ca_{16}Sb_{11}$. Size of the thermal ellipsoids (90% probability) are based on the results of the refinement of sample C44.

since two reflection spots were observed very close to each other. Observation of such double reflection spots required of a magnifying glass; otherwise they would have been unnoticed with the naked eye. The fact that $Ca_{16}Sb_{11}$ crystals grow in clusters of needle-like appearance is suggestive of their tendency to be multiple. Regarding this information, the structural refinement of C44 was attempted with the SHELX-93[142] program, including its TWIN subroutines. Efforts to refine the structure in space groups $P\bar{4}2_1m$ (#113) and $P2_12_12$ (#18) ended in solutions similar to those obtained with the TEXSAN[31] package, i.e. several large anisotropic atom positions. The space group $P2_12_12$ results as a subgroup of $P\bar{4}2_1m$ after the symmetry operations that generate the $\bar{4}$ symmetry site in $P\bar{4}2_1m$ are eliminated. Interestingly, the BASF factors or twin component contributions in SHELX-93 gave values of 0.556 and 0.479 for the tetragonal and orthorhombic solutions, respectively. Such numbers are close to 0.50 and suggestive of a 1:1 contribution of crystals to the twin. Of course, this speculation about the twin crystals is susceptible to inaccuracy because some actual twin systems do not necessarily give multiple reflections spots.[143]

Other probable causes of the structural pathologies are the large asymmetric environments characteristic of some atoms and the low packing efficiency in the T structure. Figure III-38 and III-39 depict the coordination polyhedra around Sb and Ca atoms in $Ca_{16}Sb_{11}$, respectively. The polyhedra in these figures are drawn to show their geometrical resemblances; therefore, they do not share the same orientation. Interatomic distances tabulated by coordination spheres are given in Table III-39. These distances were calculated from the refinement of C44. The Sb(1) and Sb(2) atoms, as previously mentioned, are eight-coordinate by calcium atoms in a distorted square prism and square antiprism arrangements, respectively. These polyhedra share square faces and are stacked in 1:2 sequence, see Figure III-37. Matrix effects are apparently the cause of the large cavity around Sb(1) atoms. Such a large cavity allows relaxation of the Sb(1) atom from the central position, since these atoms seem to be statistically disordered (50:50) on the 0,0,z and 0,0,$\bar{z}$ positions. Interatomic Sb(1)–Ca distances are in general larger than the sum of Ca^{2+} (1.14 Å, CN=6)[62] crystal radii and Sb^{3-} (2.17 Å, CN=6)[71] intermetallic crystal radii ~ 3.31 Å. Calculated interatomic distances Sb(1)–Ca(5)

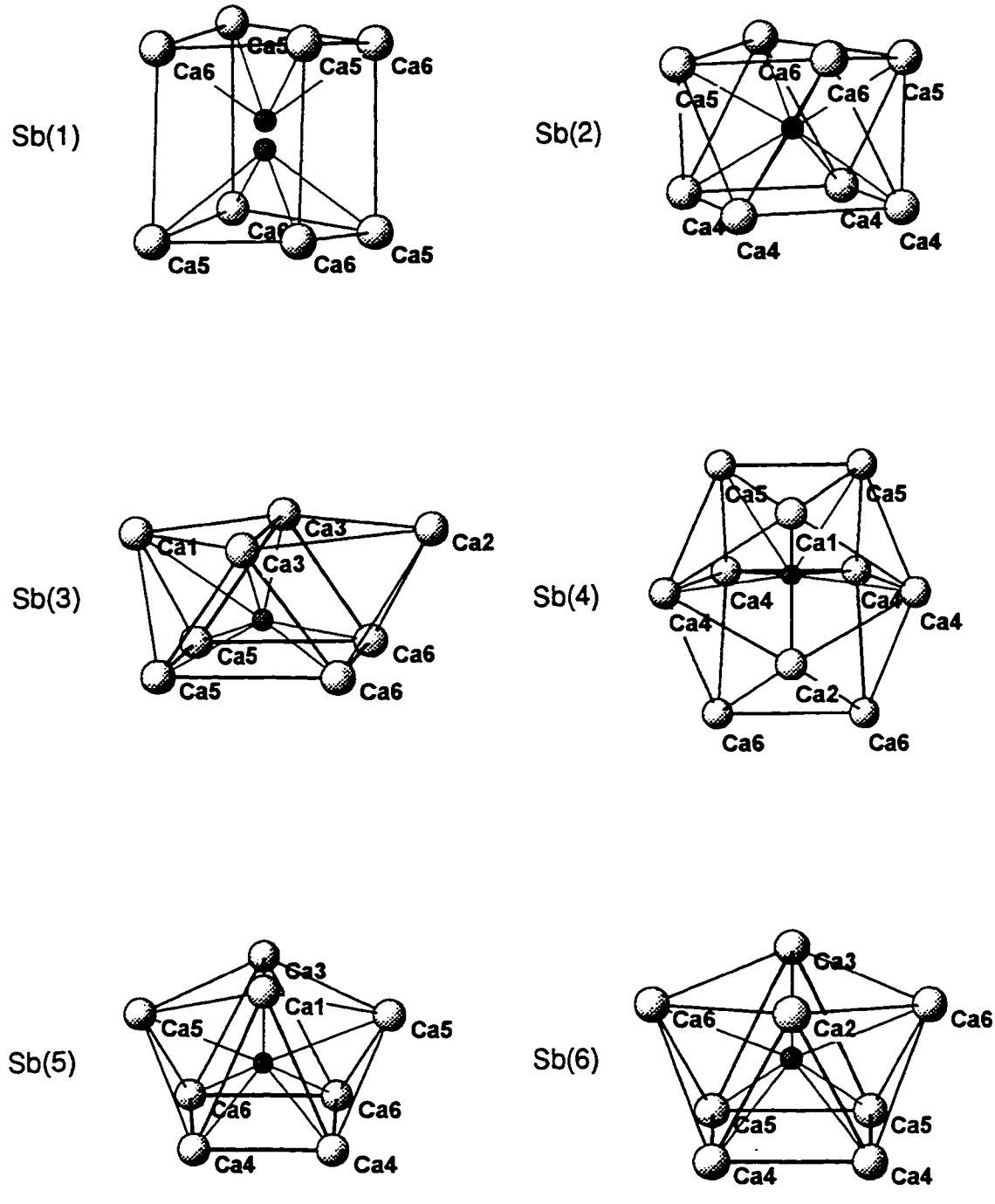

Figure III-38. Calcium atoms polyhedra surrounding the Sb atoms in $Ca_{16}Sb_{11}$. These polyhedra are not drawn with the same orientation. The Sb(1) atoms are depicted in their split position at 0,0,z.

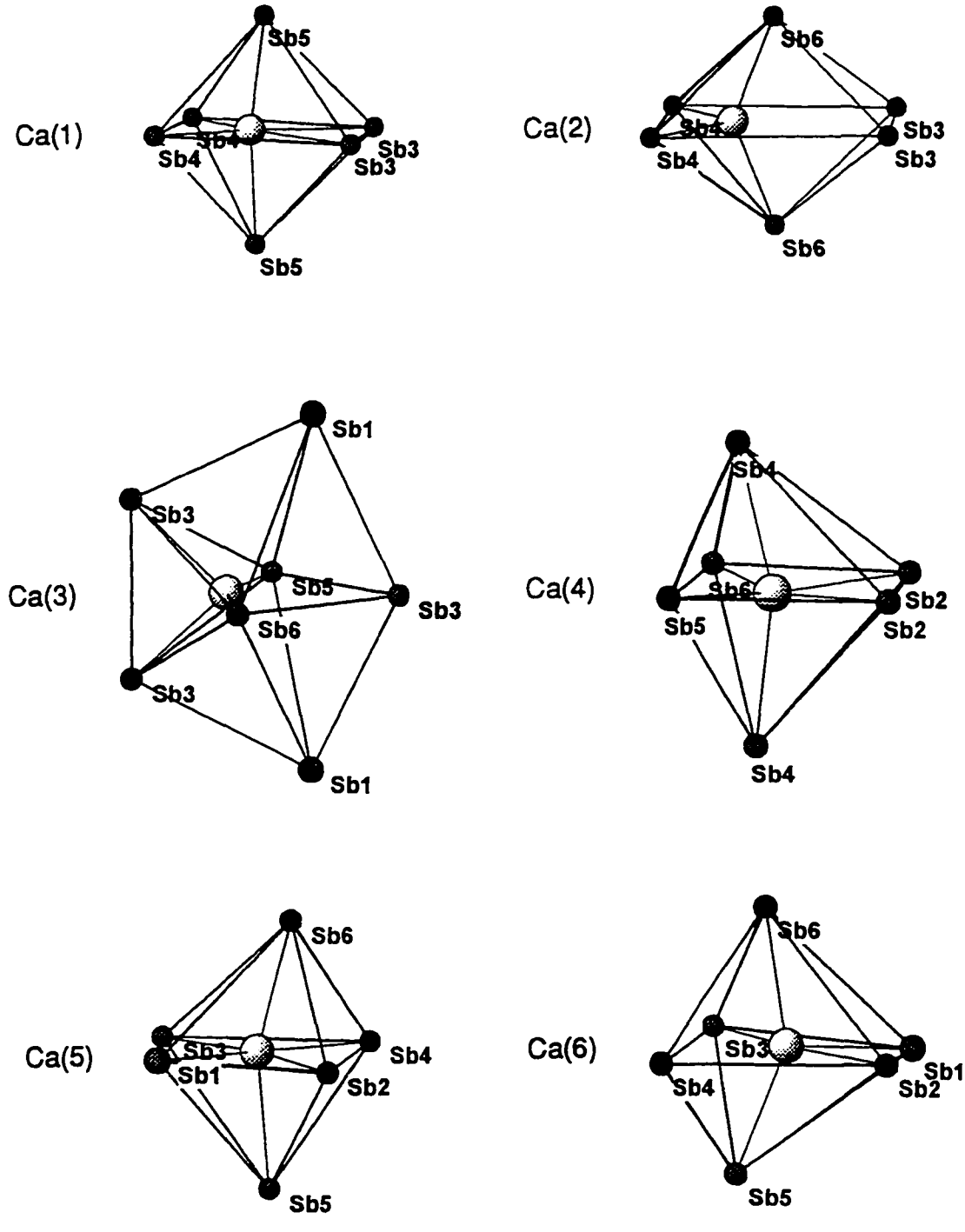

Figure III-39. Antimony atoms polyhedra surrounding the Ca atoms in $Ca_{16}Sb_{11}$. These polyhedra are not drawn with the same orientation. The Sb(1) atom is depicted on its non-split position at 0,0,½.

Table III-39. Interatomic distances in $Ca_{16}Sb_{11}$.

Atom A – Atom B		d (Å)	Atom A – Atom B		d (Å)
Sb(1)[a]	– Ca(5) (x2)	3.421(5)	Sb(5)	– Ca(1) (x1)	3.112(2)
	– Ca(5) (x2)	3.878(4)		– Ca(3) (x1)	3.085(5)
	– Ca(6) (x2)	3.168(5)		– Ca(4) (x2)	3.221(4)
	– Ca(6) (x2)	3.601(5)		– Ca(5) (x2)	3.449(4)
				– Ca(6) (x2)	3.191(4)
Sb(2)	– Ca(4) (x2)	3.240(3)			
	– Ca(4) (x2)	3.250(3)	Sb(6)	– Ca(2) (x1)	3.046(3)
	– Ca(5) (x2)	3.148(4)		– Ca(3) (x1)	3.045(5)
	– Ca(6) (x2)	3.225(4)		– Ca(4) (x2)	3.253(4)
				– Ca(5) (x2)	3.283(4)
Sb(3)	– Ca(1) (x1)	3.800(6)		– Ca(6) (x2)	3.419(4)
	– Ca(2) (x1)	4.775(6)[b]			
	– Ca(3) (x2)	3.165(4)	Sb(1)	– Sb(1) (x1)	0.695(5)
	– Ca(5) (x2)	3.073(4)		– Sb(2) (x1)	3.617(3)
	– Ca(6) (x2)	3.142(4)		– Sb(2) (x1)	4.312(3)
Sb(4)	– Ca(1) (x1)	3.250(5)	Sb(2)	– Sb(2) (x1)	3.418(3)
	– Ca(2) (x1)	3.169(5)			
	– Ca(4) (x2)	3.373(3)	All other contacts:		
	– Ca(4) (x2)	3.391(3)	Sb	– Sb	> 4.04 Å
	– Ca(5) (x2)	3.515(4)			
	– Ca(6) (x2)	4.431(5)[b]			

Table III-39. Continued

Atom A – Atom B	d (Å)	Atom A – Atom B	d (Å)
Ca(1) – Sb(3) (x2)	3.800(6)	Ca(5) – Sb(1) (x1)	3.421(5)
– Sb(4) (x2)	3.250(5)		[3.878(4)][c]
– Sb(5) (x2)	3.112(2)	– Sb(2) (x1)	3.148(4)
		– Sb(3) (x1)	3.073(4)
Ca(2) – Sb(3) (x2)	4.775(6)[b]	– Sb(4) (x1)	3.515(4)
– Sb(4) (x2)	3.169(5)	– Sb(5) (x1)	3.449(4)
– Sb(6) (x2)	3.046(3)	– Sb(6) (x1)	3.283(4)
Ca(3) – Sb(1) (x2)	4.797(2)[b]	Ca(6) – Sb(1) (x1)	3.168(5)
	[4.798(2)][c]		[3.601(5)][c]
– Sb(3) (x1)	4.183(5)[b]	– Sb(2) (x1)	3.225(4)
– Sb(3) (x2)	3.165(4)	– Sb(3) (x1)	3.142(4)
– Sb(5) (x1)	3.085(5)	– Sb(4) (x1)	4.431(5)[b]
– Sb(6) (x1)	3.045(5)	– Sb(5) (x1)	3.191(4)
		– Sb(6) (x1)	3.419(4)
Ca(4) – Sb(2) (x1)	3.240(3)		
– Sb(2) (x1)	3.250(3)	Shortest contact:	
– Sb(4) (x1)	3.373(3)	Ca(4) – Ca(4)	3.536(6)
– Sb(4) (x1)	3.391(3)		
– Sb(5) (x1)	3.221(4)	All Other	
– Sb(6) (x1)	3.045(5)	Ca – Ca	> 3.70

[a] Split position.
[b] Atom included to complete the polyhedron.
[c] Number in brackets corresponds to distance to the other split Sb(1).

and Sb(1)–Ca(6) modeled for a non-split Sb(1) position are ~3.63 and 3.36 Å, respectively. The Sb(2) atom is in a more constrictive environment; however, possible binding interactions to adjacent Sb(2) atoms drive its anisotropy in the direction of the other Sb(2) atom. Attempts to split the Sb(2) atom position during the structural refinement resulted in divergence of the least squares calculation. The Sb(3), Sb(5) and Sb(6) atoms are eight-coordinate by calcium atom in distorted bicapped trigonal prismatic arrangements.

It could be argued that a vacant square pyramidal cavity is formed by Ca(3)–Ca(6)–Ca(3)–Ca(6)–Ca(2) atoms near Sb(3), $d_{Sb(3)-Ca(2)}$= 4.775(6) Å, see Figure III-37; however, placement of a small anion, like H^-, in this cavity would give an unreasonable short Sb–H contact, d < 2.3 Å. The atoms Sb(5) and Sb(6) are located in a more regular and constrictive environments that are reflected in their smaller isotropic thermal parameters. Among all antimonys, Sb(4) is the only ten-coordinate atom; such a environment is quite spherical and can be described as a very distorted bicapped square prismatic polyhedron, where Ca(4)–Ca(5)–Ca(4)–Ca(6) atoms form the square faces of the prism. Interatomic Sb–Ca distances and Sb coordination environments are in agreement with the point group symmetries corresponding to each site. Calcium–calcium distances in $Ca_{16}Sb_{11}$ are above 3.54 Å; the shortest Ca–Ca contacts in M-Ca_5Sb_3 are ~ 3.51 Å. All the Ca atoms in $Ca_{16}Sb_{11}$, with exception of Ca(3), are six-coordinate by antimony in distorted octahedral arrangements. In general, the Ca atoms are not located at the geometrical centers of the octahedra. Thus, Ca(1) and Ca(2) have the most non-spherical environment among the six-coordinated calcium atoms. The Ca(3) atom is seven-coordinate in a distorted pentagonal bipyramid configuration of antimonys, and it is off of the polyhedral geometrical center. The asymmetric environments of these cations are in agreement with their observed thermal anisotropies. Consequently, the large asymmetric environments of several atoms in $Ca_{16}Sb_{11}$ are probably contributing to the observed structural pathologies as well. Electronic requirements may also play a important role in the characteristics of the structure, as it will be discussed later in this section.

Other $A_{16}Pn_{11}$ systems

Initial work by Hurng and Peterson suggested that phases with the T-type structure might also occur for other alkaline-earth-metal–pnictogen combinations. Such a possibility motivated us to search for new phases with this structure type. Table III-40 summarizes the results of selected reactions in the $A_{16}Pn_{11}$ systems explored (A= Ca, Sr, Ba, Eu, Yb; Pn= As, Sb, Bi). The majority of these reactions were carried under both sc and dv conditions to rule out the possible involvement of hydrogen.

All the attempted A–Pn combinations form compounds that have the T-type structure according to their Guinier powder patterns, with the exceptions of Ba–As and Yb–As that form the ATP and distorted-ATP (rhombohedral cell) structures. The cubic ATP phase was also identified for the Sr–Bi and Ba–Bi combinations for the first time. These latter two phases with the ATP structure are probably hydrogen stabilized, or may contain some hydrogen, because their yield decreased when the reactions were performed under dv conditions; however, experiments to prove this point were not made. Lattice parameters of the new phases are reported in Table III-41, where, as in the case of the $Ca_{16}Sb_{11}$ system, it is evident that these cell dimensions depend on the history of the samples. Fractional occupancies of the pnictide sites might also be responsible for these slight changes in lattice parameters. Typically, crystals in these systems grew multiple or too small for further crystallographic work, except crystals of minimal quality were found for the $Eu_{16}As_{11}$, $Ca_{16}Bi_{11}$ and $Sr_{16}Bi_{11}$ cases. Single crystal refinement to these samples resulted in solutions that were more troublesome than for T-$Ca_{16}Sb_{11}$. Diffraction data sets with low number of observed reflections (~ 20 – 30% with $I \geq 3.00\sigma_I$) were partially to blame for these results. The least troublesome solutions were achieved in space group $P\bar{4}2_1m$ (#113), where Pn(1), Pn(2), A(1), A(2) A(3) and A(6) were commonly split or highly anisotropic. Consequently, one could conceive based on these results that pathologies in the $Ca_{16}Sb_{11}$ system are characteristic of the structure type itself.

The combination Ca–Bi results were very interesting, since two phases seem to exist at the $Ca_{16}Bi_{11}$ composition. This claim is based on Guinier powder pattern and some single crystal information. When the reactions between the elements were

Table III-40. Distribution of products for reactions $A_{16}Pn_{11}$.

Rxn. No.	Loaded Composition	Conditions[a]		Product Distribution[b]
AS23	$Ca_{16}As_{11}$	i	dv/sc	T ~90%, UN
I1	$Ca_{16}Bi_{11}$	ii	sc	T ~95%, UN
I23	$Ca_{16}Bi_{11}$	i	dv/sc	T ~95%, UN
I13	$Ca_{16}Bi_{11}$	iii	dv	DT ~100%
AS24	$Sr_{16}As_{11}$	i	dv/sc	T ~90%, UN
AS21	$Sr_5As_3H_2$	iv	sc	T ~ 95%, UN
K3	$Sr_{16}Sb_{11}$	iv	sc	T ~100%
K6	$Sr_{16}Sb_{11}$	v	dv	T ~100%
L2	$Sr_{16}Bi_{11}$	ii	dv/sc	T ~80%, ATP ~20%
L5	$Sr_{16}Bi_{11}$	v	sc	T ~95%, ATP ~5%
AS25	$Ba_{16}As_{11}$	i	dv/sc	ATP ~100%
B4	$Ba_{16}Sb_{11}$	iv	sc	T ~100%
B10	$Ba_{16}Sb_{11}$	iv	dv	T ~100%
J4	$Ba_{16}Bi_{11}$	iv	sc	T ~20%, ATP ~75%, Ox
J12	$Ba_{16}Bi_{11}$	vi	dv	T ~40%, ATP ~55%, Ox
AS26	$Eu_{16}As_{11}$	i	dv/sc	T ~90%, UN
AS18	$Eu_5As_3H_2$	v	sc	T > 95%, UN

Table III-40. Continued

Rxn. No.	Loaded Composition	Conditions[a]		Product Distribution[b]
RE11	$Eu_{16}Sb_{11}$	vi	dv	T ~100%
RE12	$Eu_{16}Bi_{11}$	vi	dv	T ~85%, ATP ~15%
AS27	$Yb_{16}As_{11}$	i	dv/sc	DATP > 80%
N3	$Yb_{16}Sb_{11}$	v	sc	T ~20%, ATP ~80%
N5	$Yb_{16}Sb_{11}$	v	dv	T ~95%, ATP ~5%
N4	$Yb_{16}Bi_{11}$	v	sc	T ~10%, ATP ~90%
N6	$Yb_{16}Bi_{11}$	v	dv	T ~40%, ATP ~60%

[a] Conditions: i) Reaction under vacuum at 1100°C for 6h, then 15°C/h to 850°C and quenched to room temperature in an ice–water bath. Subsequently, samples were annealed in a sealed container at 900°C for 30 days.
ii) Reaction at 1100°C for 36h, then very slowly cooled (2°C/h) to 900°C, left at that temperature for 14 days and quenched in an ice–water bath to room temperature.
iii) Reaction at 1100°C for 24h, then cooled to 650°C at 1°C/h.
iv) Reaction at 1100°C for 3h, then 15°C/h to 825°C and kept at this temperature for 10 days. Afterwards, quenched to room temperature in an ice–water bath.
v) Reaction at 1100°C for 3h, then 10°C/h to 650°C.
vi) Similar to (v) but reaction temperature 1150°C.
sc = Reaction in a sealed fused silica container.
dv = Reaction under dynamic vacuum.

[b] Estimated from Guinier powder patterns. T= $Ca_{16}Sb_{11}$-type, DT= Distorted $Ca_{16}Sb_{11}$-type (orthorhombic cell), Y= Ca_5Sb_3F-type (formerly, β-Yb_5Sb_3-type), DH= Defect-$Ho_{11}Ge_{10}$-type ($Ca_{11}Sb_{\sim 9}$), ATP= anti-Th_3P_4-type, Ox= Ca_4Sb_2O (anti-K_2NiF_4-type), DATP= Distorted a-Th_3P_4 (rhombohedral cell), UN= Unidentified phases.

Table III-41. Lattice dimensions of the $A_{16}Pn_{11}$ compounds.

Rxn No.	Loaded Comp.	Str.Type/ Conds.[a]	a (Å)	c (Å)	Vol.(Å^3)	c/a
AS23	$Ca_{16}As_{11}$	T/dv/sc	11.686(3)	10.511(3)	1435.4(6)	0.899
I1	$Ca_{16}Bi_{11}$	T/sc	12.4944(6)	11.4347(1)	1785.1(2)	0.915
I23	$Ca_{16}Bi_{11}$	T/dv/sc	12.4949(8)	11.430(1)	1784.5(2)	0.915
AS24	$Sr_{16}As_{11}$	T/dv/sc	12.2954(4)	11.1598(8)	1687.1(2)	0.908
AS21	$Sr_5As_5H_2$	T/sc	12.2959(7)	11.159(2)	1687.2(3)	0.907
K3	$Sr_{16}Sb_{11}$	T/sc	12.9115(5)	11.8343(8)	1972.8(2)	0.917
K6	$Sr_{16}Sb_{11}$	T/dv	12.9341(5)	11.8027(7)	1974.5(2)	0.912
	$Sr_{16}Bi_{11}$[b]	T/sc	13.137(1)	11.594(2)	2000.9(5)	0.882
L2	$Sr_{16}Bi_{11}$	T/dv/sc	13.157(2)	11.935(3)	2066.0(6)	0.907
L5	$Sr_{16}Bi_{11}$	T/sc	13.152(1)	11.934(2)	2064.2(5)	0.907
AS25	$Ba_{16}As_{11}$	ATP/dv/sc	9.956(2)		987.0(7)	1.000
B4	$Ba_{16}Sb_{11}$	T/sc	13.570(2)	12.411(3)	2285.3(7)	0.915
B10	$Ba_{16}Sb_{11}$	T/dv	13.582(2)	12.393(4)	2286.3(9)	0.912
J4	$Ba_{16}Bi_{11}$	T/sc	13.746(1)	12.570(3)	2375.2(7)	0.914
J12	$Ba_{16}Bi_{11}$	T/dv	13.744(1)	12.568(1)	2374.2(4)	0.914
AS26	$Eu_{16}As_{11}$	T/dv/sc	12.0885(5)	11.040(1)	1613.3(3)	0.913
AS18	$Eu_5As_3H_2$	T/sc	12.080(2)	11.054(3)	1613.1(6)	0.915
RE11	$Eu_{16}Sb_{11}$	T/dv	12.737(1)	11.668(2)	1892.9(3)	0.916
RE12	$Eu_{16}Bi_{11}$	T/dv	12.906(3)	11.852(6)	1974(1)	0.918
N3	$Yb_{16}Sb_{11}$	T/sc	12.1638(4)	11.321(1)	1675.0(2)	0.931
N5	$Yb_{16}Sb_{11}$	T/sv	12.1686(5)	11.320(1)	1676.2(2)	0.930
N4	$Yb_{16}Bi_{11}$	T/sc	12.3692(9)	11.544(1)	1766.2(2)	0.933
N6	$Yb_{16}Bi_{11}$	T/dv	12.3694(7)	11.588(1)	1766.9(2)	0.933

[a] Cells indexed for T= $Ca_{16}Sb_{11}$-type and ATP= Anti-Th_3P_4-type. Conditions: dv= dynamic vacuum and sc= sealed container.
[b] Reported in reference 60 from a partial indexing.

annealed at temperatures above 850°C followed by quenching to room temperature, rxns I1 and I23, the product's powder pattern matched the T-type structure model. On the other hand, when the reaction was slowly cooled to 650°C, rxn I13, the product pattern showed additional lines and could not be indexed as T-type. Crystals from I13 grew in the [110] direction and could not be aligned on the single-crystal cameras due to restrictions of the goniometer head angles. Therefore, single crystal film work was not possible on these samples. Partial refinement of a small crystal from I13 indicated that the new phase may be an orthorhombic distortion of the tetragonal T-type structure. A calculated powder pattern based on the partial solution model in space group Pba2 (#32), selected through the statistics of observed reflections and partial structural refinement, matched more than 95% of the positions and intensities of the lines in the experimental pattern. Unit cell with dimensions a= 12.483(3), b= 12.555(3) and c= 11.412(2), with vol= 1788.5(7) $Å^3$, were calculated for the new, low temperature, orthorhombic phase. The composition of this orthorhombic phase is probably similar to T-$Ca_{16}Bi_{11}$, because both phases have comparable cell volumes (see Appendix B for some information about the orthorhombic phase). Studies to establish whether a real phase transition is occurring between these phases were not pursued. Finally, poor quality powder patterns of $Eu_{16}Bi_{11}$, rxn. RE12, were blamed for the large associated standard deviations reported in Table III-41, since no evidence of cell distortions, in the form of line splitting, were found for the bismuthide pattern.

Magnetic properties

Earlier, it was mentioned that the binary $Ca_{16}Sb_{11}$ is a semiconducting compound with a gap energy of 0.46(2) eV, as demonstrated by Wolfe.[56] In an effort to corroborate and complement Wolfe's findings, the molar susceptibilities of $Ca_{16}Sb_{11}$ (sample C34), $Ca_{16}Bi_{11}$ (I23), $Sr_{16}Sb_{11}$ (K3), $Sr_{16}Bi_{11}$ (L5) and $Ba_{16}Sb_{11}$ (B11) were measured as a function of temperature. Results of these measurements are pictured in Figure III-40, and their molar susceptibilities (χ_M) at 298K are listed in Table III-42. The diamagnetic or nearly diamagnetic behavior of these phases indicates that they indeed are valence compounds, and electron distributions with Pn–Pn bonding interactions should be

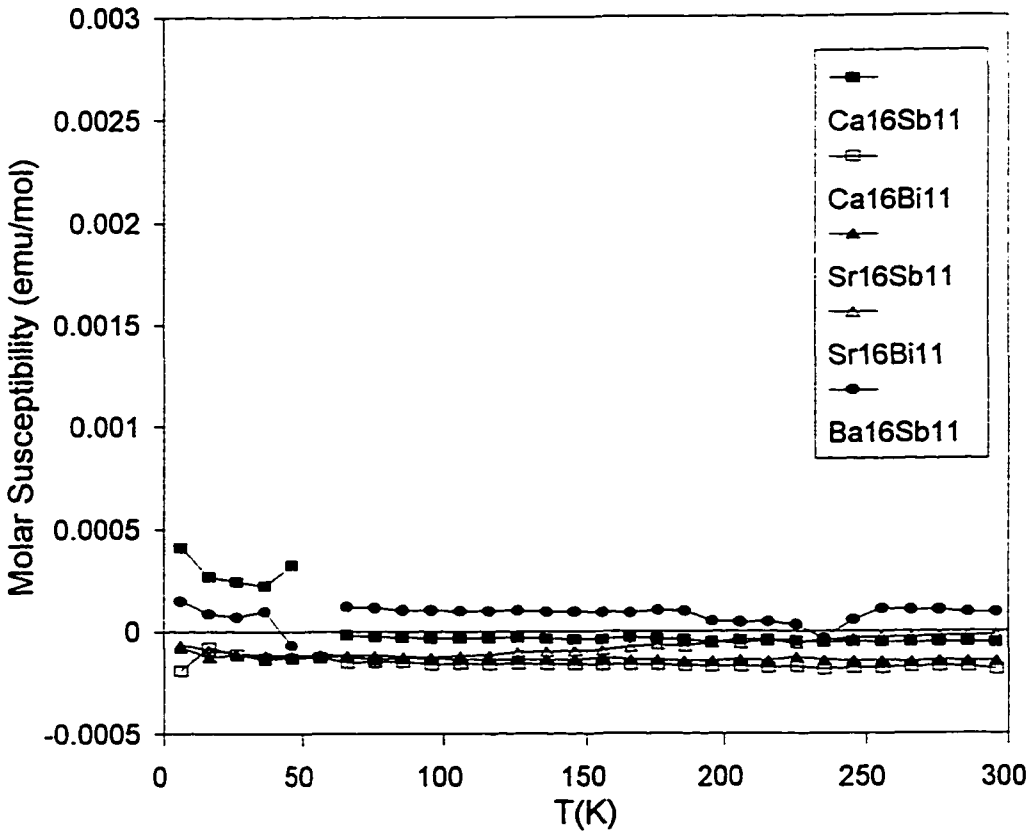

Figure III-40. Temperature dependence of the molar susceptibilities (χ) at 3 Tesla of several T-$Ae_{16}Pn_{11}$ samples prepared under dynamic vacuum.

Table III-42. Molar susceptibilities (χ_M) of $A_{16}Pn_{11}$ compounds at 298K and 3 Tesla

Phase	$\chi_{M(298K)} \times 10^{-6}$ (emu/mol)
$Ca_{16}Sb_{11}$	-54
$Ca_{16}Bi_{11}$	-180
$Sr_{16}Sb_{11}$	-14
$Sr_{16}Bi_{11}$	-16
$Ba_{16}Sb_{11}$	93

considered. Close Sb–Sb contacts in $Ca_{16}Sb_{11}$ are Sb(2)–Sb(2) and Sb(2)–$Sb(1)_{split}$, d= 3.418(3) and 3.617(3) Å, respectively, All other Sb–Sb distances are above 4.04 Å (see Table III-39). Therefore, the Sb(2)–Sb(2) contact should be considered a long distance bonding interaction. Long distance Pn–Pn bonding interactions have already been invoked in other compounds to rationalize their structures and properties. Thus, Eisenmann and coworkers[137] conceived Sb–Sb bonding distances between 2.95 – 3.36 Å to rationalize the structure of $Ca_{11}Sb_{10}$. In another, but not so different case, long Pn–Pn bonding interactions were invoked to rationalize the semiconducting properties of $Ca_{14}AlSb_{11}$-type compounds,[144] e.g. $A_{14}MPn_{11}$, A= Ca, Sr, Ba; M= Mn, Ga; Pn= As, Sb, with a $d_{ave(Sb-Sb)}$= 3.31 Å.[145,146]

In T-$A_{16}Pn_{11}$ compounds, an electron balance is achieved by including one single Sb–Sb per unit cell, i.e., $32A^{2+}$, $20Pn^{3-}$, Pn_2^{4-}. Such an assertion implies that each Pn(2)–Pn(2) contact accounts for half of a single bond interaction. Assumption of all single Sb(2)–Sb(2) bonds in $Ca_{16}Sb_{11}$ would yield an electron-rich compound with a probable metallic-like behavior, $16A^{2+}$, $9Sb^{3-}$, Sb_2^{4-}, e^-. However, single bond Sb–Sb interactions are normally considered for interatomic distances between ~ 2.9 - 3.1 Å,[137-139] e.g., d_{Sb-Sb}= 2.88 Å in Ba_5Sb_4 a Zintl phase with Sb–Sb dimers.[138] The half bonded Sb(2)–Sb(2) interaction in $Ca_{16}Sb_{11}$ is envisioned as a set of statistically

disordered dimers and isolated Sb(2) atoms that account for one single bond per cell. One-electron Sb(2)–Sb(2) interactions would suggest paramagnetic systems otherwise. The speculation of statistically disordered single bonds in $Ca_{16}Sb_{11}$ would be justified by a 2*c* supercell model. In such a model, the troublesome Sb(1) and Sb(2) atoms are ordered and a close contact between Sb(2)–Sb(2) atoms emerges, d= 3.09 Å. Figure III-41 depicts a detail of the refined cell $Ca_{16}Sb_{11}$ and the 2*c* supercell model $Ca_{32}Sb_{22}$ ($32Ca^{2+}$, $30Sb^{3-}$, Sb_2^{4-}). Fractional Pn–Pn bond orders have already been suggested by Alemany et al.[147] in $Ba_7Ga_4Sb_9$. In similarity to $Ca_{16}Sb_{11}$, this ternary antimonide, $Ba_7Ga_4Sb_9$,[148] characteristically has anisotropic Sb atoms (U_{33}/U_{11} ~ 4) that are involved in long contacts, d_{Sb-Sb}= 3.36 Å, and has an odd electron count as well. Alemany, based on theoretical calculations, suggested the presence of a half filled Sb–Sb σ^* band and its implications in possible structural-pairing distortions that may lead to opening of an energy gap at the Fermi level in $Ba_7Ga_4Sb_9$. However, electrical conductivity studies have not been reported for this ternary in order to corroborate such predictions. In a different system, Vaughey and Corbett[149] invoked fractional bonding interactions to justify the hypervalent linear Pn_3^{7-} ion in the $A_{14}MPn_{11}$ compounds. One could speculate that a fractional Sb(2)–Sb(2) bonding contact in $Ca_{16}Sb_{11}$ is a characteristic of the T-type structure, since other $A_{16}Pn_{11}$ compounds behave similarly in their structure and magnetic properties.

Conclusions About the $A_{16}Pn_{11}$ Systems

After numerous experimental efforts and three independent structural refinements, we can conclude that $Ca_{16}Sb_{11}$ crystallizes in its own structure type ($P\bar{4}2_1m$, #113, Z=2). Additionally, phases prepared under sc and dv conditions have equivalent structures. The $Ca_{16}Sb_{11}$ structure type is complex and seems to be inherently pathological. The pathologies of the structure are probably caused by the combined effect of crystal twinning, matrix effects (low packing efficiency) and structural instabilities due to half band filling, as argued above. As an example, matrix effects from large polyhedra of calcium atoms allow Sb(1) and Sb(2) to relax from their positions. Although not mentioned in detail, the combination of these effects was more apparent in crystals

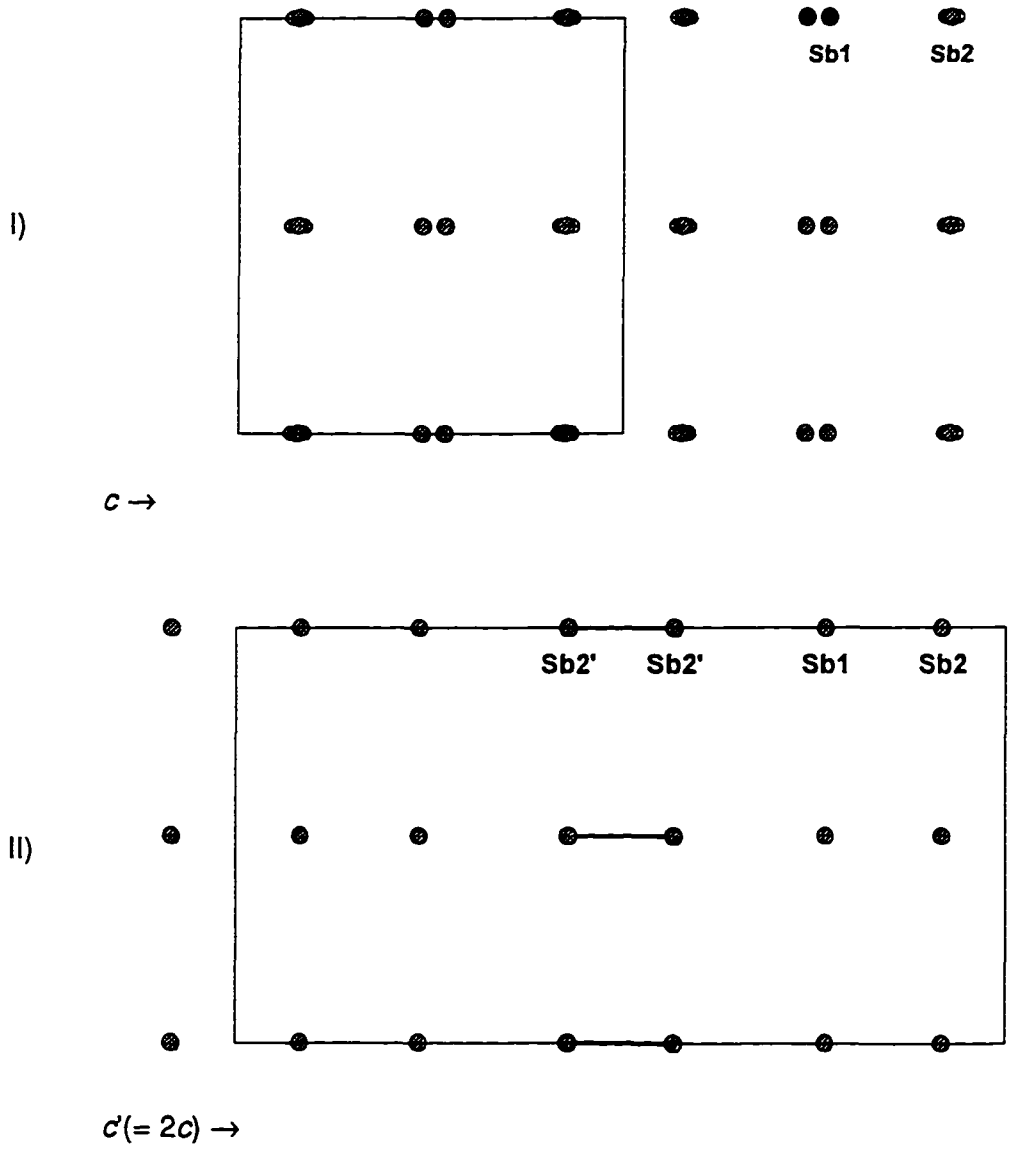

Figure III-41. Detail of (I) refined subcell and (II) 2*c* ordered supercell model structures of $Ca_{16}Sb_{11}$. For clarity, only atoms Sb(1) and Sb(2) are pictured on each cell. Short contact Sb(2)'–Sb(2)' is indicated by a heavy line. Atoms positions Sb(2) and Sb(2)' merge as Sb(2) in the subcell.

of $Eu_{16}As_{11}$, $Ca_{16}Bi_{11}$ and $Sr_{16}Bi_{11}$, where structural solutions were more troublesome. Hydrogen seems not to be involved in the stabilization of these systems, since phases with the T-type phases form under both sc and dv condition with small variations in their lattice parameters. These variations in lattice parameters are probably caused by structural modifications due to hydrogen solubilities or pnictogen deficiencies in these compounds, and they cannot be discerned by Guinier powder patterns except for the $Ca_{16}Bi_{11}$ system, where an orthorhombic modification exists. Table III-43 summarizes the results of the reactions of composition $A_{16}Pn_{11}$. Newly identified phases with the T-type structure are $Ca_{16}As_{11}$, $Ca_{16}Bi_{11}$, $Sr_{16}As_{11}$, $Sr_{16}Sb_{11}$, $Sr_{16}Bi_{11}$, $Ba_{16}Sb_{11}$, $Ba_{16}Bi_{11}$, $Eu_{16}As_{11}$, $Eu_{16}Sb_{11}$, $Eu_{16}Bi_{11}$, $Yb_{16}Sb_{11}$ and $Yb_{16}Bi_{11}$. Several of these phases have probably not been observed in the past because of the obscuring effects of hydrogen in stabilizing ternary hydride compounds.

The phases T-$A_{16}Pn_{11}$ (A= alkaline-earth metal) are diamagnetic and consequently are valence compounds. Such properties support Wolfe's report on the semiconducting $Ca_{16}Sb_{11}$. The closed shell atom configurations in T phases are achieved by statistically disordered Pn–Pn single bonding interactions. Such a disordered single bond is manifested by obtuse thermally anisotropic Pn(2) atoms involved in long Pn(2)–Pn(2) contacts that for closed shell configuration of the compound are considered half bond interactions. Thus, in $Ca_{16}Sb_{11}$ the Sb(2)–Sb(2) long contact, d= 3.418(3) Å, accounts for half of a single bond necessary for a valence composition, i.e., $16Ca^{2+}$, $10Sb^{3-}$, $½Sb_2^{4-}$. This argument is favored by a *2c* supercell model, where single bonds Sb(2)–Sb(2) could occur, d_{calc}= 3.09 Å. ($32Ca^{2+}$, $20Sb^{3-}$, Sb_2^{4-}). Assumption of this electron count justifies the lack of success in our experimental efforts to get ordered structures by change in the electron availability to the system, i.e., reactions $Ca_{16-x}(Na,K,Y,La)_xSb_{11}$. Interestingly, the structural map of earlier Figure III-33 can also be used to predict the structural tendencies of $A_{16}Pn_{11}$ systems. For example, the regions IIa and IIb compress the A–Pn combinations that adopt the T-type structure, implying that T-type structures may be characteristic of divalent metal systems. Region I contains the combination Ba–As for which T-type phase was not found. The map does not predict the structure of the Yb–As phase, and Sm derivatives were not investigated.

Table III-43. Products[a] of reactions $A_{16}Pn_{11}$. Bold entries indicate new phases.

A\Pn	As	Sb	Bi
Ca	**T**	T	**T/DT**
Sr	**T**	**T**	**T(ATP)[b]**
Ba	**ATP**	**T**	**T(ATP)[b]**
Eu	**T**	**T**	**T**
Yb	DATP	**T**	**T**

[a] Products: T= $Ca_{16}Sb_{11}$-type
DT= Distorted $Ca_{16}Sb_{11}$-type (orthorhombic cell)
ATP= Anti-Th_3P_4-type
DATP= Distorted anti-Th_3P_4-type (rhombohedral cell)

[b] Phases with the a-Th_3P_4-type structure were identified for first time for the Sr–Bi and Ba–Bi combinations.

As ending comments, the finding of T phases suggest that exploratory chemistry can still provide with new phases and structures in what are considered thoroughly investigated binary systems. Our current knowledge about some of the stabilizing effects of hydrogen may help us to better design reactions in exploratory solid state chemistry of alkaline-earth-metal pnictide compounds. The existence of new phases in these systems is shown with the binary $Ca_{11}Sb_{9+x}$ (DH) that was found through unsuccessful reactions with ternaries $Ca_{16-x}(Na,K,Y,La)_xSb_{11}$ (see Appendix A). Importantly, this primitive tetragonal structure was probably overlooked by earlier authors because of its similarity to $Ca_{11}Sb_{10}$ ($Ho_{11}Ge_{10}$-type). This DH-type structure was identified in the Ca–Bi, Sr–Sb and Sb–Bi systems as well. Existence of a new phase was also evident in the $Ca_{16}Bi_{11}$ system, where a probable low temperature orthorhombic modification was found; unfortunately, crystals of minimum quality were not obtained (see Appendix B).

New phases in the alkaline-earth-metal–pnictogen systems are not only of prime

interest for Dr Corbett's group. For instance, von Schnering's group in Germany has recently found a series of new Ae_4Pn_3[150,151] (Ae= alkaline-earth metal) phases that crystallize in the orthorhombic Ba_4P_3 structure type (Pbam, #55, Z=4)[150], This structure type seems to exist in the Sr–Sb system as well. Interestingly, in our initial efforts to prepare the $Sr_{16}Sb_{11}$ phase a reaction (K2) was unintentionally loaded Sr-deficient. The source of Sr metal was an old batch of the reagent that probably was contaminated. The components of the reaction K2 were heated under similar conditions to reaction I1 for $Ca_{16}Bi_{11}$, i.e., long annealing at 900°C followed by quenching to room temperature (see Table III-40) which gave $Sr_{11}Sb_{10}$ ($Ho_{11}Ge_{10}$-type) as the major phase product and a new ternary compound in low yield, ~15 %. Well faceted crystals of this second phase were picked up and its structure solved by means of single crystal film techniques and x-ray diffraction refinement. A remarkable structure with formula $Sr_{32}Sb_{24}Z$ was solved. This new phase crystallizes in its own structure type (Pmmn, #59, Z=2) and exhibits isolated and dimeric antimony atoms as features. Experimental efforts to reproduce the phase in high yield, as a binary (Sr_4Sb_3), a ternary hydride ($Sr_{32}Sb_{24}H_2$), a ternary fluoride ($Sr_{16}Sb_{12}F$) and a ternary oxide ($Sr_{32}Sb_{24}O$), were unsuccessful. Significantly, the results of these unsuccessful experiments seem to contradict some of the later findings in von Schnering's group, since Ae_4Pn_3 phases with the Ba_4P_3-type structure were never observed in this work. Some details about this remarkable $Sr_{32}Sb_{24}Z$ structure are given in Appendix C.

CHAPTER IV. TETRELIDE AND TRIELIDE SYSTEMS

$A_5Tt_3H_x$ and $A_5Tr_3H_x$ Systems

Introduction

Discrepancies between previous reports on the alkaline-earth-metal tetrelides, A_5Tt_3 (A= Ca, Sr, Ba; Tt= Si, Ge, Sn Pb), and results obtained in this laboratory[152] motivated us to explore the possibility of hydrogen-stabilized phases in these already well studied systems.[108] Before this work was initiated, it was known that A_5Tt_3 phases would form in the tetragonal Cr_5B_3-type structure (C) for the Ca–Si, Ca–Sn, Ca–Ge, Sr–Pb, Ba–Sn and Ba–Pb combinations;[24,108] the Sr_5Si_3,[153] Ba_5Si_3[154] and Ca_5Pb_3[155] phases would form their own structure types (referred in this work as S, B and MS, respectively). The former two phases are lower symmetry distortions of the C-type structure, where in the case of the S-type structure, the parent phase was the only report. Because of the structural similarities among the C, S and B structures, one cannot easily differentiate one from another by powder patterns techniques. The Ca_5Pb_3-type (MS) structure was recognized as a $\sqrt{3}a$ superstructure deformation of the Mn_5Si_3-type structure; however, further studies in this system suggested that a $Ca_{5.67}Pb_3$ ($Ca_{17}Pb_9$) formed instead.[53] Interestingly, compounds with ~A_5B_3 stoichiometries were known for the Ca–(Si,Ge,Pb) combinations but not for Ca–Sn, where a $Ca_{31}Sn_{20}$ composition in the tetragonal $Pu_{31}Pt_{20}$-type (P) was normally observed.[156] Ganguli et al.[152] in an attempt to prepare the missing Ca_5Sn_3 phase demonstrated that the P-type phase would indeed form when compositions close to Ca_5Sn_3 were loaded; albeit, a C-type structure was anticipated. In contradiction to previous reports, they also found that P-type structures would form when Sr_5Pb_3 compositions were loaded.

Because of the ambiguity between previous and current structural identifications for some A_5Tt_3 systems, we decided to investigate on the absent C-Ca_5Sn_3 phase. The Cr_5B_3-type structure (I4/mcm, sp.gr. No.140, Z=4)[156] has been elegantly described earlier in terms of coordination polyhedra of its individual atoms.[158,159] However, we have preferred the structural description reported by Zhao et al.[160] because it can be extrapolated to describe its lower symmetry structural variations, i.e., the S and B types. In such a description, the C-type structure, say for Ca_5Si_3, can be seen as made of two

types of layer-sections in a 1:1 intergrowth of U_3Si_2[161] and $CuAl_2$[162] like structures. Characteristically each layer contains isolated and dimers of Si(or B) atoms, as pictured in Figure IV-1. The [001] view of the U_3Si_2-like section at z= 0, ½ depicted in Figure IV-2 contains Si dimers inside bicapped face-sharing trigonal prisms of Ca(Cr) atoms and Ca centered cubes. The $CuAl_2$-like section at z= ¼, ¾ is pictured in Figure IV-3 and contains Si centered square antiprisms of Ca that form tetrahedral cavities of Ca in their interconnections. The cubes and antiprisms of these two portions share faces and alternate along 0,0,z and ½,½,z.

One important and often overlooked feature of the C structure is the tetrahedral cavities that by proper atom insertion may lead important interstitial chemistry in this structure type. In fact, Guloy and Corbett were able to incorporate oxygen and nitrogen in these cavities and stabilize the $La_5Pb_3(O,N)$ in a C-related structure;[163] the La inside the cubes (Figure IV-2) is disordered on its position. Absence of the interstitial atom leads to the M-La_5Pb_3 phase instead. These oxygen and nitrogen stabilized phases hint at the possibility of hydrogen involvement in the A_5Tt_3 systems. Significantly, C-A_5Tt_3 phases are classical examples of Zintl phases ($5A^{2+}$, Tt_2^{6-}, Tt^{4-}), and the existence of A_5Tt_3H compounds would suggest electron deficient species ($5A^{2+}$, Tt_2^{4-}, Tt^{6-}, H^-) challenges to the Zintl concepts.

The $Ca_{31}Sn_{20}$ structure ($Pu_{31}Pt_{20}$-type, I4/mcm, Z=4)[164] is quite a bit more complex and has as features isolated atoms, dimers and linear pentamers of Sn. Figure IV-4 shows the [100] view of half of the cell of $Ca_{31}Sn_{20}$ where the short Sn–Sn contacts are highlighted as heavy lines. This structure was already elegantly described as an intergrowth of W_5Si_3 and distorted Gd_3Ga_2 types by Ganguli et al.[152] They also demonstrated that $Ca_{31}Sn_{20}$, a structural Zintl phase ($31Ca^{2+}$, $5Sn^{4-}$, $5Sn_2^{6-}$, Sn_5^{12-}), is a semiconducting and diamagnetic compound.

The experimental efforts in this work were initially focused on the absent Ca_5Sn_3 phase and subsequently extended to other $A_5Tt_3(H,F)_x$ combinations (A= Ca, Sr, Ba, Sm, Eu, Yb; Tt= Si, Ge, Sn, Pb). Electrical resistivity and magnetic studies were performed on several systems in an attempt to establish structure–properties relationships.

Because a large fraction of the single crystal solutions performed in this work

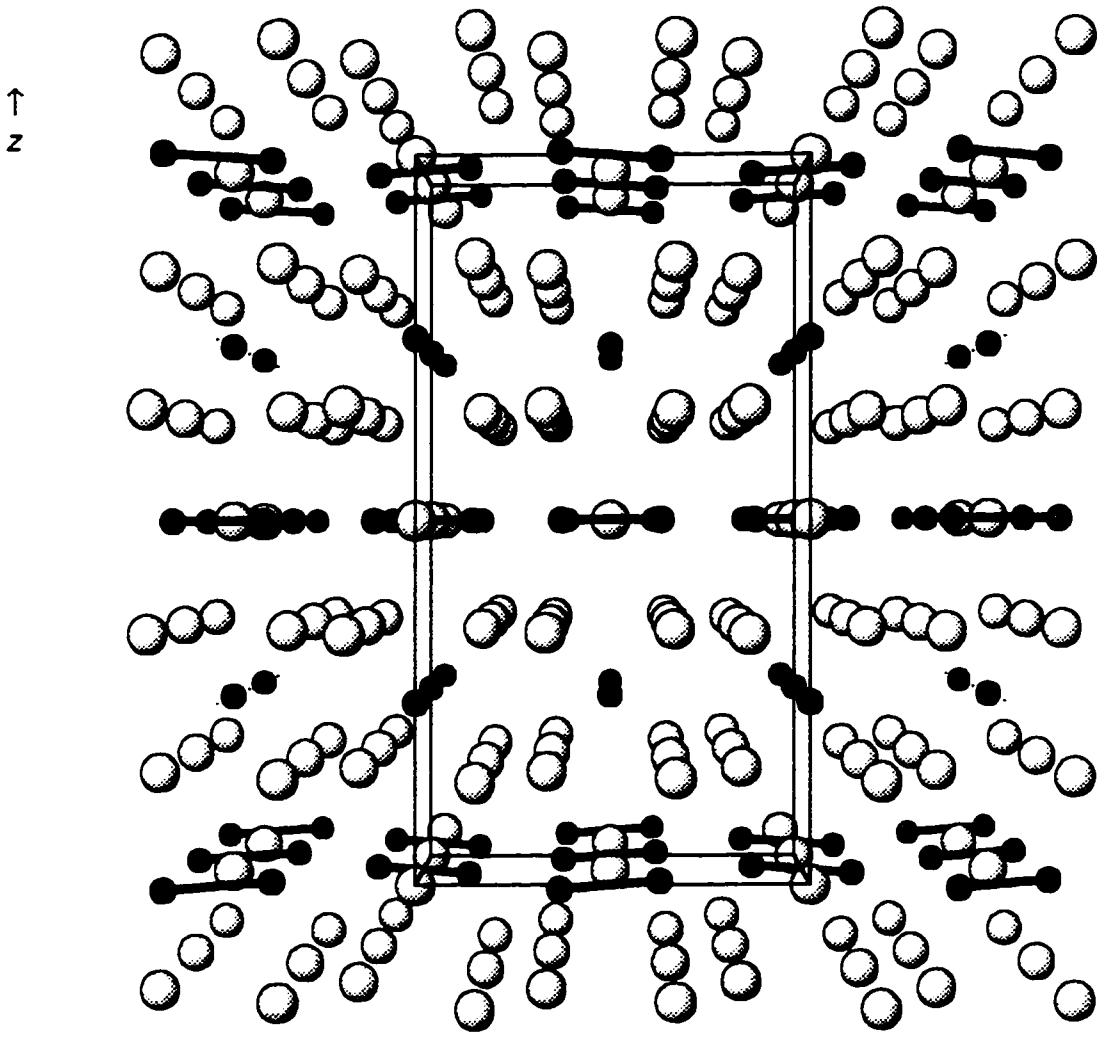

Figure IV-1. Extended [010] view of the Ca_5Si_3 structure (Cr_5B_3-type). Small and large spheres represent Si(B) and Ca(Cr) atoms, respectively. Short Si–Si contacts are emphasized as heavy lines.

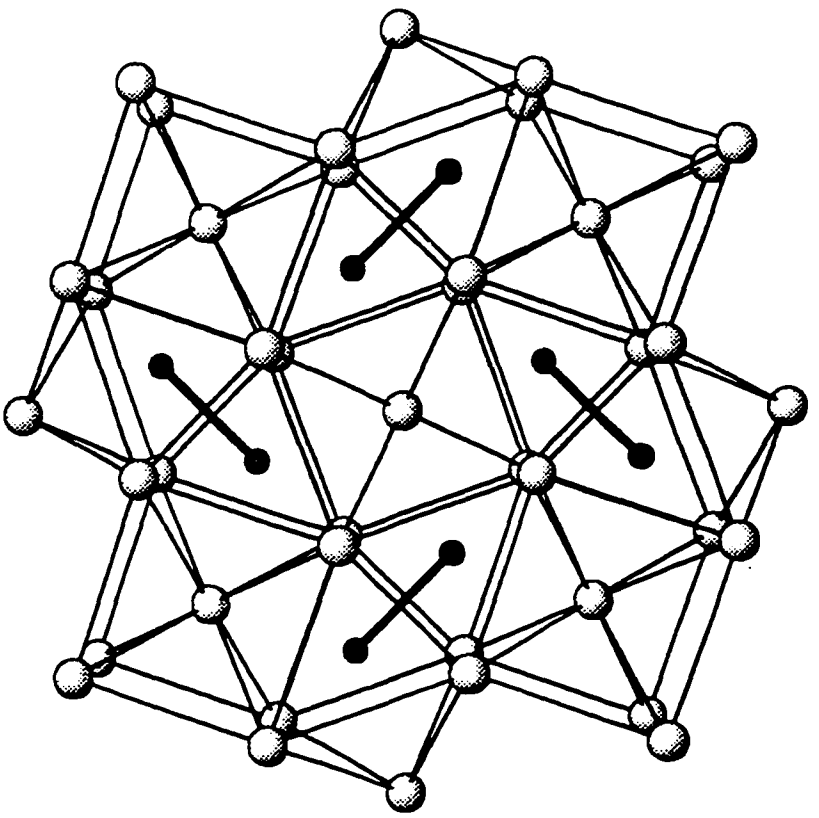

Figure IV-2. The [001] section of the Ca_5Si_3 structure with the U_3Si_2-like structure at z~ 0, ½. Small and large spheres represent Si and Ca atoms, respectively. Lines between Ca atoms do not represent bonds. Short Si–Si contacts are illustrated as heavy lines.

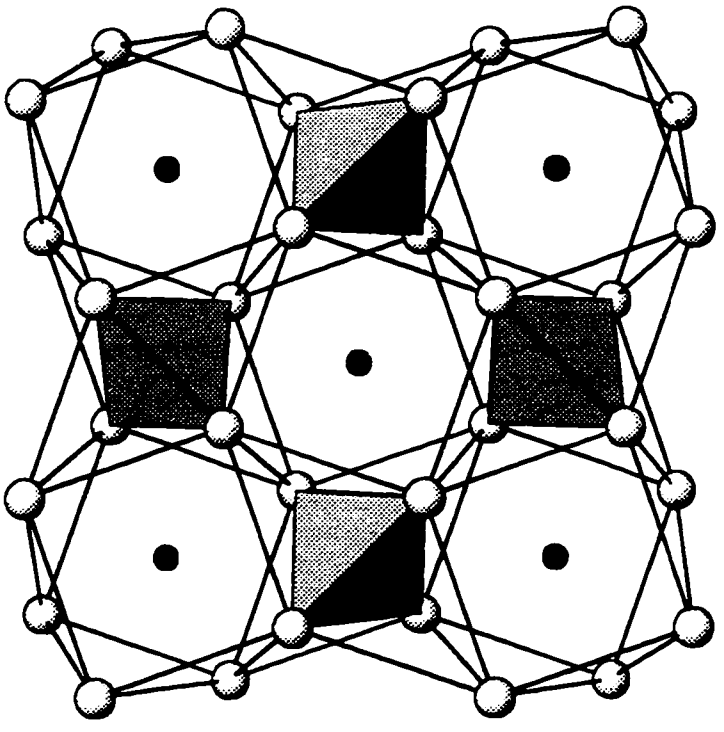

Figure IV-3. The [001] section of the Ca_5Si_3 structure with $CuAl_2$-like structure at z~ 1/4, 3/4. Small and large spheres represent Si and Ca atoms, respectively. The tetrahedral cavities are emphasized as shaded polyhedra.

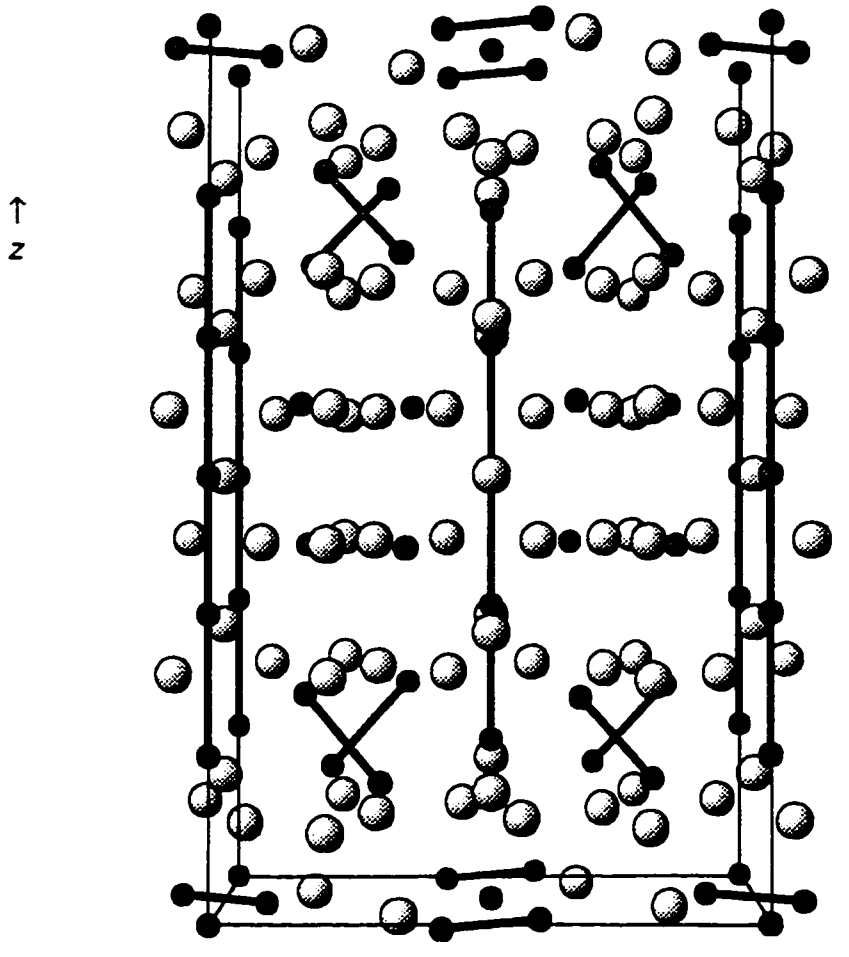

Figure IV-4. Perspective [100] view of ca. half of the $Ca_{31}Sn_{20}$ cell in the $Pu_{31}Pt_{20}$-type structure. Small and large spheres represent Sn and Ca atoms, respectively. Short Sn–Sn contacts are emphasized as heavy lines.

correspond to isomorphic compounds, they will only be discussed when special characteristics need interpretations or because of their novelty. Cases where the customary structural analysis were purposely not discussed are indicative that satisfactory solutions were achieved, and that interatomic distances and coordination spheres were within expected values or geometries.

Results and Discussion

$Ca_5Sn_3(H,D,F)_x$ systems

The reaction between Ca and Sn in presence of hydrogen excess, rxn T21 in Table IV-1, gave in high yield products with the targeted C-type structure, while reactions in the absence of hydrogen gave P-type products instead, rxn T53. These results showed that the previously unobserved C-Ca_5Sn_3H is a hydrogen-stabilized compound. The minor phase in the ternary reaction T21 was the orthorhombic CaSn in the CrB-type structure (labeled as OCB, Cmcm, sp.gr. #63),[165] which was identified for first time. Reactions with variable hydrogen content, rxns T66 to T70, gave mixtures of P and C type phases with a consistent increment of the latter phase as the amount of loaded hydrogen was increased as well. The lattice parameters of the C-type phases in reactions T68 – T70 and T21 do not vary significantly, see the values reported in Table IV-2. A 0.11% cell volume change was calculated between the products of reactions T68 and T21. Such a small cell volume change was considered indicative of a possible narrow stoichiometry range of hydrogen content in the ternary hydride, possibly close to the stoichiometric, $Ca_5Sn_3H_x$, x~1. Experiments to test if the C-phase would form for off-stoichiometric compositions, rxns T54 and T55 loaded $Ca_5Sn_{3.3}$ and $Ca_5Sn_{2.7}$, respectively, and carried under dv conditions gave only mixtures of CaSn and $Ca_{31}Sn_{20}$ phases.

The structure of a crystal from reaction T21 was successfully solved in the Cr_5B_3-type structure. The crystallographic and refined data information of the $Ca_5Sn_3H_x$ structure are reported in Tables IV-3, IV-4 and IV-5. Interestingly, when the refinement was finished, a peak of ~ 2 $e^-/Å^3$ at 0,½,¼, where hydrogen should be located, remained in the Fourier difference map. The distance between this peak, the center of the

Table IV-1. Distribution of products for reactions $Ca_5Sn_3(H,D,F)_x$.

Rxn. No.	Loaded Composition[a]	Conditions[b]		Product Distribution[c]
T53	Ca_5Sn_3	i	dv	P ~90%, OCB ~5%, Ox
T66	$Ca_5Sn_3H_{0.0}$	i	sc	P >85%, OCB ~10%, Ox
T67	$Ca_5Sn_3H_{0.25}$	i	sc	P ~60%, C ~20%, OCB ~15%, Ox
T68	$Ca_5Sn_3H_{0.5}$	i	sc	P ~50%, C ~40%, OCB ~5%, Ox
T69	$Ca_5Sn_3H_{1.0}$	i	sc	P ~25%, C ~65%, OCB ~5%, Ox
T70	$Ca_5Sn_3H_{1.5}$	i	sc	P ~5%, C ~85%, OCB ~5%, Ox
T21	$Ca_5Sn_3H_{2.0}$	i	sc	C ~95%, OCB ~5%
T54	$Ca_5Sn_{3.3}$	i	dv	P ~90%, OCB ~5%, Ox
T55	$Ca_5Sn_{2.7}$	i	dv	P ~60%, CS ~35% OCB ~25, Ox
TF2	Ca_5Sn_3F	ii	dv	C >95%, OCB <5%
TF5	$Ca_5Sn_3F_{1.5}$	i	dv	C ~85%, OCB ~10%, CaF_2
TD2	$Ca_5Sn_3D_x$	iii	dg	C ~95%, OCB ~5%
TO2	Ca_5Sn_3O	ii	dv	P ~ 70%, OCB ~25%, Ox

[a] Reactions denoted $Ca_5Sn_3H_{x.0}$ were loaded with dehydrogenated Ca metal.

[b] Conditions: i) Reaction at 1150°C for 6–8h then 10°C/h to 650°C, followed by cooling to room temperature.
ii) Reaction at 1200°C for 6 h then 10°C/h to 1100°C, kept at 1100°C for 8 h and cooled to 650°C at 10°C/h.
ii) Reaction in two steps; (a) heating at 1000°C for 1 h under vacuum and then reacted with D_2 gas at 1200°C for 6h followed by cooling to 850°C at 5°C/h. Kept at 850°C for 3 days then 10°C/h to 650°C.
sc = Reaction in a sealed fused silica container.
dv = Reaction under dynamic vacuum.
dg = Reaction under constant pressure of deuterium gas.

[c] Estimated from Guinier powder patterns. P= $Pu_{31}Pt_{20}$-type, C= Cr_5B_3-type, OCB= CrB-type (orthorhombic), CS= Co_2Si-type, Ox= Ca_3SnO (Ca_3PbO-type).

Table IV-2. Lattice dimensions of the $Ca_5Sn_3(H,D,F)_x$ compounds.

Rxn No.	Loaded Comp.	Str.Type/ Conds.[a]	a (Å)	c (Å)	Vol.(Å^3)	a/c	Ref.
	$Ca_{31}Sn_{20}$	P/sc	12.542	40.00	6292.1	0.314	156
	$Ca_{31}Sn_{20}$	P/sc	12.5267(5)	39.912(7)	6263(2)	0.314	152
T68	$Ca_5Sn_3H_{0.5}$	C/sc	8.1458(4)	15.082(3)	1000.8(2)	0.540	
T69	$Ca_5Sn_3H_{1.0}$	C/sc	8.1433(6)	15.096(4)	1001.1(3)	0.539	
T70	$Ca_5Sn_3H_{1.5}$	C/sc	8.1433(5)	15.106(4)	1001.7(3)	0.539	
T21	$Ca_5Sn_3H_{2.0}$	C/sc	8.1472(3)	15.093(2)	1001.9(1)	0.540	
TF2	$Ca_5Sn_3F_{1.0}$	C/dv	8.1331(4)	15.175(2)	1003.8(1)	0.536	
TF5	$Ca_5Sn_3F_{1.5}$	C/dv	8.1325(4)	15.155(2)	1002.3(1)	0.537	
TD2	$Ca_5Sn_3D_x$	C/dg	8.1450(3)	15.073(1)	999.97(9)	0.540	
TD2[b]	$Ca_5Sn_3D_x$	C/dg	8.1437(1)	15.0676(4)	999.29(3)	0.540	

[a] Cells indexed for P= $Pu_{31}Pt_{20}$-type and C= Cr_5B_3-type structures.
Conditions: dv= dynamic vacuum, sc= sealed container and dg= reaction with D_2 gas.
[b] Refined by powder neutron diffraction.

Table IV-3. Crystallographic data for $Ca_5Sn_3(H,F)_x$

	$Ca_{4.97(2)}Sn_{3.000(3)}(H_x)$	$Ca_{5.004(6)}Sn_{3.000(2)}F_{0.89(1)}$
Crystal from rxn.	T21	TF2
Space Group	I4/mcm (#140)	I4/mcm
Lattice parameters[a]		
a (Å)	8.1472(3)	8.1331(4)
c (Å)	15.093(2)	15.175(2)
Volume (Å^3)	1001.9(1)	1003.8(1)
Z	4	4
Density calc. (g/cm^3)	3.703	3.807
Crystal dimensions (mm)	0.18x0.26x0.30	0.20x0.20x0.24
Diffractometer	Enraf-Nonius CAD4	Enraf-Nonius CAD4
Collected octants	h,±k,l	-h,k,±l
Scan type	ω	ω-2θ
2θ limit (°)	56	56
Transmission range	0.881–1.083	0.922–1.130
Absorption coefficient (cm^{-1})	98.8	98.8
Number of reflections		
Measured (observed[b])	2658(1038)	2754(1125)
Independent (observed[b])	1105(423)	958(130)
R_{ave} (%)[c]	3.32	2.99
No. of refined variables	18	21
R/R_w (%)	1.7/1.9	1.4/1.5
Goodness of fit	1.442	1.388
Secondary extinction coeff. (x 10^{-8})	7(2)	47(2)
Max./min. peak in ΔF map (e$^-$ Å^{-3})	1.90/-0.58	0.64/-0.52

[a] Lattice parameters calculated from Guinier powder patterns.
[b] Observed reflections; $I \geq 3\sigma_I$.
[c] All data $I > 0$.

Table IV-4. Refined positional and thermal parameters for $Ca_5Sn_3(H,F)_x$ phases in stuffed-Cr_5B_3-type structure.

Atom[a]	x	y	z	B_{eq}(Å^2)	U_{11}	U_{22}	U_{33}	U_{12}	U_{13}	U_{23}
$Ca_5Sn_3(H_x)$ (T21)										
Ca(1)	0	0	0	1.81(4)	0.0140(5)	U_{11}	0.041(1)	0	0	0
Ca(2)	0.16254(7)	x + ½	0.15156(6)	1.31(2)	0.0181(3)	U_{11}	0.0134(4)	-0.0015(3)	-0.0010(2)	U_{13}
Sn(1)	0	0	¼	1.22(1)	0.0151(2)	U_{11}	0.0162(3)	0	0	0
Sn(2)	0.37401(4)	x + ½	0	1.07(1)	0.0138(2)	U_{11}	0.0130(2)	-0.0001(2)	0	0
(H	0	½	¼)							
$Ca_5Sn_3F_{0.9}$ (TF2)										
Ca(1)	0	0	0	1.62(4)	0.0101(5)	U_{11}	0.042(1)	0	0	0
Ca(2)	0.16222(6)	x + ½	0.15082(4)	1.21(1)	0.0159(2)	U_{11}	0.0141(3)	-0.0001(3)	-0.0030(2)	U_{13}
Sn(1)	0	0	¼	0.97(1)	0.0117(2)	U_{11}	0.0135(3)	0	0	0
Sn(2)	0.37401(4)	x + ½	0	0.801(8)	0.0102(1)	U_{11}	0.0100(2)	-0.0000(1)	0	0
F[b]	0	½	¼	1.2(1)	0.016(2)	U_{11}	0.015(2)	0	0	0

[a] Wyckoff for Ca(1), Ca(2), Sn(1), Sn(2) and Z(H or F) atom positions are 4c, 16l, 4a, 8h and 4b, and the site symmetries for the same atoms are 4/m, ..m, 422, m.2m and 42m, respectively.
[b] Occupancy refined to 0.89(1).

Table IV-5. Important interatomic distances[a] (Å) in $Ca_5Sn_3(H,F)_x$ structures.

Atom(1) – Atom(2)	$Ca_5Sn_3H_x$	$Ca_5Sn_3F_{0.9}$
Sn(2) – Sn(2) (1x)	2.9034(8)	2.9105(6)
Sn(1) – Ca(1) (2x)	3.7733(5)	3.7939(5)
Sn(1) – Ca(2) (8x)	3.3941(5)	3.3990(4)
Sn(2) – Ca(1) (2x)	3.2154(2)	3.2071(2)
Sn(2) – Ca(2) (2x)	3.342(1)	3.3381(8)
Sn(2) – Ca(2) (4x)	3.2935(8)	3.2921(6)
Ca(1) – Ca(2) (8x)	3.8138(6)	3.8114(5)
Ca(2) – Ca(2) (1x)	3.591(2)	3.732(1)
Ca(2) – Ca(2) (1x)	3.746(2)	3.625(1)
Ca(2) – Ca(2) (2x)	3.981(2)	4.003(1)
Ca(2) – Ca(2) (4x)	4.3157(4)	4.3099(4)
Ca(2) – Z	2.3906(9)[b]	2.3972(7)

[a] Distances < 4.5 Å.
[b] Refining H as fractional He.

tetrahedral hole, to the surrounding Ca atoms is 2.3906(9) Å and slightly larger than the anticipated for Ca–H from the sum of crystal radii for Ca^{2+} (1.14 Å)[62] and H^- (1.10 Å).[57] The Sn(2)–Sn(2) dimer distance of 2.9034(8) Å is shorter than the Sn–Sn distances in the Zintl phase $Ca_{31}Sn_{20}$, d = 3.063(4) – 3.158(2) Å. Distances Ca–Sn and Ca–Ca are above 3.21 and 3.59 Å, respectively, and typical of intermetallic compounds.[152]

In an effort to further prove that hydrogen was truly located in the interstitial position, the fluoride and deuteride derivatives $Ca_5Sn_3(F,D)_x$ were prepared in reactions TF2 and TD1, respectively, and their structure characterized by single crystal X-ray and powder neutron diffraction techniques. Crystallographic and refined data information of the $Ca_5Sn_3F_{0.89(1)}$ structure are given in Tables IV-3, IV-4 and IV-5. Corroborating the information obtained for $Ca_5Sn_3H_x$ (T21), the results of this latter structural solution

indicated that the fluoride ions are located at 0,½,¼, inside the tetrahedral cavities, see Figure IV-5. Other features of the ternary fluoride structure are a short Sn(2)–Sn(2) interatomic distance, d= 2.9105(6) Å, and the rather anisotropic Ca(1) atom, U_{33}/U_{11} ~4, that is positioned at 0,0,0. Attempts to split this position to 00,±z did not improve the statistics of the solution; however, this is probably caused by its irregular octahedral coordination of Sn atoms, and can additionally be considered a feature of the structure. In actuality, both the Sn(1) and Ca(1) atom positions in $Ca_5Sn_3F_{0.9}$ located at 0,0,z and ½,½,z have characteristically larger isotropic thermal parameters when compared to those of Sn(2) and Ca(2), which are caused by their more relaxed octahedral and bicapped square antiprismatic coordination environments, respectively, depicted in Figure IV-6. Recently, Pöttgen and Simon[166] in describing the structure of C-$Eu_5Ge_3(H_x)$, a ternary hydride according to our results on the same system, noticed the large anisotropic Eu ion at 0,0,0, U_{33}/U_{11} ~4.9, and after several experimental and refinement attempts concluded that this atom characteristically has a static disorder along z. Guloy and Corbett encountered a similar problem in La_5Pb_3O;[163] however, in their case the splitting of the troublesome atom position resulted in a improvement of the solution statistics; a 0.33 Å distance was calculated between the split atom positions. Therefore, the structure of the ternary oxide La_5Pb_3O is a distortion variant of the C-type. Refinement of the atom occupancies in the ternary fluoride structure gave a formula $Ca_{4.97(2)}Sn_{3.000(3)}F_{0.89(1)}$ for the crystal that supports the assumptions about the hydrogen content in $Ca_5Sn_3H_x$ phases as near stoichiometry, x ~1.

The results of the powder neutron diffraction refinement further supported the information gathered from single crystal refinements, i.e., the D(H) atoms are located inside the tetrahedral interstices. The results of this refinement are given in Tables IV-6 and IV-7. Figure IV-7 shows the observed and calculated values of the profiles and the difference between them, where the calculated profiles include the simultaneous two-phase refinement of Ca_5Sn_3D and the impurity phase CaSn from reaction TD1. Refinement of the D occupancy did not improve the statistics; therefore it was restrained to 1 or full occupancy. The absence of D in the refinement leads to unacceptable residuals, R_p/R_{wp} = 11.07/15.27 %. The minor phase CaSn (OCB-type) does not contain

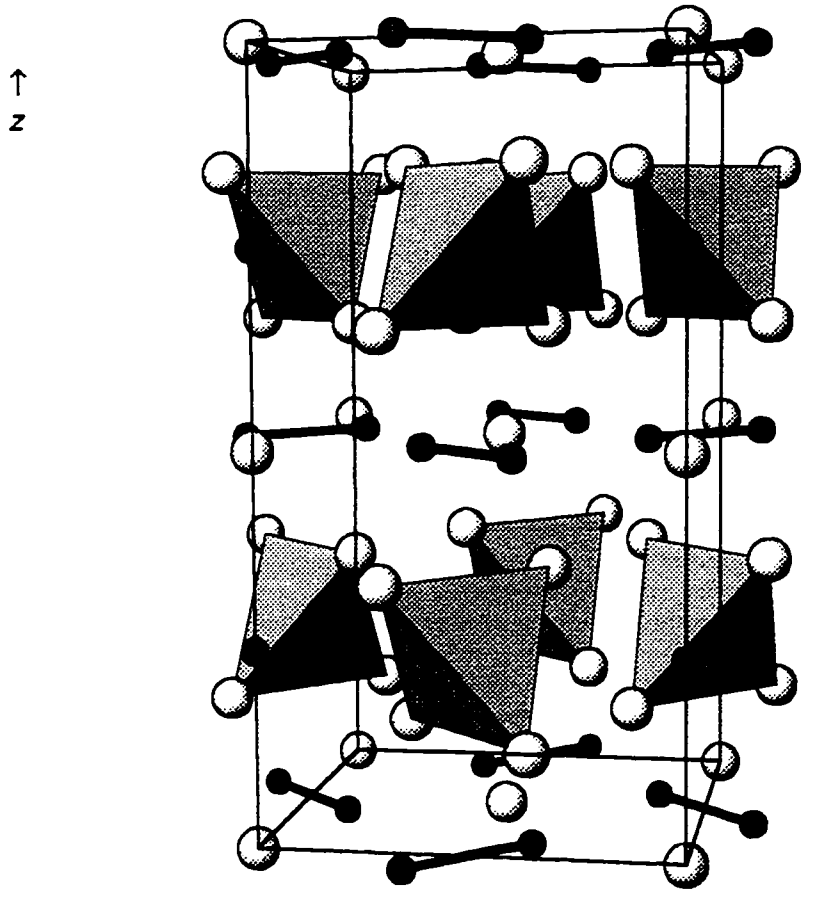

Figure IV-5. Perspective view ca. [100] of the $Ca_5Sn_3F_{0.9}$ structure. Small and large spheres represent Sn and Ca atoms, respectively. Interstitial atoms F^- are located at the center of the tetrahedral cavities which are highlighted as shaded polyhedra. Short Si–Si contacts are illustrated as heavy lines.

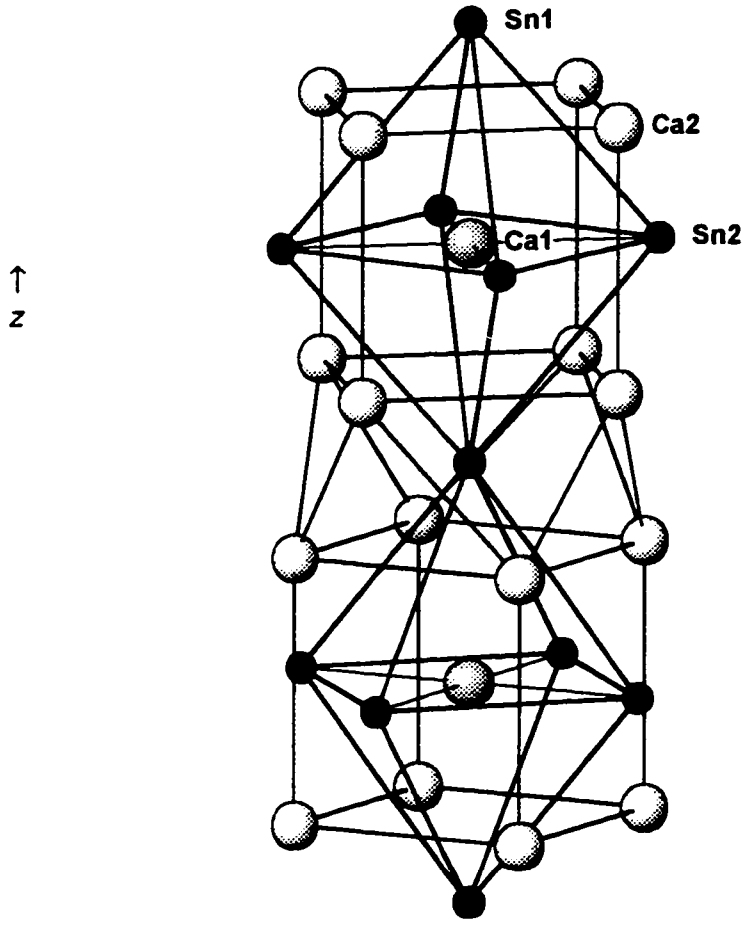

Figure IV-6. Detail section of the $Ca_5Sn_3F_{0.9}$ structure (Cr_5B_3(Z)-type) and the polyhedra surrounding Sn(1) and Ca(1). Lines between atoms do not represent bonds. Ca(1)–Sn distances below 3.5 Å are denoted by thin lines.

Table IV-6. Neutron crystallographic data for Ca_5Sn_3D and CaSn.

	Ca_5Sn_3D	CaSn (Impurity phase)
Sample from rxn.	FD2	
Space group	I4/mcm (#140)	Cmcm (#63)
Lattice parameters		
a (Å)	8.1437(1)	4.8122(5)[a]
b (Å)		11.539(1)
c (Å)	15.0676(4)	4.3483(4)
Volume ($Å^3$)	999.29(3)	241.45(3)
Density calc. (g/cm^3)	3.712	4.368
Experimental temperature (K)	298	
Neutron wavelength (Å)	1.4177	
Refined 2θ region (°)	10 – 140	
Total number of points	2424	
Number of variables	22	
Component fraction	0.54(8)	0.46(8)
Weighted fraction (mol %)	80.2	19.8
R_p (%)	5.29	
R_{wp} (%)	6.71	
Reduced χ^2	1.954	
Final maximum atom shift	0.00	

[a] Guinier lattice parameters for CaSn (rxn T76) are; a= 4.8121(5), b= 11.544(1), c= 4.3502(4) Å and vol= 241.65(5) $Å^3$.

Table IV-7. Refined neutron data atom positions and isotropic thermal parameters of Ca_5Sn_3D and CaSn.

Atom	x	y	z	U_{iso}·100	Occupancy
Ca_5Sn_3D (stuffed Cr_5B_3-type)					
Ca(1)	0	0	0	2.2(1)	1.00
Ca(2)	0.1605(3)	x + ½	0.1521(2)	1.20(7)	1.00
Sn(1)	0	0	¼	0.9(1)	1.00
Sn(2)	0.3747(2)	x + ½	0	0.41(6)	1.00
D	0	½	¼	2.2(1)	1.00[a]
CaSn (impurity phase, CrB-type)					
Ca(1)	0	0.1326(9)	¼	2.0(3)	1.00
Sn(2)	0	0.4157(7)	¼	0.7(2)	1.00

[a] Refinement of D occupancy did not result in better statistics for the solution.

hydrogen (deuterium) since its lattice parameters are equivalent to those of a CaSn phase prepared under dv conditions (rxn T76, not included in the tables); a= 4.8121(5), b= 11.544(1) c= 4.3502(4) Å and vol= 241.65(5) $Å^3$, compare with data in Table IV-6.

Attempts to prepare oxygen substituted compound, $Ca_5Sn_3O_{0.5}$ (rxn TO2 in Table IV-1), failed, and gave a mixture of the P, OCB and oxide (Ca_3SnO) phases instead.

Other $A_5Tt_3(H,F)_x$ systems

The experiments in the remaining $A_5Tt_3H_x$ systems (A= Ca, Sr, Ba, Sm, Eu, Yb; Tt= Si, Ge, Sn, Pb) were limited to reactions in presence and absence of hydrogen, and in some instances fluorides. Yields of reaction and estimated product distributions are given in Table IV-8. Discerning among the B, S and C type structures by Guinier powder patterns is not an easy task, it requires of exceptional quality patterns and the

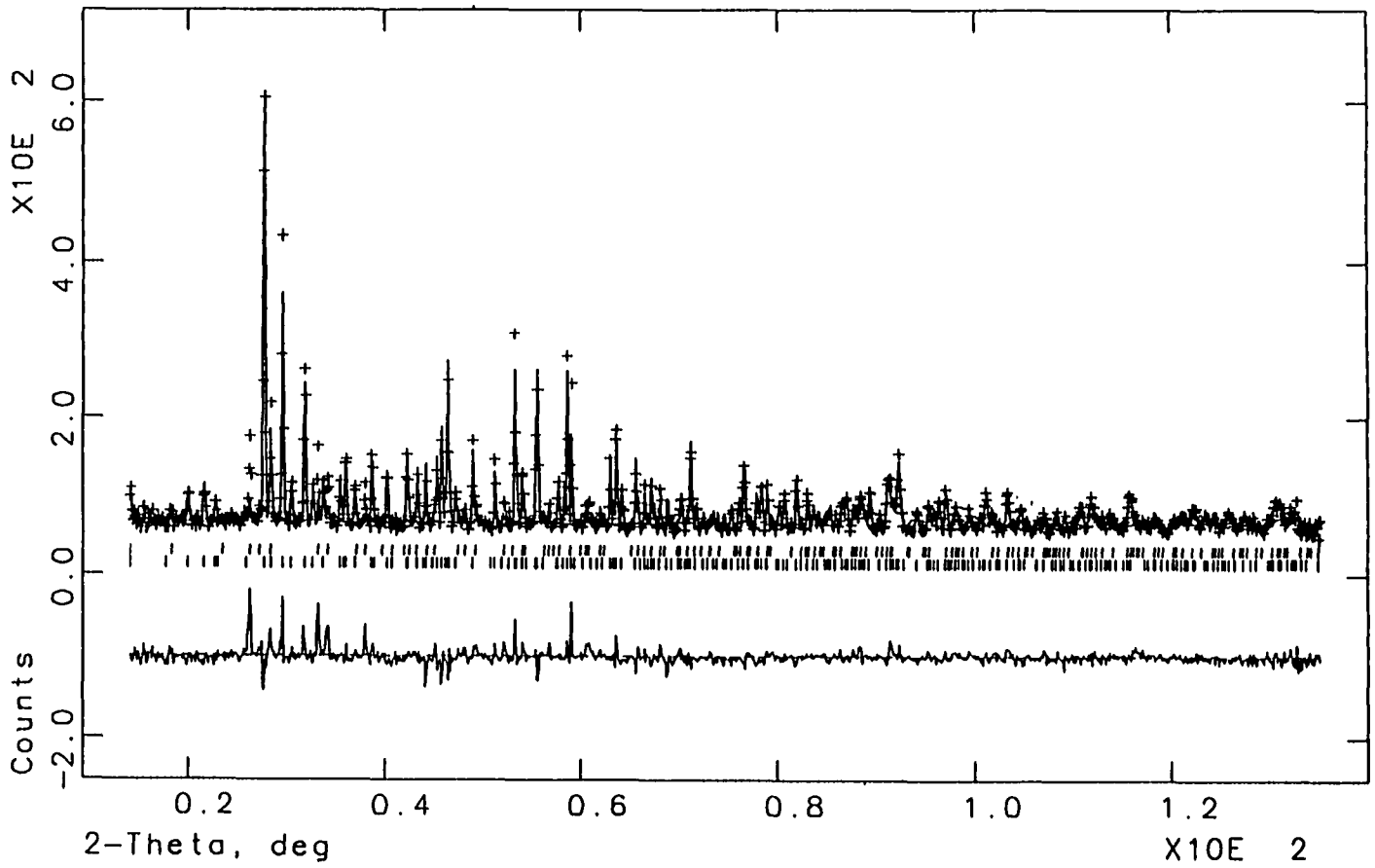

Figure IV-7. Powder neutron diffraction pattern of sample TD1, mixture of Ca_5Sn_3D and CaSn phases. Lines and points represent the calculated and observed values of the profiles, respectively, and the bottom curve indicates the difference between them.

preconception of which lines to look for. The estimated product distribution reported in Table IV-8 was influenced by results from the single crystal refinements, where the S-type structure was not found. Cases in which the product, or part of it, could not be assigned to any binary in the corresponding system are denoted as Un for unknown or UT# when the unknown appeared in other reactions but was first recognized in the reaction T#. Guinier lattice parameters are listed in Table IV-9, where for comparison purposes the previously reported values are included as well.

Silicides

Several binaries A_5Tt_3 phases form in the C-type structure without the need of a third stabilizing element, like Ca_5Si_3, rxns T42 and T62, and can be considered structural examples of Zintl phases. It was necessary to increase the reaction temperature to 1300°C to get high yield of the C-type phase, see Table IV-8. We were able to partially incorporate hydrogen and fluoride in this calcium silicide structure, as established from the ~ 0.88% cell volume decrement calculated between products of reactions T50 (loaded $Ca_5Si_3H_{2.0}$) and T62 (Ca_5Si_3), and from the single crystal solution for the ternary fluoride, rxn TF6 loaded Ca_5Si_3F, where a formula of $Ca_{5.00(3)}Si_{3.000(6)}F_{0.42(1)}$ was refined. Tables IV-10 and IV-11 give the crystallographic and refined data information of the Ca_5Si_3 (T62) and $Ca_5Si_3F_{0.4}$ (TF6) structures. Table IV-12 enlists important interatomic distances in these structures. Important features between these structures, other than the presence of fluoride, are the Si–Si distances that decrease from 2.447(1) to 2.435(2) Å from the binary to the ternary fluoride. A rational about this change in interatomic distances will be given later in this chapter.

The Sr_5Si_3 structure (S, Sr_5Si_3-type, I4cm, sp.gr.#108, Z=4)[153] was earlier recognized as a lower symmetry distortion of the C-type, where the mirror perpendicular to c axis is lost, allowing the troublesome atom at 0,0,0 in the undistorted structure be refined as two independent positions at 0,0,z and 0,0,-z. Nargorsen et al.[153] in their original report on Sr_5Si_3 claimed the existence of this distortion based on Weissenberg and precession film work on a single crystal of the phase. In opposition, we could successfully refine the structure of the silicide in the typical Cr_5B_3-type for a crystal from

Table IV-8. Distribution of products for reactions $A_5Tt_3(H,D,F)_x$.

Rxn. No.	Loaded Composition[a]	Conditions[b]		Product Distribution[c]
Silicides				
T42	Ca_5Si_3	i	dv	C ~60%, CS ~35%, Un
T62	Ca_5Si_3	ii	dv	C ~90%, CS ~10%
T50	$Ca_5Si_3H_{2.0}$	iii	sc	C >95%
TF6	Ca_5Si_3F	ii	dv	C ~75%, CS ~10%, CaF_2 ~15%
T43	Sr_5Si_3	i	dv	C ~75%, CS ~20%, Un
T61	Sr_5Si_3	ii	dv	C ~95%, Un
T51	$Sr_5Si_3H_{2.0}$	iii	sc	C ~100%
T20	Ba_5Si_3	iv	dv	B ~90%, UT20
T60	Ba_5Si_3	ii	dv	B ~80, CS ~15%, UT20
T52	$Ba_5Si_3H_{2.0}$	iii	sc	B >>95%, UT20
TF11	Ba_5Si_3F	ii	dv	B ~80%, BaF_2 ~15%, UT20
TR1	Sm_5Si_3	i	dv	M ~95%
T96	$Sm_5Si_3H_{2.0}$	iii	sc	M ~70%, Un ~30%
TR2	Eu_5Si_3	i	dv	C ~40%, M ~20%, Un
T97	$Eu_5Si_3H_{2.0}$	iii	sc	C ~95%
TR3	Yb_5Si_3	i	dv	M ~20%, OCB ~60%, Un
T98	$Yb_5Si_3H_{2.0}$	iii	sc	M >95%, OCB <5%

Table IV-8. Continued

Rxn. No.	Loaded Composition[a]	Conditions[b]		Product Distribution[c]
Germanides				
T34	Ca_5Ge_3	iii	dv	C ~95%, OCB ~5%
T33	$Ca_5Ge_3H_{2.0}$	iv	sc	C ~100%
TF1	$Ca_5Ge_3F_{1.0}$	i	dv	C >90%, OCB ~5%, CaF_2 <5%
TF4	$Ca_5Ge_3F_{1.5}$	iii	dv	C ~60%, OCB ~30%, CaF_2 ~10%
TO1	Ca_5Ge_3O	i	dv	C ~75%, OCB ~10%, Ox
T35	Sr_5Ge_3	iii	dv	C ~95%, OCB ~5%
T41	$Sr_5Ge_3H_{2.0}$	iii	sc	C ~100%
T36	Ba_5Ge_3	iii	dv	C >>95%
T46	$Ba_5Ge_3H_{2.0}$	iii	sc	C ~95%, OCB ~5%
T37	Sm_5Ge_3	iii	dv	M ~85%, SG ~10%, Un
T47	$Sm_5Ge_3H_{2.0}$	iii	sc	M ~90%, SG ~10%
T38	Eu_5Ge_3	iii	dv	C ~90%, OCB ~10%
T99	$Eu_5Ge_3H_{2.0}$	iii	sc	C ~100%
T59	Yb_5Ge_3	ii	dv	CS ~70%, OCB ~30%
T49	$Yb_5Ge_3H_{2.0}$	iii	sc	M ~100%
Stannides				
T1	Sr_5Sn_3	iv	dv	C >>95%
T23	$Sr_5Sn_3H_{2.0}$	iv	sc	C ~95%, OCB ~5%

Table IV-8. Continued

Rxn. No.	Loaded Composition[a]	Conditions[b]		Product Distribution[c]
T15	Ba_5Sn_3	iv	dv	CS ~65%, OCB ~30%, Ox
T25	$Ba_5Sn_3H_{2.0}$	iv	sc	C ~80%, OCB ~20%, Ox
TF8	Ba_5Sn_3F	iii	dv	C ~80%, OCB ~15%, BaF_2 ~5%
T91	Sm_5Sn_3	iv	dv	M >>95%
T31	$Sm_5Sn_3H_{2.0}$	iv	sc	M ~100%
T17	Eu_5Sn_3	iv	dv	CS ~60%, OCB ~35%
T27	$Eu_5Sn_3H_{2.0}$	iv	sc	C ~90%, OCB ~5%, Un
T3	Yb_5Sn_3	iv	dv	YS ~ 95%, NI ~5%
T85	$Yb_5Sn_3H_{2.0}$	v	sc	YS ~85%, C ~10%, NI ~5%
TD3	$Yb_5Sn_4D_{4.0}$	iii	sc	SG ~80%, C ~15%, GC ~5%
Plumbides				
T6	Ca_5Pb_3	iv	dv	MS ~100%
T79	$Ca_{17}Pb_9$ ($Ca_{5.67}Pb_3$)	iii	dv	CS ~90%, MS >5%, Ox
T22	$Ca_5Pb_3H_{2.0}$	iv	sc	MS ~85%, AC ~20%
TF3	Ca_5Pb_3F	i	dv	MS ~85%, AC ~10%, CaF_2 ~5%
T2	Sr_5Pb_3	iv	dv	P ~95%, OCB ~5%
T24	$Sr_3Pb_3H_{2.0}$	iv	sc	C ~95%, OCB ~5%
TF12	Sr_5Pb_3F	iii	dv	C >95%, OCB
T16	Ba_5Pb_3	iv	dv	WS >95%, Ox
T26	$Ba_5Pb_3H_{2.0}$	iv	sc	WS ~80%, C ~15%, Ox

Table IV-8. Continued

Rxn. No.	Loaded Composition[a]	Conditions[b]		Product Distribution[c]
TF9	Ba_5Pb_3F	iii	dv	WS ~70%, C ~20%, BaF_2 ~5%, Ox
T95	Sm_5Pb_3	iv	dv	M ~100%
T32	$Sm_5Pb_3H_{2.0}$	iv	sc	M ~100%
T10	Eu_5Pb_3	iv	dv	WS ~100%
T28	$Eu_5Pb_3H_{2.0}$	iv	sc	WS ~70%, C ~30%
T4	Yb_5Pb_3	iv	dv	P >95%
T86	Yb_5Pb_3	v	dv	M(S) >95%
T30	$Yb_5Pb_3H_{2.0}$	iv	sc	P >95%
T19	$Yb_5Pb_3H_{2.0}$	vi	sc	M(S) ~100%
T84	$Yb_5Pb_3H_{2.0}$	v	sc	M(S) >95%

[a] Reactions denoted $A_5Tt_3H_{x.0}$ were loaded with dehydrogenated A metal.

[b] Conditions:
- i) Reaction at 1200°C for 6h then 20°C/h to 1100°C, kept at 1100°C for 6h then 10°C/h to 650°C, afterwards the furnace was turned off.
- ii) Reaction at 1300°C for 6h in a high temperature furnace then reduced to 600°C at 8°C/h, then the furnace was turned off.
- iii) Reaction at 1150°C then cooling to 650°C at 10–12 °C/h.
- iv) Similar to (iii) but reaction temperature was 1100°C.
- v) Reaction at 1150°C for 2h then cooled to 900°C at 5°C/h. Annealed at 900°C for 3 days and quenched in an ice–water bath.
- vi) Reaction at 1100°C for 2h then reduced to 825°C at 10°C/h. Annealed at 825°C for 7 days and then quenched in an ice–water bath.

sc = Reaction in a sealed fused silica container.
dv = Reaction under dynamic vacuum.
dg = Reaction under constant pressure of deuterium gas.

[c] Estimated from Guinier powder patterns. C= Cr_5B_3-type, CS= Co_2Si-type, B= Ba_5Si_3-type, M= Mn_5Si_3-type, OCB= CrB-type (orthorhombic), SG= Sm_5Ge_4-type, NI= Ni_2In-type, YS= $Yb_{36}Sn_{23}$-type, MS= Ca_5Pb_3-type (M-superstructure), AC= AuCu-type, P= $Pu_{31}Pt_{20}$-type, WS= W_5Si_3-type, Ox= A_3TtO (Ca_3PbO-type) and Un or UT# as unidentified structures.

Table IV-9. Lattice dimensions of reaction products $A_5Tt_3(H,F)_x$.

Rxn No.	Loaded Comp.[a]	Str.Type/ Conds.[b]	a (Å)	c (Å)	Vol.(Å^3)	a/c	Ref.
Silicides							
	Ca_5Si_3	C/sc	7.64	14.62	853.4	0.522	167
T62	Ca_5Si_3	C/dv	7.6495(4)	14.835(2)	868.1(1)	0.516	
T50	$Ca_5Si_3H_{2.0}$	C/sc	7.6386(3)	14.747(1)	860.50(9)	0.518	
TF6	Ca_5Si_3F	C/dv	7.6354(4)	14.829(2)	864.5(1)	0.515	
	Sr_5Si_3	S/sc	8.055	15.688	1017.9	0.513	153
T43	Sr_5Si_3	C/dv	8.0980(4)	15.707(1)	1030.0(1)	0.516	
T61	Sr_5Si_3	C/dv	8.0966(5)	15.703(2)	1029.9(2)	0.516	
T51	$Sr_5Si_3H_{2.0}$	C/sc	8.0468(4)	15.761(1)	1020.5(1)	0.510	
	Ba_5Si_3	B/sc	8.436(6)	16.53(1)	1176(1)	0.510	154
T20	Ba_5Si_3	B/dv	8.4855(6)	16.421(3)	1182.4(3)	0.517	
T60	Ba_5Si_3	B/dv	8.4837(5)	16.428(1)	1182.3(1)	0.516	
T52	$Ba_5Si_3H_{2.0}$	B/sc	8.4558(4)	16.484(2)	1178.6(1)	0.513	
TF11	Ba_5Si_3F	B/dv	8.4726(2)	16.443(1)	1180.3(1)	0.515	

Table IV-9. Continued

Rxn No.	Loaded Comp.[a]	Str.Type/ Conds.[b]	a (Å)	c (Å)	Vol.(Å^3)	a/c	Ref.
	Sm_5Si_3	M/sc	8.56	6.45	409.3	0.753[c]	168
	Sm_5Si_3	M/sc	8.58(1)	6.48(1)	413(1)	0.755[c]	169
TR1	Sm_5Si_3	M/dv	8.5916(8)	6.4990(9)	415.45(9)	0.756[c]	
T96	$Sm_5Si_3H_2$	M/sc	8.6217(5)	6.3751(8)	410.39(7)	0.739[c]	
TR2	Eu_5Si_3	C/dv	7.919(2)	15.384(6)	964.9(5)	0.515	
T97	$Eu_5Si_3H_{2.0}$	C/sc	7.9052(4)	15.281(2)	954.9(1)	0.517	
	Yb_5Si_3	M/am	8.215	6.28	367.0	0.764[c]	170
	Yb_5Si_3	M/am	8.25(1)	6.19	364.9	0.750[c]	171
TR3	Yb_5Si_3	M/dv	8.252(1)	6.228(2)	367.2(2)	0.755[c]	
T98	$Yb_5Si_3H_{2.0}$	M/sc	8.2815(7)	6.3147(9)	375.06(8)	0.762[c]	
Germanides							
	Ca_5Ge_3	C/sc	7.74(2)	14.66(2)	878(3)	0.527	167
T34	Ca_5Ge_3	C/dv	7.7156(5)	14.885(2)	886.1(1)	0.518	
T33	$Ca_5Ge_3H_{2.0}$	C/sc	7.7218(5)	14.660(2)	874.2(1)	0.527	
TF1	Ca_5Ge_3F	C/dv	7.7093(3)	14.789(2)	879.0(1)	0.521	

Table IV-9. Continued

Rxn No.	Loaded Comp.[a]	Str.Type/ Conds.[b]	a (Å)	c (Å)	Vol.(Å^3)	a/c	Ref.
TF4	$Ca_5Ge_3F_{1.5}$	C/dv	7.7101(3)	14.787(2)	879.0(1)	0.521	
T35	Sr_5Ge_3	C/dv	8.1675(4)	15.730(3)	1049.4(1)	0.519	
T41	$Sr_5Ge_3H_{2.0}$	C/sc	8.1236(5)	15.732(2)	1038.2(2)	0.516	
T36	Ba_5Ge_3	C/dv	8.557(1)	16.465(1)	1205.8(4)	0.520	
T46	$Ba_5Ge_3H_{2.0}$	C/sc	8.5106(5)	16.549(2)	1198.7(2)	0.514	
	Sm_5Ge_3	M/sc	8.65(2)	6.49(1)	420(2)	0.750[c]	172
	Sm_5Ge_3	M/sc	8.653	6.471	419.6	0.748[c]	173
	Sm_5Ge_3	M/sc	8.54(1)	6.52(1)	412(1)	0.763[c]	171
T37	Sm_5Ge_3	M/dv	8.6530(6)	6.5234(8)	423.00(8)	0.754[c]	
T47	$Sm_5Ge_3H_{2.0}$	M/sc	8.6705(3)	6.4237(5)	418.22(4)	0.741[c]	
	Eu_5Ge_3	C/sc	7.990(1)	15.367(1)	981.0(1)	0.520	166
T38	Eu_5Ge_3	C/dv	7.9987(8)	15.380(3)	984.0(2)	0.520	
T99	$Eu_5Ge_3H_{2.0}$	C/sc	7.9853(5)	15.281(2)	974.4(1)	0.522	

Table IV-9. Continued

Rxn No.	Loaded Comp.[a]	Str.Type/ Conds.[b]	a (Å)	c (Å)	Vol.(Å^3)	a/c	Ref.
	Yb_5Ge_3[d]	M/sc	8.360	6.421	388.6	0.768[c]	173
	Yb_5Ge_3	M/dv	8.350(1)	6.407(3)	386.9(2)	0.767[c]	24
T49	$Yb_5Ge_3H_{2.0}$	M/sc	8.3466(5)	6.3995(8)	386.09(7)	0.767[c]	
Stannides							
	Sr_5Sn_3	C/sc	8.54(1)	16.06(2)	1171(3)	0.532	174
	Sr_5Sn_3	C/sc	8.565	16.261	1192.9	0.527	47
	Sr_5Sn_3	C/sc	8.567(2)	16.254(7)	1192.9(8)	0.527	175
T1	Sr_5Sn_3	C/dv	8.5757(8)	16.318(2)	1200.1(2)	0.525	
T23	$Sr_5Sn_5H_{2.0}$	C/sc	8.5694(5)	16.027(3)	1176.9(2)	0.535	
	Ba_5Sn_3	C/sc	9.02(1)	16.78(2)	1365(3)	0.537	174
	Ba_5Sn_3	C/sc	8.959	16.941	1359.7	0.529	47
T25	$Ba_5Sn_3H_{2.0}$	C/sc	8.941(5)	17.037(3)	1364.4(2)	0.525	
TF8	Ba_5Sn_3F	C/dv	8.9470(5)	17.014(3)	1361.9(2)	0.526	

Table IV-9. Continued

Rxn No.	Loaded Comp.[a]	Str.Type/ Conds.[b]	a (Å)	c (Å)	Vol.(Å^3)	a/c	Ref.
	Sm_5Sn_3	M/sc	9.089	6.610	472.9	0.727[c]	24
	Sm_5Sn_3	M/am	9.106(4)	6.651(4)	477.6(5)	0.730[c]	176
T91	Sm_5Sn_3	M/dv	9.1090(7)	6.655(1)	478.2(1)	0.731[c]	
T31	$Sm_5Sn_3H_{2.0}$	M/sc	9.095(1)	6.656(2)	476.8(2)	0.732[c]	
T27	$Eu_5Sn_3H_{2.0}$	C/sc	8.4645(3)	15.589(1)	1116.9(1)	0.543	
	Yb_5Sn_3	M/sc	9.47	6.90	535.9	0.729[c]	177
	Yb_5Sn_3	C/sc	7.939	14.686	925.6	0.540	177
T3	Yb_5Sn_3	YS/dv	12.3869(5)	22.935(1)	3519.0(3)	0.540	
TD3	$Yb_5Sn_4D_{4.0}$	C/sc	8.0952(4)	14.695(1)	963.0(1)	0.550	
Plumbides							
	Ca_5Pb_3	M/sc	9.355	7.004	530.8	0.749[c]	178
	Ca_5Pb_3	MS/sc	16.23(2)	7.04(6)	1606(4)	0.434[c]	155
	$Ca_{17}Pb_9$	MS/sc	16.1618(2)	6.9831(6)	1579.6(1)	0.432[c]	53
T6	Ca_5Pb_3	MS/dv	16.2026(8)	6.9999(9)	1591.5(1)	0.432[c]	

Table IV-9. Continued

Rxn No.	Loaded Comp.[a]	Str.Type/ Conds.[b]	a (Å)	c (Å)	Vol.(Å^3)	a/c	Ref.
T24	$Ca_5Pb_3H_{2.0}$	MS/sc	16.244(4)	7.007(4)	1601(1)	0.431[c]	
TF3	Ca_5Pb_3F	MS/dv	16.235(1)	7.059(2)	1611.2(6)	0.435[c]	
	Sr_5Pb_3	C/sc	8.67	15.94	1198.2	0.544	47
	Sr_5Pb_3	P/sc	13.282(5)	42.698(7)	7532(4)	0.311	152
T2	Sr_5Pb_3	P/dv	13.2839(7)	42.704(4)	7535.8(8)	0.311	
T24	$Sr_5Sn_3H_{2.0}$	C/sc	8.6674(5)	15.932(1)	1196.7(1)	0.544	
TF12	Sr_5Sn_3F	C/dv	8.6579(5)	15.958(2)	1196.2(2)	0.542	
	Ba_5Pb_3	C/sc	9.040	16.816	1364.2	0.538	179
	Ba_5Pb_3	C/sc	9.04(1)	16.943(7)	1385(2)	0.533	180
	Ba_5Pb_3	WS/sc	14.132(7)	6.436(4)	1285(1)	0.455[c]	175
T16	Ba_5Pb_3	WS/dv	14.148(2)	6.4288(9)	1286.8(3)	0.454[c]	
TF9	Ba_5Pb_3F	C/dv	9.0538(5)	16.845(1)	1380.8(2)	0.537	
	Sm_5Pb_3	M/sc	9.170(3)	6.699(3)	487.8(4)	0.730[c]	176
T95	Sm_5Pb_3	M/dv	9.1660(4)	6.7045(6)	487.82(6)	0.731[c]	
T32	$Sm_5Pb_3H_{2.0}$	M/sc	9.1516(6)	6.712(1)	486.8(1)	0.733[c]	

Table IV-9. Continued

Rxn No.	Loaded Comp.[a]	Str.Type/ Conds.[b]	a (Å)	c (Å)	Vol.(Å^3)	a/c	Ref.
	Eu_5Pb_3	WS/sc	13.184(5)	6.214(2)	1080.1(8)	0.471[c]	181
T10	Eu_5Pb_3	WS/dv	13.191(1)	6.205(1)	1079.7(3)	0.470[c]	
T28	$Eu_5Pb_3H_{2.0}$	C/sc	13.196(2)	6.207(2)	1080.9(4)	0.470[c]	
	Yb_5Pb_3	M/sc	9.325(3)	6.929(3)	521.8(4)	0.743[c]	3
T4	Yb_5Pb_3	P/dv	12.5270(8)	40.453(4)	6348.2(9)	0.310[c]	
T86	Yb_5Pb_3	M/dv	9.3600(5)	7.0001(9)	531.17(9)	0.748[c]	
		MS[e]	16.2120(9)	7.0001(9)	1593.3(3)	0.432[c]	
T19	$Yb_5Pb_3H_{2.0}$	M/sc	9.3384(4)	6.9789(8)	527.07(7)	0.747[c]	
		MS[e]	16.1746(7)	6.9789(8)	1581.2(2)	0.431[c]	
T84	$Yb_5Pb_3H_{2.0}$	M/sc	9.3347(4)	6.9846(6)	517.07(6)	0.748[c]	
		MS[e]	16.1682(7)	6.9846(6)	1581.2(2)	0.432[c]	

[a] Reactions denoted $A_5Tt_3H_{x.0}$ were loaded with dehydrogenated A metal.
[b] Cells indexed for C= Cr_5B_3-type, S= Sr_5Si_3-type, B= Ba_5Si_3-type, M= Mn_5Si_3-type, MS= Ca_5Pb_3-type ($Ca_{17}Pb_3$, $\sqrt{3}$a-superstructure) structures.
Conditions: dv= dynamic vacuum, sc= sealed container and am= arc melting.
[c] $(a/c)^{-1}$.
[d] Originally reported as a carbon-stabilized phase, ref 173.
[e] Cell dimensions calculated in $Yb_5Pb_3H_x$ phases for an indeal $\sqrt{3}$a supercell.

Table IV-10. Crystallographic data for $Ca_5Si_3(F_x)$.

	Ca_5Si_3	$Ca_{5.00(3)}Si_{3.000(6)}F_{0.42(1)}$
Crystal from rxn.	T62	TF6
Space Group	I4/mcm (#140)	I4/mcm
Lattice parameters[a]		
a (Å)	7.649(4)	7.6354(4)
c (Å)	14.835(2)	14.829(2)
Volume ($Å^3$)	868.1(1)	864.5(1)
Z	4	4
Density calc. (g/cm^3)	2.178	2.333
Crystal dimensions (mm)	0.12x0.20x0.32	~0.16x0.30x0.36
Diffractometer	Enraf-Nonius CAD4	Enraf-Nonius CAD4
Collected octants	h,-k,±l	-h,-k,±l
Scan type	ω-2θ	ω-2θ
2θ limit (°)	54	54
Transmission range	0.899–1.079	0.870–1.091
Absorption coefficient (cm^{-1})	33.3	33.7
Number of reflections		
Measured (observed[b])	2182(837)	2173(812)
Independent (observed[b])	700(275)	807(130)
R_{ave} (%)[c]	5.55	7.79
No. of refined variables	16	21
R/R_w (%)	1.5/1.9	2.5/2.6
Goodness of fit	1.120	0.946
Secondary extinction coeff. (x 10^{-8})	11.6(9)	14(2)
Max./min. peak in ΔF map ($e^- Å^{-3}$)	0.25/-0.26	0.43/-0.42

[a] Lattice parameters calculated from Guinier powder patterns.
[b] Observed reflections; $I \geq 3\sigma_I$.
[c] All data $I > 0$.

Table IV-11. Refined positional and thermal parameters for $Ca_5Si_3(F)_x$ phases in stuffed-Cr_5B_3-type structure.

Atom[a]	x	y	z	$B_{eq}(Å^2)$	U_{11}	U_{22}	U_{33}	U_{12}	U_{13}	U_{23}
Ca_5Si_3 (T62)										
Ca(1)	0	0	0	1.27(2)	0.0108(3)	U_{11}	0.0267(4)	0	0	0
Ca(2)	0.17978(3)	x + ½	0.13986(2)	1.00(2)	0.0141(2)	U_{11}	0.0099(2)	-0.0008(1)	-0.0005(1)	U_{13}
Si(1)	0	0	¼	1.13(2)	0.0147(3)	U_{11}	0.0134(5)	0	0	0
Si(2)	0.38693(6)	x + ½	0	0.83(2)	0.0109(2)	U_{11}	0.0097(3)	-0.0005(2)	0	0
$Ca_5Si_3F_{0.4}$ (TF6)										
Ca(1)	0	0	0	1.64(3)	0.0127(4)	U_{11}	0.0371(7)	0	0	0
Ca(2)	0.17407(5)	x + ½	0.14386(3)	1.34(2)	0.0178(3)	U_{11}	0.0153(3)	0.0017(2)	-0.0039(1)	U_{13}
Si(1)	0	0	¼	1.27(3)	0.0167(6)	U_{11}	0.0150(7)	0	0	0
Si(2)	0.38724(8)	x + ½	0	0.88(2)	0.0119(3)	U_{11}	0.0096(4)	0.0006(3)	0	0
F[b]	0	½	¼	0.9(1)	0.015(2)	U_{11}	0.005(3)	0	0	0

[a] Wyckoff for Ca(1), Ca(2), Si(1), Si(2) and F atom positions are 4c, 16l, 4a, 8h and 4b, respectively, and site symetries for the same atoms are 4/m, ..m, 422, m.2m and 42m, respectively.
[b] Occupancy refined to 0.42(1).

Table IV-12. Important interatomic distances[a] (Å) in $Ca_5Si_3(F)_x$ structures.

Atom(1) – Atom(2)	Ca_5Si_3	$Ca_5Si_3F_{0.4}$
Si(2) – Si(2) (1x)	2.447(1)	2.435(2)
Si(2) – Si(2) (4x)	4.3608(5)	4.3551(7)
Si(1) – Ca(1) (2x)	3.7088(5)	3.7073(5)
Si(1) – Ca(2) (8x)	3.2498(3)	3.2306(3)
Si(2) – Ca(1) (2x)	3.0836(3)	3.0795(5)
Si(2) – Ca(2) (2x)	3.0539(6)	3.1383(9)
Si(2) – Ca(2) (4x)	3.0957(5)	3.0930(6)
Ca(1) – Ca(2) (8x)	3.4923(3)	3.5370(4)
Ca(2) – Ca(2) (1x)	3.6039(8)	3.549(1)
Ca(2) – Ca(2) (1x)	3.8897(7)	3.759(1)
Ca(2) – Ca(2) (1x)	4.1495(9)	4.267(1)
Ca(2) – Ca(2) (2x)	4.2714(7)	4.120(1)
Ca(2) – Ca(2) (4x)	3.9728(2)	3.9899(3)
Ca(2) – Z	—	2.4516(5)

[a] Distances < 4.5 Å.

reaction T43. Attempts to refine the structure in the lower space group I4cm led to unstable solutions. Tables IV-13, IV-14 and IV-15 give the crystallographic and refined data for Sr_5Si_3 in the C-type structure. As in previous cases, the atom at 0,0,0 is quite anisotropic, U_{33}/U_{11} ~4.3. Attempts to split the troublesome position did not improve the statistics of the solution. Consequently, our results indicate that the more accurate structural description for the binary Sr_5Si_3 is in the C-type. The ternary hydride $Sr_5Si_3H_x$ from reaction T61 certainly forms in the C structure as well. The newly identified Eu_5Si_3 and $Eu_5Si_3H_x$ phases from reactions TR2 and T97, respectively, form in the C-type structure. Crystallographic and refined data information for $Eu_5Si_3H_x$ structure are given in Tables IV-13, IV-14 and IV-15 as well. The formation of the Eu derivatives in the C

Table IV-13. Crystallographic data for $A_5Si_3(H,F)_x$ phases.

	Sr_5Si_3	$Eu_5Si_3H_x$	$Ba_5Si_3F_{0.16(2)}$
Crystal from rxn.	T43	T97	TF11
Space Group	I4/mcm(#140)	I4/mcm	P4/ncc(#130)
Lattice parameters[a]			
a (Å)	8.0980(40	7.9052(4)	8.4726(2)
c (Å)	15.707(1)	15.281(2)	16.443(1)
Volume ($Å^3$)	1030.0(1)	954.9(1)	1180.3(1)
Z	4	4	4
Density calc. (g/cm^3)	3.368	5.887	4.445
Crystal dim. (mm)	0.15x0.18x0.26	0.18x0.24x0.32	0.12x0.25x0.0.30
Diffractometer	Enraf-Nonius CAD4	Enraf-Nonius CAD4	Enraf-Nonius CAD4
Collected octants	h.-k,±l	-h,-k,±l	h,-k,±l
Scan type	ω-2θ	ω-2θ	ω-2θ
2θ limit (°)	54	54	54
Transmission range	0.873–1.252	0.774–1.150	0.859–1.143
Absorption coeff. (cm^{-1})	252.2	327.1	167.0
Number of reflections			
Measured (observed[b])	2571(744)	2164(828)	2898(1893)
Independent (observed[b])	139(45)	821(301)	1115(673)
R_{ave}[c] (%)	15.8(7.85[b])	4.30	9.75
No. of refined variables	16	16	23
R/R_w (%)	3.5/3.7	2.1/2.4	3.2/3.6
Goodness of fit	1.166	1.926	1.927
Secondary ext.coeff. ($x10^{-7}$)	4.5(7)	7.4(2)	6.7(4)
Max./min. peak in ΔF map ($e^- Å^{-3}$)	1.35/-1.21	1.10/-1.08	2.40/-1.03

[a] Lattice parameters calculated from Guinier powder patterns.
[b] Observed reflections; $I \geq 3.00\sigma_I$.
[c] All data $I > 0$.

Table IV-14. Refined positional and thermal parameters for $A_5Si_3(H,F)_x$ phases in B and C structure types.

Atom	x	y	z	$B_{eq}(Å^2)$	U_{11}	U_{22}	U_{33}	U_{12}	U_{13}	U_{23}
Sr_5Si_3 (T43, Cr_5B_3-type)										
Sr(1)	0	0	0	1.27(5)	0.0077(7)	U_{11}	0.033(1)	0	0	0
Sr(2)	0.18003(7)	x + ½	0.14008(6)	0.74(2)	0.0106(4)	U_{11}	0.0070(5)	-0.0014(3)	-0.0010(3)	U_{13}
Si(1)	0	0	¼	1.0(1)	0.013(2)	U_{11}	0.013(3)	0	0	0
Si(2)	0.3920(3)	x + ½	0	0.59(9)	0.008(1)	U_{11}	0.006(2)	-0.000(1)	0	0
$Eu_5Si_3H_x$ (T97, stuffed-Cr_5B_3-type)										
Eu(1)	0	0	0	1.98(3)	0.0134(4)	U_{11}	0.0485(8)	0	0	0
Eu(2)	0.17414(4)	x + ½	0.14786(3)	1.09(2)	0.0157(3)	U_{11}	0.0099(3)	-0.0001(2)	-0.0024(1)	U_{13}
Si(1)	0	0	¼	1.1(1)	0.015(1)	U_{11}	0.011(3)	0	0	0
Si(2)	0.3925(3)	x + ½	0	0.86(8)	0.012(1)	U_{11}	0.008(2)	0.001(1)	0	0
(H	0	½	¼)							
$Ba_5Si_3F_{0.2}$[a] (TF11, stuffed-Ba_5Si_3-type)										
Ba(1)	¼	¼	0.2716(1)	2.11(3)	0.0203(3)	U_{11}	0.0394(8)	0	0	0
Ba(2)	0.06191(5)	0.91935(5)	0.39388(3)	1.42(3)	0.0206(3)	0.0187(3)	0.0147(4)	-0.0008(2)	0.0046(2)	-0.0043(3)
Si(1)	¼	¼	0.4915(3)	1.4(1)	0.020(1)	U_{11}	0.013(3)	0	0	0
Si(2)	0.6481(2)	-x	¼	1.00(6)	0.0157(8)	U_{11}	0.007(2)	0.002(1)	-0.0011(9)	U_{13}
F[a]	¾	¼	0	0.8(5)						

Table IV-15. Selected interatomic distances of $A_5Tt_3(H,F)_x$, (Å).

Cr_5B_3(Z)-type			Ba_5Si_3(Z)-type	
Atom(1) – Atom(2)	Sr_5Si_3	$Eu_5Si_3H_x$	Atom(1) – Atom(2)	$Ba_5Si_3F_{0.2}$
Si(1) – Si(2) (1x)	2.474(7)	2.403(7)	Si(2) – Si(2) (1x)	2.442(6)
Si(1) – A(1) (2x)	3.9267(3)	3.8203(3)	Si(1) – Ba(1) (1x)	3.617(5)
Si(1) – A(2) (8x)	3.4380(5)	3.3116(3)	Si(1) – Ba(2) (4x)	3.549(3)
Si(2) – A(1) (2x)	3.276(3)	3.217(2)	Si(1) – Ba(2) (4x)	3.601(2)
Si(2) – A(2) (2x)	3.293(2)	3.327(3)	Si(2) – Ba(1) (2x)	3.500(1)
Si(2) – A(2) (4x)	3.259(2)	3.215(1)	Si(2) – Ba(2) (2x)	3.378(1)
A(1) – A(2) (8x)	3.6987(6)	3.6927(4)	Si(2) – Ba(2) (2x)	3.458(1)
A(2) – A(2) (1x)	3.807(2)	3.553(1)	Si(2) – Ba(2) (2x)	3.538(2)
A(2) – A(2) (1x)	4.401(2)	[4.519(1)][a]	Ba(1) – Ba(2) (4x)	3.7991(9)
A(2) – A(2) (1x)	4.124(2)	3.894(1)	Ba(1) – Ba(2) (4x)	4.055(1)
A(2) – A(2) (2x)	[4.519(2)][a]	4.1622(9)	Ba(2) – Ba(2) (1x)	3.892(1)
A(2) – A(2) (4x)	4.2046(4)	4.1306(3)	Ba(2) – Ba(2) (2x)	4.2526(6)
A(2) – H	—	[2.4952(5)][a]	Ba(2) – Ba(2) (1x)	4.2887(9)
			Ba(2) – F	2.7646(5)

[a] Included to complete the table.

type structure would have been anticipated if presence of divalent Eu ions in the compound were assumed; the crystal radii of Eu^{2+} and Sr^{2+} for CN=6 are 1.31 and 1.32 Å, respectively.[62]

The lattice parameters from products of reactions involving Ba indicated that some hydrogen and fluoride was substituted in the structure, rxns T20, T60, T52 and TF11; however, it was not clear whether the presence of hydrogen in the structure may have stabilized the $Ba_5Si_3(H,F)_x$ in the C-type structure. Discerning between the B and C type structures by powder patterns is not definitive; therefore, single crystal work on the ternary fluoride was pursued. Solution of the structure for the ternary indicated that the structure remain in the B-type and some fluoride insertion occurred; the refined formula was $Ba_5Si_3F_{0.16(2)}$. Crystallographic and refined data information for the ternary are given in Tables IV-13, IV-14 and IV-15. The Ba_5Si_3-type structure (P4/ncc, sp.gr. #130, Z=4),[154] in resemblence to the Cr_5B_3-type, can be described as built of two layer sections of U_3Si_2- and $CuAl_2$-like structures, each containing dimers and isolated silicon atoms, respectively. Significantly, tetrahedral cavities in the $CuAl_2$-like section are still present in the B-type structure. Figure IV-8 shows the [100] extended view of the Ba_5Si_3-type structure. A combination of matrix and electronic effects seems to play an important role in the formation of this primitive structure, because it is frequently observed when combinations of small anions and either large or trivalent cations are involved. Therefore, the deformation from the C structure seems to be caused by the displacement of the small Si(1) towards the large Ba(1) atoms, formerly at 0,0,z in the undistorted structure. This displacement results in the disappearance of the mirror plane perpendicular to the c axis in the original I4/mcm group. Figure IV-9 shows the coordination environments of Ba(1) and Si(1) atoms in $Ba_5Si_3F_{0.2}$ where, as in the C-type structures, they present larger isotropic or anisotropic thermal parameters. Importantly, the structural solution of the ternary indicated that only fractional insertion of fluoride in the tetrahedral interstices occurred, which suggests that the electronic requirements in this structure might be different from those for the C-type structure. The ternaries $Ba_5Si_3H_x$ and $Ba_5Si_3F_{0.2}$ are the first documented examples of interstitially derivatized Ba_5Si_3-type.

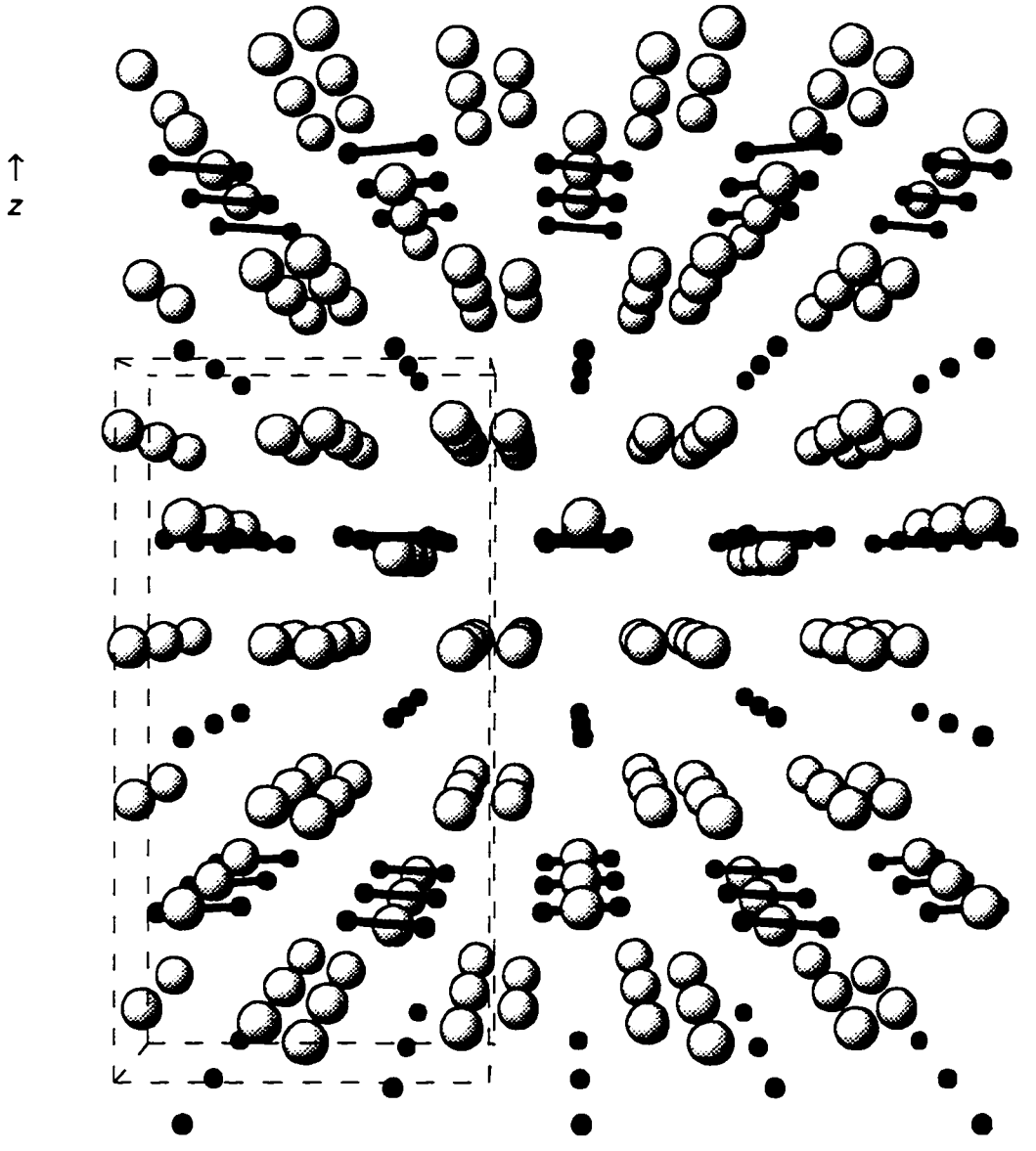

Figure IV-8. Extended [010] view of the Ba_5Si_3-type structure. Small and large spheres represent Si and Ba atoms, respectively. Dashed lines correspond to the unit cell. The cell view was drawn such to ease the comparison with that in Figure IV-1. Short Si–Si contacts are depicted as heavy lines.

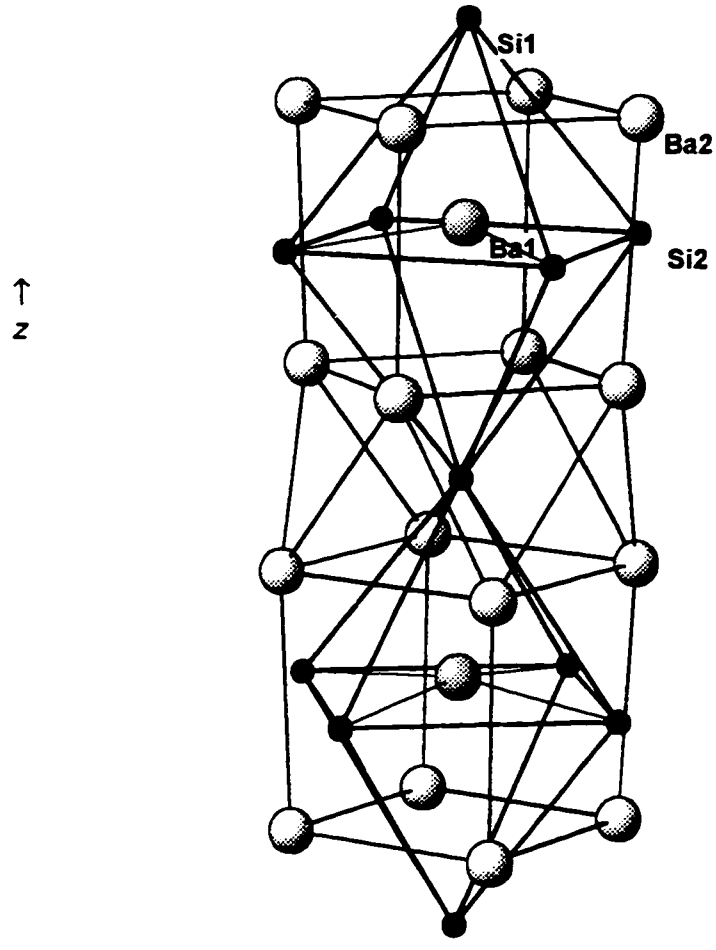

Figure IV-9. Detail section of the $Ba_5Si_3F_{0.2}$ structure, Ba_5Si_3(Z)-type. Atoms polyhedra surrounding the S1(1) and Ba(1) atoms, compare with Figure IV-6. Lines between atoms do not represent bonds. Ba(1)–Si distances below 3.5 Å are denoted as thin lines.

The derivatives of Sm and Yb form both as binaries and as ternary hydrides in the M-type structure, rxns TR1 and T96 for $Sm_5Si_3H_x$ and TR3 and T98 for $Yb_5Si_3H_x$. Although magnetic measurements on these samples were not performed, the rare-earth ions seem to be in a trivalent state since the c/a ratios of their cell dimensions are close to 0.75. Trivalent M-RE_5Si_3 and M-RE_5Ge_3 have been reported to have a c/a ratio of ~0.75. The 1.02% cell volume increment that occurred between the Yb_5Si_3 and $Yb_5Si_3H_x$ products is still unexplained. Such a volume increment cannot be attributed solely to the presence of hydrogen in the structure. The low yield of the M-Yb_5Si_3 phase is suggestive that extra factors contributed to the formation of this phase. Additional experimental efforts are necessary to illuminate this problem.

Germanides

In general, the metal germanides A_5Ge_3 studied, with the exception of the Sm and Yb derivatives, form both as binaries and as ternary hydrides in the C-type structure, see Table IV-8. Hydrogen in bound in different amounts by these compounds as observed from their cell volume variations, see Table IV-9, with decrements of 0.59, 0.98, 1.08 and 1.36% for the compounds $Ba_5Ge_3H_x$, $Eu_5Ge_3H_x$, $Sr_5Ge_3H_x$ and $Ca_5Ge_3H_x$, respectively. Single crystal structures were solved for the Ca_5Ge_3 (T34), $Ca_5Ge_3H_x$ (T33) and $Ca_5Ge_3F_{0.7}$ (TF1) phases and their crystallographic and refined data information are given in Tables IV-16 and IV-17. Calculated interatomic distances in these structures are listed in Table IV-18. Significantly, refined formula for the ternary fluoride of $Ca_{5.000(8)}Ge_{2.995(4)}F_{0.66(2)}$ indicates that a trend exist in the fluorine content among the $Ca_5Tt_3F_x$ compounds, i.e., $Ca_5Sn_3F_{0.9} > Ca_5Ge_3F_{0.7} > Ca_5Si_3F_{0.4}$, and a similar trend of hydrogen content can be assumed for the corresponding ternary hydrides. Interestingly, the atom positions in the original structural report for Ca_5Ge_3 by Eisenmann and Schäfer[167] correspond to those of the ternary hydride $Ca_5Ge_3H_x$ in this work.

In concordance with previous reports, the $Sm_5Ge_3H_x$ derivatives, rxns T37 and T47, form in the M type structure. The M form of $Yb_5Ge_3H_x$ was only observed when the reaction was carried out in presence of hydrogen, rxn T49. A mixture of newly identified YbGe and Yb_2Ge phases in the CrB and Co_2Si types is otherwise observed, rxn T59.

Table IV-16. Crystallographic data for $Ca_5Ge_3(H,F)_x$ phases.

	Ca_5Ge_3	$Ca_5Ge_3H_x$	$Ca_{5.000(8)}Ge_{2.995(4)}F_{0.66(2)}$
Crystal from rxn.	T34	T33	TF1
Space Group	I4/mcm(#140)	I4/mcm	I4/mcm
Lattice parameters[a]			
a (Å)	7.7156(5)	7.7218(5)	7.7093(3)
c (Å)	14.885(2)	14.660(2)	14.789(2)
Volume ($Å^3$)	886.1(1)	874.2(1)	879.0(1)
Z	4	4	4
Density calc. (g/cm^3)	3.134	3.185	3.303
Diffractometer	Enraf-Nonius CAD4	Enraf-Nonius CAD4	Enraf-Nonius CAD4
Crystal dim.(mm)	0.11x0.16x0.22	0.16x0.22x0.25	0.17x0.20x0.28
Collected octants	-h,k,±l	h,k,±l	h,±k,±l
Scan type	ω-2θ	ω-θ	ω-2θ
2θ limit (°)	56	56	56
Transmission range	0.546–1.000	0.830–1.256	0.885–1.163
Absorption coeff. (cm^{-1})	127.2	129.0	128.5
Number of reflections			
Measured (observed[b])	2443(817)	2397(849)	3104(1176)
Independent (observed[b])	824(281)	1184(430)	832(321)
R_{ave}[c] (%)	6.70	7.23	10.9
No. of refined variables	16	16	21
R/R_w (%)	1.9/2.2	2.9/3.0	2.1/2.4
Goodness of fit	1.171	1.527	0.981
Secondary ext.coeff. ($x10^{-7}$)	4.0(5)	1.3(6)	9(1)
Max./min. peak in ΔF map ($e^- Å^{-3}$)	0.67/-0.59	0.94/-0.75	0.62/-0.88

[a] Lattice parameters calculated from Guinier powder patterns.
[b] Observed reflections; $I \geq 3.00\sigma_I$.
[c] All data $I > 0$.

Table IV-17. Refined positional and thermal parameters for $Ca_5Ge_3(H,F)_x$ phases in stuffed-Cr_5B_3-type structure.

Atom	x	y	z	B_{eq}(Å^2)	U_{11}	U_{22}	U_{33}	U_{12}	U_{13}	U_{23}
Ca_5Ge_3 (T34)										
Ca(1)	0	0	0	1.18(4)	0.0079(5)	U_{11}	0.029(1)	0	0	0
Ca(2)	0.17807(8)	x + ½	0.13998(6)	0.95(2)	0.0122(3)	U_{11}	0.0117(4)	-0.0008(3)	-0.0006(2)	U_{13}
Ge(1)	0	0	¼	1.04(2)	0.0124(3)	U_{11}	0.0148(5)	0	0	0
Ge(2)	0.38200(6)	x + ½	0	0.70(1)	0.0074(2)	U_{11}	0.0117(3)	-0.0004(3)	0	0
$Ca_5Sn_3(H_x)$ (T33)										
Ca(1)	0	0	0	1.50(5)	0.0116(6)	U_{11}	0.034(1)	0	0	0
Ca(2)	0.16797(8)	x + ½	0.14852(8)	1.09(2)	0.0153(3)	U_{11}	0.0108(6)	-0.0001(3)	-0.0018(3)	U_{13}
Ge(1)	0	0	¼	1.08(3)	0.0136(3)	U_{11}	0.0139(6)	0	0	0
Ge(2)	0.38296(6)	x + ½	0	0.85(2)	0.0114(3)	U_{11}	0.0096(4)	-0.0004(3)	0	0
(H	0	½	¼)							
$Ca_5Ge_3F_{0.7}$ (TF1)										
Ca(1)	0	0	0	1.69(4)	0.0118(6)	U_{11}	0.041(1)	0	0	0
Ca(2)	0.16964(7)	x + ½	0.14617(5)	1.26(2)	0.0167(3)	U_{11}	0.0146(4)	0.0013(3)	-0.0036(2)	U_{13}
Ge(1)	0	0	¼	1.16(2)	0.0151(3)	U_{11}	0.0138(4)	0	0	0
Ge(2)	0.38224(4)	x + ½	0	0.81(1)	0.0108(2)	U_{11}	0.0091(3)	0.0002(2)	0	0
F	0	½	¼	1.4(2)	0.020(3)	U_{11}	0.013(3)	0	0	0

[a] Occupancy refined to 0.66(2).

Table IV-18. Important interatomic distances[a] (Å) in $Ca_5Ge_3(F)_x$ structures.

Atom(1) – Atom(2)	Ca_5Ge_3	Ca_5Ge_3H	$Ca_5Ge_3F_{0.6}$
Ge(2) – Ge(2) (1x)	2.575(1)	2.556(1)	2.5678(9)
Ge(2) – Ge(2) (4x)	4.3626(5)	4.3730(5)	4.3607(4)
Ge(1) – Ca(1) (2x)	3.7213(5)	3.6650(5)	3.6972(5)
Ge(1) – Ca(2) (8x)	3.2771(5)	3.2356(6)	3.2488(4)
Ge(2) – Ca(1) (2x)	3.0848(4)	3.0922(4)	3.0835(2)
Ge(2) – Ca(2) (2x)	3.048(1)	3.202(1)	3.1695(9)
Ge(2) – Ca(2) (4x)	3.1264(8)	3.121(1)	3.1212(7)
Ca(1) – Ca(2) (8x)	3.5212(6)	3.6050(8)	3.5875(5)
Ca(2) – Ca(2) (1x)	3.632(2)	3.473(2)	3.536(1)
Ca(2) – Ca(2) (1x)	3.886(2)	3.669(2)	3.699(2)
Ca(2) – Ca(2) (1x)	4.167(2)	4.355(2)	4.323(2)
Ca(2) – Ca(2) (2x)	4.0143(4)	3.947(2)	4.034(1)
Ca(2) – Ca(2) (4x)	4.0143(4)	4.0634(5)	4.0489(4)
Ca(2) – Z	—	2.362(1)	2.4038(8)

[a] Distances < 4.5 Å.

Consequently, the M-$Yb_5Ge_3H_x$ phase was considered a hydrogen-stabilized and probably a Zintl phase. It appears that these hexagonal germanides M-$(Sm,Yb)_5Ge_3H_x$ involve trivalent rare-earth metal ions, because its c/a ratios are around 0.74 – 0.77; RE_5Ge_3 phases that contain characteristic trivalent rare-earth metals have c/a ratios between 0.75 – 0.77.[24,173] Buschow et al.[173] while studying the magnetic behavior of several rare-earth-metal germanides, RE_5Ge_3, mentioned that they were unable to get monophasic products of the Sm and Yb derivatives and consequently could not analyze them. One could assume that they were working in low hydrogen conditions. The temperature dependence of the molar susceptibilities of samples T37 and T47 as pictured in Figure IV-10 show a complex set of magnetic phase transformations below

100K. Such a complex behavior resembles the already discussed $Sm_5Sb_3H_x$ systems given in the Figure III-7 of that chapter. The molar susceptibilities of Sm_5Ge_3 (T37) are nearly temperature independent from room temperature to ~58K, where they modestly increase to two maxima at ~41K and ~23K, followed by a decrease in the susceptibilities at lower temperatures. The presence of hydrogen in the compound, $Sm_5Ge_3H_x$ (T47) causes significant changes in the magnetic behavior of the compound as seen in Figure IV-10. The molar susceptibilities of the ternary hydride are quite temperature independent from room temperature to approximately 100K, where they rapidly increase to two maxima as in the binary; however, these two maxima are now at ~65 and ~39K, and as the temperature is decreased show a rapid descend to a small maximum at ~ 13K. Low temperature magnetic transitions have already been recognized in M-$RE_5(Si,Ge)_3$ phases, $RE_5(Si,Ge)_3$; RE= Pr, Nd, Gd, Tb, Dy, Ho, Er, by Buschow's[173,182] and Roudaut's[183,184,185] groups. These reported transitions have been rationalized in terms of magnetic spirals and sublattice interactions in the structures, as in the case of the pnictides. The reader is referred to the original reports.

The molar susceptibilities of the hydrogen-stabilized M-$Yb_5Ge_3H_x$ phase (sample T49) as depicted in Figure IV-11 show a distinctive Curie-Weiss temperature dependence, with a calculated effective moment and Weiss constant of μ_{eff}= 7.52(8) BM and θ= -66 K for T > 100K, respectively. These results are evidence that the compound probably contains 3 of 5 trivalent Yb ions, because a saturated moment of ($\mu_{eff}/\sqrt{3}$ =) 4.343 BM is calculated when $3Yb^{3+}$ ions are assumed; reported effective moments for Yb^{3+} ions are between 4.3 – 4.9 BM and Yb^{2+} is diamagnetic.[94] This information supports the assumed valence distribution of the ternary hydride, Yb_5Ge_3H; $3Yb^{3+}$, $2Yb^{2+}$, $3Ge^{4-}$, H^-. However, the single crystal structure of the ternary hydride was not supportive of this claim. A crystal from reaction T49 was solved in the M-type structure and its crystallographic and refined data are given in Tables IV-19, IV-20 and IV-21. The lower than average quality of the crystal are blamed for the large residuals and thermally anisotropic Yb(1) atom. To our interest, the short Yb(1)–Yb(1) interatomic distance of 3.1997(4) Å indicates that the trivalent Yb ions are located in the infinite linear chains that run along the c direction. A distance of 3.4512(3) Å was observed earlier for the

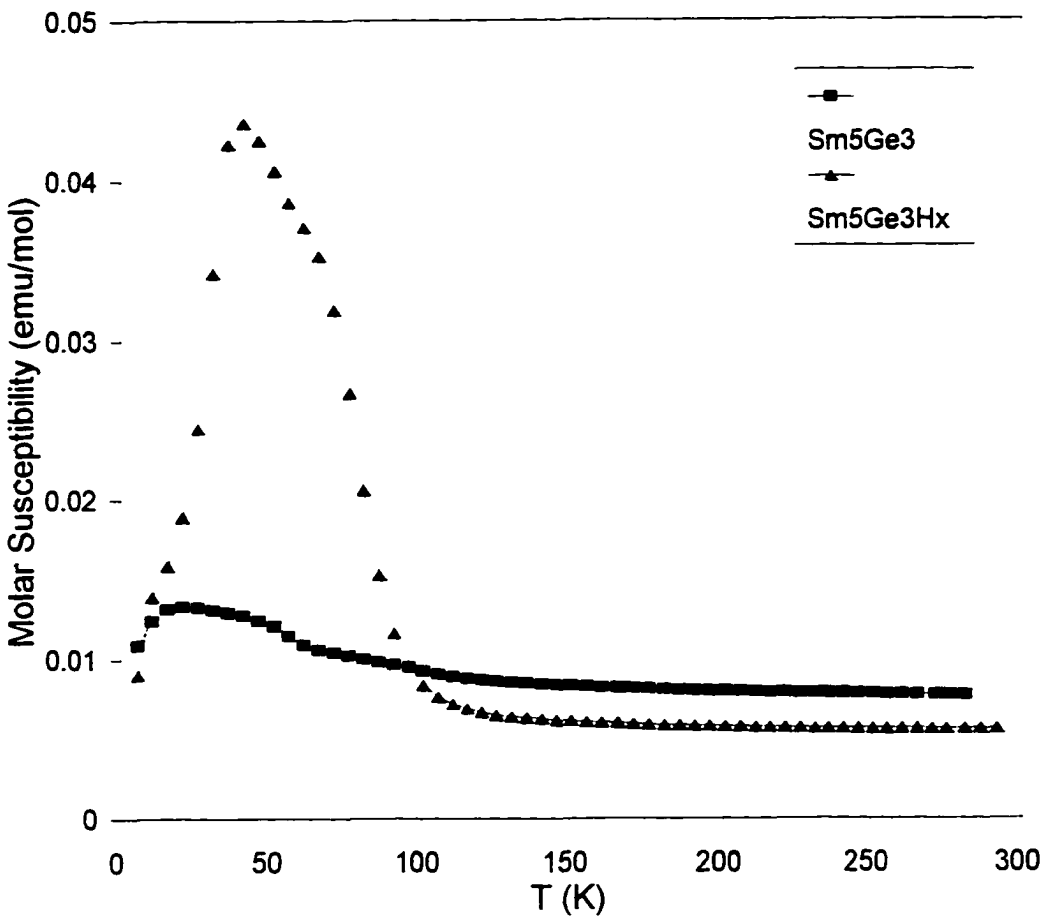

Figure IV-10. Temperature dependence of the molar susceptibilities (χ) at 3 Tesla of Sm_5Ge_3 (■) and $Sm_5Ge_3H_x$ (▲).

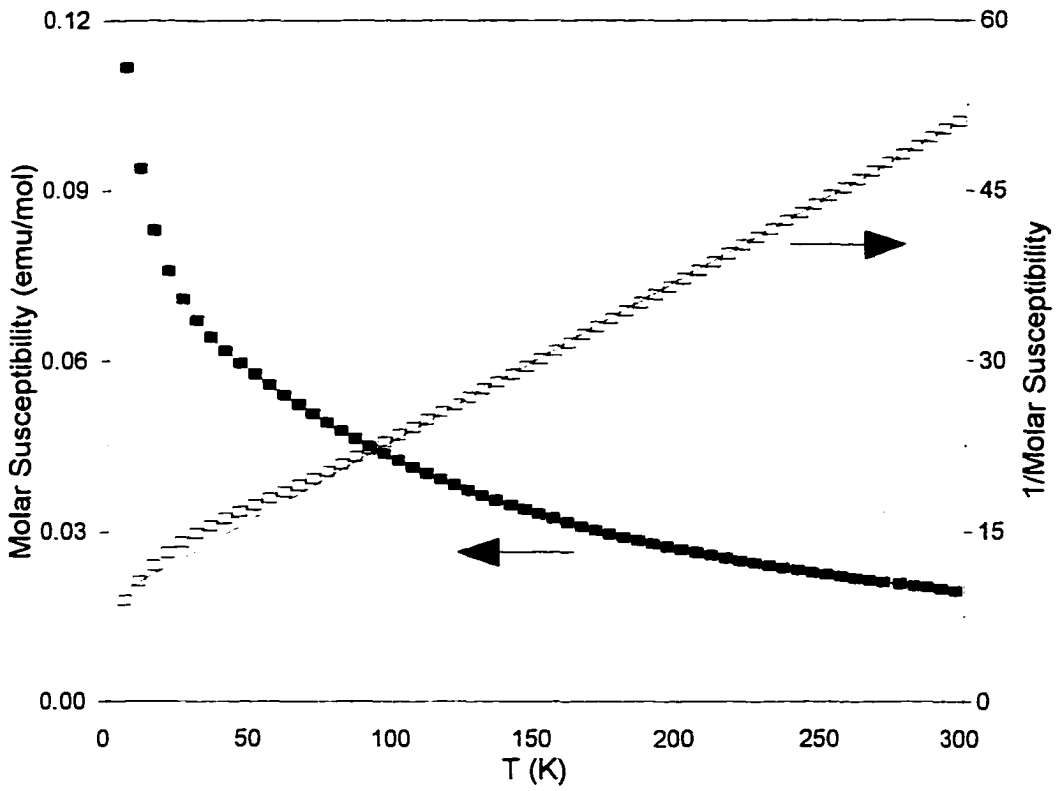

Figure IV-11. Temperature dependence of the molar susceptibilities (χ) at 3 Tesla of $Yb_5Ge_3H_x$, (■) for χ vs. T plot and (□) for $1/\chi$ vs. T; linear fit for T>100K.

Table IV-19. Crystallographic data for $A_5Tt_3(H,F)_x$ phases.

	$Yb_5Ge_3H_x$	$Eu_5Sn_3H_x$	Sr_5Pb_3F
Crystal from rxn.	T49	T27	TF12
Space Group	$P6_3/mcm$(#193)	I4/mcm(#140)	I4/mcm
Lattice parameters[a]			
a (Å)	8.3466(5)	8.4645(3)	8.6679(5)
c (Å)	6.3995(8)	15.589(1)	15.958(2)
Volume ($Å^3$)	386.09(7)	1116.9(1)	1196.2(2)
Z	2	4	4
Density calc. (g/cm^3)	9.323	6.635	5.975
Crystal dim. (mm)	0.15x0.15x0.22	0.12x0.21x0.24	0.20x0.26x0.30
Diffractometer	Rigaku AFC6R	Enraf-Nonius CAD4	Enraf-Nonius CAD4
Collected octants	h,±k,±l	-h,-k,±l	h,±k,±l
Scan type	ω-2θ	ω-2θ	ω-2θ
2θ limit (°)	50	50	52
Transmission range	0.420-1.269	0.722-1.413	0.623-1.697
Absorption coeff. (cm^{-1})	710.3	342.3	636.7
Number of reflections			
Measured (observed[b])	1456(1096)	2260(896)	2664(960)
Independent (observed[b])	170(126)	1103(411)	1089(364)
R_{ave}[c] (%)	22.5	11.1	16.0
No. of refined variables	12	16	17
R/R_w (%)	5.3/5.6	3.5/4.3	4.6/5.1
Goodness of fit	1.403	2.422	1.951
Secondary ext.coeff. ($x10^{-7}$)	33(4)	1.4(1)	2.2(2)
Max./min. peak in ΔF map ($e^- Å^{-3}$)	7.38/-4.06	2.76/-3.48	4.40/-3.10

[a] Lattice parameters calculated from Guinier powder patterns.
[b] Observed reflections; $I \geq 3.00\sigma_I$.
[c] All data $I > 0$.

Table IV-20. Refined positional and thermal parameters for $A_5Tt_3(H,F)_x$ phases.

Atom	x	y	z	B_{eq}(Å^2)	U_{11}	U_{22}	U_{33}	U_{12}	U_{13}	U_{23}
Yb_5Ge_3 (T49, Mn_5Si_3-type)										
Yb(1)	1/3	2/3	0	1.03(7)	0.018(1)	U_{11}	0.004(1)	$1/2U_{11}$	0	0
Yb(2)	0.2425(2)	0	1/4	1.1(1)	0.014(1)	0.012(1)	0.016(1)	$1/2U_{22}$	0	0
Ge(1)	0.6035(4)	0	1/4	1.1(2)	0.015(2)	0.014(2)	0.013(2)	$1/2U_{22}$	0	0
(H	0	0	0)							
$Eu_5Sn_3H_x$ (T27, Stuffed-Cr_5B_3-type)										
Eu(1)	0	0	0	1.81(5)	0.0113(7)	U_{11}	0.046(1)	0	0	0
Eu(2)	0.16820(7)	x + ½	0.14967(5)	1.19(3)	0.0168(4)	U_{11}	0.0118(5)	0.0003(4)	-0.0035(2)	U_{13}
Ge(1)	0	0	¼	1.02(5)	0.0137(8)	U_{11}	0.011(1)	0	0	0
Ge(2)	0.3795(1)	x + ½	0	0.80(3)	0.0103(5)	U_{11}	0.0099(7)	-0.0004(7)	0	0
(H	0	½	¼)							
Sr_5Pb_3F (TF12, Stuffed-Cr_5B_3-type)										
Sr(1)	0	0	0	1.6(2)	0.009(1)	U_{11}	0.044(5)	0	0	0
Sr(2)	0.1616(2)	x + ½	0.1504(2)	1.23(6)	0.0152(9)	U_{11}	0.016(2)	0.0014(9)	-0.0050(7)	U_{13}
Pb(1)	0	0	¼	1.06(6)	0.0125(7)	U_{11}	0.015(1)	0	0	0
Pb(2)	0.3733(1)	x + ½	0	0.74(4)	0.0087(5)	U_{11}	0.0107(9)	-0.0005(5)	0	0
F	0	½	¼	1.3(6)						

Table IV-21. Important interatomic distances (Å) in $Yb_5Ge_3H_x$, $Eu_5Sn_3H_x$ and Sr_5Pb_3F structures.

Atom(1) – Atom(2)	$Yb_5Ge_3H_x$ (M-type)	Atom(1) – Atom(2)	$Eu_5Sn_3H_x$ (C-type)	Sr_5Pb_3F (C-type)
Ge – Ge (2x)	3.636(3)	Tt(2) – Tt(2) (1x)	2.884(3)	3.106(3)
Ge – Ge (4x)	4.433(2)	Tt(1) – A(1) (2x)	3.8972(3)	3.9895(5)
Ge – Yb(1) (6x)	3.019(1)	Tt(1) – A(2) (8x)	3.5158(4)	3.619(2)
Ge – Yb(2) (2x)	2.890(3)	Tt(2) – A(1) (2x)	3.3704(8)	3.4170(6)
Ge – Yb(2) (1x)	3.013(4)	Tt(2) – A(2) (2x)	3.441(2)	3.534(3)
Ge – Yb(2) (2x)	3.448(1)	Tt(2) – A(2) (4x)	3.403(1)	3.478(3)
Yb(1) – Yb(1) (2x)	3.1997(4)	A(1) – A(2) (8x)	3.9190(6)	4.040(2)
Yb(1) – Yb(2) (6x)	3.6033(8)	A(2) – A(2) (1x)	3.691(2)	3.848(6)
Yb(2) – Yb(2) (2x)	3.506(2)	A(2) – A(2) (1x)	4.027(2)	3.962(5)
Yb(2) – Yb(2) (4x)	3.7862(8)	A(2) – A(2) (2x)	4.230(2)	4.238(6)
		A(2) – A(2) (4x)	4.4530(4)	4.597(1)
		A(2) – Z	2.5497(9)	2.540(3)

equivalent position in the M-Yb_5Sb_3 phase where all the Yb ions are in a divalent state. The new electron count based on information from the single crystal refinement suggest that the sample T49 is a valence compound, i.e, $2Yb^{3+}$, $3Yb^{2+}$, $3Ge^{4-}$. Because additional experiments were not performed in this system, at present time we do no have a satisfactory answer to the problem. Experiments involving variable hydrogen content and electrical resistivity measurements on the phase may give more insights.

Stannides

Among the stannides, the Sr derivative was the only combination that formed in the C-type structure as a binary and ternary hydride, rxns T1 and T23. Characteristically, this system showed the largest cell volume decrement of 1.96% when in its hydrided form. Derivatives involving Ca (earlier discussed), Ba, Eu and Yb in the same structure

type are hydrogen-stabilized compounds. The crystal structure of the previously unknown $Eu_5Sn_3H_x$ was successfully solved in the C-type structure. Crystallographic and refined data of this new phase are given in Tables IV-19, IV-20 and IV-21. Reactions under dynamic vacuum for Ca_5Sn_3 and Yb_5Sn_3 compositions gave in high yields the $Ca_{31}Sn_{20}$ (P-type) and the unprecedented $Yb_{36}Sn_{23}$ (YS), respectively. Mixed phase products with the CrB and Co_2Si type structures were observed when the reaction for either Ba_5Sn_3 (rxn T15) or Eu_5Sn_3 (rxn T17) were carried under vacuum. High yields of the hydrogen-stabilized C-$Yb_5Sn_3H_x$ compound were not achieved, since the YS phase was normally the major product. Nevertheless, the C phase was observed as a byproduct when compositions $Yb_5Sn_4D_{4.0}$ (rxn TD3) were loaded while studying another composition in the Yb–Sn–H(D) system. Additionally, the Sm derivatives, $Sm_5Sn_3H_x$, formed in the M-type structure, but Palenzona's[177] reported M-Yb_5Sn_3 was never observed during this work.

Plumbides

In comparison with the previous tetrels systems, the plumbides $A_5Pb_3(H,F)_x$ presented a richer and more complex chemistry, where matrix effects might play a very important role in the structural tendencies of each system; nevertheless, structural solutions in these systems were not very successful. Thus, in an effort to explore the possible effects of hydrogen in the well studied Ca–Pb system, reactions in absence and presence of hydrogen or fluorine were carried out. Helleis et al.[155] in 1963 reported the single crystal structure of Ca_5Pb_3 as a $\sqrt{3}a \times \sqrt{3}a \times c$ supercell of the Mn_5Si_3-type structure (MS). Following in 1976, Bruzzone and Merlo[178] by means of powder pattern analysis reported the structure of such a phase as the standard M-type, i.e, the subcell. The lack of information that might have indicated Pb–Pb contacts in the Ca_5Pb_3 structure, an otherwise $2e^-$-deficient phase ($5Ca^{2+}$, $3Pb^{4-}$), motivated Guloy in 1992 to revisit the system.[53] He, through extensive experimental and crystallographic work, showed that the phase indeed forms in a superstructure distortion of the M form, and that its composition was more accurately described as $Ca_{17}Pb_9$ ($Ca_{5.67}Pb_3$). Additionally, he demonstrated that $Ca_{17}Pb_9$ was a Zintl phase, i.e., semiconducting and diamagnetic,

since the new structural solution of $Ca_{5.67}Pb_9$ ($Ca_{17}Pb_3$-type, $P6_3mc$, sp.gr. #186, Z=2) featured one long 3.5080(1) Å Pb–Pb bond per formula unit and an ordered occupancy of 2/3rds of the octahedral cavities by Ca^{2+}; $17Ca^{2+}$, $7Pb^{4-}$, Pb_2^{6-}. Because all these previous experiments were carried out in closed fused-silica containers, the involvement of hydrogen was potential.

In this experimental approach, the product of a reaction Ca_5Pb_3 (rxn T6) carried under dynamic vacuum resembled the $Ca_{17}Pb_9$-type; however, disparities in the intensities and absence of several lines from the M-type associated with the supercell model were evident and suggestive of structural distortions in T6 (Ca_5Pb_3). A crystal from this reaction was mounted on the diffractometer and data were collected on the supercell, which was readily found during SEARCH. Attempts to solve the structure in sp.gr. $P6_3mc$ (#186) using the $Ca_{17}Pb_9$ model positions failed; least-squares convergence could not be achieved. Additional efforts to solve the structure in the space groups $P6_3$ (#173) and P3m1 (#156) while maintaining the three-fold axis led to unstable solutions as well, then the problem was abandoned. Solutions to this problem require careful and comprehensive single crystal film work to better illustrate the symmetry of the cell.

Importantly, the cell volume calculated for Ca_5Pb_3 (T6) was 0.75% larger than the one reported by Guloy for $Ca_{17}Pb_9$, see Table IV-9, and the molar susceptibilities of this sample as depicted in Figure IV-12 were temperature-independent paramagnetic, $\chi_{M(298K)} = 1.24 \times 10^{-4}$ emu/mol after core-correction ($\chi_{M(298K)} \sim 7.5 \times 10^{-8}$ emu/mol without corrections). The disparity in results between Ca_5Pb_3 (T6) and reported $Ca_{17}Pb_9$ suggested that different phases may form near the 5:3 in the Ca–Pb system. Consequently, reactions with the $Ca_{17}Pb_9$ composition were loaded, rxns T76 and T94 (only results of the former reaction are listed in Table IV-8). In agreement with the Ca–Pb phase diagram reported by Bruzzone and Merlo,[178] the mayor products of these reactions were Ca_2Pb in the Co_2Si-type and traces of the hexagonal supercell phase (MS). Additional reactions in presence of hydrogen and fluoride gave mixed phase products, where the hexagonal phase, probably MS-type, was the mayor product, rxns T24 ($Ca_5Pb_3H_{2.0}$) and TF3 (Ca_5Pb_3F). Further distortions of the MS-type structure may

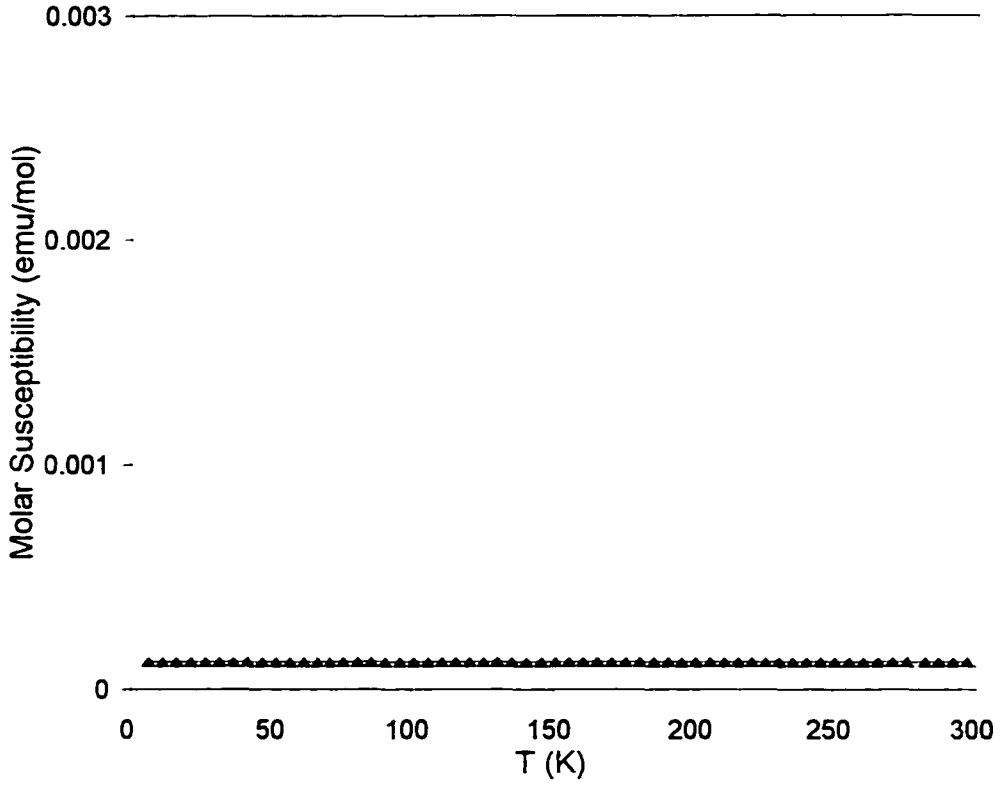

Figure IV-12. Temperature dependence of the molar susceptibilities (χ) at 3 Tesla of Ca_5Pb_3 (sample T6).

have occurred in the products of these ternary reactions because they could only be partially indexed to the MS-type structure. Characteristically, the calculated cell volumes of these ternaries were larger than that of the binary T6. At present time a satisfactory explanation to these ambiguities is lacking; one could speculate that effects like fractional occupancies of the lead atom positions might be occurring.

The plumbides of Sr and Ba in the C-type structure are hydrogen-stabilized compounds, rxns T24 and T26, respectively, and interstitial fluoride is able to stabilize the C-type structures as well, rxns TF12 and TF9. The single crystal structure of Sr_5Pb_3F that was satisfactorily refined as the C-type, and its crystallographic and refined data information are given in Tables IV-19, IV-20 and IV-21. In equivalence to previous related systems, the fluoride ion is located at the center of the tetrahedral interstice of the structure, at 0,½,¼. Reactions intended to prepare the binaries Sr_5Pb_3 and Ba_5Pb_3, rxns T2 and T16 respectively, gave in high yield products with the $Pu_{31}Pt_{20}$ and W_5Si_3 type structures, respectively. Both of these phases are observed for first time, and the latter constitutes the first example of a binary alkaline-earth-metal tetrelide with the tetragonal W_5Si_3-type structure.

The W_5Si_3-type structure (I4/mcm, sp.gr.#140, Z=4)[136] can be described as made of two infinite chains, the first is a chain of Si-centered face-sharing W antiprisms surrounded edge-bridging Si atoms $^1_\infty[W_{8/2}(Si)Si_{8/2}]$ that extends along the c direction. Figure IV-13 depicts the extended [001] view of the W_5Si_3 structure, where the $^1_\infty[W_{8/2}(Si)Si_{8/2}]$ can be observed along 0,0,z and ½,½,z. The lines between atoms are drawn to help visualize these features. The second chain in the structure, $^1_\infty[WSi_{4/2}]$, constitutes of a linear array of W atoms at 0,½,z, etc, that are each bound to four of the same Si atoms from the parallel antiprismatic chain in edge-sharing tetrahedral arrangements. The upper part of Figure IV-14 shows a detail of the [001] infinite perspective view of the WS structure, and in the lower part shows a ~[100] perspective view of the same structure. Characteristically, this structure has short c/2 repeats that reflect in the W–W short contacts in the linear chain. This feature is probably caused by the large bonding interactions occurring in the adjacent chain. The W_5Si_3-type structure is probably the four-fold symmetry equivalent of the self-interstitial Mn_5Si_3-type (= Ti_5Ga_4-

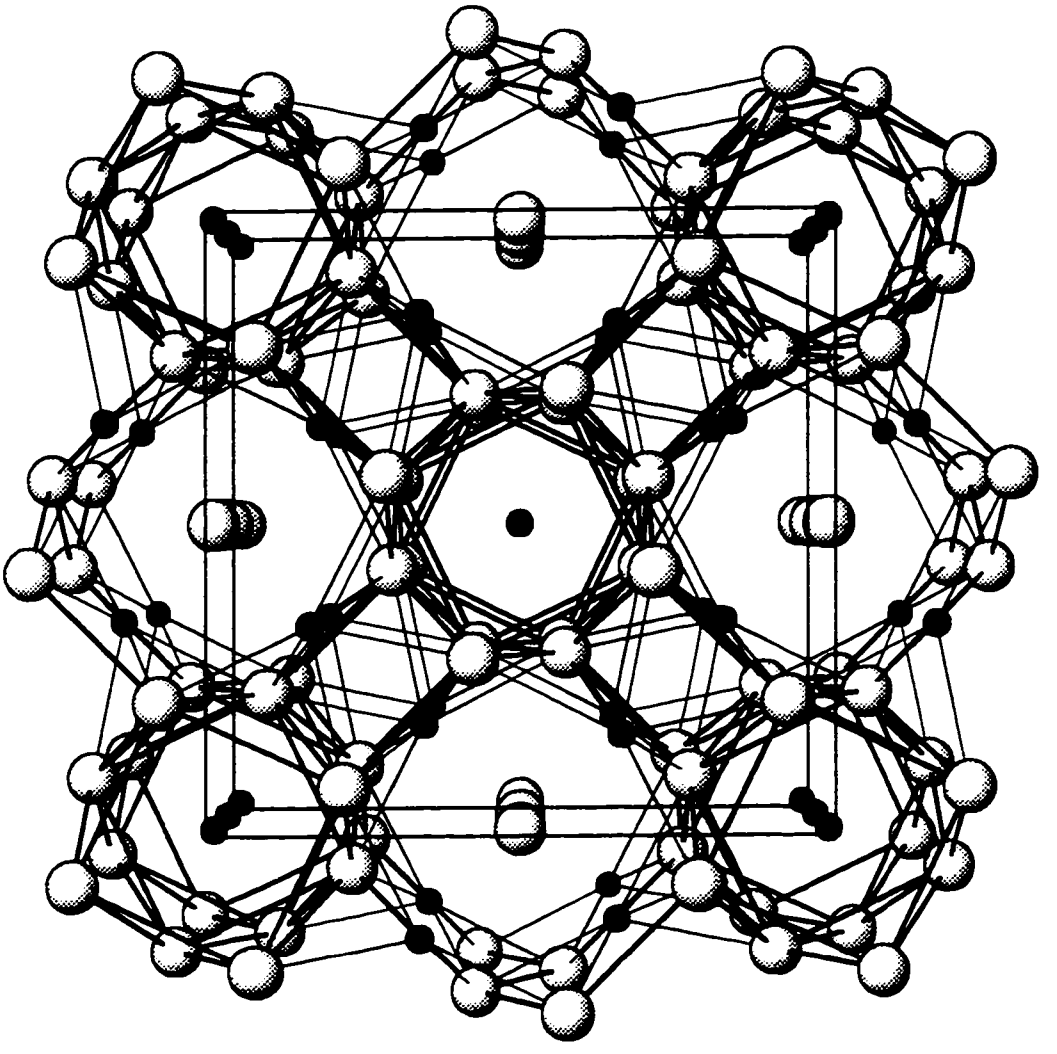

Figure IV-13. Extended [001] view of the W_5Si_3 structure. Small and large spheres represent Si and W atoms, respectively. Lines between atoms do nor represent bonds.

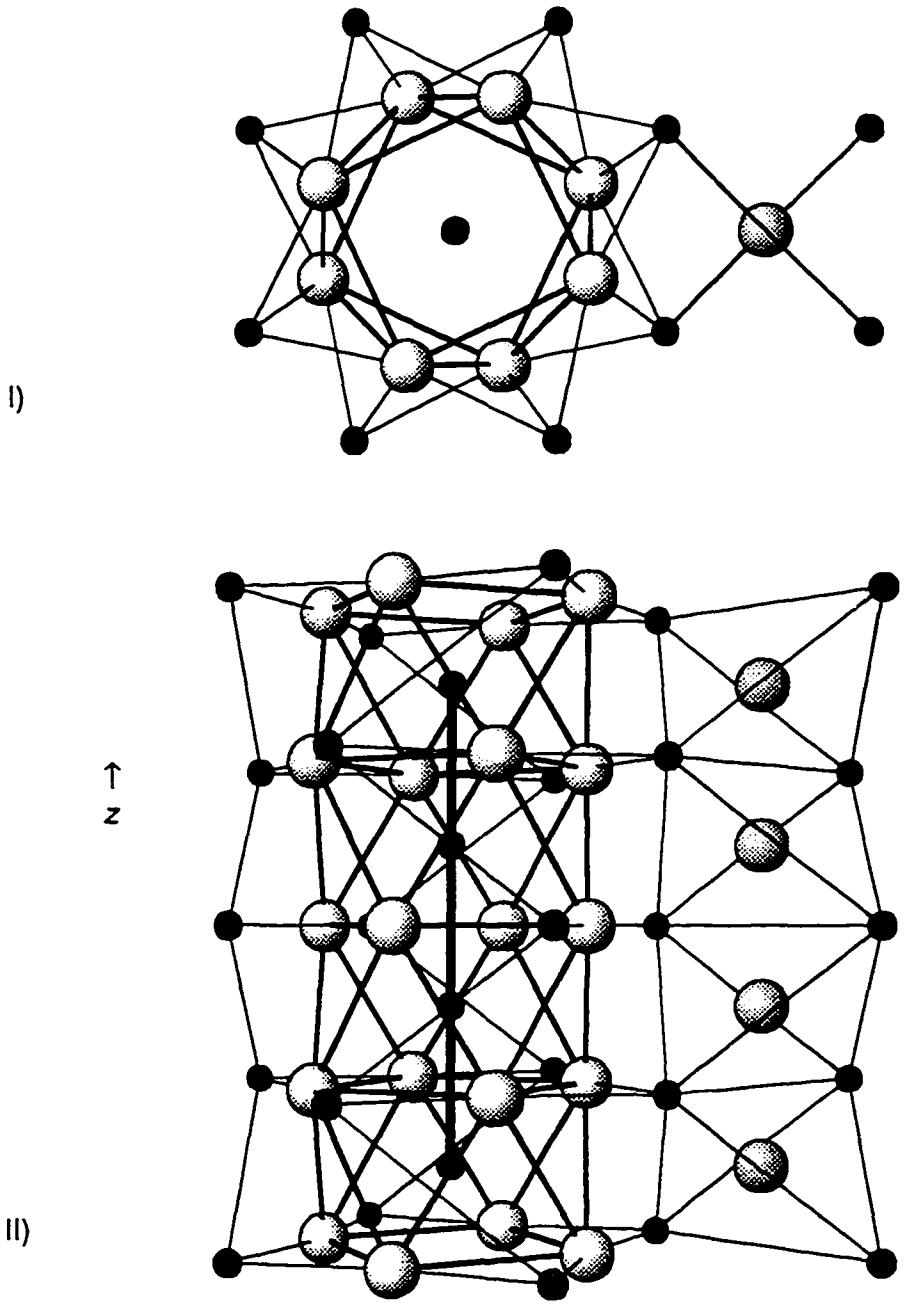

Figure IV-14. Features of the W_5Si_3-type structure. I) Detail of the [001] section; II) Side view of the confacial $^1_\infty[W_{8/2}(Si)Si_{8/2}]$ chain and the linear $^1_\infty[WSi_{4/2}]$ chain. Large and small spheres represent W and Si atoms, respectively. Short Si–Si contact are represented as heavy lines.

type). Significantly, slabs that resemble this structure type are found in sections of other structure types that form part of the $A_{5n+6}B_{3n+5}$ homologous series predicted by Parthé,[186] where n is the number of W_5Si_3-like slabs, e.g., n= 2, 5 and 6 for $Ca_{16}Sb_{11}$, $Ca_{31}Sn_{20}$ and $Yb_{36}Sn_{23}$, respectively, and n= ∞ for the parent compound.

The single crystal structure of the Ba–Pb binary could not satisfactorily be refined in the WS-type structure, since the Ba atoms in the linear chain $^1_\infty[BaPb_{4/2}]$ were troublesome; an anisotropic thermal displacement of U_{33}/U_{11} ~ 125 resulted when the structure was solved in *I4/mcm*. Consequently, problems in the correct selection of the space group were evident. Single crystal film work was not performed in this system, but probably would give some information about the structure of this binary. However, large thermal displacements for the atom that form the linear chain in compounds with the WS-type structure have been observed. For instance, Schewe-Miller[187] found that the $Ca_{0.47}K_4Te_3$ and $Sr_{0.5}K_4Te_3$ phases with the WS-type structure, the alkaline-earth metal atoms are located in the linear chains and are largely anisotropic as well; U_{33}/U_{11} ~16.3 and 7.9, respectively.

The Sm and Eu derivatives form in the M and WS structure types, respectively, either in presence or absence of hydrogen. The former compound takes up some hydrogen as observed from the change in lattice parameters, rxns T95 and T32.

Suspicions about the involvement of hydrogen in the Yb–Pb were prompted by the disparity between previously reported information in the Yb_5Pb_3 system and the results from reaction T4, where products with the P-type structure were found. Gschneidner et al.[3] in the study of the Yb-Pb system identified the Yb_5Pb_3 (M-type) as a phase stable from room temperature up to 1150°C, where a peritectic was detected. However, when such a composition was formed at 1150°C and slowly cooled to 650°C, products in high yield with the P-type structure were identified, either in absence or presence of hydrogen, rxns T4 and T30, respectively; therefore, hydrogen was not stabilizing the reported M-type phase. Such a M-type compound was observed when the reactions were quenched from 900 or 825°C to room temperature, in either the presence or absence of hydrogen, rxns T19, T84 and T84. These results indicated that the hexagonal form of Yb_5Pb_3 is stable at temperatures above 825°C; however, no further

experiments were performed to test other temperatures or compositional effects. Changes in lattice parameters of the products with the M structure indicated that hydrogen can be incorporated in these phases, since a cell volume decrement of ~0.78% was calculated between reactions for the binary (T86) and hydrided form (T19).

Concerns about the shell configuration of the atoms in M-Yb_5Pb_3 were raised when an effective moment of μ_{eff}= 1.55(2) BM (θ= -294K), from a linear least squares fitting to $1/\chi$ vs. T curves (for T >100K); in similarity to the M-$Yb_5Ge_3H_x$ system, a mixed valence compound was expected. Figure IV-15 shows the temperature dependencies of the molar susceptibilities of sample T19 (M-$Yb_5Pb_3H_x$). Despite that the calculated moment suggested a $1e^-$ localized system, it also indicated the lack of significant trivalent ions in the compound; for Yb^{3+}, free ion μ_{eff} = 4.54 BM.[94] Unexpectedly, M-$Yb_5Pb_3H_x$ appears to be an electron-deficient compound, i.e., $5Yb^{2+}$, $3Pb^{4-}$, xH^-. The major divalency of the Yb ions in the compound was also implied by the c/a ratio calculated for the M products of ~ 0.75, since typical trivalent RE_5Pb_3 compounds present c/a ratios between 0.72 – 0.73.[176] Efforts to solve the structure of a crystal from reaction T19 in the standard M cell were not successful. Therefore, it is possible that the superstructure deformations that the Ca_5Pb_3 system undergoes may also occur in the M-Yb_5Pb_3; the Ca^{2+} and Yb^{2+} have similar crystal radii.[62] In partial evidence for this argument, the cell dimensions of the $Yb_5Pb_3H_x$ phases if they had the Ca_5Pb_3-type structure are very similar to those calculated for the parent compound, see Table IV-9. Hence. it would be very interesting to investigate how these two systems relate structurally each other.

Trielides ($A_5Tr_3H_x$)

In an effort to expand the study of the 5:3 systems and the effects of hydrogen on the alkaline-earth or divalent rare-earth metal trielides, several reactions for $A_5Tr_3H_x$ compositions (A= Ca, Sr, Ba, Sm, Eu, Yb; Tr= Al, Ga, In, Tl; for x= 0 and 2.0) were carried out. Information about the chemistry and structures for several of these combinations is very limited; therefore, many of the products of reactions performed in this work could not be identified, but constitute a source for future work. Products in

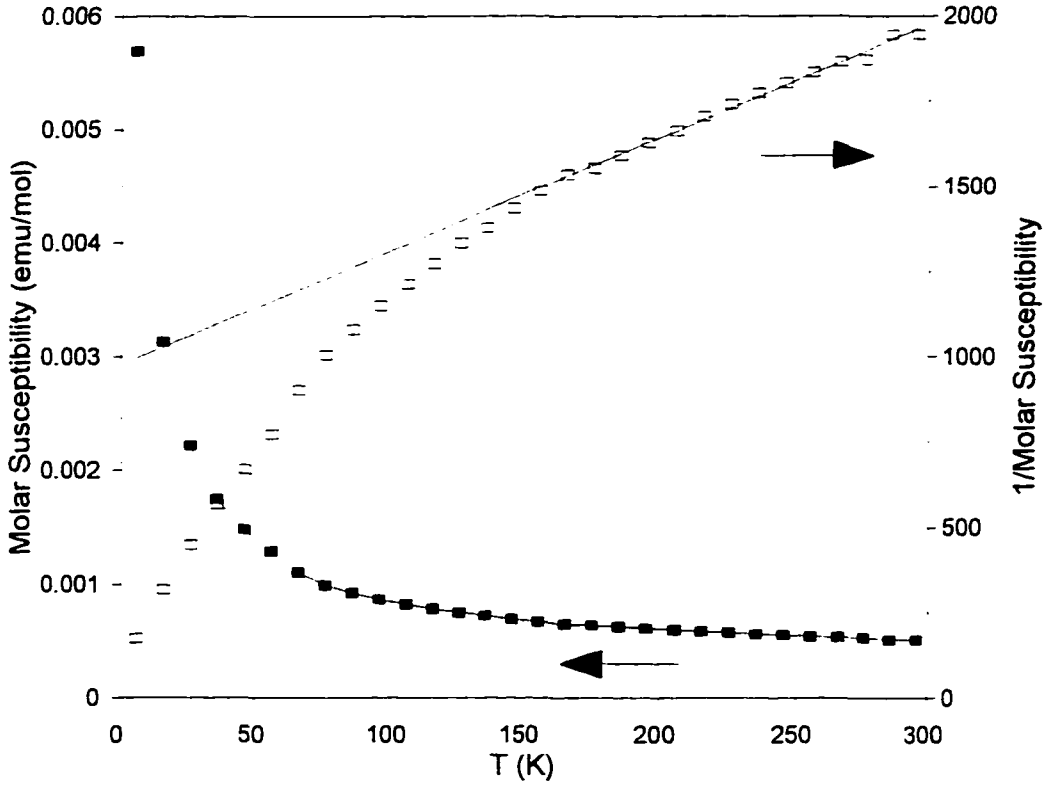

Figure IV-15. Temperature dependence of the molar susceptibilities (χ) at 3 Tesla of M-$Yb_5Pb_3H_x$, (▪) for χ vs. T plot and (▫) for $1/\chi$ vs. T; linear fit for T>150K.

several systems were successfully identified; however, they relate to systems different than 5:3 and will not be discussed. The results of the experimental efforts in these systems and pertinent to $A_5Tr_3H_x$ compositions are listed in Table IV-22. Important lattice parameters are reported in Table IV-23, where previous reported values are included for comparison purposes.

Prior this work, Franceschi et al. reported that Ca_5Ga_3, Sr_5In_3, Sr_5Tl_3[47] and Sm_5Ga_3[189] phases crystallize in the C-type structure and Sm_5Tl_3 in the WS-type.[190,191] Franceschi also reported that elements of the group 12 of the periodic table would adopt the C-type structure, i.e., Ca_5Zn_3, Sr_5Cd_3 and Ca_5Hg_3.[47] More recently, Zhao and Corbett[160] while searching for possible RE_5Ga_3 Zintl phases reported that the Y, La, Gd, Ho and Er derivatives crystallize in the Ba_5Si_3-type structure. Additionally, they suggested that Sm_5Ga_3 should crystallize in this structure type as well.

The results of our experiments showed that the binaries Ca_5Ga_3 and Sr_5In_3 indeed form in the C-type structure, rxns PE3 and PE6, respectively. The gallide and indide compounds do not take up hydrogen in sizable quantities, since the lattice parameter of the products that saw hydrogen remained invariant, rxns PE11 and PE16, respectively. The single crystal structure of Ca_5Ga_3 was successfully solved in the C-type and its crystallographic and refined data information are given in Tables IV-24, IV-25 and IV-26. An important feature of this structure is the short Ga(2)–Ga(2) dimer interatomic distance of 2.493(1) Å. Such a distance is shorter than that reported for Ga–Ga dimers in RE_5Ga_3 (RE= Y, La, Gd) of 2.637 – 2.654 Å.[160] Reactions in the presence of hydrogen in the Ga and In systems gave among the products the cubic $Ca_{11}Ga_7$-type (CG) as major phase, where the $Sr_{11}In_7$ phase was identified for first time. Initially, the cubic phases with $Ca_{11}Ga_7$-type structure were believed to be a hydrogen-stabilized compound; however, subsequent experiments in each system demonstrated that they form under dv conditions as well, with no evident change in their lattice parameters, rxns PE32 and PE33. Consequently, the formation of CG phases in reactions PE11 and PE16 (loaded $Ca_5Ga_5H_{2.0}$) and PE18 ($Sr_5In_5H_{2.0}$), were caused by an upset in the reaction composition due to nonreactivity of the AH_2 or AF_2 components.

The $Sr_5Tl_3H_x$ phase in the C-type structure is a hydrogen-stabilized compound. It

Table IV-22. Distribution of products for reactions $A_5Tr_3(H,F)_x$.

Rxn. No.	Loaded Composition[a]	Conditions[b]		Product Distribution[c]
PE3	Ca_5Ga_3	i	dv	C ~85, OCB ~10%
PE11	$Ca_5Ga_3H_{2.0}$	ii	sc	CG ~75%, C ~10%, OCB ~15%
PE32	$Ca_{11}Ga_7$	ii	dv	CG ~50%, C ~45%, OCB ~5%
PE41	$Ca_{11}Ga_7H_{3.0}$	ii	sc	CG ~90%, OCB~10%
PEF4	Ca_5Ga_3F	i	dv	CG ~50%, C ~35%, OCB ~10%, CaF_2 ~5%
PE35	Sm_5Ga_3	ii	dv	C ~70%, GC ~30%
PE44	$Sm_5Ga_3H_{2.0}$	ii	sc	UPE44
PE6	Sr_5In_3	i	dv	C ~95%, Un
PE16	$Sr_5In_3H_{2.0}$	ii	sc	CG ~70%, C ~25%, OCB ~5%
PE33	$Sr_{11}In_7$	ii	dv	CG ~ 98%
PE42	$Sr_{11}In_7H_{3.0}$	ii	sc	C ~40%, Un
PE25	Sr_3Tl_3	ii	dv	UPE25
PE34	Sr_5Tl_3	iii	dv	UPE25
PE17	$Sr_5Tl_3H_{2.0}$	ii	sc	C >>95%
PE43	$Sr_5Tl_3H_{2.0}$	iii	sc	C ~98%, Cl ~2%
PEF9	Sr_5Tl_3F	ii	dv	UPE25, CC ~10%, SrF_2 ~10%
PE27	Sm_5Tl_3	ii	dv	WS ~65%, ANI ~30%, Un
PE46	$Sm_5Tl_3H_{2.0}$	ii	sc	WS ~80%, Un

[a] Reactions denoted $A_5Tr_3H_{x.0}$ were loaded with dehydrogenated A metal.

[b] Conditions: i) Reaction at 1100°C for 2h then cooled to 550 at 5°C/h. Annealed for 30h at 550°C and then cooled to 350–300°C at 10°C/h.
ii) Similar to (1) but reaction temperature 1150°C.
sc = Reaction in a sealed fused silica container.
dv = Reaction under dynamic vacuum.

[c] Estimated from Guinier patterns.; C= Cr_5B_3-type, OCB= CrB-type, CG= $Ca_{11}Ga_7$ type, GG= Gd_3Ga_2-type, Cl= $CaIn_2$-type, CC= CSCl-type, ANI= anti-$NiIn_2$, Un or UPE#= unidentified and unidentified in reaction PE#.

Table IV-23. Lattice dimensions of reactions some $A_5Tr_3(H,F)_x$.

Rxn No.	Loaded Comp.[a]	Str.Type/ Conds.[b]	a (Å)	c (Å)	Vol.(Å^3)	a/c	Ref.
	Ca_5Ga_3	C/sc	7.954	15.084	954.3	0.527	47
	$Ca_{11}Ga_7$	CG/sc	16.109(2)		4180.3	1.000	188
PE3	Ca_5Ga_3	C/dv	7.9737(4)	14.989(1)	953.0(1)	0.532	
PE11	$Ca_5Ga_3H_{2.0}$	C/sc	7.9801(7)	14.981(2)	954.1(2)	0.533	
PE11	$Ca_5Ga_3H_{2.0}$	CG/sc	16.1289(5)		4195.8(4)	1.000	
PE32	$Ca_{11}Ga_7$	CG/dv	16.1165(9)		4186.2(7)	1.000	
PE41	$Ca_{11}Ga_7H_{3.0}$	CG/sc	16.1194(4)		4188.4(3)	1.000	
	Sm_5Ga_3	C/sc	7.796	14.420	876.4	0.541	189
	Sm_5Ga_3	C/sc	7.783	14.24	862.6	0.547	24
PE35	Sm_5Ga_3	B/dv	7.788(1)	14.280(2)	866.1(2)	0.545	
	Sr_5In_3	C/sc	8.738	16.442	1255.4	0.531	47
PE6	Sr_5In_3	C/dv	8.7570(6)	16.440(2)	1260.7(2)	0.533	
PE16	$Sr_5In_3H_{2.0}$	C/sc	8.7582(8)	16.431(2)	1260.4(2)	0.533	
PE42	$Sr_{11}In_7H_{3.0}$	C/sc	8.7592(7)	16.429(2)	1260.5(2)	0.533	
PE33	$Sr_{11}In_7$	CG/dv	17.6992(7)		5544.5(6)	1.000	

Table IV-23. Continued

Rxn No.	Loaded Comp.[a]	Str.Type/ Conds.[b]	a (Å)	c (Å)	Vol.(Å^3)	a/c	Ref.
	Sr_5Tl_3	C/sc	8.635	16.389	1220.0	0.527	47
PE17	$Sr_5Tl_3H_{2.0}$	C/sc	8.6502(4)	16.414(1)	1228.2(1)	0.527	
PE43	$Sr_5Tl_3H_{2.0}$	C/sc	8.6497(6)	16.431(2)	1229.3(2)	0.526	
	Sm_5Tl_3	WS/sc	12.346	6.140	935.9	0.497[c]	190
	Sm_5Tl_3	WS/sc	12.35	6.145	937.2	0.498[c]	191
PE27	Sm_5Tl_3	WS/dv	12.3523(5)	6.1078(9)	931.9(1)	0.494[c]	

[a] Reactions denoted $A_mTr_nH_{x.0}$ were loaded with dehydrogenated A metal.
[b] Cells indexed for C= Cr_5B_3-type, B= Ba_5Si_3-type, CG= $Ca_{11}Ga_7$-type (cubic) and WS= W_5Si_3-type structures. Conditions: dv= dynamic vacuum and sc= sealed container.
[c] $(a/c)^{-1}$.

Table IV-24. Crystallographic data for $A_5Tr_3H_x$ phases.

	Ca_5Ga_3	$Sr_5Tl_3H_x$	Sm_5Ga_3
Crystal from rxn.	PE3	PE43	PE35
Space Group	$I\bar{4}/mcm$(#140)	I4/mcm	P4/nnc(#130)
Lattice parameters[a]			
a (Å)	7.9737(4)	8.6497(6)	7.788(1)
c (Å)	14.989(1)	16.431(2)	14.280(2)
Volume ($Å^3$)	953.0(2)	1229.3(3)	866.1(2)
Z	4	4	4
Density calc. (g/cm^3)	2.854	5.685	7.370
Crystal dim. (mm)	0.06x0.20x0.28	0.11x0.14x0.28	0.09x0.16x0.26
Diffractometer	Enraf-Nonius CAD4	Enraf-Nonius CAD4	Rigaku AFC6R
Collected octants	-h,-k,±l	-h,k,l	±h,k,±l
Scan type	ω-2θ	ω-2θ	ω-2θ
2θ limit	54	50	50
Transmission range	0.898–1.059	0.624–1.238	0.872–1.148
Absorption coeff. (cm^{-1})	109.5	603.9	425.5
Number of reflections			
Measured (observed[b])	2381(963)	1289(361)	3299(2082)
Independent (observed[b])	836(343)	861(228)	514(329)
R_{ave} (%)[c]	3.46	17.7(4.95[b])	6.21
No. of refined variables	16	16	22
R/R_w (%)	1.7/2.4	4.5/4.8	2.3/3.1
Goodness of fit	2.454	1.565	2.958
Secondary ext.coeff. ($x10^{-7}$)	6.3(6)	5(2)	2.9(3)
Max./min. peak in ΔF map ($e^- Å^{-3}$)	0.52/-0.46	2.51/-2.80	2.44/-1.79

[a] Lattice parameters calculated from Guinier powder patterns.
[b] Observed reflections; $I \geq 3.00\sigma_I$.
[c] All reflections $I > 0$.

Table IV-25. Refined positional and thermal parameters for $A_5Tr_3(H_x)$ phases.

Atom	x	y	z	$B_{eq}(Å^2)$	U_{11}	U_{22}	U_{33}	U_{12}	U_{13}	U_{23}
Ca_5Ga_3 (PE3, Cr_5B_3-type)										
Ca(1)	0	0	0	1.52(3)	0.0151(5)	U_{11}	0.0276(8)	0	0	0
Ca(2)	0.17673(6)	x + ½	0.14431(5)	1.30(2)	0.0178(3)	U_{11}	0.0138(3)	0.0001(3)	-0.0016(2)	U_{13}
Ga(1)	0	0	¼	1.47(2)	0.0170(3)	U_{11}	0.0218(5)	0	0	0
Ga(2)	0.38944(5)	x + ½	0	1.20(2)	0.0148(3)	U_{11}	0.0160(3)	-0.0006(2)	0	0
$Sr_5Tl_3H_x$ (PE43, stuffed-Cr_5B_3-type)										
Sr(1)	0	0	0	1.9(2)	0.015(2)	U_{11}	0.042(5)	0	0	0
Sr(2)	0.1702(3)	x + ½	0.1475(2)	1.32(8)	0.020(1)	U_{11}	0.010(2)	-0.001(1)	-0.004(1)	U_{13}
Tl(1)	0	0	¼	1.47(7)	0.018(1)	U_{11}	0.020(2)	0	0	0
Tl(2)	0.3774(2)	x + ½	0	1.00(5)	0.0131(7)	U_{11}	0.012(1)	-0.001(1)	0	0
(H	0	½	¼)							
Sm_5Ga_3[a] (PE35, Ba_5Si_3-type)										
Sm(1)	¼	¼	0.2671(1)	1.59(4)	0.0122(5)	U_{11}	0.036(1)	0	0	0
Sm(2)	0.07290(8)	0.91072(8)	0.39868(5)	0.95(4)	0.0129(4)	0.0127(4)	0.0105(6)	0.0001(2)	0.0011(3)	-0.0009(3)
Ga(1)	¼	¼	0.4957(2)	0.86(7)	0.0101(8)	U_{11}	0.012(2)	0	0	0
Ga(2)	0.6293(2)	-x	¼	0.78(5)	0.0097(6)	U_{11}	0.010(1)	-0.0004(8)	-0.0003(6)	U_{13}

[a] Origin at $\bar{1}$.

Table IV-26. Selected interatomic distances of $A_5Tr_3(H_x)$, (Å).

$Cr_5B_3(Z)$-type			Ba_5Si_3-type	
Atom(1) – Atom(2)	Ca_5Ga_3	$Sr_5Tl_3H_x$	Atom(1) – Atom(2)	Sm_5Ga_3
Tr(1) – Tr(2) (1x)	2.493(1)	2.999(4)	Ga(2) – Ga(2) (1x)	2.658(4)
Tr(1) – A(1) (2x)	3.7473(4)	4.1077(5)	Ga(2) – Ga(2) (4x)	4.384(1)
Tr(1) – A(2) (8x)	3.3376(4)	3.625(2)	Ga(1) – Sm(1) (1x)	3.264(3)
Tr(2) – A(1) (2x)	3.2280(3)	3.433(1)	Ga(1) – Sm(1) (1x)	3.876(3)
Tr(2) – A(2) (2x)	3.2300(8)	3.507(4)	Ga(1) – Sm(2) (4x)	3.189(2)
Tr(2) – A(2) (4x)	3.1946(7)	3.529(3)	Ga(1) – Sm(2) (4x)	3.287(1)
A(1) – A(2) (8x)	3.6482(5)	4.022(3)	Ga(2) – Sm(1) (2x)	3.1096(9)
A(2) – A(2) (1x)	3.573(2)	3.894(7)	Ga(2) – Sm(2) (2x)	3.083(1)
A(2) – A(2) (1x)	3.986(1)	4.165(6)	Ga(2) – Sm(2) (2x)	3.144(1)
A(2) – A(2) (1x)	4.326(2)	[4.847(8)]	Ga(2) – Sm(2) (2x)	3.160(1)
A(2) – A(2) (2x)	4.241(1)	4.475(7)	Sm(1) – Sm(2) (4x)	3.523(1)
A(2) – A(2) (4x)	4.1545(4)	[4.540(1)]	Sm(1) – Sm(2) (4x)	3.674(1)
A(2) – H	—	2.676(4)	Sm(2) – Sm(2) (1x)	3.405(2)
			Sm(2) – Sm(2) (1x)	3.725(1)
			Sm(2) – Sm(2) (1x)	4.250(2)
			Sm(2) – Sm(2) (2x)	3.913(1)
			Sm(2) – Sm(2) (2x)	3.973(1)
			Sm(2) – Sm(2) (2x)	4.215(1)

was observed only in reactions that involved hydrogen, rxns PE17 and PE43. Reactions under dynamic vacuum gave products that could not be identified to any binary in the Sr–Tl system or in other reported A–Tr systems. Near reproducibility of lattice parameters of the ternary hydride suggests that the phase is probably stoichiometric, $Sr_5Tl_3H_x$, x~1; albeit, experiments with variable hydrogen content were not performed. The structure of this thalide was solved as the C-type and its crystallographic and refined data information are given in Tables IV-24, IV-25 and IV-26. Importantly, the Tl–Tl distance of 2.999(4) Å in the dimer is shorter than from other reports of compounds containing dimers. e.g., in Li_5Tl_2, d_{Tl-Tl} = 3.01 Å.[192] An attempt to incorporate fluoride in the interstitial cavities of the structure was unsuccessful, rxn PEF9 in Table IV-22.

In concordance with Zhao and Corbett predictions,[160] the binary Sm_5Ga_3 phase crystallizes in the Ba_5Si_3-type, rxn PE35, as determined by single crystal diffraction work. Crystallographic and refined data information for the binary are given Tables IV-24, IV-25 and IV-26. A reaction in the presence of hydrogen gave unidentified products, rxn PE44. Formation of the Sm_5Ga_3 in the B-type structure supports our claim that systems that involve small anions, Si or Ga, and large cations in electron deficient or electron precise systems, e.g., Ba_5Si_3 ($5Ba^{2+}$, Si_2^{6-}, Si^{4-}) and $Ba_5Si_3(H,F)_x$, or trivalent metal ions for electron rich systems, e.g., La_5Si_3 ($5La^{3+}$, Si_2^{6-}, Si^{4-}) and La_5Ga_3 ($5La^{3+}$, Ga_2^{8-}, Ga^{5-}),[160] would probably to crystallize in the B-type structure. Apparently, the specific electronic requirements for this primitive distortion of the C-type structure are the source of our lack of success in inserting either hydrogen or fluoride in the tetrahedral cavities of the Sm_5Ga_3 phase, rxns PE44 and PEF4, respectively.

In agreement with previous reports, the Sm_5Tl_3 was found to crystallize in the WS-type structure, rxns PE27 and PE43. Additional experiments for the Ca_5Zn_3 system, rxns CL2 (loaded Ca_5Zn_5), CL4 ($Ca_5Zn_3H_{2.0}$) and CLF1 (Ca_5Zn_3F) not listed in tables, indicated that hydrogen or fluoride were not involved in their formation. Böttcher and group in recent years have solved the structure of the Ca_5Zn_3,[158] Sr_5Cd_3 and Ca_5Hg_3[159] compounds and found them to be in the C-type in concordance with Franceschi's original report.

Electrical resistivity and magnetic properties

The mere existence of the hydrogen or fluoride stabilized $A_5Tt_3(H,F)_x$ compounds as well as the possibility of interstitially inserting hydrogen or fluoride in several of the phases with the C-type structure, prompted us to question how the systems cope with their electron deficiency without distorting towards formation of additional Tt–Tt bonds or even extended structures. Use of the two–electron–two–center ideas or Zintl concepts cannot illuminate more about these compounds, e.g., Ca_5Sn_3H; $5Ca^{2+}$, Sn_2^{6-}, Sn^{4-}, H^-, since the binaries are already considered electron precise compounds, e.g., Ca_5Ge_3; $5Ca^{2+}$, Ge_2^{6-}, Ge^{4-}. Some chemical intuition would suggest that the hydride, or fluoride, is withdrawing electrons from the Tt–Tt dimer states.

Certainly, extended Hückel-MO band calculation for the Ca_5Sn_3H model suggest that the Sn(2) π^* electronic states in the dimer are partially depleted by hydrogen to form a H^- band. The left of Figure IV-16 shows the DOS plot for the Ca_5Sn_3H model; s states at ~ -19 and ~ -15 eV and p at ~ -9 eV from the Sn(2)–Sn(2) dimer and H^- band at ~ -14 ev, where the Fermi level (ε_F) at –7.361 eV (for a $40e^-$ and 50 k-point calculation) falls on a energy band of substantial size made primarily of p states of the Sn(2) atoms. The Sn(2) total atom orbital contribution is shaded in this plot. The right of Figure IV-16 depicts the COOP curves for the Sn(2)–Sn(2) and average Ca-Sn interactions, where π^* antibonding interactions of the former fall around the Fermi level. The destabilizing effect of the antibonding Sn(2)–Sn(2) interactions are partially cancel by the large bonding interactions below the level. In principle, the results of these calculations could be partially predicted by a simple MO calculation for a $[Sn–Sn]^{6-}$ species, where the HOMO states are those of π^*_p. The last COOP curve in Figure IV-16 suggest that Ca–Sn bonding interactions occur at the Fermi level as well. According to these EHMO band calculations, the Ca_5Sn_3H, and Ca_5Sn_3F phases should be metallic conductors and consequently Pauli paramagnetic. The molar susceptibilities of samples T21 ($Ca_5Sn_3H_{\sim 1}$) and TF2 (Ca_5Sn_3F) are in fact essentially temperature-independent paramagnetic as shown in Figure IV-17. The slight temperature dependence is probably due to spin contributions to the magnetism. Extrapolating the results of these calculations to other equivalent systems enables us to anticipate metallic-like resistivities and temperature

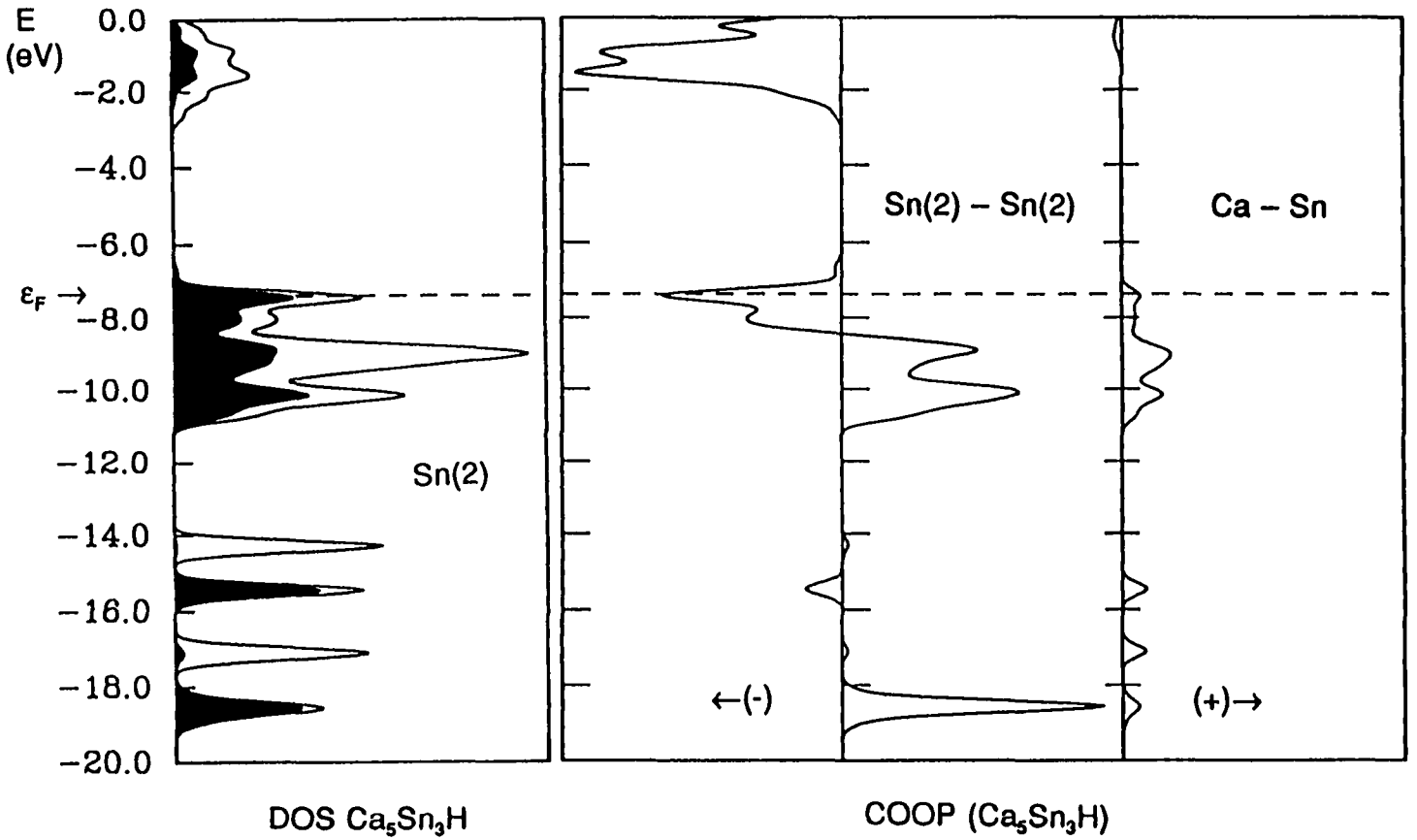

Figure IV-16. Graphical results of the Extended Hückel-MO band calculations for Ca_5Sn_3H with the C-type structure. To the left, the total DOS of Ca_5Sn_3H with the Sn(2) total atomic orbital projection shaded; To the right the COOP curves for the Sn(2)–Sn(2) dimer and average Ca–Sn interactions. Dashed lines signify the Fermi level (ε_F).

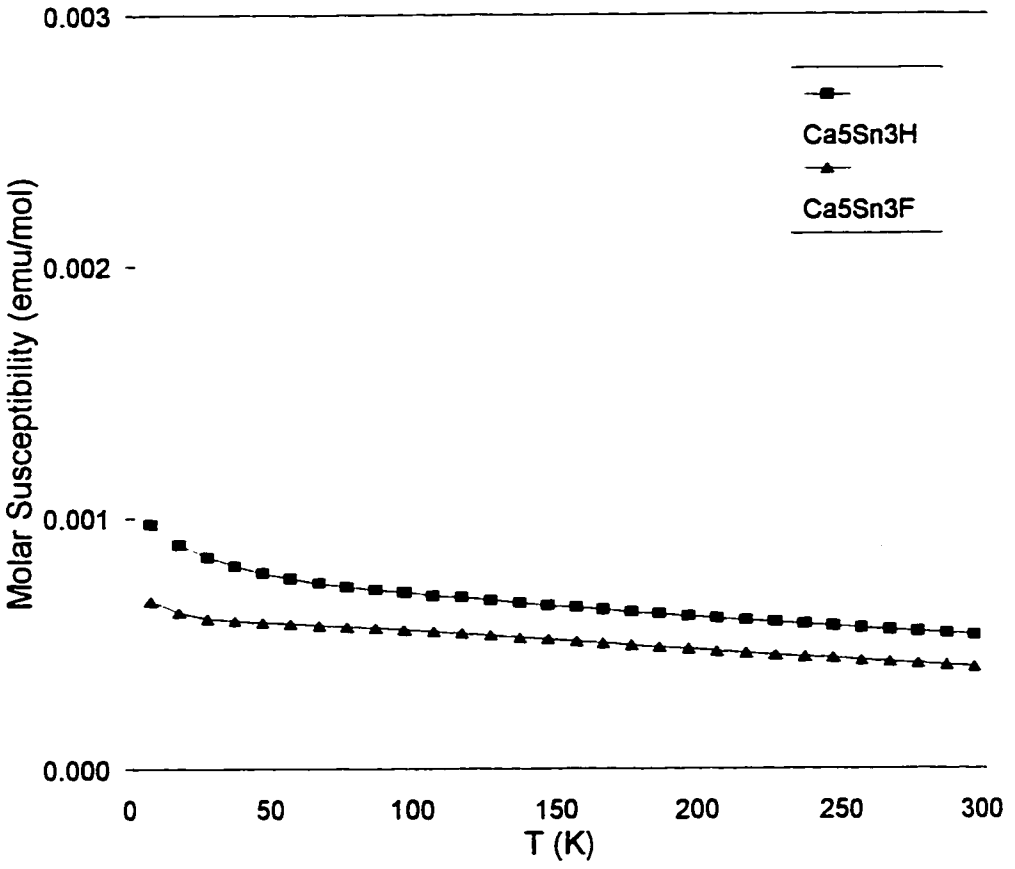

Figure IV-17. Temperature dependence of the molar susceptibilities (χ) at 3 Tesla of $Ca_5Sn_3H_x$ (■) and $Ca_5Sn_3F_{0.9}$ (▲).

independent paramagnetic behaviors for all ternary phases C-$A_5Tt_3(H,F)_x$. The results of magnetic measurements of several $A_5Tt_3(H,F)_x$ samples are summarized in Table IV-27, where in some instances the effective moment (μ_{eff}) and Weiss constant (θ) were calculated as a means to quantify the temperature dependencies. In general, the electrical resistivity and magnetic properties of these ternaries should be those of metallic-like compounds.

At difference from the ternaries, the binaries A_5Tt_3 are expected to be valence compounds since close shell configurations are formally achieved. Theoretical band calculations for C-Ca_5Ge_3 would suggest that the Fermi level is located within an energy gap, indicative of semiconducting and diamagnetic compounds in these systems. However, as depicted in Figure IV-18, the molar susceptibilities of sample T34, binary Ca_5Ge_3, are temperature-independent paramagnetic. Because such an unexpected behavior might have been onset by the minor percentage phase component in T34, the electrical resistivity of sample T34 was measured by the Q method. The impurity phase CaGe in T34 was expected to show a metallic behavior. In support of the magnetic measurements, sample T34 presented a positive temperature factor of 0.32(4)% K and a room temperature electrical resistivity of ~ 88 Ω·cm, characteristic of poor metallic systems, see Figure IV-19. One could speculate that the metallic behavior in Ca_5Ge_3 is caused small quantities of hydrogen in the compound that could not be removed totally during the reactions under vacuum, similar to the Y-$A_5Pn_3H_x$ systems in the previous chapter. As predicted, the ternaries $Ca_5Ge_3H_x$ and $Ca_5Ge_3F_{\sim 0.7}$ show paramagnetic temperature independent molar susceptibilities, see Figure IV-18, where the larger susceptibility values for the ternary hydride have probably some van Vleck contribution to the magnetism. The temperature dependence of the electrical resistivity of the ternary hydride (sample T34) presents a positive slope with a calculated temperature coefficient and room temperature electrical resistivity values of 0.24(4) % K and ~ 170 Ω·cm, respectively, see Figure IV-20. It is still not clear how electrical conductivity is achieved in the binary systems, and further experiments and calculations are required.

Deviations from the predicted metallic like behaviors are observed for systems involving larger cations or anions. Thus, the Sr_5Ge_3 (sample T35) and $Sr_5Ge_3H_x$ (T41)

Table IV-27. Magnetic measurements on several compounds with the C-type structure.

Rxn. No.	Loaded Composition	Magnetic Information		
		Interpreted Behavior[a]	μ_{eff}(BM)/θ(K)[b]	$\chi_{M(298K)} \times 10^{-6}$ (emu/mol)
T34	Ca_5Ge_3	PP	—	189
T33	$Ca_5Ge_3H_{2.0}$	PP	—	7860
TF1	Ca5Ge3F	PP	—	585
T35	Sr_5Ge	PP	—	163
T41	$Sr_5Ge_3H_{2.0}$	PCW	1.67(5)/-161	767
T21	$Ca_5Sn_3H_{2.0}$	PP	—	531
TF2	Ca_5Sn_3F	PP	—	404
T1	Sr_5Sn_3	PP	—	144
T23	$Sr_5Sn_3H_{2.0}$	PCW	1.59(4)/-64	888
TF12	Sr_5Pb_3F	PP	—	346
PE17	$Sr_5Tl_3H_{2.0}$	PP	—	343

[a] Interpreted behavior of the molar susceptibilities after corrections: D= Diamagnetic; PP= Pauli Paramagnetic; PCW= Paramagnetic Curie-Weiss.
[b] Effective moment (μ_{eff}) and Weiss constant (θ) calculated from a linear fit of $1/\chi$ vs. T plots; for T >100K.

phases showed Pauli and Curie-Weiss-like behaviors, respectively, as delineated in Figure IV-21. An effective moment and Weiss constant of 1.67(5) BM and ~ -161 K were calculated from $1/\chi$ vs. T curves for the latter phase, T > 100K. Such a Curie-Weiss behavior became more definite in the $Sr_5Sn_3H_x$ phase (T23), see Figure IV-22, an effective moment of 1.59(4) BM (θ = -64 K) are calculated for this phase, for T > 100K. One could consider that some localization of the holes created by H^- is occurring in the structure. Curie-Weiss magnetic behaviors are unconventional in compounds involving only p elements and require more study. Adversely, the sample $Sr_5Sn_3H_x$ was EPR silent from liquid N_2 to room temperature. Ternary fluorides of later elements like Sr_5Pb_3F

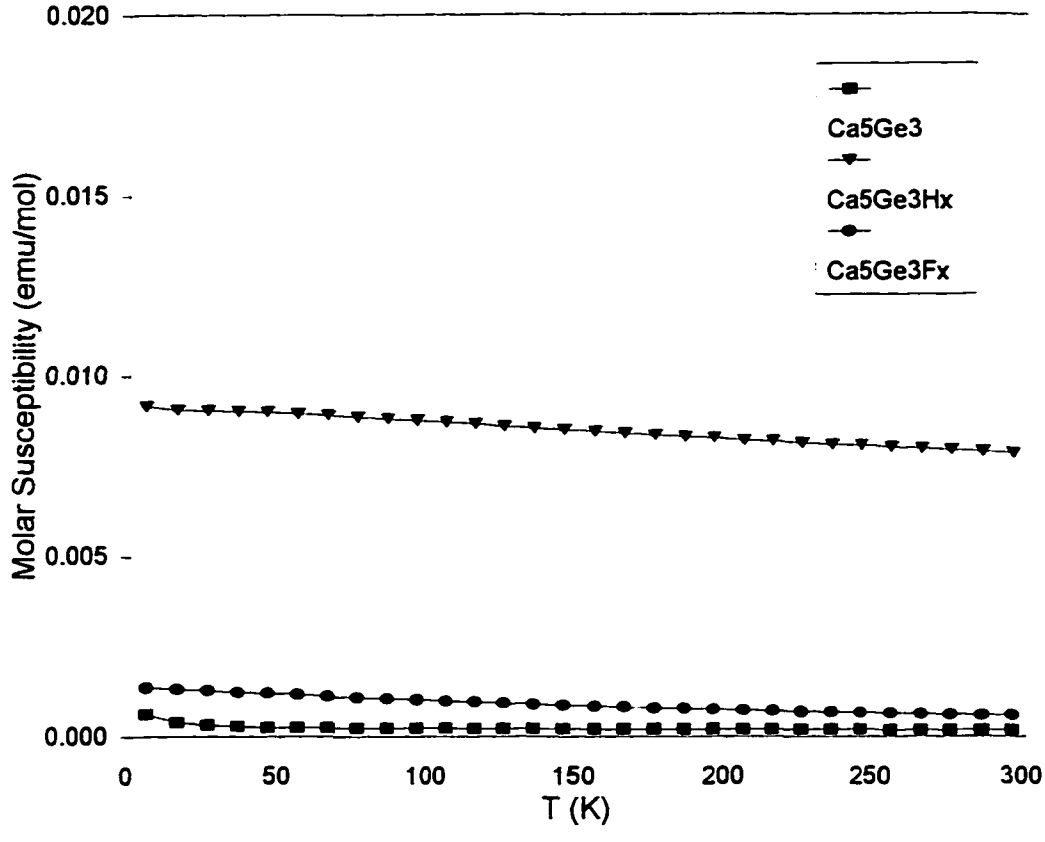

Figure IV-18. Temperature dependence of the molar susceptibilities (χ) at 3 Tesla of Ca_5Ge_3 (■), $Ca_5Ge_3H_{2.0}$ (▾) and $Ca_5Ge_3F_{0.7}$ (•).

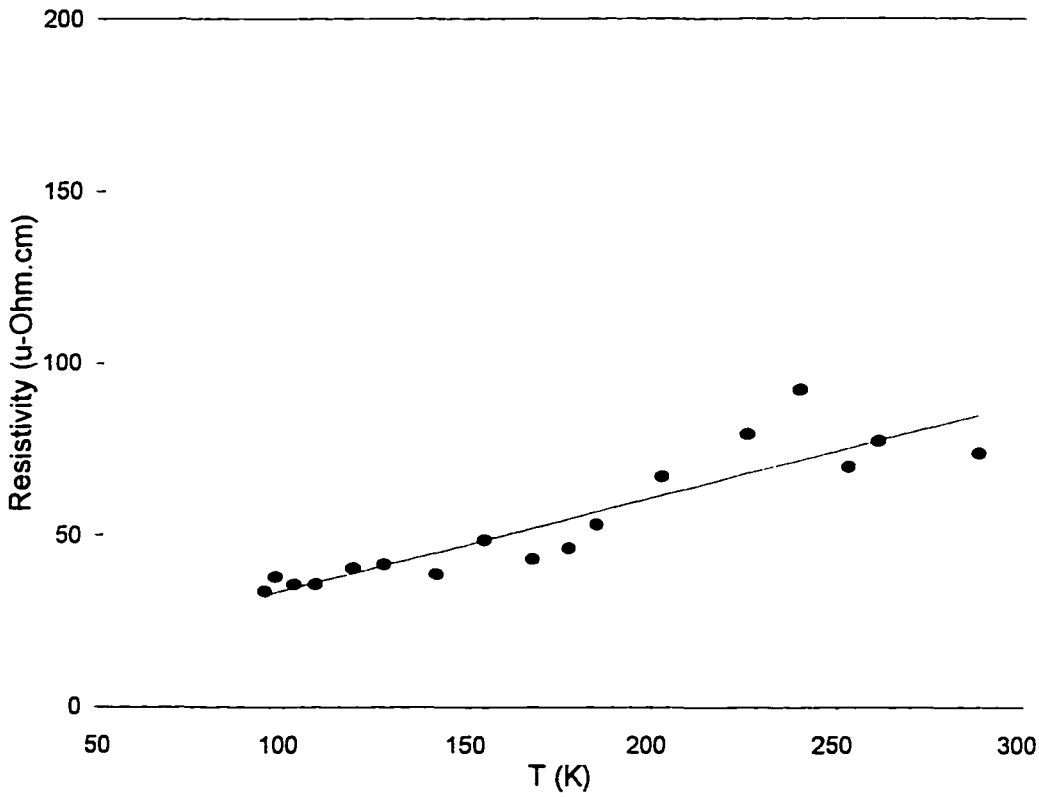

Figure IV-19. Temperature dependence of the electrical resistivity (μΩ·cm) of sample T34, Ca_5Ge_3, measured by the Q method. The temperature coefficient calculated from the slope of the ρ versus T curve is 0.32(4)% K^{-1}.

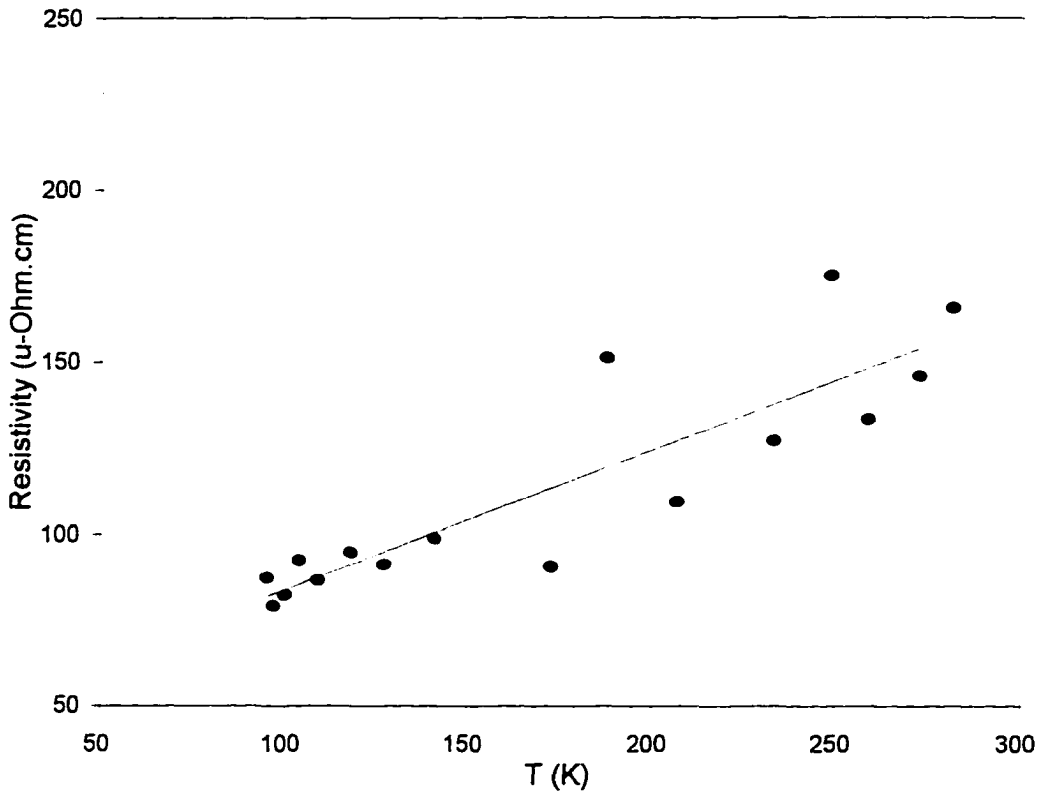

Figure IV-20. Temperature dependence of the electrical resistivity (μΩ·cm) of sample T33, $Ca_5Ge_3H_x$ measured by the Q method. Temperature coefficient 0.24(6)% K^{-1}.

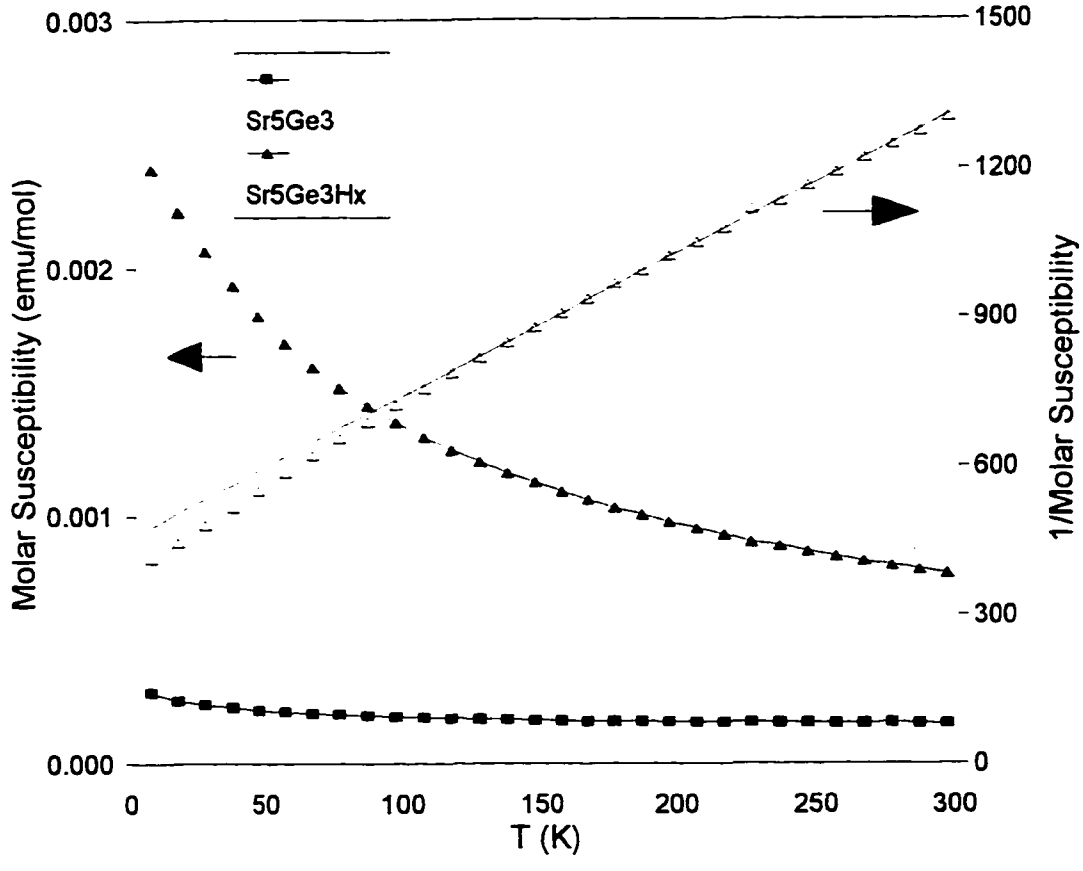

Figure IV-21. Temperature dependence of the molar susceptibilities (χ) at 3 Tesla of Sr_5Ge_3 (■) and $Sr_5Ge_3H_x$ (▲). Solid symbols correspond to χ vs. T plots and empty symbols to $1/\chi$ vs. T; linear fit for T > 100K.

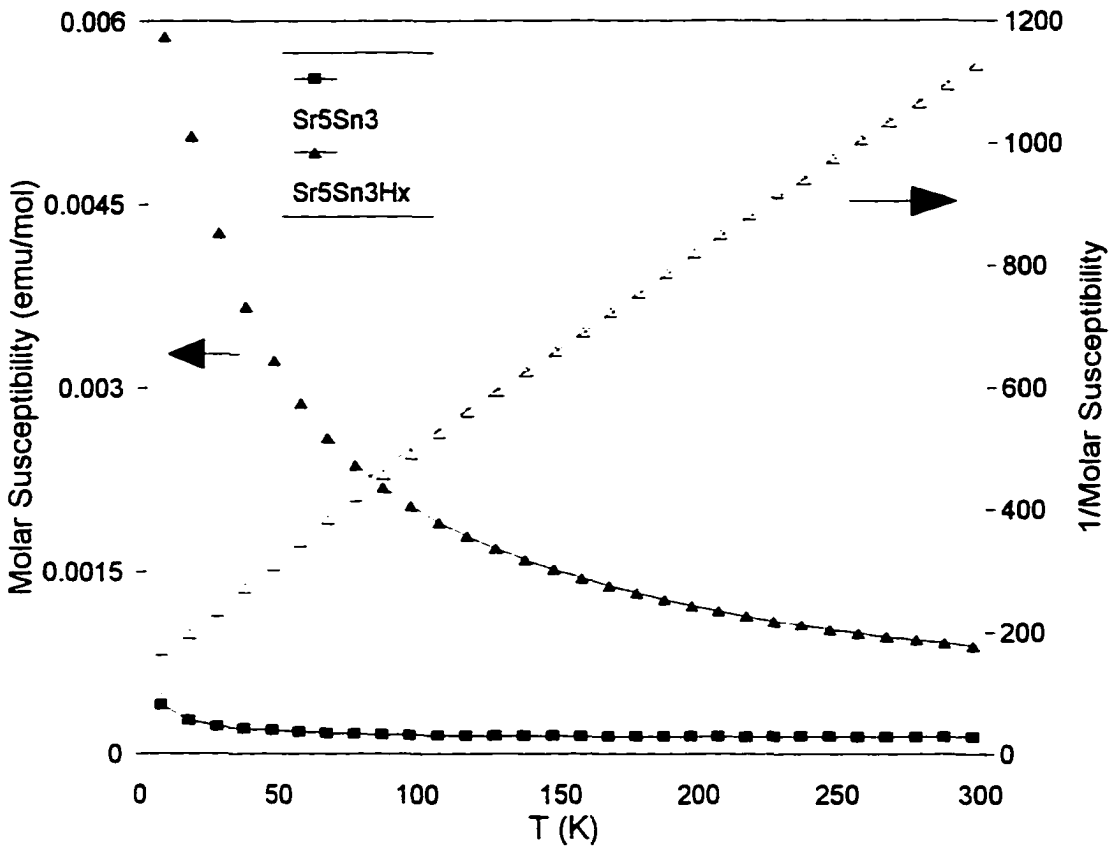

Figure IV-22. Temperature dependence of the molar susceptibilities (χ) at 3 Tesla of Sr_5Sn_3 (■) and $Sr_5Sn_3H_x$ (▲). Solid symbols correspond to χ vs. T plots and empty symbols to $1/\chi$ vs. T; linear fit for T > 100K.

(TF12) showed nearly temperature independent paramagnetic signals as do other ternary fluorides, see Figure IV-23.

The oxidation of the Tt–Tt dimers by hydrogen or fluoride suggest that multiple bond interactions may occur in the ternary systems. Assumption of localized states in the stoichiometric compound Ca_5Sn_3H implies a 1.5 bond order (b.o.) between the tin atoms, $5A^{2+}$, Sn_2^{5-}, Sn^{4-}, H^-. Multiple bonds between elements from the third or higher periods are traditionally considered unstable because their large atomic radii impede effective $p\pi$-$p\pi$ overlap between neighboring atoms, and oligomerization or atomization become energetically more favorable. Nonetheless, several examples exist, e.g. the lithium compounds $Li_{14}Si_6$, Li_9Ge_4, $Li_{13}Sn_5$, Li_8Pb_3, etc.,[11,193] where double bonds $[Tt{=}Tt]^{4-}$ have been claimed. Miller recently in a review about the structure and bonding of Zintl compounds discussed the possibility of multiple bonds in intermetallic systems.[15]

The ease of oxidation of the Tt–Tt bond in binaries and ternaries with the C-type structure follows a recognizable trend; Si < Ge < Sn. This trend can be inferred from the fluoride content in the Ca derivatives, i.e., $Ca_5Si_3F_{0.4} < Ca_5Ge_3F_{0.7} < Ca_5Sn_3F_{0.9}$, that when extrapolated to include the Pb derivatives becomes $A_5Si_3Z_x < A_5Ge_3Z_x < A_5Sn_3Z_x < A_5Pb_3Z_x$ (all the plumbides with the C-type structure are hydrogen-stabilized phases). Interestingly, this apparent trend of ease of oxidation is the inverse of the well known Tt–Tt bond energies trend, i.e, B.E.: Si–Si > Ge–Ge > Sn–Sn > Pb–Pb.[194] Therefore, one could argue that the stabilizing effects of hydrogen or fluoride in the C-type structure are to reduce the large charge repulsion in the Tt–Tt bond by increasing their bonding interaction through oxidation of the dimer.

Arguments of multiple bond interactions are necessary to explain the existence of alkaline-earth-metal trielides in the C-type structure as well. These compounds, in addition to size effects, manifest similar trends to those of the tetrelides. Thus, the Ca_5Ga_3 and Sr_5In_3 compounds do not bind hydrogen and a 2.5 b.o. would be calculated if localization is assumed, $5A^{2+}$, Tr_2^{5-}, Tr^{5-}; a $3e^-$ deficient system otherwise ($5A^{2+}$, Tr_2^{8-}, Tr^{4-}). The extreme case in this family of compounds is the hydrogen stabilized Sr_5Tl_3H for which a hypothetical triple bond is necessarily invoked to allow the closed shell configuration of the compound, $5Sr^{2+}$, $[Tl{\equiv}Tl]^{4-}$, Tl^{5-}, H^-. Extended Hückel calculations on

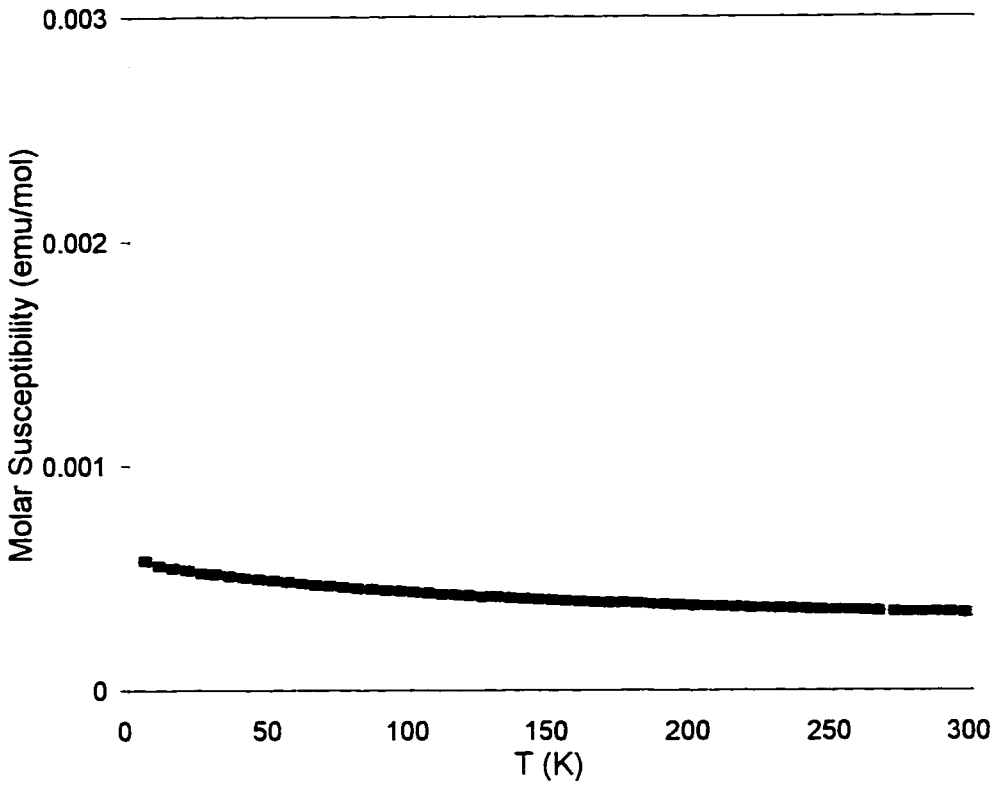

Figure IV-23. Temperature dependence of the molar susceptibilities (χ) at 3 Tesla of Sr_5Pb_3F (▪).

the C-Sr_5Tl_3H model suggest that the compound would be metallic-like in its electrical conductivity because the Fermi level at -6.024 eV (for $40e^-$, 50 k-point calculation) is located in a band of ample DOS, see left of Figure IV-24. COOP curves for the Tl(2)–Tl(2) interactions indicate that all the π bonding states are filled; consistent with simple MO calculations for the Tl_2^{4-} species. The temperature independent paramagnetism of sample PE17, Sr_5Tl_3H, depicted in Figure 25, supports the results of the theoretical calculations.

Evidence of multiple bond interactions in the solid state can be argumented for metal acetylide compounds because molecular counterparts are known. For instance, MC_2 compounds, where M is a electropositive metal, show a lengthening of the C–C distance as the valence of M increases, associated with variations in their bond order, e.g. in the isotypic CaC_2, d_{C-C} = 1.19 Å and for trivalent ions; YC_2, TbC_2, YbC_2, etc, d = 1.28 – 1.30 Å.[195] Off course, matrix effects must also play an important role in these distances. In a gross analogy to the carbides, a comparison of the changes in the Tt–Tt interatomic distances in C-$A_5Tt_3Z_x$ compounds and its association with variation of bond orders is valid, because the comparison is made within a series of both isotypic and isopointal compounds. For example, the decrement in the Si–Si distance in Ca_5Si_3 vs. $Ca_5Si_3F_{0.4}$ although small, is indicative of the enhanced bonding interactions. Similar effects are observed in the series of $Ca_5Ga_3Z_x$ compounds. Table IV-28 lists the Tt–Tt distances of the C-$A_5Tt_3Z_x$ compounds characterized by single crystal studies in this work; phases with the B-type structure are included as well. It is important to mention that the Tl–Tl distance of 2.999(4) Å in Sr_5Tl_3H constitutes the shortest interatomic distances reported for a Tl–Tl dimer, other reported distances of significance are; for a triply bonded Tl–Tl in Li_5Tl_2, d = 3.01 Å,[192] for the double bonded section in the Tl_3^{7-} species, d= 3.13 Å, and single bonded in deltahedral arrangements d_{ave} ~ 3.25 Å.[196]

$Yb_{36}Sn_{23}$ System

Experiments intended to prepare $Yb_5Sn_3H_x$ phases led to the discovery of the new binary $Yb_{36}Sn_{23}$. This phase forms in high yield in either the absence or presence of hydrogen. In the eariier part of this work, the products that involved this phase were

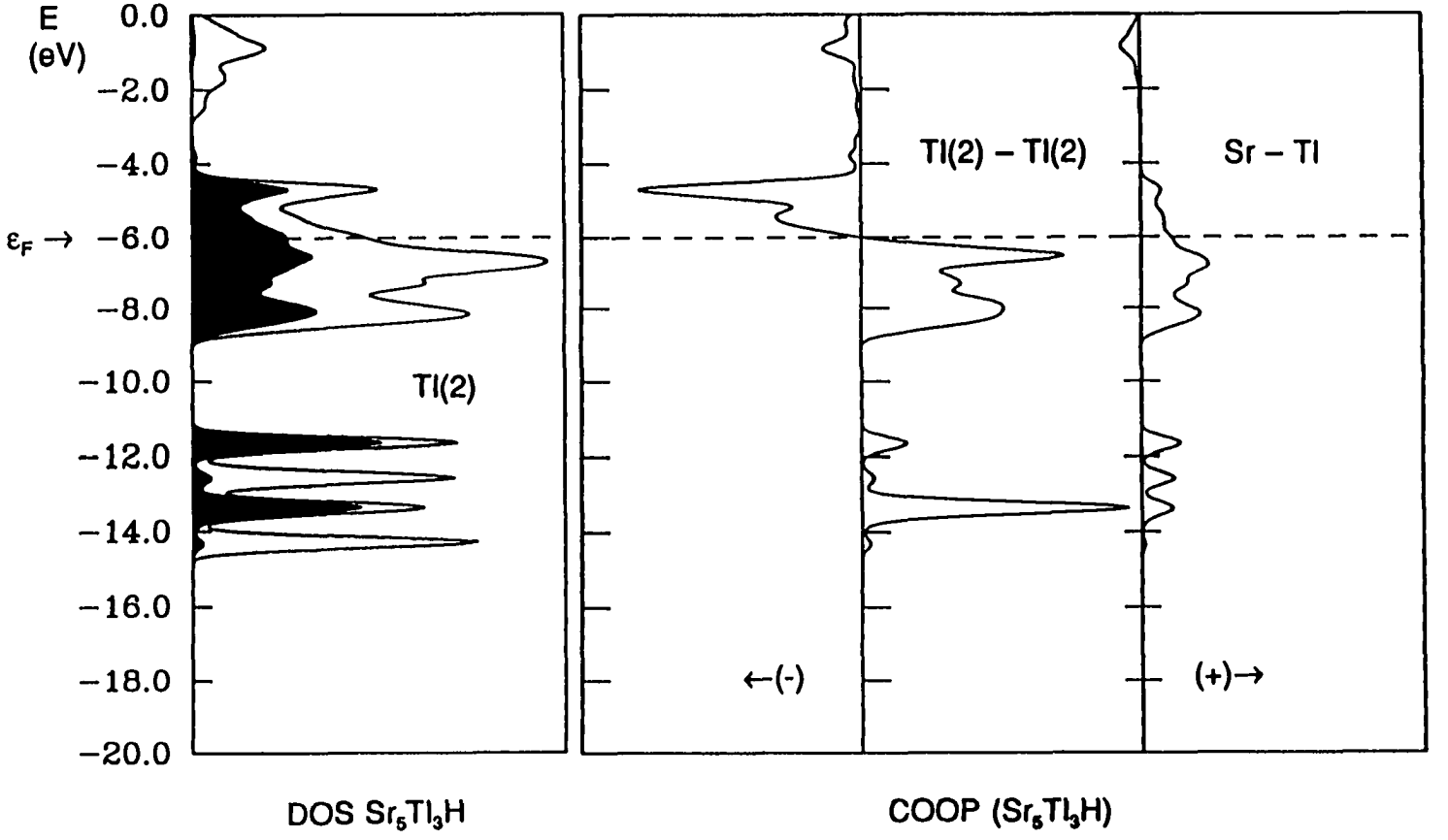

Figure IV-24. Graphical results of the Extended Hückel-MO band calculations for Sr_5Tl_3H with the C-type structure. To the left, the total DOS of Sr_5Tl_3H with the Tl(2) total atomic orbital projection shaded, H^- band at ~ -14 eV. To the rigth, the COOP curves for the Tl(2)–Tl(2) and averaged Sr–Tl interactions. Dashed lines signify the Fermi level (ε_F).

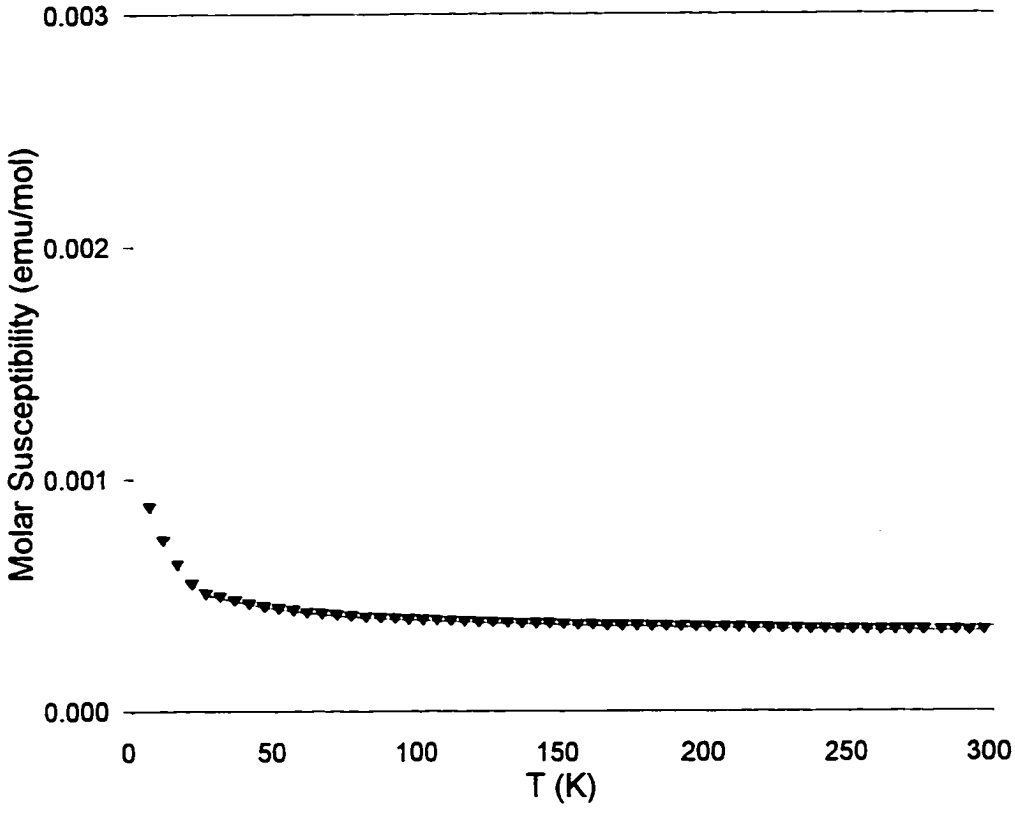

Figure IV-25. Temperature dependence of the molar susceptibilities (χ) at 3 Tesla of Sr_5Tl_3H (▾).

Table IV-28. Interatomic X–X (Tt–Tt or Tr–Tr) distance in several compounds with the Cr_5B_3-type structure refined in this work.

Compound	d_{X-X} (Å)
Ca_5Si_3	2.447(1)
$Ca_5Si_3F_{0.4}$	2.435(1)
Sr_5Si_3	2.474(7)
$Eu_5Si_3H_x$	2.403(7)
$Ba_5Si_3F_{0.2}$ [a]	2.442(6)
Ca_5Ge_3	2.575(1)
$Ca_5Ge_3H_x$	2.556(1)
$Ca_5Ge_3F_{0.7}$	2.5678(9)
$Ca_5Sn_3H_x$	2.9034(8)
$Ca_5Sn_3F_{0.9}$	2.9105(6)
$Eu_5Sn_3H_x$	2.884(3)
Sr_5Pb_3F	3.106(3)
Ca_5Ga_3	2.493(1)
Sm_5Ga_3 [a]	2.658(4)
$Sr_5Tl_3H_x$	2.999(4)

[a] In the Ba_5Si_3-type structure.

believed to be the hypothetical $Yb_{31}Sn_{20}$ (P-type), because of the high similarity between ideal model and experimental powder patterns; however, successful indexing of the cell based on the P-type model was never achieved. Suitable crystals for X-ray diffraction work were obtained in a reaction loaded $Yb_5Sn_3H_{2.0}$, rxn T29, which was heated at 1100°C for four hours and slowly cooled to 650°C at 10°C/h. Good quality crystals were also obtained from a reaction under dv conditions after the product was annealed at 900°C for one week, rxn T87 loaded as Yb_5Sn_3. A crystal from reaction T29 was mounted on the diffractometer and data collected for a primitive tetragonal cell. Statistics of observed reflections indicated presence of the 0kl and 0k0 (k≠2n) absence conditions

suggesting the centric space group P4/mbm (#127) or the acentric $P\bar{4}2c$ (#117) and P4bm (#100). Successful solution of the structure was achieved in the centric space group based on a initial model provided by SHELX-86. Tables IV-29 and IV-30 give the crystallographic and refined data information of the $Yb_{36}Sn_{23}$ structure ($Yb_{36}Sn_{23}$-type, P4/mbm, Z=2). Interatomic distances below 4.5Å are listed in Table IV-31.

The structure of $Yb_{36}Sn_{23}$ (YS) contains 17 independent atom positions, 9 Sn and 7 Yb, and as main features it has seven isolated, five dimers and one linear hexamer of tin per formula unit. Figure IV-26 pictures the [100] perspective view of the $Yb_{36}Sn_{23}$ structure, where one immediately can recognize its similarity with the $Ca_{31}Sn_{20}$ half cell depicted in Figure IV-5. In analogy to $Ca_{31}Sn_{20}$, the YS structure can be described as built of single layer sections that contain Sn-centered elongated Yb cubes that face-share with square antiprisms of Yb centered by Sn in a 1:6 sequence and run parallel to the c direction. Figure IV-27 shows the [001] perspective view of the $Yb_{36}Sn_{23}$ cell, where the Sn centered polyhedra at 0,0,z and ½,½,z can be recognized, and the left of Figure IV-28, shows the 1:6 sequence of Sn centered face-sharing polyhedra. Notice the resemblence of this structure to that of $Ca_{16}Sb_{11}$ in the equivalent view given in Figure III-34.

Four layer sections constitute the $Yb_{36}Sn_{23}$ structure at z ~ 0.43, 0.30, 0.17 and 0. The first sections at z ~0.43 depicted in Figure IV-29 is essentially a section of the W_5Si_3-type structure; compare with Figures IV-12 and IV-13. This section contains square antiprisms of Yb(5) and Yb(8) atoms that are centered by Sn(4) atoms at 0,0,0.43 and ½,½,0.43 and are interconnected by Sn(6) and Sn(9) atoms to adjacent square antiprisms. The Sn(6) and Sn(9) atoms form the edge-sharing tetrahedra that surround Yb(3) atoms along 0,½,z. The second section at z ~ 0.30 is nearly equivalent to the first section, but the Yb(8) and Yb(6) atoms in the square antiprism have twisted and are now centered by Sn(3). The third section at z ~ 0.17 shows the related network around Sn(2) atoms at the ends of the hexamer, where the square antiprisms of Yb(6) and Yb(7) have twisted again, and the Sn(7) and Sn(8) have formed dimers by opening the sharing edge of the nominal tetrahedra, see Figure IV-30. This section is still related to the WS structure. The fourth section at 0,0,0 illustrated in Figure IV-31 contains the

Table IV-29. Crystallographic data for $Yb_{36}Sn_{23}$.

	$Yb_{36.00(3)}Sn_{22.95(4)}$[a]
Crystal from rxn.	T29 (loaded Yb_5Sn_3)
Space group	P4/mbm (#127
Lattice parameters[b]	
a (Å)	12.3869(5)
c (Å)	22.935(1)
Volume (Å^3)	3519.0(3)
Z	2
Density calc. (g/cm^3)	8.455
Diffractometer	Enraf-Nonius CAD4
Crystal dimensions (mm)	0.10x0.18x0.23
Collected octants	-h,k,±l
Scan type	ω-2θ
Maximum 2θ (°)	50
Transmission range	0.632–1.165
Absorption coefficient (cm^{-1})	551.9
Number of reflections	
Measured (observed[c])	6790(3291)
Independent (observed[b])	2343(1205)
R_{ave} (%)[d]	9.70
No. of refined variables	88
R/R_w (%)	3.1/3.6
Goodness of fit	1.200
Secondary ext.coeff. (x10^{-8})	2.9(1)
Max./min. peak in ΔF map. (e$^-$ Å^{-3})	2.24/-3.18

[a] For 92 variables refined.
[b] Lattice parameters calculated from Guinier powder patterns.
[c] Observed reflections; $I \geq 3.00\sigma_I$.
[d] Average for all data; $I > 0$.

Table IV-30. Refined positional and thermal parameters of $Yb_{36}Sn_{23}$.

Atom	Wyck.	x	y	z	B_{eq}(Å^2)	U_{11}	U_{22}	U_{33}	U_{12}	U_{13}	U_{23}
Yb(1)	4f	0	½	0.12807(9)	0.78(4)	0.0111(7)	U_{11}	0.007(1)	-0.002(1)	0	0
Yb(2)	4f	0	½	0.2789(1)	0.74(4)	0.0102(7)	U_{11}	0.008(1)	0.000(1)	0	0
Yb(3)	4f	0	½	0.4293(1)	0.71(4)	0.0098(6)	U_{11}	0.0076(9)	-0.002(1)	0	0
Yb(4)	4g	0.3330(1)	x + ½	0	1.12(5)	0.0191(8)	U_{11}	0.005(1)	-0.006(1)	0	0
Yb(5)	8j	0.0824(1)	0.2199(1)	½	0.80(6)	0.0080(8)	0.0092(9)	0.0132(7)	-0.0017(6)	0	0
Yb(6)	16l	0.07601(8)	0.21237(9)	0.23792(4)	0.61(4)	0.0081(6)	0.0069(6)	0.0082(5)	-0.0011(5)	0.0014(4)	0.0013(4)
Yb(7)	16l	0.05618(8)	0.79001(9)	0.09202(4)	0.73(4)	0.0079(6)	0.0079(5)	0.0118(5)	0.0003(4)	0.0009(4)	-0.0029(4)
Yb(8)	16l	0.41239(8)	0.28485(9)	0.36815(5)	0.76(4)	0.0081(5)	0.0078(6)	0.0130(5)	-0.0018(5)	0.0001(5)	0.0008(4)
Sn(1)	2a	0	0	0	1.0(1)	0.014(2)	U_{11}	0.013(2)	0	0	0
Sn(2)	4e	0	0	0.1663(1)	0.53(7)	0.006(1)	U_{11}	0.008(2)	0	0	0
Sn(3)	4e	0	0	0.3018(1)	0.44(6)	0.007(1)	U_{11}	0.002(1)	0	0	0
Sn(4)	4e	0	0	0.4336(1)	0.50(6)	0.006(1)	U_{11}	0.007(1)	0	0	0
Sn(5)	4g	0.0884(2)	x + ½	0	0.66(7)	0.009(1)	U_{11}	0.007(2)	0.003(1)	0	0
Sn(6)	4h	0.1569(2)	x + ½	½	0.65(7)	0.008(1)	U_{11}	0.010(2)	0.001(1)	0	0
Sn(7)	8k	0.1641(1)	x + ½	0.2156(1)	0.78(5)	0.0083(8)	U_{11}	0.013(1)	-0.001(1)	0.0010(7)	U_{13}
Sn(8)	8k	0.3059(1)	x + ½	0.1308(1)	0.55(5)	0.0079(7)	U_{11}	0.005(1)	0.001(1)	0.0000(7)	U_{13}
Sn(9)	8k	0.3484(1)	x + ½	0.3595(1)	0.67(5)	0.0070(8)	U_{11}	0.012(1)	0.000(1)	-0.0002(7)	U_{13}

Table IV-31. Interatomic distances of the $Yb_{36}Sn_{23}$ structure, d < 4.5 Å.

Atom(1) – Atom(2)	d (Å)	Atom(1) – Atom(2)	d (Å)	Atom(1) – Atom(2)	d(Å)
Sn(1) – Sn(2) (2x)	3.814(3)	Sn(7) – Yb(2) (1x)	3.219(3)	Yb(2) – Yb(8) (4x)	4.221(2)
Sn(2) – Sn(3) (1x)	3.107(5)	Sn(7) – Yb(6) (2x)	3.315(2)	Yb(3) – Yb(3) (1x)	3.242(4)
Sn(3) – Sn(4) (1x)	3.023(5)	Sn(7) – Yb(6) (2x)	3.384(1)	Yb(3) – Yb(5) (4x)	3.963(2)
Sn(4) – Sn(4) (1x)	3.046(7)	Sn(7) – Yb(7) (2x)	3.501(2)	Yb(3) – Yb(8) (4x)	3.949(1)
Sn(5) – Sn(5) (1x)	3.098(7)	Sn(7) – Yb(8) (2x)	3.921(2)	Yb(4) – Yb(7) (4x)	3.797(1)
Sn(7) – Sn(8) (1x)	3.156(3)	Sn(8) – Yb(1) (1x)	3.401(2)	Yb(4) – Yb(7) (4x)	4.062(2)
Sn(1) – Yb(7) (8x)	3.421(1)	Sn(8) – Yb(4) (1x)	3.037(2)	Yb(5) – Yb(5) (1x)	3.464(3)
Sn(2) – Yb(6) (4x)	3.241(2)	Sn(8) – Yb(6) (2x)	3.086(2)	Yb(5) – Yb(5) (2x)	4.113(2)
Sn(2) – Yb(7) (4x)	3.186(2)	Sn(8) – Yb(7) (2x)	3.224(2)	Yb(5) – Yb(8) (2x)	3.685(1)
Sn(3) – Yb(6) (4x)	3.154(2)	Sn(8) – Yb(7) (2x)	3.437(2)	Yb(5) – Yb(8) (2x)	3.812(1)
Sn(3) – Yb(8) (4x)	3.256(2)	Sn(9) – Yb(2) (1x)	3.236(3)	Yb(6) – Yb(6) (1x)	3.707(2)
Sn(4) – Yb(5) (4x)	3.283(2)	Sn(9) – Yb(3) (1x)	3.100(3)	Yb(6) – Yb(6) (2x)	3.951(2)
Sn(4) – Yb(8) (4x)	3.245(2)	Sn(9) – Yb(5) (2x)	3.695(2)	Yb(6) – Yb(7) (1x)	3.726(1)
Sn(5) – Yb(1) (2x)	3.321(2)	Sn(9) – Yb(6) (2x)	3.391(2)	Yb(6) – Yb(7) (1x)	4.207(1)
Sn(5) – Yb(4) (2x)	3.310(3)	Sn(9) – Yb(8) (2x)	3.331(2)	Yb(6) – Yb(8) (1x)	3.610(1)
Sn(5) – Yb(4) (1x)	4.285(4)	Sn(9) – Yb(8) (2x)	3.397(1)	Yb(6) – Yb(8) (1x)	3.779(1)
Sn(5) – Yb(7) (4x)	3.294(2)	Yb(1) – Yb(2) (1x)	3.459(3)	Yb(7) – Yb(7) (2x)	3.808(2)
Sn(6) – Yb(3) (2x)	3.190(3)	Yb(1) – Yb(4) (2x)	4.145(2)	Yb(7) – Yb(7) (1x)	4.096(2)
Sn(6) – Yb(5) (2x)	3.323(4)	Yb(1) – Yb(6) (4x)	4.464(2)	Yb(7) – Yb(7) (1x)	4.221(2)
Sn(6) – Yb(5) (2x)	3.334(2)	Yb(1) – Yb(7) (4x)	3.751(1)	Yb(8) – Yb(8) (1x)	3.455(2)
Sn(6) – Yb(8) (4x)	3.520(1)	Yb(2) – Yb(3) (1x)	3.451(3)	Yb(8) – Yb(8) (2x)	4.070(2)
Sn(7) – Yb(1) (1x)	3.506(3)	Yb(2) – Yb(6) (4x)	3.803(1)		

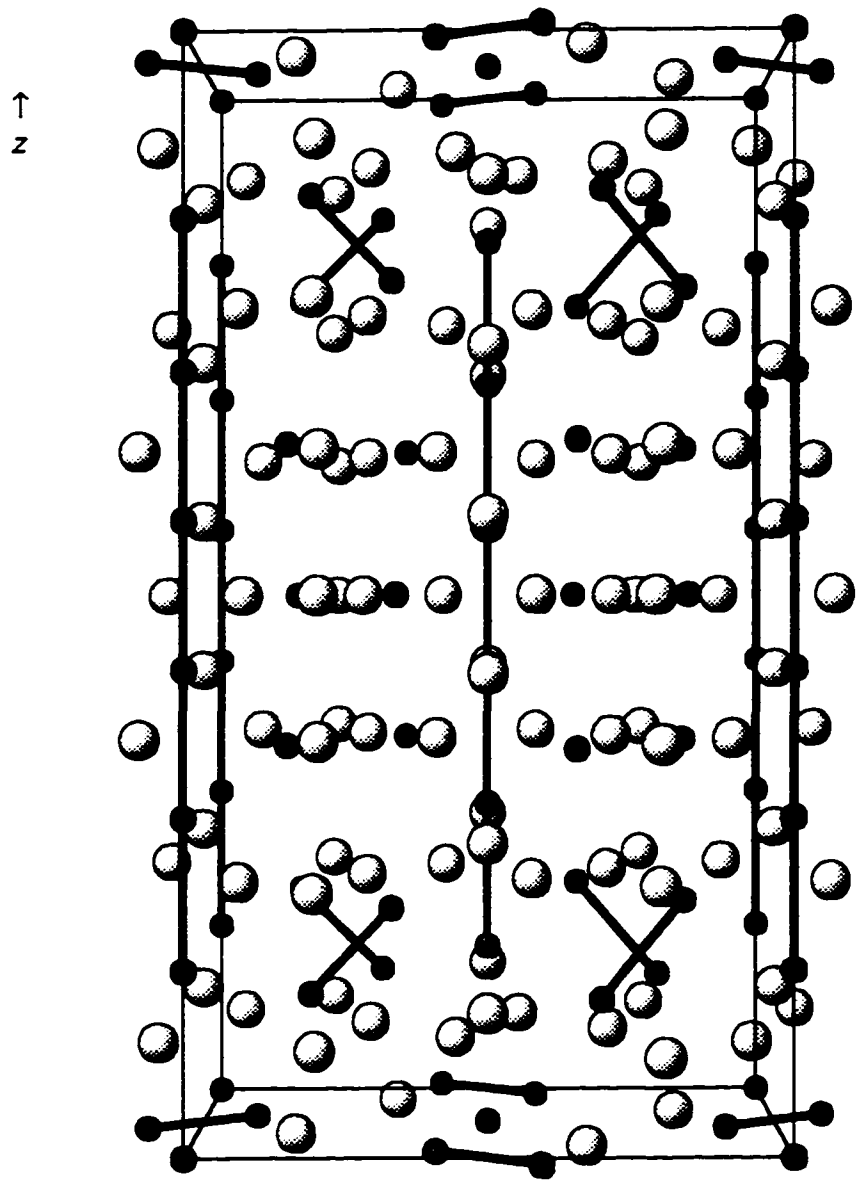

Figure IV-26. Perspective view [100] of the $Yb_{36}Sn_{23}$ structure. Small and large spheres represent Sn and Yb atoms, respectively. Short Sn–Sn contacts are emphasized as heavy lines.

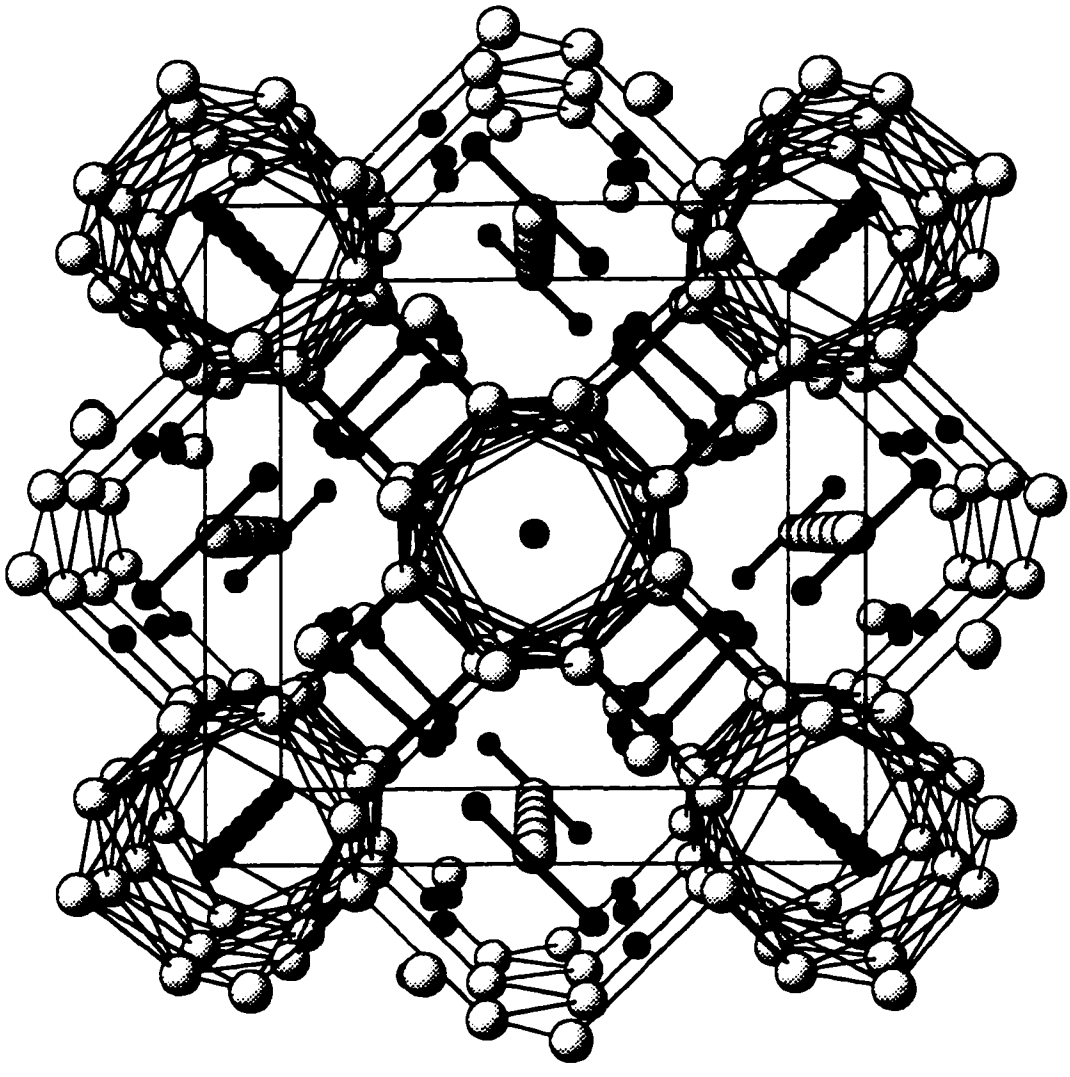

Figure IV-27. Perspective view [100] of the $Yb_{36}Sn_{23}$ structure. Small and large spheres represent Sn and Yb atoms, respectively. Short Sn–Sn contacts are emphasized as heavy lines.

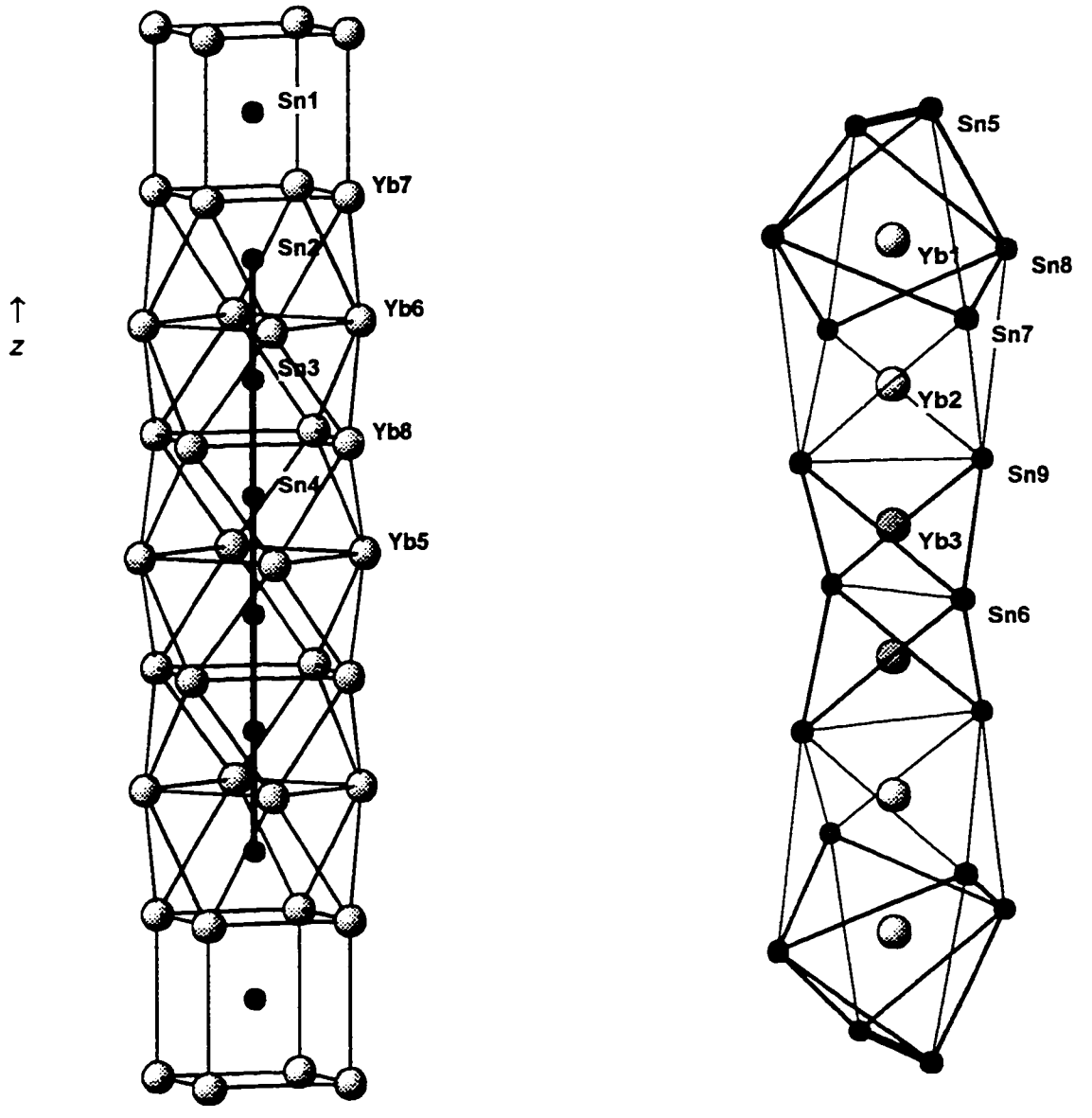

(I) (II)

Figure IV-28. Details of the $Yb_{36}Sn_{23}$ structure, I) Sequence of Sn centered square prim and square antiprisms of Yb atoms at 0,0,z and ½,½,z, short Sn–Sn contacts are emphasized as heavy lines. (II) Yb atoms at 0,½,z and their Sn environment, thin lines symbolize interatomic distances above 5.0 Å. Small and large spheres represent Sn and Yb atoms, respectively.

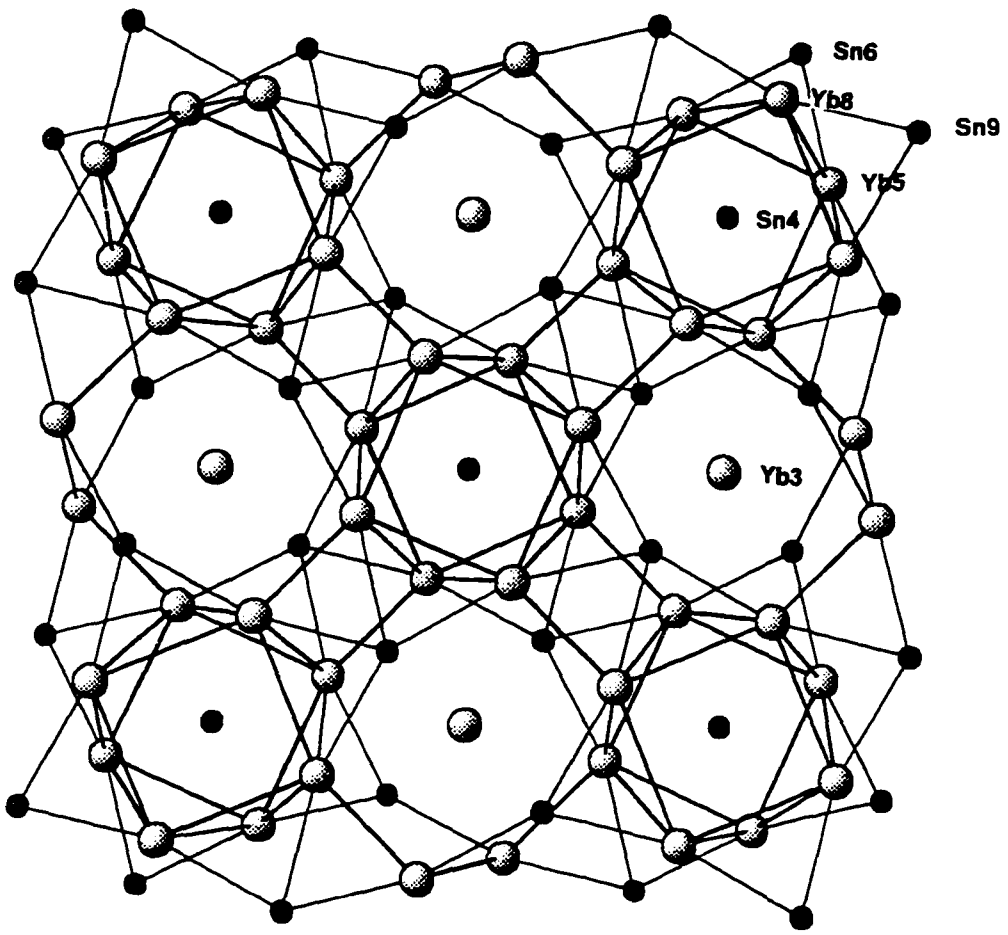

Figure IV-29. W_5Si_3-like section at z ~0.43 in the $Yb_{36}Sn_{23}$ structure. Small and large spheres represent Sn and Yb atoms, respectively. Lines between atoms do not represent bonds.

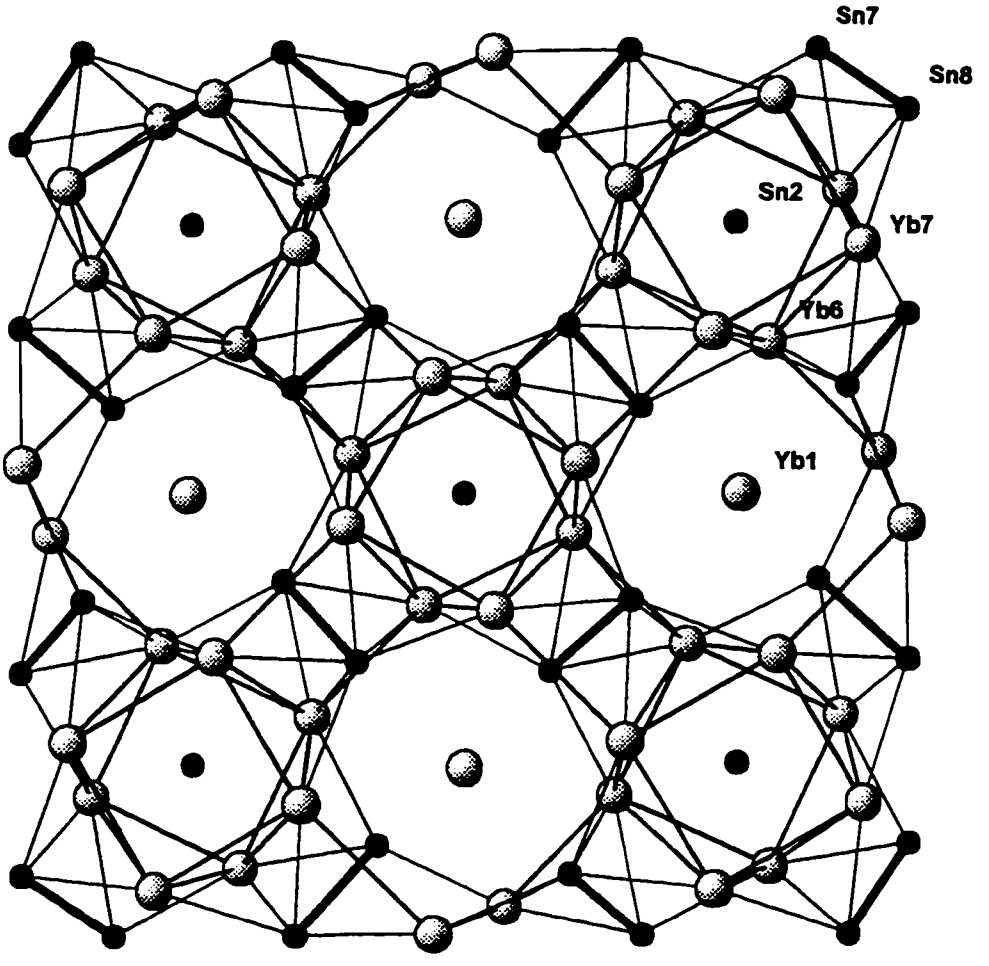

Figure IV-30. Distorted W_5Si_3-like section at z ~0.17 in the $Yb_{36}Sn_{23}$ structure. Small and large spheres represent Sn and Yb atoms, respectively. Short Sn–Sn contacts are emphasized as heavy lines.

Sn(5) dimers, formerly one edge of the tetrahedra along 0,½,z that were generated by further twisting of the antiprisms and displaced into cavities at 0,½,0. The main features of the WS structure are lost at this point. The Yb(7) elongated cubes arrangement is now centered by Sn(1).

Important Sn–Sn interatomic distances in this structure are 3.098(7) and 3.156(3)Å for the Sn(5)–Sn(5) and Sn(7)–Sn(8) dimers, respectively, as well as 2 x [3.107(5), 3.023(5)] and 3.046(7) Å for [Sn(2)–Sn(3)–Sn(4)–Sn(4)] in the hexamer, respectively. The next Sn–Sn contact in the structure is 3.814(3) Å between Sn(1) and Sn(2). The Yb–Sn and Yb–Yb distances, with exception of Yb(3)–Yb(3), are above 3.03 and 3.45 Å, respectively, and within observed distances for structures involving divalent Yb ions. The short Yb(3)–Yb(3), d= 3.242(4) Å, is probably caused by matrix effects resulting from the two "authentic" W_5Si_3 sections of the structure at z ~0.43 and 0.57, see the right part of Figure IV-28. Cation–cation distances inside the edge sharing tetrahedra chains in the WS structure are characteristically short; in the YS structure they are ~0.19% shorter than sum of Yb metallic radii (2 x 1.933 Å).[61] Such a feature hints the possibility of stabilizing the next member of the $A_{5n+6}B_{3n+5}$ series, n=7, by substituting a smaller isovalent cations inside the tetrahedra. The larger isotropic thermal parameters of Yb(4) and Sn(1) are due to the large cavities in which they locate. The Sn and Sb atoms inside the equivalent elongated cubes in the $Ca_{31}Sn_{20}$ and $Ca_{16}Sb_{11}$ structures show similar or worse thermal problems. Parthé's $A_{5n+6}B_{3n+5}$ homologous series is reviewed in a recent publication about $Ca_{16}Sb_{11}$.[197]

Assumption that all the Yb ions in $Yb_{36}Sn_{23}$ are divalent would make the phase a Zintl compound, $36Yb^{2+}$, $7Sn^{4-}$, $5Sn_2^{6-}$, Sn_6^{14-}; therefore, semiconducting and diamagnetic. The temperature dependence of the molar susceptibilities of the binary phase (rxn T83) depicted in Figure IV-32 do not disprove the assumption about the valence state of the Yb ions; however, it is temperature-independent paramagnetic above 50K, $\chi_{M(298K)} = 6.68 \times 10^{-4}$ emu/mol. The large molar susceptibilities in these compound suggest that contributions additional to free electrons are involved in the total magnetism of the sample. Electrical resistivity measurements in support of the magnetic measurements indicated that the sample is metallic, and a room temperature resistivity

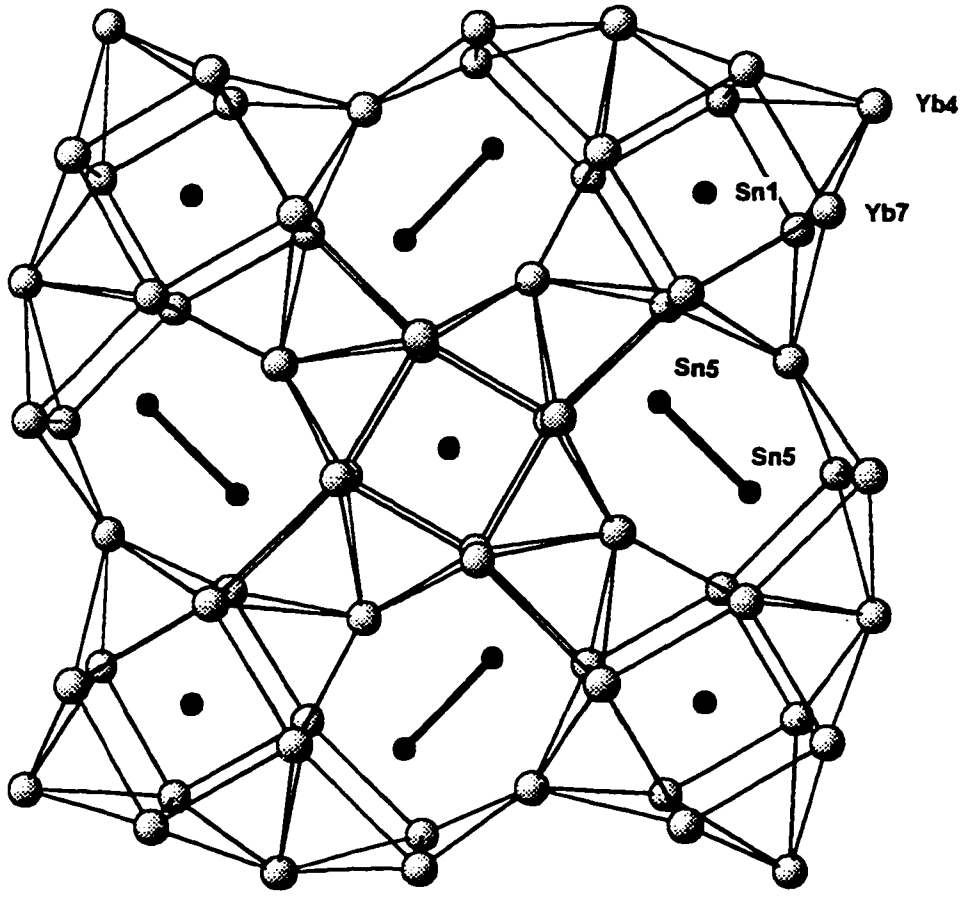

Figure IV-31. The [001] section at z ~0 in the $Yb_{36}Sn_{23}$ structure. Small and large spheres represent Sn and Yb atoms, respectively. Short Sn–Sn contacts are emphasized as heavy lines.

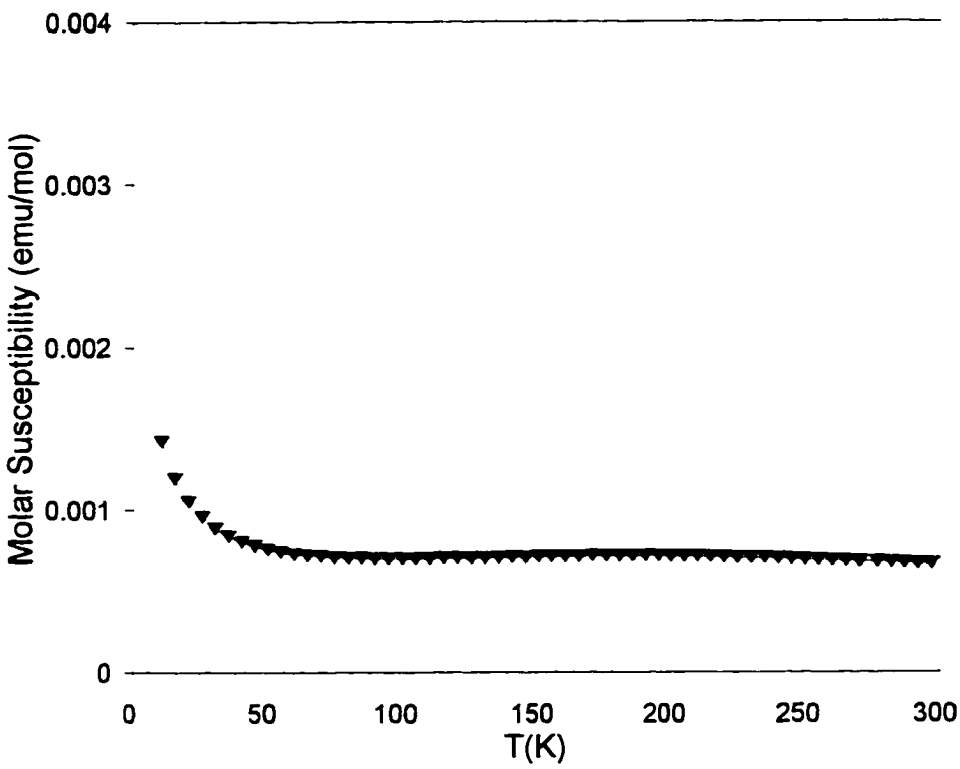

Figure IV-32. Temperature dependence of the molar susceptibilities (χ) at 3 Tesla of $Yb_{36}Sn_{23}$ (▾).

and thermal coefficient of 132 μΩ·cm and 0.42(4) %K were calculated from ρ vs. T curves, see Figure IV-33.

At present time an explanation about the disparity between observed and predicted electrical properties is not available. One could speculate that a possible small overlap between the valence and conduction bands may exist. Extra factors like a slight Yb(3) deficiency in the compound could cause holes in the valence band and probably allow the electron mobility in the system. The Yb(3) atom is located at the same position that is often fractionally occupied in phases with the W_5Si_3-type structure. In fact, slight variations in the cell parameters were observed from product to product that amounted to maximum calculated cell volume variation of ~ ± 0.07%. Theoretical calculations for a $Yb_{36}Sn_{23}$ model systems were not performed; however, they might help us to illuminate this problem. Despite the discrepancies between predicted and observed properties for the unprecedented $Yb_{36}Sn_{23}$, the phase is the first example of a compound containing linear hexamers of tin atoms.

Conclusions About the Tetrelide and Trielide Systems

We have demonstrated that hydrogen plays a very important role in the chemistry of the alkaline-earth and divalent rare-earth metal tetrelides and trielides with $A_5(Tt,Tr)_3H_x$ compositions. Several tetrelides compounds with the Cr_5B_3-type structure previously considered classical examples of Zintl phases are indeed hydrogen-stabilized compounds, i.e. $Ba_5Sn_3H_x$, $Yb_5Sn_3H_x$, $Sr_5Pb_3H_x$ and $Ba_5Pb_3H_x$. Fluoride can also be interstitially introduced in many of these compounds. Table IV-32 summarizes the results of products identified from reactions $A_5Tt_3(H,F)_x$. Evidence indicates that M-$Yb_5Ge_3H_x$ is a hydrogen-stabilized and mixed-valence compound. Two new examples of hydrogen-stabilized compounds with the C-type structure were found, $Ca_5Sn_3H_x$ and $Eu_5Sn_3H_x$. Reactions in absence of hydrogen, or fluoride, in these systems led to mixtures of binaries in the CrB and Co_2Si types or to the $Pu_{31}Pt_{20}$-type, with a clear tendency to form the latter structure type when large anions were involved.

Single crystal x-ray and neutron powder diffraction of fluoride and

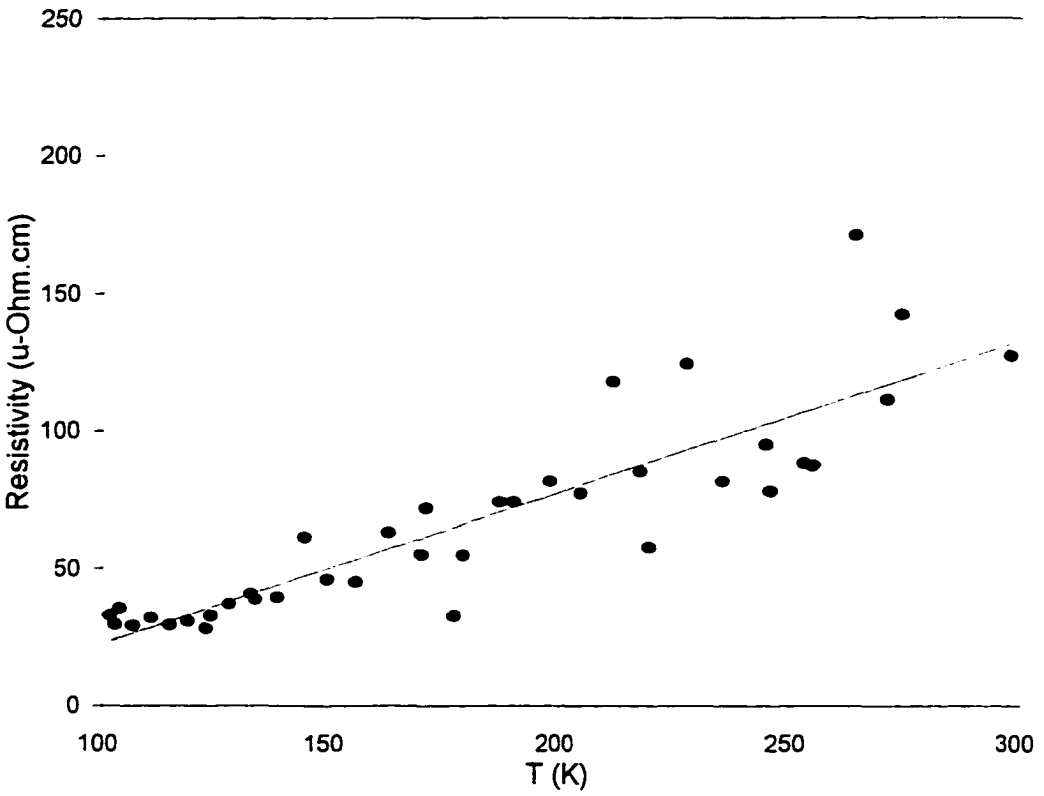

Figure IV-33. Temperature dependence of the electrical resistivity (μΩ·cm) for $Yb_{36}Sn_{23}$ measured by the Q method. The temperature coefficient calculated from the slope of the ρ versus T curve is 0.42(4)% K^{-1}.

Table IV-32. Products of the reactions in absence (-[H]) and presence of hydrogen or fluoride (+[H,F])[a]. Bold and underlined letters indicate new and previously misidentifled phases, respectively.

A\Tt	Si		Ge		Sn		Pb	
	-[H]	+[H,F]	-[H]	+[H,F]	-[H]	+[H,F]	-[H]	+[H,F]
Ca	**C**[b]	<u>CH</u>,**CF**[b]	**C**[b]	<u>CH</u>[b],**CF**[b]	P	**CH**[b,c,d]**CF**[b,d]	MS	**(MSH,MSF)**
Sr	**C**[b]	**CH**,□	**C**	**CH**,□	**C**	<u>CH</u>,**CF**	**P**	<u>CH</u>,**CF**[b]
Ba	**B**	<u>BH</u>,**BF**[b]	**C**	**CH**,□	⊕	<u>CH</u>,**CF**	**WS**	<u>CH</u>,**CF**
Sm	**M**	<u>MH</u>	**M**	<u>MH</u>	**M**	<u>MH</u>	M	**MH**
Eu	**C**	**CH**[b]	**C**	<u>CH</u>	⊕[d]	**CH**[b]	WS	WS
Yb	M	**MH**	⊕[d]	<u>MH</u>[b]	**YS**[b]	<u>CH</u>	**P(MS)**	**P(<u>MSH</u>)**

[a] Products:
C = Cr_5B_3-type
P = $Pu_{31}Pt_{20}$-type
MS = Ca_5Pb_3-type
B = Ba_5Si_3-type
M = Mn_5Si_3-type
WS = W_5Si_3-type
YS= $Yb_{36}Sn_{23}$-type
CH, CF = Hydrogen or fluoride stuffed Cr_5B_3-type (Ca_5Sn_3F)
□ = Signifies reaction never loaded
MSH, MSF= Probably hydrogen or fluoride containing Ca_5Pb_3-type
BH, BF = Hydrogen or fluoride containing Ba_5Si_3-type (Ba_5Si_3F)
MH= Hydrogen stuffed Mn_5Si_3-type
⊕ = Mixture of CrB and Co_2Si types

[b] Phase characterized by single crystal x-ray diffraction.
[c] Phase characterized by powder neutron diffraction on a deuterated sample, Ca_5Sn_3D.
[d] Newly identified phases of the CrB-type are CaSn and YbGe, and new with the Co_2Si-type are Yb_2Ge and Eu_2Sn.

deuteride derivatives $Ca_5Sn_3(F,D)_x$ demonstrated that the interstitial atom is located at the center of the tetrahedral cavities in the structure, in similarity to the $La_5Pb_3(N,O)$ systems that are a distorted variant of the stuffed Cr_5B_3-type or Ca_5Sn_3F-type structure. We were also able to partially incorporate H^- or F^- in the Ba_5Si_3 phases. The ternaries $Ba_5Si_3(H,F)_x$ are the first examples of interstitial compounds with the Ba_5Si_3-type structure. This structure type constitutes a primitive distortion of the body-centered C-type and tends to form when small anions, i.e., Si and Ga, and either large or trivalent cations are involved. New binaries and their ternaries phases with the Cr_5B_3 and Ca_5Sn_3F structure types are $Sr_5Si_3H_x$, $Eu_5Si_3H_x$, $Sr_5Ge_3H_x$, $Ba_5Ge_3H_x$. New binaries with the P-type structure are $Sr_{31}Pb_{20}$ and $Yb_{31}Pb_{20}$ and new with the WS-type related is Ba_5Pb_3. Additionally, a unprecedented binary was found in the Yb–Sn system; $Yb_{36}Sn_{23}$ a phase that features isolated, dimers and linear hexamers of tin and constitutes the n=6 member of Parthé's homologous series $A_{5n+6}B_{3n+5}$.

Several phases can form in the C-type cell and can bind hydrogen as observed from the variation in their cell volumes. Table IV-33 summarizes all the calculated cell volume variations for phases that do not change in structure type in the presence of hydrogen. Thus, the cell volume variation for these systems followed the trends; $Sr_5Sn_3H_x > Ca_5Ge_3H_{3x} > Sr_5Ge_3H_{3x} > Eu_5Si_3H_x > Eu_5Ge_3H_x > Sr_5Si_3H_{3x} > Ca_5Si_3H_x > Ba_5Ge_3H_x$ for phases with the C-type cell, and $Sm_5Si_3H_x > Sm_5Ge_3H_x > Sm_5Sn_3H_x > Sm_5Pb_3H_x$ for the M-type phases. It was also found that the MS-Ca_5Pb_3 and M-$Yb_5Pb_3H_x$ may share a common structural chemistry. The former is likely a distortion of the reported $Ca_{17}Pb_9$, and the latter is a high temperature phase. In the trials, matrix effects seem to play a very important role in the formation of the compounds with the C-type or related structures; thus Ca_5Ge_3 and Sr_5In_3 are binary compounds and $Sr_5Tl_3H_x$ is a hydrogen stabilized compound. The Sm_5Ga_3 derivative crystallized in the Ba_5Si_3-type as predicted by Zhao et al.[160]

The ease with which fluoride or hydrogen can be incorporated in the tetrelide compounds with the C structure follows the trend $A_5Si_3(H,F)_x < A_5Ge_3(H,F)_x < A_5Sn_3(H,F)_x < A_5Pb_3(H,F)_x$ that seem to be directly associated with the stabilization of

Table IV-33. Calculated cell volume decrements (%) for phases $A_5Tt_3H_x$ that are not hydrogen-stabilized.

A\Tt	Si	Ge	Sn	Pb
Ca	0.88[a]	1.36	—	{-0.60}[b]
Sr	0.92	1.08	1.96	—
Ba	(0.32)[c]	0.59	—	—
Sm	[1.23][d]	[1.14][d]	[0.29][d]	[0.21][d]
Eu	1.05	0.98	—	—
Yb	[-1.02][d]	—	—	[0.78][d]

[a] Cr_5B_3-type.
[b] Probably Ca_5Pb_3-type.
[c] Ba_5Si_3-type.
[d] Mn_5Si_3-type.

these compounds by hydrogen or fluoride, and is the reverse of the trend known for Tt–Tt bond energies, i,e, Si–Si > Ge–Ge > Sn–Sn > Pb–Pb. The presence of hydrogen or fluoride in compounds with the C-type structure raised important questions on how these systems cope with the electron deficiency. EHMO band calculations suggest electrons from π^* states in the Tt–Tt interactions are being depleted by the interstitial atom in the compound. These calculations also suggest that the ternaries would show metallic-like properties. Magnetic measurements on several samples supported these predictions. Nevertheless, the binaries A_5Tt_3 that are structurally Zintl phases showed in some instances Pauli paramagnetic behaviors and positive temperature coefficients in their electrical resistivities.

Arguments of multiple bonds interaction were invoked to rationalize the formal closed shell configurations of the C-$A_5(Tt,Tr)_3Z_x$ compounds, with some evidence of an

increment in bonding interactions between Tt–Tt dimers through decrements of their interatomic distances as the samples are oxidized, i.e., Si–Si distance in Ca_5Si_3 vs. $Ca_5Si_3F_{0.4}$. The extreme example is Sr_5Tl_3H, were an ideal triple bond is necessary to rationalize the closed shell configuration of the compound. Electrical resistivity and magnetic measurements support the predictions based on theoretical calculations about the possible involvement of multiple bonds in this hydrogen-stabilized compound.

Hydrogen-stabilized compounds are not limited only to $A_5(Tt,Tr)_3H_x$ compositions. For instance, the Ba_5Ga_6 phase initially reported by Fornasini[198] features regular octahedral clusters of Ga atoms that according to electron counts is formally Ga_6^{10-}, which is two more electrons than required by the well-established polyhedral electron counting rules of Wade and Mingos.[199] Theoretical calculations performed by Liu el al.[46] in this system suggested that the cluster should suffer Jahn-Teller-type distortions in order to accommodate for such a number of electrons. Based on these calculations, they suggested that the phase might be a ternary hydride instead. Indeed, Henning et al.[199] in a recent neutron diffraction study of the phase confirmed that $Ba_5Ga_6H_2$ is its more accurate description.

CHAPTER V. SUMMARY AND FUTURE WORK

We have demonstrated that hydrogen plays a very important role in the chemistry of the alkaline-earth and divalent rare-earth metal pnictide and tetrelide compounds $A_5(Pn,Tt)_5H_x$. Reactions in presence of fluorides to large extent follow a chemistry parallel to that of the hydrides with the advantage that the F^- ion can easily be located through single crystal X-ray diffraction. Our results prove that all the pnictogen $A_5Pn_3H_x$ that involve divalent metals and form in the so-called β-Yb_5Sb_3-type structure (=Ca_5Sb_3F) are hydrogen-stabilized compounds, while the hexagonal Mn_5Si_3-type (M) forms for the binaries. The orthorhombic Ca_5Sb_3F-type structure is characteristic of ternary systems and has inaccurately being assigned to binaries of trivalent rare-earth-metal antimonides and bismuthides, $RE_5(Sb,Bi)_3$.[24,107] These electron-richer binary phases $RE_5(Sb,Bi)_3$ form in the Y_5Bi_5-type instead when the proper combination of small cation and large anion are involved.

Size effects play an important role in the chemistry of the pnictogens as well. Thus, the H^- or F^- ions stabilize the Ca_5Sb_3F-type structure in the Ca–Sb, Ca–Bi, Sr–Sb and Sr–Bi systems. On the other hand, when ions like either Cl^- or Br^- are present in the reactions, phases with the M-type structure form. Our current knowledge on the structural trends as well as our ability to control the experimental conditions, i.e, reaction in absence or presence of hydrogen, should in principle allow us to design new compounds. For instance, we could prepare mixed-metal pnictogen phases like $Sr_3Eu_2Sb_3$ designed for specific studies. Such an imaginary compound would probably form in the M-type structure when the reaction is carried under dv conditions, and possibly would be ordered in their cation positions, with Eu restrained to the linear chain in the structure that shows short cation–cation distances. Therefore, one could study the magnetic interaction of paramagnetic $Eu^{(II)}$ when in a linear arrangement. Phases like M-$Ca_2Sm_3Sb_3$ and M-$Sr_3Sm_2Sb_3$ come to mind that may help us understand the complex magnetic behavior observed in the $Sm_5Sb_3H_x$ and $Sm_5Ge_3H_x$ phases. Cases of pnictide phases that require attention are the A_5Pn_4 (Sm_5Ge_4-type)[201] that appear to be Zintl phases because they feature one Sb–Sb dimer and two isolated Sb atoms per formula unit. Phases with this composition have only been observed for Ba_5Sb_4[138] and

Yb_5Sb_4,[49,71] and hydrogen impurities instead of stabilizing are probably obscuring the discovery other members of the series. Such an obscuring effect of hydrogen was already revealed in the $Ca_{16}Sb_{11}$ $Ca_{31}Sn_{20}$ systems.

We have demonstrated that several of the classical Zintl phases $A_5Tt_3(H_x)$ that form in the Cr_5B_3-type structure are hydrogen-stabilized compounds as well. The mere existence of these electron deficient compounds imposes limitations to the Zintl concept. Two–electron–two–center bond arguments are not sufficient to explain these structures. Theoretical calculations suggest that the interstitial atoms, H^- or F^-, withdraw electrons from the π^* states of the Tt–Tt dimer causing increments in their bonding interactions. Decrements in the Tt–Tt dimer interatomic distances are observed between binary and interstitially substituted compounds, and interpreted as a proof of the multiple bond interactions invoked in these compounds; e.g. Ca_5Ge_3 versus $Ca_5Ge_3H_x$. The extreme case reviewed was Sr_5Tl_3H, where a triply bonded $[Tl{\equiv}Tl]^{4-}$ dimer species was necessary to rationalize the closed-shell structure. Another system that seem to be electron deficient as well is Yb_5Sn_4 that crystallizes in a distorted-Sm_5Ge_4-type structure;[71,177] two Sn–Sn dimers are now the feature of the structure and Yb ions appear to be divalent. Test reactions in this system suggest that hydrogen is involved in its stabilization; albeit without hydrogen the phase seems to already be electron deficient.

The structures of Ca_5Pb_3 and $Yb_5Pb_3(H_x)$ require a more conscientious investigation. They could provide information on how these systems deal with their electron deficiencies. The troublesome structure of Ba_5Pb_3 requires a similar study as well. The unprecedented $Yb_{36}Sn_{23}$ phase presumably is not the only example that can be prepared. One should probably be able to prepare new isomorphic phases of this structure by mixing isovalent cations and tin. The right combination of cations and composition might lead to next member of Parthé's $A_{5n+6}B_{3n+5}$ isomorphous series,[186] n=7, where three "actual" W_5Si_3-type sections would form part of the structure; short cation–cation contacts are to be expected to occur. Thus, compositions like $Ca_{38}Yb_3Sn_{26}$ could lead to such compounds.

The trielides already promise a myriad of new phases and probably new structures as well; however, the presence of hydrogen in some already reported phases

like $Ca_{28}Ga_{11}$[201] and $Ba_{10}Ga$[203] should be seriously reconsidered. These compounds characteristically have isolated Ga atoms and are electron rich according to simple electron counts, e,g. for $Ca_{28}Ga_{11}$; $28Ca^{2+}$, $11Ga^{5-}$. In similarity, the fascinating NaBa,[204] Na_2Ba,[205] $NaBa_3N$,[206] etc. phases invite to their study because these electron-rich systems feature octahedral and tetrahedral cavities where hydrogen might locate.

Adventitious hydrogen impurities in $A_5Pn_3(H_x)$ compounds were responsible for the previously unexplained discrepancies between observed and predicted electrical resistivity behaviors. However, some systems where the Zintl compositions were achieved, deviations from semiconducting and diamagnetic properties were observed. These deviations from predictions are more distinct when element of the later periods of the periodic table are involved, e.g., Sr_5Bi_3F, and indicate that the magnitude of charge transfer from the electropositive element to the electronegative varies depending the combination of elements; nevertheless, the structure can still be explained by Zintl ideas. Consequently, the Zintl concept for its simplicity is a great tool for chemists to understand intermetallic compounds based on their structure and many times to predict with some accuracy their electrical properties.

APPENDIX A. $Ca_{11}Sb_{9+x}$

Reactions $Ca_{16-x}(Na,K)_xSb_{11}$, intended to generate ordered $Ca_{16}Sb_{11}$ (T-type) structures, gave instead products initially identified as $Ca_{11}Sb_{10}$ in the $Ho_{11}Ge_{10}$-type structure (I4/mmm, #139, Z=4).[137] Presence of unidentified lines in the powder patterns of these products suggested unaccounted phasesor probable structural distortions of $Ca_{11}Sb_{10}$. In an attempt to explain these additional lines, the structure of a crystal from reaction C14, loaded as $Ca_{15}KSb_{11}$, was solved. Because of the large number of violations to the body-centered reflection condition and absences for 0kl, 0k0 and 00l ($\neq$2n), the structure was refined in space group $P4_2/mnm$ (#136) giving a formula of ~$Ca_{11-x}K_xSb_9$ and some troublesome positions. Subsequent experiments in search of the binary, $Ca_{11}Sb_{10-x}$; x=0, 1.2, 1.4, 1.9 and 2.1 (rxns C26, C39, C37, C30 and C37, respectively), demonstrated the existence of the $Ca_{11}Sb_{9+x}$ (DH) phase. The single crystal structure of C37 (loaded $Ca_{11.5}Sb_9$ and heated as rxn. L3, see Table III-40) gave a solution equivalent to that of C14. i.e., best in $P4_2/mnm$ with similarly troublesome positions. Tables A-1 and A-2 give the refined data of C37. The solution indicates a fractional occupancy of 0.16(2) for the Sb(7) atom position. Therefore, this new DH phase can have a variable composition of Sb. Interestingly, full occupancy of both Sb(6) and Sb(7) positions would give the $Ca_{11}Sb_{10}$ structure as observed in Figure A-1, where $Ca_{11}Sb_{9+x}$ is represented in its idealized form, i.e., when x=0. Troublesome atoms Sb(6), Sb(7) and Ca(5) are located on the planes at z ~ 0, ½. Absence of the two diagonally opposite Sb atoms in the Sb_4-square planar array in $Ca_{11}Sb_{10}$ allows space for Ca(5) to relax from its original position, i.e., large anisotropic thermal parameters. Additionally, absence of these antimonys enhances the Ca–Ca repulsions in $Ca_{11}Sb_9$; therefore, a 0.54% cell volume increment with respect to $Ca_{11}Sb_{10}$ is observed, see Table A-3. Because of the high structural similarity between these two phases, a reliable quantification by Guinier powder patterns is not quite feasible, see Figure A-2. Importantly, the new phase was identified in products for the Ca–Bi, Sr–Sb and Sr–Bi combinations as well.

Table A-1. Crystallographic data for $Ca_{11}Sb_{9+x}$.

	$Ca_{11}Sb_{9.16(14)}$
Crystal from rxn.	C37
Space group	$P4_2/mnm$ (#136)
Lattice parameters[a]	
a (Å)	12.013(1)
c (Å)	17.258(2)
Volume (Å^3)	2490.5(4)
Z	4
Density calc. (g/cm^3)	4.098
Diffractometer	Enraf-Nonius CAD4
Crystal dimensions (mm)	0.30 x 0.15 x 0.05
Collected octants	h,k,l
Scan type	ω-2θ
Maximum 2θ (°)	60
Transmission range	0.749–1.112
Absorption coefficient (cm^{-1})	118.8
Number of reflections	
Measured	8079
Independent (observed[b])	2847(1308)
R_{ave} (%)[c]	11.9
No. of refined variables	65
R/R_w (%)	5.7/5.7
Goodness of fit	1.420
Secondary extinction coefficient	$4.5(2) \times 10^{-7}$
Max./min. peak in ΔF map. (e$^-$ Å^{-3})	5.43/-3.71

[a] Lattice parameters calculated from Guinier powder patterns.
[b] Observed reflections; $I \geq 3.00\sigma_I$.
[c] Average for all data; $I > 0$.

Table A-2. Refined positional and thermal parameters of $Ca_{11}Sb_9$ phase (C37).

Atom	x	y	z	B_{eq}(Å^2)	U_{11}	U_{22}	U_{33}	U_{12}	U_{13}	U_{23}
Sb(1)	0	½	¼	0.87(4)	0.0107(5)	U_{11}	0.0117(9)	0	0	0
Sb(2)	0	0	0.1395(1)	1.50(4)	0.0151(5)	U_{11}	0.027(1)	-0.0018(9)	0	0
Sb(3)	0.0119(2)	0.6566(1)	0	1.62(6)	0.035(1)	0.0114(6)	0.0155(7)	0.0085(7)	0	0
Sb(4)	0.19603(8)	x	0.3281(1)	1.61(4)	0.0175(4)	U_{11}	0.026(1)	0.0054(6)	0.0072(5)	U_{13}
Sb(5)	0.28353(8)	x	0.1813(1)	1.31(3)	0.0144(4)	U_{11}	0.0210(9)	0.0027(5)	-0.0013(5)	U_{13}
Sb(6)[a]	0.3834(2)	x	0	3.69(7)	0.061(1)	U_{11}	0.018(1)	-0.009(2)	0	0
Sb(7)[a]	0.319(1)	-x	0	3.5(5)	0.045(8)	U_{11}	0.04(1)	-0.022(9)	0	0
Ca(1)	0	0	0.3424(4)	2.0(2)	0.022(2)	U_{11}	0.034(4)	-0.006(3)	0	0
Ca(2)	0.1889(5)	x	0	3.2(2)	0.040(3)	U_{11}	0.040(5)	0.020(4)	0	0
Ca(3)	-0.0049(3)	0.2528(2)	0.1897(2)	1.5(1)	0.023(1)	0.014(1)	0.018(1)	-0.002(1)	-0.001(2)	-0.002(1)
Ca(4)	0.0100(3)	0.6614(2)	0.3968(2)	1.4(1)	0.021(1)	0.017(1)	0.014(1)	-0.003(1)	0.002(1)	0.001(1)
Ca(5)	0.131(1)	-x	0	11.2(5)	0.20(1)	U_{11}	0.021(5)	-0.19(1)	0	0

[a] Sb(7) refined to 16(1)% occupancy.

Table A-3. Lattice dimensions of the $Ca_{11}Sb_{10-x}$ (x= 0, 1) compounds.

Rxn No.	Loaded Comp.	Str.Type/ Conds.[a]	a (Å)	c (Å)	Vol.(Å^3)	c/a
C26	$Ca_{11}Sb_{10}$	H/sc	11.996(1)	17.214(2)	2477.1(4)	1.435
C37	$Ca_{11.5}Sb_{9.16}$	DH/dv	12.013(1)	17.258(2)	2490.5(4)	1.437

[a] Cell: H= $Ho_{11}Ge_{10}$-type, DH= $Ca_{11}Sb_9$-type, Conds: sc= sealed cont., dv= dyn. vac.

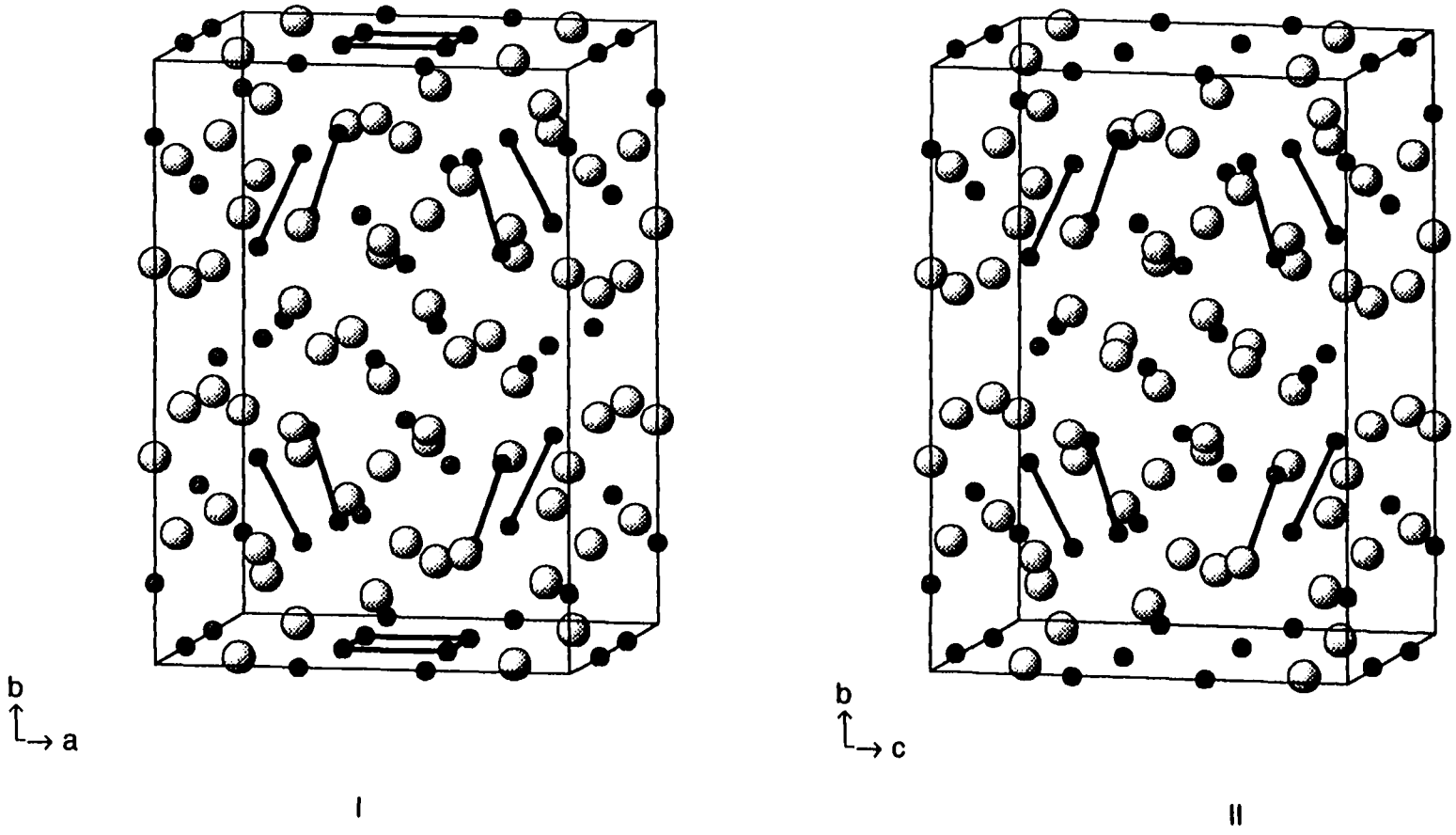

Figure A-1. Approximate [100] view of the I) $Ca_{11}Sb_{10}$ ($Ho_{11}Ge10$-type, I4/mmm, #139) and II) $Ca_{11}Sb_{9+x}$ ($P4_2/mnm$, #136, idealized model, x=0) . Large and small dark atoms represent Ca and Sb, respectively. Lines between atoms represent short Sb–Sb contacts, d < 3.1 Å. Troublesome atoms in the latter structure are at z ≈ 0, 1/2.

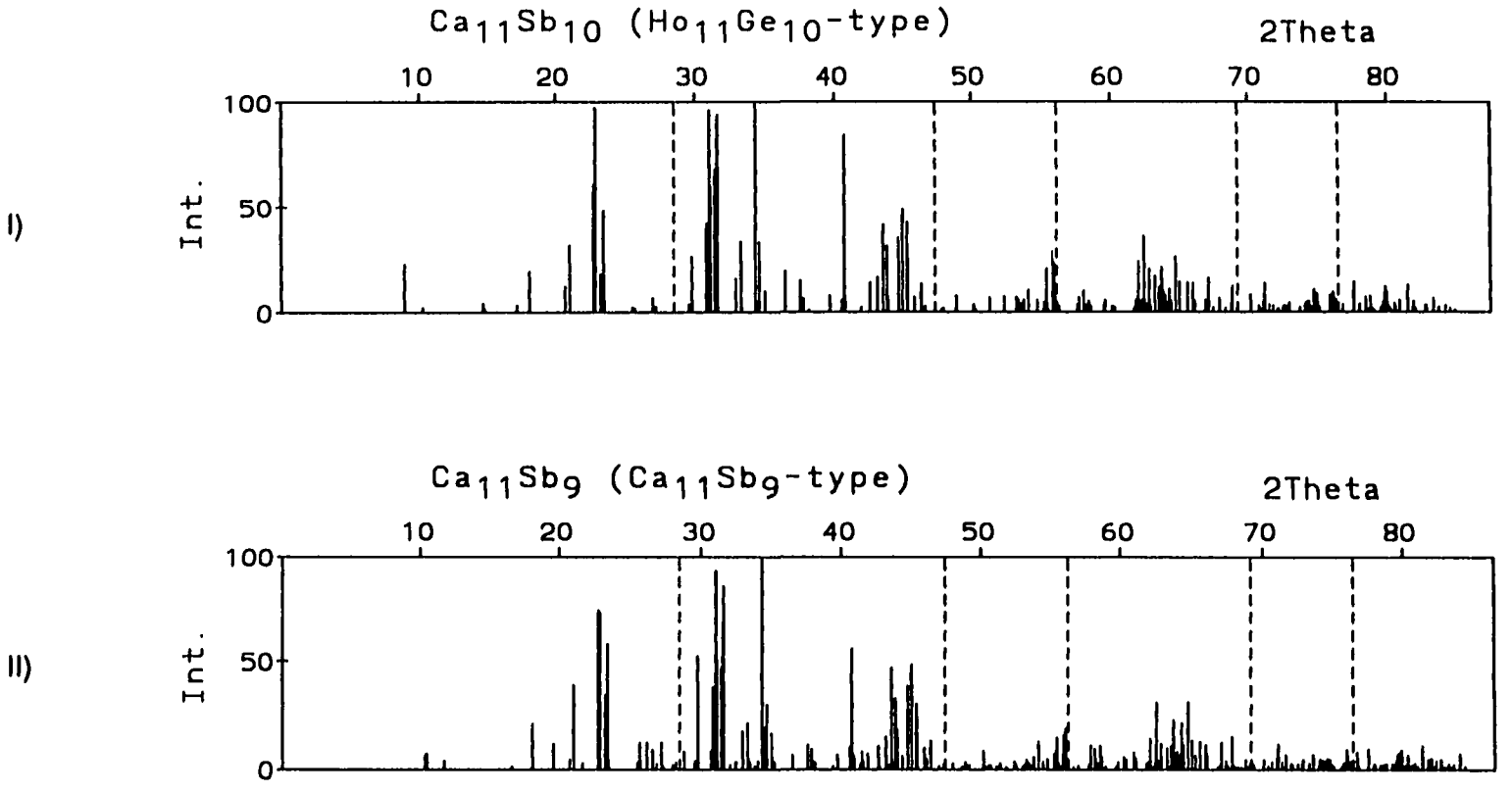

Figure A-2. Calculated Guinier powder patterns of the phases I) $Ca_{11}Sb_{10}$ ($Ho_{11}Ge_{10}$-type I4/mmm, #139) and II) $Ca_{11}Sb_9$ ($P4_2/mnm$, #136). Major differences between the patterns are at ~2θ = 27 – 30°. Experimental patterns are duplicated by these models.

APPENDIX B. DISTORTED $Ca_{16}Bi_{11}$

Experiments to prepare T-$Ca_{16}Bi_{11}$ phases gave products with two distinctive powder patterns. On one hand, when phases were prepared by the reaction between the elements at 1100°C, annealed above 850°C and subsequently quenched to room temperature, rxns I1 and I23 in Table III-40, the products powder patterns matched the T-type structure, see upper plot of Figure B-1. On the other hand, when a reaction was slowly cooled from 1100°C to 650°C, rxn I13, its product pattern could not be identified to the T-type structure, since several additional lines were present; lower plot of Figure B-1. The position and intensity of these additional lines suggested that the new phase crystallized in a symmetry lower than the tetragonal $P\bar{4}2_1m$. One very small crystal, probably multiple, was mounted on the Enraf-Nonius CAD4 diffractometer and data collected for a orthorhombic cell. The structure of the compound was partially solved in space group Pbm2 (#32) to convergence of the atom positions. The space group was selected based on the statistics of the observed reflections, see Table B-1. The calculated powder pattern based on these refined positions reproduced in more than 95% the lines of the experimental pattern. Discrepancies between the intensity of the first four low angle lines of the calculated pattern with (~50% more intense) respect to the experimental one were observed. Attempts to solve the structure in the monoclinic space group $P2_1/c$ (#14) did not give better statistics than for the orthorhombic model. Interestingly, the cell volume of the orthorhombic cell, v = 1788.5(7) $Å^3$, is only 0.22% larger than the volume of T-$Ca_{16}Bi_{11}$, v= 1784.5(2) $Å^3$, suggesting that they have similar compositions. Analysis of the orthorhombic structure with respect to the tetragonal T-type was not performed, because of the unreliability of the model. Table B-1 contains some of the crystallographic and refined information for sample I13.

It would be very interesting to study the factors that may be involved in the structural distortion from tetragonal T-$Ca_{16}Bi_{11}$ to the lower symmetry cell; however, the growth of good quality single crystals of the latter phase is primarily necessary to reliably solve its structure.

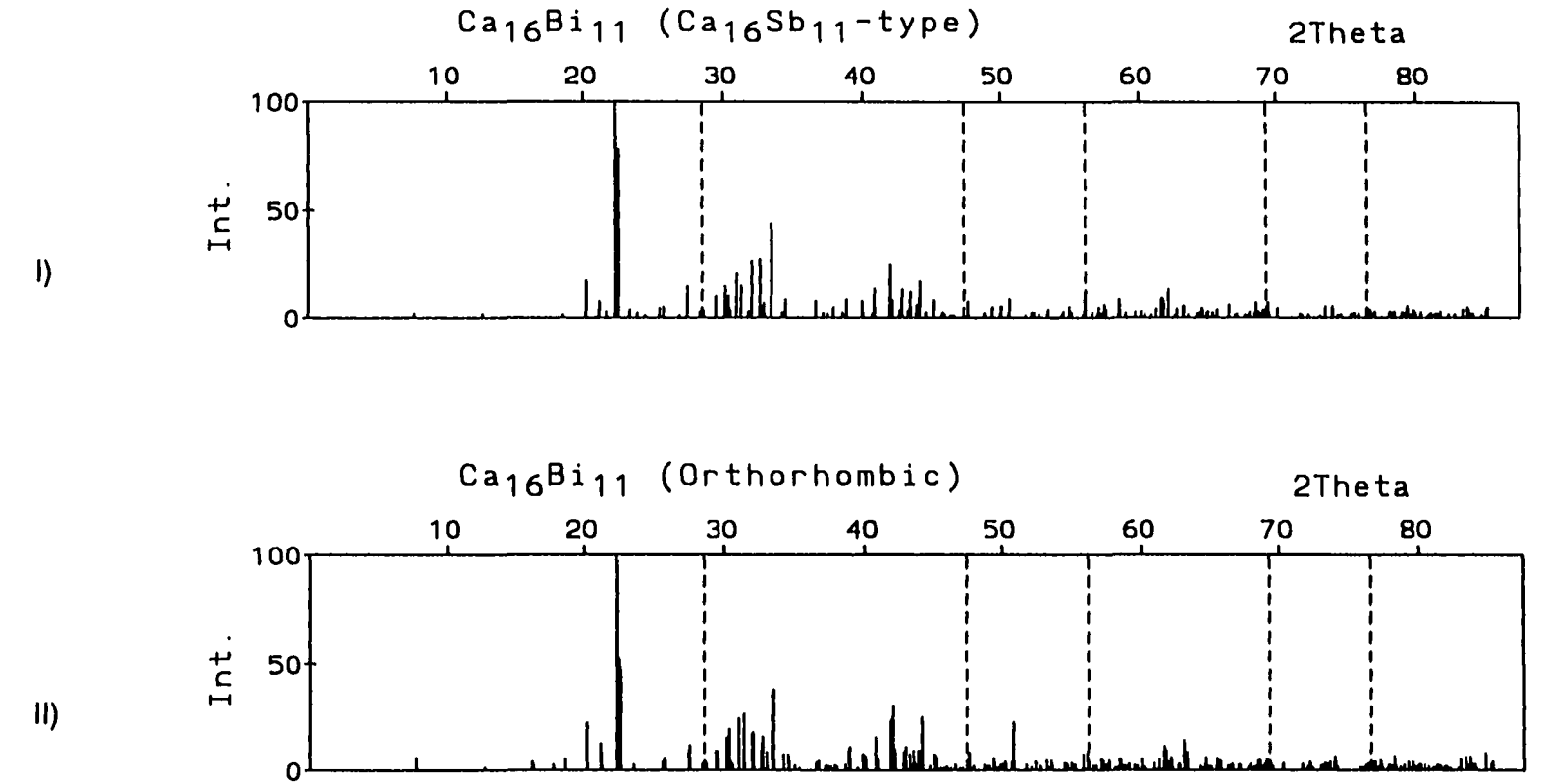

Figure B-1. Guinier powder patterns of $Ca_{16}Bi_{11}$ in I) the T-type structure ($P\bar{4}2_1m$, #113) and II) the distorted T-type partially solved in space group Pba2 (#32). Experimental powder patterns match quite accurately the models. The latter model disagrees only in the first four high-angle lines by ~ 50% more intense.

Table B-1. Some crystallographic and refined data of sample I13 (loaded $Ca_{16}Bi_{11}$).

Space group		Pbm2 (#32)
Lattice parameters[a]	a(Å)	12.483(3)
	b(Å)	12.555(3)
	c(Å)	11.412(2)
	Volume (Å^3), Z	1788.5(7), 2
Collected octants		h,k,±l
Transmission range		0.230–1.000
No. of Refl. Measured (observed[b]), R_{ave} (%)[c]		6245(3289), 17.8
R/R_w (%)		13.7/16.2[d]

Atom	x	y	z
Bi(1)	0.1738(6)	0.8242(6)	0.4693[e]
Bi(2)	0.1676(5)	0.8290(5)	0.9395(4)
Bi(3)	0.1259(4)	0.1217(3)	0.2016(6)
Bi(4)	-0.1458(4)	0.8527(4)	0.6820(4)
Bi(5)	0	½	0.2212(5)
Bi(6)	0	½	0.5476(6)
Bi(7)	0	½	0.8572(6)
Ca(1)	0.088(3)	0.709(2)	0.707(4)
Ca(2)	-0.081(3)	0.725(3)	0.991(3)
Ca(3)	-0.077(3)	0.702(3)	0.390(3)
Ca(4)	-0.177(4)	0.173(4)	0.465(3)
Ca(5)	0.290(2)	0.918(2)	0.708(4)
Ca(6)	0.187(3)	0.570(3)	0.380(3)
Ca(7)	0.212(3)	0.574(3)	0.008(2)
Ca(8)	0	0	0.510(3)
Ca(9)	0	0	0.869(3)

[a] Lattice parameters calculated from Guinier powder patterns.
[b] Observed reflections; $I \geq 3.00\sigma_I$.
[c] Average for all data; $I > 0$.
[d] Isotropic refinement.
[e] Fixed coordinate.

APPENDIX C. $Sr_{32}Sb_{24}Z$

During the initial experimental efforts to prepare $Sr_{16}Sb_{11}$ a reaction was unintentionally loaded Sr-deficient (rxn K2). This reaction was carried under sc conditions at 1100°C and annealed at 900°C for 2 weeks before quenching to room temperature. Incidentally, the Sr metal in this reaction was an old batch of Aesar 98% reagent that visually appeared quite oxidized. The major and minor products of reaction K2 were the tetragonal $Sr_{11}Sb_{10}$ ($Ho_{11}Ge_{10}$-type) and a phase that could not be identified with any binary in the Sr–Sb system, in a ~ 80:15 ratio, respectively. Some oxide Sr_4Sb_2O, <5%, was observed as well among the products. Well faceted crystals of the unidentified phase were picked up and their structure solved by X-ray diffraction. The selection of the space group was based the systematic absences in the zeroeth, first and second Weissenberg layer photographs of the crystal. Systematic absences for a orthorhombic lattice h00, 0k0 and hk0 for $h=2n+1$, $k=2n+1$ and $h+k=2n+1$, respectively, suggested the space groups $Pm2_1n$ (#39) and Pmmn (#59) for the structure. The best solution, based on the initial model provided by SHELX-86, was achieved in the latter space group, Pmmn, with the origin choice number 2. Attempts to refine the structure in the origin choice No. 1 resulted in bad statistics. Tables C-1, C-2 and C-3 summarize the crystallographic and refined data information of the new phase $Sr_{32}Sb_{24}Z$. Evaluation of the difference Fourier map after all Sr and Sb atoms positions were refined indicated an additional $6e^-$ peak (Z) that was refined as oxygen. The weak diffracting capacity of the crystal measured is blamed for the uneven anisotropic thermal parameters of Sb(1), Sb(6), Sb(8) and Sr(2) atoms. These apparent anisotropies would probably diminish if a larger number of observed reflections were available for the structural refinement.

The structure of the new orthorhombic phase can be described as stacking of layers of isolated Sb atoms that are eight- to ten-coordinate by strontium at $x\approx 0$, 1/2 and layers of isolated and dimers of Sb atoms at $x\approx 0.25$ and 0.75. Characteristically, the layers that contain the Sb dimers also contain octahedral cavities of Sr atoms centered by Z. The stacking of layers, 1:1, can be appreciated in the [010] view of $Sr_{32}Sb_{24}Z$ as depicted in Figure C-1, where the octahedral cavities are highlighted as

Table C-1. Crystallographic data for $Sr_{32}Sb_{24}Z$.

	$Sr_{32.0(3)}Sb_{23.9(2)}Z^a$
Crystal from rxn.	K2 (loaded $Sr_{16}Sb_{11}$)
Space group	Pmmn (#59, setting 2)
Lattice parameters	
a (Å)	16.712(2)
b (Å)	19.630(3)
c (Å)	11.885(2)
Volume ($Å^3$)	3899(2)
Z	2
Density calc. (g/cm^3)	4.890
Diffractometer	Rigaku AFC6R
Crystal dimensions (mm)	0.18 x 0.06 x 0.04
Collected octants	h,k,±l
Scan type	ω-2θ
Maximum 2θ (°)	50
Transmission range	0.925–1.104
Absorption coefficient (cm^{-1})	292.4
Number of reflections	
Measured	10258
Independent (observed[b])	5289(1520)
R_{ave} (%)[c] (observed[b])	20.2(4.36)
No. of refined variables	154
R/R_w (%)	4.1/4.4
Goodness of fit	1.030
Max./min. peak in ΔF map. ($e^- Å^{-3}$)	2.10/-2.05

[a] Z refined as oxygen, 167 variables.
[b] Observed reflections; $I \geq 3.00\sigma_I$.
[c] Average for all data; $I > 0$.

Table C-2. Refined positional and thermal parameters of $Sr_{32}Sb_{24}Z$ phase (K2).

Atom	x	y	z	B_{eq}(Å^2)	U_{11}	U_{22}	U_{33}	U_{12}	U_{13}	U_{23}
Sb(1)	¼	¼	0.4925(4)	0.8(2)	0.015(2)	0.004(3)	0.011(2)	0	0	0
Sb(2)	¼	¼	0.7361(4)	0.8(2)	0.008(3)	0.010(3)	0.012(2)	0	0	0
Sb(3)	¼	0.5575(2)	0.9936(3)	1.2(2)	0.010(2)	0.023(2)	0.014(2)	0	0	-0.005(2)
Sb(4)	¼	0.5547(2)	0.2362(3)	1.3(1)	0.013(2)	0.026(2)	0.012(2)	0	0	0.007(2)
Sb(5)	¼	0.6707(2)	0.6045(3)	0.9(1)	0.009(1)	0.011(2)	0.015(1)	0	0	0.001(2)
Sb(6)	¼	0.3270(2)	0.0996(3)	1.6(1)	0.017(1)	0.033(2)	0.011(2)	0	0	0.009(2)
Sb(7)	¼	0.4874(2)	0.6036(3)	0.9(1)	0.014(1)	0.008(2)	0.012(1)	0	0	0.001(2)
Sb(8)	-0.0562(2)	¼	0.1111(3)	1.1(1)	0.008(1)	0.025(2)	0.010(1)	0	-0.001(1)	0
Sb(9)	-0.0500(2)	¼	0.6725(3)	1.0(1)	0.012(2)	0.013(2)	0.011(2)	0	0.000(1)	0
Sb(10)	0.0449(1)	0.4249(1)	0.8494(2)	1.04(8)	0.014(1)	0.012(1)	0.014(1)	-0.000(1)	0.0007(8)	-0.001(1)
Sb(11)	0.0432(1)	0.3981(1)	0.3724(2)	0.86(8)	0.0104(9)	0.011(1)	0.011(1)	0.001(1)	-0.0004(8)	-0.001(1)
Sr(1)	¼	¾	0.3449(7)	1.4(3)	0.012(3)	0.019(5)	0.021(4)	0	0	0
Sr(2)	¼	¾	0.8773(8)	1.7(3)	0.011(3)	0.018(4)	0.034(4)	0	0	0
Sr(3)	¼	0.4110(2)	0.8536(4)	0.9(2)	0.015(2)	0.009(3)	0.012(3)	0	0	-0.001(2)
Sr(4)	¼	0.4048(2)	0.3660(4)	0.9(2)	0.012(2)	0.010(3)	0.013(3)	0	0	0.001(2)
Sr(5)	-0.0753(2)	¼	0.4011(4)	0.8(2)	0.013(2)	0.008(2)	0.011(2)	0	0.000(2)	0
Sr(6)	0.0912(3)	¼	0.9194(4)	1.5(2)	0.022(2)	0.014(3)	0.019(3)	0	0.007(2)	0
Sr(7)	0.1134(3)	¼	0.2626(4)	1.0(2)	0.012(2)	0.010(2)	0.017(2)	0	0.000(2)	0
Sr(8)	0.1211(2)	0.6607(2)	0.1135(3)	1.3(1)	0.026(1)	0.013(2)	0.011(1)	0.006(1)	0.001(1)	-0.001(2)
Sr(9)	0.0964(1)	0.4554(2)	0.1097(3)	1.1(1)	0.013(1)	0.014(2)	0.015(1)	0.001(1)	0.000(1)	-0.000(2)
Sr(10)	0.1200(2)	0.5771(2)	0.7745(3)	1.1(1)	0.013(1)	0.013(2)	0.016(2)	-0.001(1)	-0.003(1)	0.002(1)
Sr(11)	0.1100(2)	0.3553(2)	0.6170(3)	0.9(1)	0.013(1)	0.010(2)	0.011(1)	0.003(1)	-0.002(1)	0.001(2)
Sr(12)	0.1017(2)	0.5647(2)	0.4341(3)	1.4(1)	0.021(2)	0.013(2)	0.020(2)	0.003(1)	0.007(1)	0.001(1)
Z[a]	¼	¾	0.116(5)	2(1)						

[a] Refined as oxygen.

Table C-3. Important interatomic distances in $Sr_{32}Sb_{24}Z$.[a]

Atom(1) – Atom(2)	d(Å)	Atom(1) – Atom(2)	d(Å)
Sb(1) – Sb(2)	2.896(6)	Other Sb – Sb	> 4.32
Sb(3) – Sb(4)	2.883(4)	Z^a – Sr(1) (x1)	2.72(6)
Sb(5) – Sb(5)	3.115(6)	Z^a – Sr(2) (x1)	2.84(6)
Sb(5) – Sb(7)	3.597(4)[b]	Z^a – Sr(8) (x4)	2.778(3)
Sb(6) – Sb(6)	3.022(8)	All Sr – Sr	> 3.51

[a] Z refined as oxygen.
[b] Sb–Sb bonding interaction considered d < 3.2 Å.

shaded polyhedra. The Sb dimers Sb(1)–Sb(2), Sb(3)–Sb(4), Sb(5)–Sb(5) and Sb(6)–Sb(6) and isolated Sb(7) as observed in Figure C-2, are eight-coordinate in bicapped trigonal prismatic arrangements of Sr atoms that share faces or edges. The Sb–Sb dimers are both perpendicular (⊥) and parallel (∥) to the b axis and alternated with Z-centered octahedral cavities (◊) in a $[\perp : \parallel : \perp : \Diamond]_n$ succession. Parallel to this succession, isolated and dimers of Sb atoms run along the b axis as well. An infinite $[\perp : \parallel]_n$ succession extends on the c direction; such an infinite succession of pnictide dimers $[\perp : \parallel]_n$ has already been observed in the orthorhombic Ba_4P_3-type structure.[150] The isolated Sb atoms, Sb(8), Sb(9), Sb(10) and Sb(11), at x ≈ 0, 1/2 are enclosed in a more complex and irregular polyhedra of Sr atoms. Figure C-3 gives a detail of the coordination environment of these isolated Sb atoms, where the Sb(8) and Sb(9) atoms are ten-coordinate and nine-coordinate, respectively. The Sb(10) and Sb(11) atoms are eight-coordinate in a distorted pentagonal-bipyramidal arrangement of Sr atoms. Although not specifically depicted, the Sr(1) and Sr(2) atoms are seven-coordinate in a distorted pentagonal bipyramidal arrangement of Sb and Z atoms. The other Sr atoms are enclosed in six-coordinate arrangements of Sb or Sb and Z atoms.

The electron count based on current structural information suggest that the phase might be a Zintl or valence compound. If Sb–Sb interatomic distances lower than 3.2 Å are considered single bond interactions, the electron count is $32Sr^{2+}$, $5Sb_2^{4-}$,

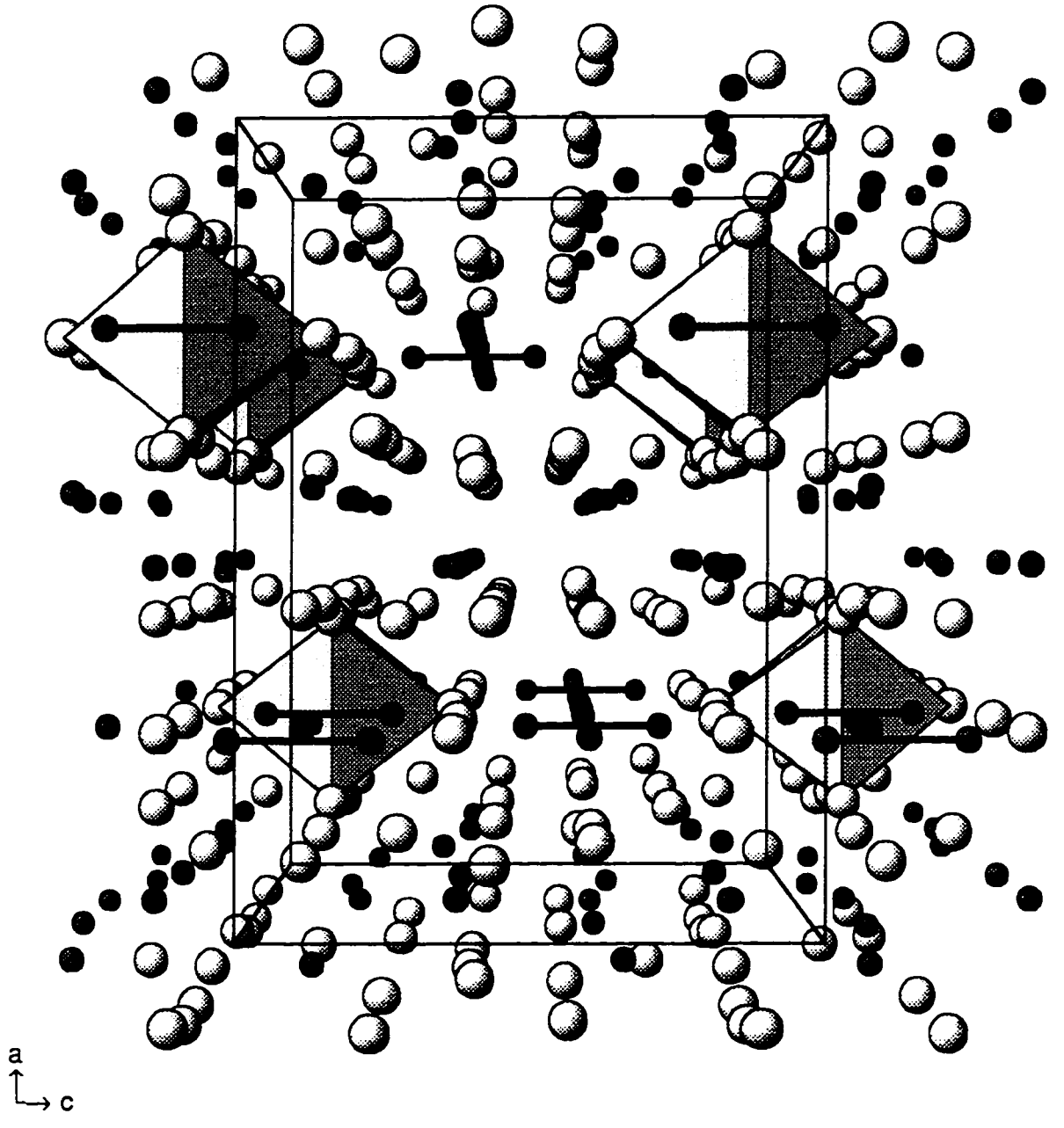

Figure C-1. The [010] view of one and a half cells of the $Sr_{32}Sb_{24}Z$ structure. Large light and small dark spheres represent Sr and Sb atoms, respectively. Short Sb–Sb contacts, d < 3.2 Å, are represented as heavy lines. Octahedral interstices are highlighted as shaded polyhedra. The interstitial atom Z centers these polyhedra.

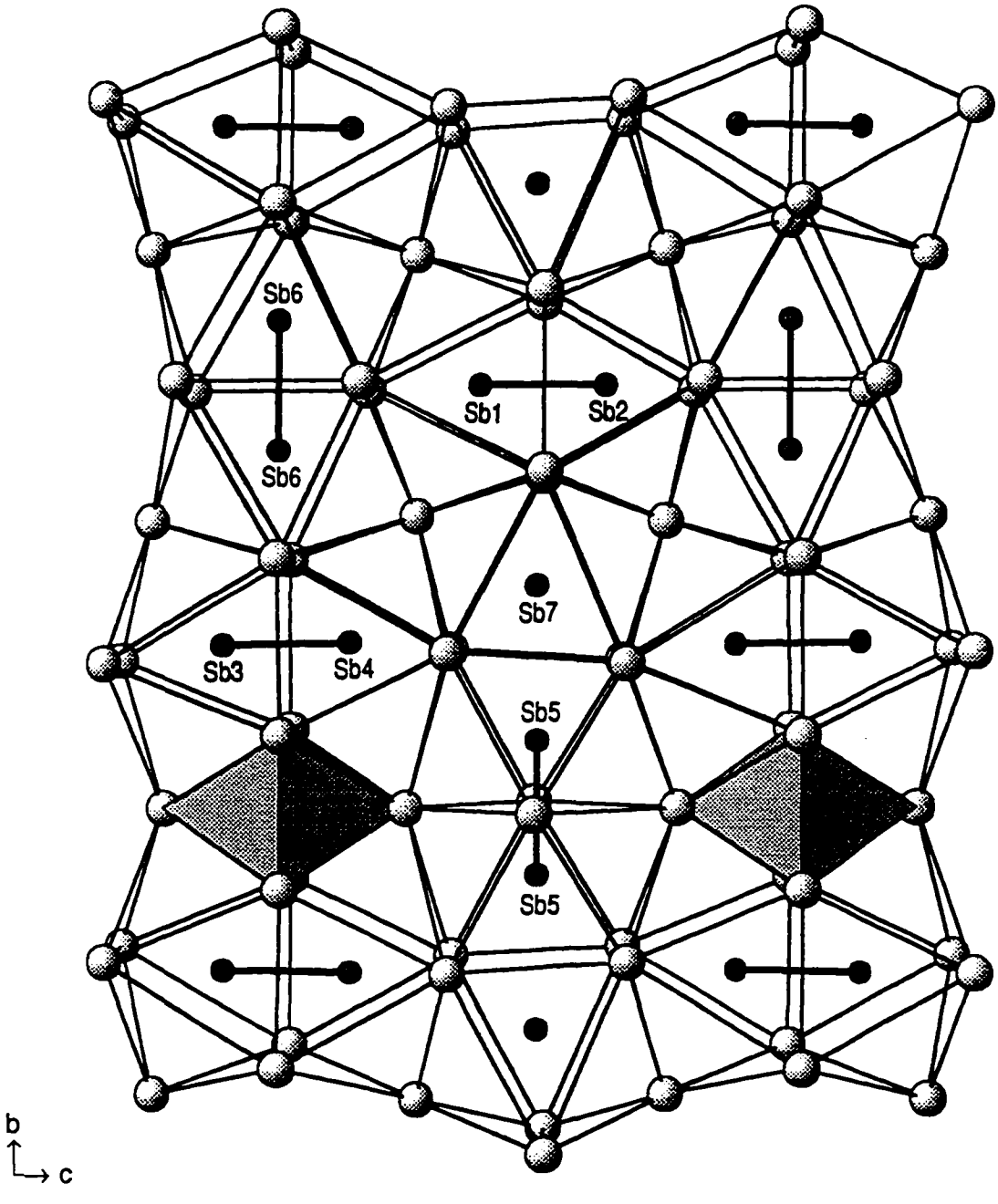

Figure C-2. Layer at x ~0.25 of the $Sr_{32}Sb_{24}Z$ structure. Large light and small dark spheres represent Sr and Sb atoms, respectively. Lines between Sr atoms do not represent bonds. Short Sb–Sb contacts, d< 3.2 Å, are represented as heavy lines. Octahedral interstices are highlighted as shaded polyhedra.

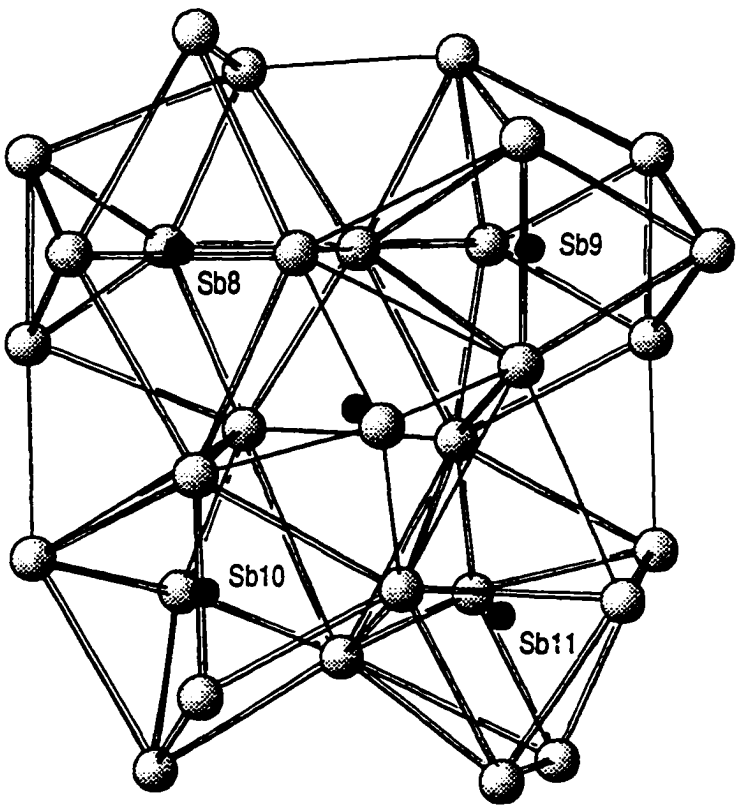

Figure C-3. Detail of the layer at x ≈ 0.0 of the $Sr_{32}Sb_{24}Z$ structure. Large light and small dark spheres represent Sr and Sb atoms, respectively. Coordination environments around Sb(8), Sb(9), Sb(10) and Sb(11) atoms are highlighted with double lines.

$14Sb^{3-}$, $2e^-$. Consequently, presumption of the presence of oxygen in the interstitial position would have assured the electroneutrality of the compound, i.e., $32Sr^{2+}$, $5Sb_2^{4-}$, $14Sb^{3-}$, O^{2-}. The distance from the edges to the center of the octahedral cavity, d_{ave}= 2.78Å, are close to the sum of crystal radii for the Sr^{2+} and O^{2-} ions, 2.61 Å.[62] However, experiments to reproduce the compound as a ternary oxide, $Sr_{32}Sb_{24}O$, were not successful, rxns G8, G13 and G15, they formed $Sr_{11}Sb_{10}$ instead. Reactions involving hydrogen, $Sr_{32}Sb_{24}H_{(2,4)}$ (rxn. G17 and G18, respectively), fluorides, $Sr_{16}Sb_{12}F$ (rxn. GF1) and as a binary Sr_4Sb_3 (rxn. G5, G6, G7 and G14) did not form the phase sought as well. Reactions involving other interstitial atoms like B, C or N were not attempted; although, an electron count involving the Sb(5)–Sb(7) interaction, d= 3.597(4) Å, as a half bond suggests that the interstitial atom might be a tetravalent ion, Z^{4-}, in order to achieve closed shell configuration, i.e., $32Sr^{2+}$, $4Sb_2^{4-}$, Sb_4^{8-}, $12Sb^{3-}$, Z^{4-}. Presence of tetrahedral cavities in the structure do not preclude the possibility of two different interstitial atoms like H^- and N^{3-} in the compound. Presumption of bonding interaction between the Sb(7) and Sb(5) atoms implies that the structure contains a linear hypervalent $[Sb(7)–Sb(5)–Sb(5)–Sb(7)]^{8-}$ unit. It would be very interesting to test whether this supposition is close to correctness by reactions between Sr and Sb in presence of carbon and, subsequently, to measure the properties of single phase products with this unprecedented structure.

Interestingly, the unsuccessful reactions for the binary, Sr_4Sb_3, seem to contradict some of the recent results obtained in von Schnering's group in Germany[150]. They have found the "binary" Sr_4Sb_3 phase in the Ba_4P_3-type structure by reaction among Sb, Sr and SrO; such a binary phase was never observed during this work.

BIBLIOGRAPHY

1. Smith, J.F.; Bernstein,B.T., *Acta Crystallogr.*, **1959**, *12*, 419.
2. Peterson, D.T.; Fattore, V.G., *J. Phys. Chem.*, **1961**, *65*, 2062.
3. McMasters, D.T.; Gschneidner, Jr., K.A., *Trans. Met. Soc. AIME*, **1967**, *239*, 781.
4. Novotny, H.; Parthé, E.; Kieffer, R.; Benesovsky, F., *Monatsch. Chem.*, **1954**, *85*, 255.
5. Novotny, H.; Seary, A.W.; Orr, J.E., *J. Phys. Chem.*, **1956**, *60*, 677.
6. Kwon, Y.-U.; Rzeznik, M.A.; Guloy, A.M.; Corbett, J.D., *Chem. Mater.*, **1990**, *2*, 546.
7. Schäfer, H.; Einsenmann, B.; Müller, W., *Angew. Chem. Int. Ed. Engl.*, **1973**, *12*, 694.
8. Schäfer, H.; Einsenmann, B., *Rev. Inorg. Chem.*, **1981**, *3*, 29.
9. Schäfer, H., *Ann. Rev. Mater. Sci.*, **1985**, *15*, 1.
10. Hughbanks, T., in *Inorganometallic Chemistry*, T. Fehlner ed., Plenum Press, New York, **1992**, p291.
11. Nesper, R., *Prog. Solid State Chem.*, **1990**, *20*, 1.
12. Hirano, T., *J. Less-Common Met.*, **1991**, *167*, 329.
13. Fahy, S.; Hamann, D.R., *Phys. Rev. B*, **1990**, *41*, 7587.
14. Imai, M.; Hirano, T., *J. Alloys Compd.*, **1995**, *224*, 111.
15. Miller, G.J., in *Chemistry, Structure and Bonding of Zintl Phases and Ions*, Kauzlarich, S., ed; VCH Publishers, Boca Raton, FL, Chapter 5, to be published.
16. Wiswall, R., in *Hydrogen in Metals II*, Alefeld, G.; Völk, J. eds. Springer Verlag, New York, **1978**, p201.
17. Sandrock, G.; Suda, S.; Schlapbach, L., *Hydrogen in Intermetallic Compounds II*, Schlapbach, L. ed. Springer Verlag, New York, **1988**, ch.5.
18. Fukai, J., *The Metal–Hydrogen System*, Springer Verlag, New York, **1993**.
19. Peterson, D.T., *J. Metals*, **1987**, *39*, 20.
20. Corbett, J.D., *Inorg. Synth.*, **1983**, *22*, 15.
21. Imoto, H.; Corbett, J.D., *Inorg. Chem.*, **1981**, *20*, 145.
22. Galaktinova, N.A., *Hydrogen–Metal Systems Databook*, Ordentlich Press, Israel, **1980**, p64.
23. Magee, C.B., in *Metal Hydrides*, Mueller, W.M.; Backledge, J.P.; Libowitz, G.G., eds., Academic Press, NY, **1968**, Ch 6.

24. Villars, P.; Clavert, L.D., *Pearson's Handbook of Crystallographic Data for Intermetallic Phases*, 2nd ed., American Society for Metals International, Metals Park, OH, **1991**.

25. Brückner, R., *J.Non-Cryst. Solids*, **1971**, *6*, 177.

26. Clark, C.M.; Smith, D.K.; Johnson, G.J., *A Fortran IV Program for Calculating X-Ray Powder Diffraction Patterns*, Version V, Dept. of Geosciences, Pennsylvania State University, University Park, PA., **1973**.

27. Takusawa, F., *A Fortran Program for Least Squares of Indexed Guinier X-Ray Powder Patterns*, Unpublished research, Ames Laboratory, Iowa State University, **1981**.

28. Werner, P.-E., *SCANPI (Scan-Calculate-Analyze-Numerical-Powder-Intensities)*, Version 8, A program to evaluate data collected by the Film Scanner LS20, Arrhenius Laboratory, Stockholm University, Sweden, **1990**.

29. Walker, N.; Stuart, D., *Acta Crystallogr.*, **1983**, *A39*, 158.

30. Sheldrick, G.M., *SHELX86*, A program package for single crystal x-ray structure solutions, Universität Göttingen, Germany, **1986**.

31. TEXSAN, *Single Crystal Structure Analysis Software*, Version 5.0, Molecular Structure Corporation, The Woodlands, TX, **1989**.

32. Fisher, R.X.; Tilmanns, E, *Acta Crystallogr.*, **1988**, *C44*, 775.

33. Yethiraj, M.; Fernandez-Baca, J.A., *Neutron Scattering at the High Flux Isotope Reactor at Oak Ridge National Laboratory*; Users manual; Neutron Scattering Group, Solid State Division ORNL, Oak Ridge, TN, **1994**.

34. Larson, A.C.; Von Dreele, R.B., *GSAS: General-Structure-Analysis-System*; LANSCE, MS-805, Los Alamos National Laboratory, Los Alamos, NM., **1994**.

35. Rietveld, H.J., *J. Appl. Cryst.*, **1969**, *2*, 65.

36. Shinar, J.; Dehner, B.; Beaundry, B.J.; Peterson, D.T, *Phys. Rev. B*, **1988**, *37*, 2066.

37. El-Hannay, U., *Rev. Sci. Instrum.*, **1973**, *44*, 1069.

38. van der Pauw, L.J., *Phillips Res. Rep.*, **1958**, *13*, 1.

39. Dong, Z.C.; Corbett, J.C., *J. Cluster Sci.*, **1995**, *6*, 187.

40. Sevov, S.C.; Corbett, J.D., *Inorg. Chem.*, **1992**, *31*, 1895.

41. Selwood, P.W., *Magnetochemistry*, 2nd.ed., Interscience Publishers Inc., New York, **1956**, p.78.

42. Hoffmann, R., *J. Chem. Phys.*, **1963**, *39*, 1397.

43. Whangbo, M.H.; Hoffmann, R.; Woodward, R.B., *Proc. Royal Soc. London Ser.*, **1978**, *100*, 3686.

44. Chadi, D.J.; Cohen, M.L., *Phys. Rev B*, **1973**, *8*, 5747.

45. Alvarez, S., *Tables of Parameters for Extended Hückel Calculations*, Universitat de Barcelona, Barcelona, Spain, **1989** and references therein.

46. Liu, Q.; Hoffmann, R.; Corbett, J.D., *J. Phys. Chem.*, **1994**, *98*, 9360.

47. Bruzzone, G.; Franceschi, E.; Merlo, F., *J. Less-Common Met.*, **1978**, *60*, 59.

48. Rehr, A.; Kauzlarich, S.M., *Acta Crystallogr.*, **1993**, *C49*, 1442.

49. Bodnar, R.E.; Steinfink, H., *Inorg. Chem.*, **1967**, *6*, 327.

50. Hurng W.-M.; Corbett, J.D., *Chem. Mater.*, **1989**, *1*, 311.

51. Potel, M.; Chevrel, R.; Sergent, M.; Fisher, O.C.R., *Seances Acad. Sci. Ser. C*, **1979**, *288*, 429.

52. Kwon Y.-U.; Corbett, J.D., *Chem. Mater.*, **1992**, *4*, 1348.

53. Guloy, A.M., *Ph.D. Thesis*, Iowa State University, **1992**.

54. Brunton, G.D.; Steinfink, H., *Inorg. Chem.*, **1971**, *10*, 2301.

55. Eisenmann, B.; Limartha, H., Schäfer, Graf, H.A.; *Z. Naturforsch.*, **1980**, *35b*, 1518.

56. Wolfe, L.G., *M.S. Thesis*, Iowa State University, **1990**.

57. Marek, H.S.; Corbett, J.D., *Inorg. Chem.*, **1983**, *22*, 3194.

58. Eisenmann, B.; Deller, K., *Z. Naturforsch.*, **1975**, *30b*, 66.

59. Rustad, D.S.; Gregory, N.W., *Inorg. Chem.*, **1982**, *21*, 2929.

60. Hurng, W.-M., *Ph.D. Thesis*, Iowa State University, **1988**.

61. Pauling, L., *The Nature of the Chemical Bond*, 3rd ed., Cornell University Press, Ithaca, New York, **1960**, p403.

62. Shannon, R.D., *Acta Crystallogr.*, **1976**, *A32*, 751.

63. Meisel, K., *Z. Anorg. Allg. Chem.*, **1939**, *240*, 300.

64. Maass, K.E.Z., *Z. Anorg. Allg. Chem.*, **1970**, *374*, 11.

65. Hulliger, F; Vogt, O., *Solid State Commun.*, **1970**, *8*, 771.

66. Martinez-Ripoll, M.; Bauer, G., *Acta Crystallogr.*, **1974**, *30B*, 1083.

67. Bronger, W., *Z. Anorg. Allg. Chem.*, **1996**, *622*, 9.

68. Niyazova, Z.U., Vakhobov, A.V.; Dzhuraev, T.D., *Inorg.Mater.* (Engl.), **1976**, *12*, 1074.

69. Notin, M.; Mejbar, J.; Bouhajib, A.; Charles, J.; Hertz, J., *J. Alloys Compd.*, **1995**, *220*, 62.

70. Abdusalyamova, M.N., *J. Alloys Compd.*, **1993**, *202*, L15.

71. Leon-Escamilla, E.A., *Research Report*, Ames Laboratory-DOE, Iowa State University, Fall **1996**.

72. Gschneidner, Jr, K.A. in *Handbook of Physics and Chemistry of Rare Earths*, Cumulative Index Volume 1-15, Gschneidner, Jr., K.A.; Eyring, L. eds., North-Holland Science Publishers B.V. Amsterdam, **1993**, p509.

73. Smornov, M.P.; Rudnichenko, V.E., *Russ. J. Inorg. Chem.*, (Engl) **1963**, *8*, 728.

74. Martinez-Ripoll, M.; Hoose, A.; Bauer, B., *Acta Crystallogr.*, **1974**, *30B*, 2004.

75. Hösel, S., *Z. Phys. Chem.*, **1962**, *219*, 205.

76. Better, B.; Hütz, A.; Nagorsen, G., *Z. Metal.*, **1976**, *67*, 118.

77. Hütz, A.; Nargosen, G., *Z. Metal.*, **1975**, *66*, 314.

78. Hütz, A.; Nargosen, G., *Z. Metal.*, **1976**, *67*, 181.

79. Martinez-Ripoll, M.; Bauer, G., *Acta Crystallogr.*, **1973**, *29B*, 2717.

80. Taylor, J.B.; Calvert, L.D.; Despault, J.G.; Gabe, E.J.; Murray, J.J., *J. Less-Common Met.*, **1974**, *37*, 217.

81. Borzone, G.; Borese, A.; Delfino, S.; Ferro, R., *Z. Metal.*, **1985**, *76*, 208.

82. Abdulsaljamova, M.N.; Albuchaev, V.D.; Levitin, R.Z.; Markosijan, A.S.; Popov, V.F.; Yumaguzhin, R., *J. Less-Common Met.*, **1986**, *120*, 281.

83. Sadigov, F.M., Shahguliev, N.S., Aliyev, O.M., *J. Less-Common Met.*, **1988**, *144*, L5.

84. Sadigov, F.M.; Geidarova, F.A.; Aliev, I.I., *Russ. J. Inorg. Chem.*, (Engl.) **1988**, *33*, 1238.

85. Wang, Y.; Calvert, L.D.; Taylor, J.B.; Gabe, E.J., *Acta Crystallogr.*, **1978**, *34A*, S156.

86. Wang, Y.; Calvert, L.D.; Gabe, E.J.; Taylor, J.B., *Acta Crystallogr.*, **1978**, *34B*, 2281.

87. Taylor, J.B.; Calvert, L.D.; Wang, Y., *J. Appl. Cryst.*, **1979**, *12*, 249.

88. Ono, S.; Despault, J.G., Calvert, L.D., Taylor, J.B., *J. Less-Common Met.*, **1970**, *22*, 51.

89. Maskudova, T.F.; Rustamov, P.G.; Aliev, O.M., *J. Less-Common Met.*, **1985**, *109*, L19.

90. Ono, S.; Hui, F.L.; Despault, J.G.; Calvert, L.D.; Taylor, J.B., *Sol.State Commun.*, **1971**, *25*, 287.

91. Taylor, J.B.; Calvert, L.D.; Utsunomija, T., Wang, Y; Despault, J.G., *J.Less-Common Metals*, **1978**, *57*, 39.

92. Wang, Y. Calvert, L.D., Gabe, E.J., *Acta Crystallogr.*, **1980**, *B36*,221.

93. Leon-Escamilla, E.A.; Corbett, J.D., *J. Alloys Compd.*, **1994**, *206*, L15.

94. Kittel, C, *Introduction to Solid State Physics*, 2nd ed., J. Wiley, New York, **1956**, p218.

95. Abdusalyamova, M.N.; Abulkhaev, V.D.; Levitin, R.Z.; Markosyan, A.S.; Popov, Y.F.; Yumaguzhin, R.Y., *Sov. Phys. Sol. St.*, (Engl.) **1984**, *26*, 343.

96. Abdusalyamova, M.N.; Albuchaev, V.D.; Kruglyashov, S.B.; Levitin, R.Z.; Markosyan, A.S.; Snegirev, V.V., *Sov. Phys. Sol. St.*, (Engl.) **1982**, *24*, 824.

97. Yakinthos, J.K.; Semitelou, I.P.; Roudaut, E., *Sol. State Commun.*, **1986**, *59*, 227.

98. Yakinthos, J.K.; Semitelou, I.P., *J. Magn. Mag. Mat.*, **1983**, *36*, 136.

99. Gordon, R.A.; Ijiri, Y.; Spencer, C.M.; DiSalvo, F.J., *J. Alloys Compd.*, **1995**, *224*, 101.

100. *CRC Handbook of Chemistry and Physics*, 66th ed., Weast, R.C, ed.-in-chief, CRC Press, Inc., Boca Raton, FL, **1986**, pF120.

101. Spedding, F.H.; Croat, J.J., *J. Chem. Phys.*, **1973**, *58*, 5514.

102. Spedding, F.H.; Croat, J.J., *J. Chem. Phys.*, **1973**, *59*, 2451.

103. Jacobson, A.J.; Newsman, J.M.; Johnston, D.C.; Goshorn, D.P.; Lewandowski, J.T.; Alvarez, M.S., *Phys. Rev. B*, **1989**, *39*, 254.

104. Sröder, K., *Electronic, Magnetic and Thermal Properties of Solid Materials*, Marcel Dekker, Inc., New York, **1978**, Ch 2.

105. Collings, E.W., *Phys. Kondens. Mat.*, **1965**, *3*, 335.

106. Yee, K.A.; Hughbanks, T., *Inorg. Chem.*, **1992**, *31*, 1620.

107. Borzone, G.; Fornasini, M.L., *Acta Crystallogr.*, **1990**, *C46*, 2456.

108. *Binary alloy phase diagram*, 2nd ed., Massalski, T.B. editor-in-chief, The Materials Information Society, ASM International, Materials Park, OH, **1990**.

109. Wang, Y.; Gabe, E.J.; Calvert, L.D.; Taylor, J.D., *Acta Crystallogr.*, **1976**, *B32*, 1440.

110. Garcia, E.; Corbett, J.D., *Inorg. Chem.*, **1988**, *27*, 2353.

111. Yoshihara, K.; Taylor, J.B.; Calvert, L.D.; Despault, J.G., *J.Less-Common. Met.*, **1975**, *41*, 329.

112. Berger, R., *Acta Chem. Scand.*, **1976**, *A30*, 363.

113. Schmidt, F.A.; McMasters, O.D., *J.Less-Common Met.*, **1970**, 21, 415.

114. Borzone, G.; Borese, A.; Saccone, A.; Ferro, R., *J. Less-Common Met.*, **1979**, *65*, 253.

115. Wang, Y.; Calvert, L.D.; Taylor, J.D., *Acta Crystallogr.*, **1966**, *21*, 435.

116. Hulliger, F.; Ott, H.R., *J.Less-Common Met.*, **1977**, *55*, 103.

117. Hohnke, D.; Parthé, E., *J.Less-Common Met.*, **1969**, *17*, 291.

118. Holtzberg, F.; McBuire, T.R,; Methfessel, S.; Suits, J.C., *J.* Appl. Phys., **1964**, *35*, 1033.

119. Rieger, W.; Parthé, E., *Acta Crystallogr.*, **1968**, *24B*, 456.

120. Abdusalyamova, M.N.; Abulkhaev, V.D.; Checernikov, V.I., *Inorg. Mater.*, (Engl.) **1981**, *17*, 1696.

121. Abdusalyamova, M.N.; Burnashev, O.R.; Mironov, K.Y., *J. Less-Common Met.*, **1986**, *125*, 1.

122. Bärnighausen, H.; Knausenberger, M.; Bauer, G., *Acta Crystallogr.*, **1965**, *19*, 1.

123. Berger, R., *Acta Chem. Scand.*, **1980**, *A34*, 231.

124. Berger, R., *Acta Chem. Scand.*, **1977**, *A31*, 514.

125. Carrillo-Cabrera, W.; Lundström, T., *Acta Chem. Scand.*, **1979**, *A33*, 401.

126. Carrillo-Cabrera, W.; Lundström, T., *Acta Chem. Scand.*, **1980**, *A34*, 415.

127. Berger, R., *Acta Chem. Scand.*, **1977**, *A31*, 889.

128. Berger, R., *Acta Chem. Scand.*, **1975**, *A29*, 641.

129. Beaudry, B.J.; Gschneidner, Jr., K.A.; in *Handbook on the Physics and Chemistry of Rare Earths*, Gschneidner, Jr., K.A; Eyring, L. eds., North-Holland Publishing Co., Amsterdam, **1978**, *Vol 1*, p173.

130. Guloy, A.M.; Corbett; J.D., *Inorg. Chem.*, **1993**, *32*, 3532.

131. Corbett, J.D.; in *Chemistry, Structure and Bonding of Zintl Phases and Ions*, Kauzlarich, S., ed; VCH Publishers, Boca Raton, FL, Chapter 3, in press.

132. Somer, M.; Carrillo-Cabrera, W.; Peters, E.-M.; Peters, K.; von Schneing, H.G., *Z. Kristall.*, **1995**, *210*, 875.

133. Peterson, E., *Research Report*, Ames Laboratory-DOE, Iowa State University, **1990**.

134. Moreau, J.-M.; Paccard, D; Parthé, E., *Acta Crystallogr.*, **1976**, *32B*, 1767.

135. Cromer, D.T.; Larson, A.C., *Acta Crystallogr.*, **1977**, *33B*, 2620.

136. Aronson, B., *Acta Chem. Scan.*, **1955**, *9*, 1107.

137. Deller, K.; Eisenmann, B., *Z. Naturforsch.*, **1976**, *31b*, 29.

138. Brechtel, E.; Cordier, G.; Schäfer, H., *Z. Naturforsch.*, **1981**, *36b*, 1341.

139. Bolloré, G; Ferguson, M.J.; Hushagen, R.W.; Mar, A., *Chem. Mater.*, **1995**, *7*, 2229.

140. Smith, G.S.; Johnson, Q.; Tharp, A.G., *Acta Crystallogr.*, **1967**, *23*, 640.

141. Leon-Escamilla, E.A., *Quarterly Research Report*, Ames Laboratory DOE, Spring **1992**.

142. Sheldrick, G,M., *SHELX-93, Program for Crystal Structure Refinement*, University of Göttingen, Germany, **1993**.

143. Bloss, F.D., *Crystallography and Crystal Chemistry, An Introduction*, **1971**, Holt, Rinehart and Winston Publ., New York, p 325.

144. Cordier, G.; Schäfer, H.; Stelter, M., *Z. anorg. allg. Chem.*, **1984**, *519*, 183.

145. Gallup, R.F.; Fong, C.Y.; Kauzlarich, S.M., *Inorg. Chem.*, **1992**, *31*, 115.

146. Rehr, A.; Kuromoto, T.Y.; Kauzlarich, S.M.; Del Castillo, J; Webb, D.J., *Chem. Mater.*, **1994**, *6*, 93.

147. Alemany, P; Alvarez, S.; Hoffmann, R., *Inorg. Chem.*, **1990**, *29*, 3070.

148. Cordier, G.; Schäfer, H.; Selter, M., *Z. anorg. allg. Chem.*, **1986**, *534*, 137.

149. Vaughey, J.T.; Corbett, J.D., *Chem. Mater.*, **1996**, *8*, 671.

150. Hadenfeldt, C.; Terschüren, H.-U.; Hönle, W.; Schröder, L.; von Schnering, H.G., *Z. anorg. allg. Chem.*, **1993**, *619*, 843.

151. Somer, M.; Carrillo-Cabrera, W.; Peters, K.; von Schnering, H.G., *Z. Kristall.*, **1995**, *210*, 876.

152. Ganguli, A.K.; Guloy A.M; Leon-Escamilla, E.A.; Corbett, J.D., *Inorg. Chem.*, **1993**, *32*, 4349.

153. Nargosen, G.; Rocktäschel, G.; Schäfer, H., Weiss, A., *Z. Naturforsh.*, **1967**, *22B*, 101.

154. Janzon., K.; Schäfer, H.; Weiss, A., *Z. Naturforsh.*, **1966**, *21B*, 287.

155. Helleis, V.O.; Kandler, H.; Leicht, E.; Quiring, W.; Wölfel, E., *Z. anorg. allg. Chem.*, **1963**, *320*, 86.

156. Fornasini, M.L.; Franceschi, E., *Acta Crystallogr.*, **1977**, *33B*, 3476.

157. Bertaut, F.; Blum, P., *C.R. Acad. Sci. Paris*, **1953**, *236*, 1055.

158. Druska, C.; Böttcher, P., *J. Alloys Compd.*, **1993**, *201*, 5.

159. Druska. C.; Böttcher, P., *Z. anorg. allg. Chem.*, **1994**, *620*, 1845.

160. Zhao, J.-T.; Corbett, J.D., *J. Alloys Compd.*, **1994**, *210*, 1.

161. Zachariasen, W.H., *Acta Crystallogr.*, **1948**, *1*, 265.

162. Meetsma, A.; de Boer, J.L.; van Smaalen, S., *J. Solid State Chem.*, **1989**, *83*, 370.

163. Guloy., A.M.; Corbett, J.D., *Z. anorg. allg. Chem.*, **1992**, *616*, 61.

164. Lugscheider, E.; Knotek, O.; Reimann, H., *Monatsch. Chem.*, **1974**, *105*, 80.

165. Okada, S.; Atoda, T; Higashi, I., *J. Sol. State Chem.*, **1987**, *68*, 61.

166. Pöttgen, R.; Simon, A., *Z. anorg. allg. Chem.*, **1996**, *622*, 779.

167. Eisenmann, B.; Schäfer, H., *Z. Naturforsch.*, **1974**, *29B*, 460.

168. Gladyshevskii, E.I.; Kripyakevich, P.I., *Inorg. Mat.* (Engl.), **1965**, *1*, 644.

169. Hohnke, D.; Parthé, *Acta Crystallogr.*, **1966**, *20*, 572.

170. Tchernev, D.I.; Narasimhan, K.S.V.L.; Steinfink, H., *IEEE Trans. Magns.*, **1969**, *5*, 222.

171. Mayer, I.; Shidlovsky, I., *Inorg. Chem.*, **1969**, *8*, 1240.

172. Gladyshevskii, E.I., *J. Struct. Chem.* (Engl.), **1964**, *21*, 593.

173. Buschow, K.H.J.; Fast, J.F., *Phys. Status Solidi*, **1967**, *21*, 593.

174. Dorrscheidt, W.; Widera, A.; Schàfer, H., *Z. Naturforsch.*, **1977**, *32B*, 1097.

175. Harp, J., *M.S. Thesis*, Iowa State University, **1994**.

176. Jeitschko, W.; Parthé, *Acta Crystallogr.*, **1967**, *22*, 551.

177. Palenzona, A.; Cirafici, S., *J. Less-Common Met.*, **1976**, *46*, 321.

178. Bruzzone, G.; Merlo, F., *J. Less-Common Met.*, **1976**, *48*, 103.

179. Bruzzone, G.; Franceschi, E., *J.* Less-Common Met., **1977**, *52*, 211.

180. Sands, D.E.; Wood, D.H.; Ramsey, W.J., *Acta Crystallogr.*, **1964**, *17*, 986.

181. Franceschi, E., *J. Less-Common Met.*, **1970**, *22*, 249.

182. Schobinger-Paramantellos, P.; Buschow, K.H.J., *J. Magn. Mag. Mat.*, **1985**, *49*, 349.

183. Semitelou, I.P.; Konguetsof, H.; Yakinthos, J.K., *J.* Magn. Mag, Mat., **1989**, *79*, 131.

184. Schobinger-Paramantellos, P., *J. Magn. Mag. Mat.*, **1982**, *28*, 97.

185. Semitelou, I.P.; Yakinthos, J.K.; Roudaut, E., *J. Phys. Chem. Solids*, **1995**, *56*, 891.

186. Leroy. J.; Moreau, J.M.; Paccard, D.; Parthé, E., *J. Less-Common Met.*, **1980**, *76*, 131.

187. Schewe-Miller, I., *Ph.D. Thesis*, Universität Stuttgart and Max-Planck-Institut für Festkörperforschung, Stuttgart, Germany, **1990**.

188. Fornasini, M.; Merlo, F., *Z. Krisatllogr.*, **1989**, *187*, 111.

189. Palenzona, A.; Franceschi, E., *J. Less-Common Met.*, **1968**, *14*, 47.

190. Franceschi, E.; Palenzona, A., *J. Less-Common Met.*, **1969**, *18*, 93.

191. Delfino, S.; Saccone, A.; Borzone, G.; Ferro, R., *Z. anorg. allg. Chem.*, **1983**, *503*, 184.

192. Stöhr, J.; Schàfer, H., *Z. Naturforsch.*, **1979**, *34b*, 653.

193. von Schnering, H.-G., *Angew. Chem. Int. Ed. Engl.*, **1981**, *20*, 33.

194. *CRC Handbook of Chemistry and Physics*, &0th ed., Weast, R.C. ed.-in-chief, CRC Press, Boca Raton, Fl., **1989**, p F197.

195. Cotton, F.A.; Wilkinson, G., *Advanced Inorganic Chemistry*, John Wiley and Sons, New York, **1988**, p240.

196. Dong, Z.-C.; Corbett, J.D., *Inorg. Chem.*, **1996**, *35*, 3107.

197. Leon-Escamilla, E.A.; Hurng, W.-M.; Peterson, E.S.; Corbett, J.D., *Inorg.Chem.*, **1996**, submitted.

198. Fornasini, M.L.; Pani, M.J., *J. Alloys Compd.*, **1994**, *205*, 179.

199. Albright, T.A.; Burdett, J.K.; Whangbo, M.-H., *Orbital Interactions in Chemistry*, Wiley-Interscience, New York, **1985**, Ch. 22.

200. Henning, R.S.; Leon-Escamilla, E.A., Zhao, J.-T., Corbett, J.D., *Inorg.Chem.*, Manuscript in preparation.

201. Smith, G.S.; Johnson, Q.; Tharp, A.G., *Acta Crystallogr.*, **1967**, *22*, 269.

202. Fornasini, M.L.; Pani, M., *Acta Crystallogr.*, **1986**, *42C*, 394.

203. Fornasini, M.L.,; Merlo, F., *Rev. Chim. Minerale*, **1979**, *16*, 458.

204. Snyder, G.J.; Simon, A., *J. Chem. Soc. Dalton Trans.*, **1994**, 1159.

205. Snyder, G.J.; Simon, A., *Z. Naturforsch.*, **1994**, *49b*, 189.

206. Snyder, G.J.; Simon, A., *J. Am. Chem. Soc.*, **1995**, *117*, 1996.

ACKNOWLEDGMENTS

The author wishes to thank Professor John. D. Corbett for his guidance, support and patience throughout the course of this research. He has provided the author the freedom to explore new fields in solid state chemistry as well as to question prior findings.

Dr. Victor Young, Professor Robert A. Jacobson and his group are thanked for their assistance with the single crystal diffractometers; Mr. Jerome E. Osterson for conducting the magnetic susceptibility measurements; Professor Constantine Stassis and Dr. Panagiotis Dervenagas for the powder neutron diffraction experiments; Professor Gordon Miller is thanked for allowing the author to access the extended Hückel calculations programs; Professor Hugo F. Franzen is acknowledged for the use of the induction furnace.

Past and present members of the Corbett's group and Ms. Shirley Standley will warmly be remembered. All provided patient support, lively discussions and their immeasurable friendship.

Professor Roald Hoffmann is greatly acknowledged for his friendly advice and support that allowed the author to pursue his aspiration of a higher education degree in the United States.

The author is greatly indebted to his parents *Elvira* and *Efigenio*. They allowed the author to pursued his own goals, his sisters (*Elia, Silvia, Martha, Elizabeth, Araceli* and *Susana*) and brothers (*Marco Antonio* and *Noé*) are thanked for their uninterrupted support and encouragement.

Finally, the author expresses his immense gratitude to Dr. Julia Bas for her love, patience and understanding. This work would have never been completed without her help.